Dinuclear Metal Complexes：Multifunctional Properties and Applications

Guangfu Li,[a] Dongxia Zhu,[a*] Xinlong Wang,[a] Zhongmin Su,[a,b*] and Martin R. Bryce[b*]

The development of metal complexes for optoelectronic applications is a fertile area of research. In contrast to the rigorous development of mononuclear metal complexes, dinuclear species have been less well studied and their fundamental chemistry and applications are under-explored. However, dinuclear species present special properties and functions compared with mononuclear species as a consequence of tuning the bridging ligands, the cyclometalated ligands or the two metal centers. More recently, dinuclear species have enabled important breakthroughs in the fields of OLEDs, photocatalytic water splitting and CO_2 reduction, DSPEC, chemosensors, biosensors, PDT, smart materials and so on. Here we present an overview of recent developments of dinuclear metal complexes, their multifunctional properties and their various applications. The relationship between structure and property of dinuclear species and important factors which influence device performance are discussed. Finally, we illustrate some challenges and opportunities for future research into dinuclear metal complexes. This review aims to provide an up-to-date summary and outlook of functional dinuclear metal complexes and to stimulate more researchers to contribute to this exciting interdisciplinary field.

[a] Department of Chemistry, Northeast Normal University, 5268 Renmin Street, Changchun, Jilin Province 130024, P. R. China. E-mail: zhudx047@nenu.edu.cn,zmsu@nenu.edu.cn

[b] School of Chemistry and Environmental Engineering, Changchun University of Science and Technology, Changchun, 130022, China

[c] Department of Chemistry, Durham University, Durham, DH1 3LE, UK. E-mail: m.r.bryce@durham.ac.uk

Guang-Fu Li received his BS (2011) in Chemical Engineering and Technology from Yanbian University and his PhD (2017) in Chemistry department from NENU in the group of Prof. Zhong-Min Su under the supervision of Prof. Li-Kai Yan and Prof. Dong-Xia Zhu. In 2015–2016, he was an joint PhD student at Durham University (UK) under the supervision of Prof. Martin R. Bryce. He currently carries out his postdoctoral work in Chemistry department at NENU. His research is mainly on the development of functional organic/polymeric photoelectric materials and devices.

Prof. Dong-Xia Zhu received her PhD (2005) in chemistry department under the supervision of Prof. Zhong-Min Su from NENU. In 2001–2002, she was a joint PhD student at Jilin University under the supervision of Prof. Yue Wang. In 2011–2012, she was an academic visitor at Durham University (UK) in the group of Prof. Martin R. Bryce and Prof. Todd B. Marder. She has been a full professor in chemistry department at NENU since 2017. Her research interests mainly focus on functional organic/polymeric photoelectric materials and devices.

Prof. Xin-Long Wang received his PhD (2006) from NENU under the supervision of Prof. En-Bo Wang. He has been a full professor at NENU since 2009. In 2014, he worked as a visiting scholar in Rutgers University. His main research interest is the syntheses, structures and properties of POMs and the design and application of POMs-based battery materials.

Prof. Zhong-Min Su received his BS (1983) and then his PhD in inorganic chemistry under the supervision of Prof. Rong-Shun Wang and Prof. Chi-Ming Che from NENU (1997). He has been a full professor at NENU since 1994. Later, he worked as a visiting scholar in the group of Prof. Chi-Ming Che and Prof. Guan-Hua Chen (The University of Hong Kong), in Prof. Koji

Ohta's group (National Industrial Technology Research Institute, Japan), and in Prof. N. Roesch's group (Technical University of Munich, Germany). His research interests focus on functional material chemistry and quantum chemistry.

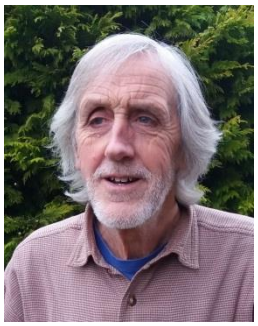

Prof. Martin Bryce received his B.Sc. from Wolverhampton Polytechnic and his D.Phil. from the University of York, UK. After postdoctoral work at the University of British Columbia in Prof. Larry Weiler's group, and Bristol University in Prof. Roger Alder's group, he moved to Durham University. Since 1995 he has been a full professor of chemistry at Durham. He has held visiting scientist positions at the University of California, Santa Barbara, the University of Copenhagen and the University of Florida, Gainesville. His research covers molecular design, synthesis and properties of optoelectronic materials (small molecules and polymers), molecular electronics and nano-scale chemistry.

Chem Soc Rev

REVIEW ARTICLE

1. Introduction

The continued development of organometallic complexes is a very important and intriguing topic due to their established applications in optoelectronic devices such as organic light emitting diodes (OLEDs),[1-6] light-emitting electrochemical cells (LEECs),[7-12] electrochemical luminescence (ECL),[13-18] chemosensors,[19-23] biosensors,[24-28] and photodynamic therapy (PDT),[29-33] as well as emerging areas including photocatalytic water splitting and CO_2 reduction,[34-44] dye-sensitized photoelectrosynthesis cells (DSPEC),[45-49] and smart materials.[50-54] Compared with the rigorous development of mononuclear metal complexes, dinuclear metal complexes have been less well studied and in many ways are in their infancy. The major challenges are as follows: (i) Obtaining dinuclear complexes can require complicated synthetic processes that give low production yields.[55-57] (ii) Dinuclear complexes are often obtained as a mixture of diastereomers which are very difficult to separate.[58-62] (iii) Complicated inter- and intra-molecular electron and energy transfer processes can make their properties hard to predict.[63-67] (iv) Dinuclear complexes often feature poor optical properties with low photoluminescence quantum yields (PLQYs) and short excited state lifetimes due to the large contribution of non-radiative excited states from the bridging ligands.[59, 68-71] (v) Stable true-blue phosphors, especially blue electroluminescene (EL), is still difficult to obtain in dinuclear systems due to the more conjugated structure compared with their mononuclear analogues.[72] (vi) Dinuclear complexes have relatively large molecular weights so they generally cannot be thermally evaporated to form thin films when making optoelectronic devices, requiring solution processing instead.[73-77] Therefore, it is not surprising that dinuclear systems have attracted less attention than mononuclear counterparts. Nonethless, important progress has been made with dinuclear metal complexes in optoelectronic applications, as summarised in Fig. 1. These studies clearly reveal that dinuclear species are viable for practical applications, and a better understanding of their structure-property relationships will accelerate the development of more efficient materials and devices.

This review article presents important advances in dinuclear metal complexes and their various applications, with emphasis on recent developments. Fundamental studies on these complexes are also discussed. The aim of this review is to provide an in-depth understanding of the structure-property relationships of dinuclear complexes and to highlight key aspects for improving their photoelectronic performance. It is our intention to stimulate more researchers to enter into this fascinating field.

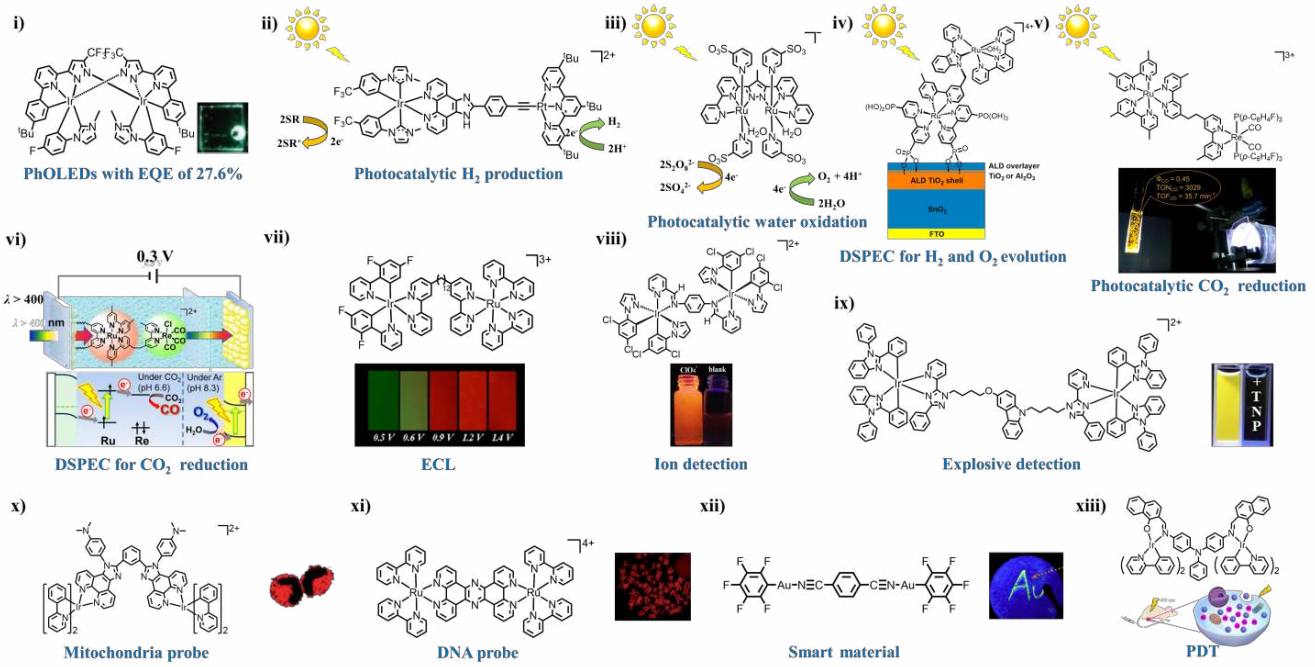

Fig. 1 Representative breakthroughs in the development of dinuclear complexes for various applications. i) In 2018, Liao *et al.* reported OLEDs with EQE of 27.6% using dinuclear Ir(III) complexes.[78] ii) In 2015, Yu *et al.* reported photocatalytic H_2 production with TONs of 1672 using an Ir(III)−Pt(II) supramolecular photocatalyst.[79] iii) In 2015, Berardi *et al.* reported photocatalytic O_2 production with TONs and TOFs of 2373 and 11.1 s^{-1}, respectively, using a dinuclear Ru(II) supramolecular photocatalyst.[80] iv) In 2015, Alibabaei *et al.* reported a "core–shell" photoanode based on a dinuclear Ru(II) complex with photocurrent reaching 1.97 mA cm^{-2}; the Faradaic efficiencies of DSPEC for H_2 and O_2 generation after 100 s were calculated as 57% and 41%, respectively.[81] v) In 2013, Tamaki *et al.* reported photocatalytic CO_2 reduction with TONs of 3029 using a Ru(II)−Re(I) supramolecular photocatalyst.[82] vi) In 2016, Sahara *et al.* reported DSPEC with a NiO−RuRe hybrid photocathode for photoelectrochemical CO_2 reduction in an aqueous solution.[83] vii) In 2015, Sun *et al.* reported adjustable emission color in an ECL based on an Ir(III)−Pt(II) emitter *via* alternation of the scanning potentials.[84] viii) In 2015, Li *et al.* reported an AIE-active dinuclear Ir(III) complex for the rapid, highly selective and sensitive sensing of perchlorate ions.[85] ix) In 2017, Cui *et al.* reported an AIE-active dinuclear Ir(III) complex for the rapid, highly selective and sensitive sensing of the explosive trinitrophenol (TNP).[86] x) In 2015, Chen *et al.* reported a dinuclear Ir(III) complex for mitochondrial imaging and tracking.[87] xi) In 2014, Baggaley *et al.* reported two-photon phosphorescent lifetime imaging microscopy (PLIM) probes based on a dinuclear Ru(II) emitter for nuclear DNA in both live and fixed cells.[88] xii) In 2008, Ito *et al.* described reversible mechanochromic luminescence in a dinuclear Au(I) complex.[89] xiii) In 2019, Zhang *et al.* presented AIE-active Ir(III) complexes as photosensitizers for PDT *in vitro* and *in vivo*.[90]

2. Basic properties of dinuclear complexes

Several important questions immediately arise when considering dinuclear systems and their optoelectronic properties, such as: i) Diastereoisomers or geometrical isomers usually exist in the dinuclear systems: is there any tendency for one isomer to predominate over others? What is the structure-property relationship within such isomer systems? Can these isomers be separated? ii) What are the mechanisms of electron/energy transfer in the dinuclear systems? iii) What is the influence on the spin-orbit coupling (SOC) when another metal atom is introduced in the same molecule? iv) When combining two individual metal components in one molecule, are the properties essentially a summation of those of the individual components, or are they very different? In this section, questions i) and ii) will be discussed in detail based on recent progress in dinuclear metal complexes. Questions iii) and iv) will be discussed in the next section.

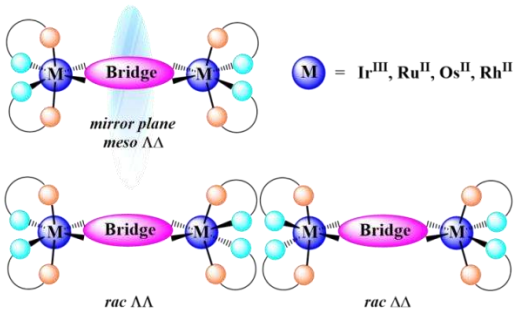

Fig. 2 Diagrammatic representation of the *meso* and *racemic* forms of dinuclear transition metal complexes.

2.1 Isomers of dinuclear metal complexes

2.1.1 Diastereoisomers

Diastereomers mixtures of *meso* (ΛΔ) and *rac* (ΔΔ/ΛΛ) isomers are usually present in dinuclear metal systems due to the chiral nature of the metal centers. The most fundamental example of the genre is $[M(CL)_2]_2(BL)$, where CL is a cyclometallated ligand such as bidentate 2-phenylpyridine (ppy), and BL is a symmetrical bridging ligand including a flexible bis-atoms bridge and a rigid aromatic bridge (Fig. 2). The separation of diastereomers is crucial for understanding their detailed structure-property relationships and for further applications. However, until now, only a few cases have been reported of complete separation of diastereomers.[85, 91-96] Hua and von Zelewsky first reported a successful way for the selective preparation of isomerically pure dinuclear complexes by using an enantiomerically pure chiral building block for Ru complexes.[91] Keene *et al.* developed chromatographic methods for separation of Ru enantiomers by ion-exchange chromatography, using chiral eluents.[92] Ye *et al.* have recently developed a useful tactic for avoiding the formation of diastereomeric mixtures *via* a chiral precursor strategy using *L*- or *D*-proline as an auxiliary ligand.[95] The direct synthetic routes for pure enantiomers, ΛΛ and ΔΔ, are shown in Fig. 3. This strategy has also been applied to the larger enantiopure multimetallic Ir(III) systems.[97, 98] Until recently, the separation of diiridium diastereomers was achieved by facile fractional crystallization, silica column chromatography without chiral eluents, or a combination of the two techniques.[94, 96] The ratios of diiridium diastereomers are still hard to predict: for example, the *meso*-isomer is usually favoured over the *rac*-isomer in a diiridium system with diarylhydrazide bridging ligands. However, opposite results were obtained from the parent diiridium dimers $[Ir(ppy)_2(\mu\text{-}Cl)_2]_2$, where the ratio of *rac*-isomer is higher than *meso*-isomer.[99, 100] These different results are probably induced by the interligand steric interactions.

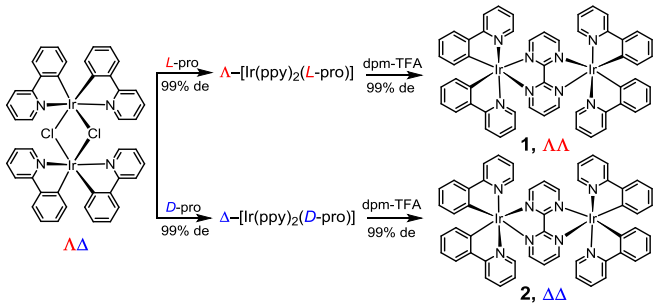

Fig. 3 The synthetic routes for enantiomers **1**, ΛΛ and **2**, ΔΔ.[95]

Meso (ΛΔ) and *rac* (ΔΔ/ΛΛ) isomers often exhibit distinguishing photophysical properties due to their different molecular conformations. For example, Williams and Lincoln *et al*. had successfully reported a series of dinuclear Ru(II) complexes isomers *via* a chiral precursor strategy. The photoluminescent properties of these complexes upon binding to DNA has been studied.[101-108] In aqueous solution, the luminescence of dinuclear Ru(II) complex **3** ([μ-(11,11'-bidppz)(phen)$_4$Ru$_2$]$^{4+}$; phen = 1,10-phenanthroline, 11,11'-bidppz = 11,11'-bi(dipyrido[3,2-*a*:2',3'-*c*]phenazinyl)) is essentially quenched at ambient temperatures, probably by protonation of the phenazine nitrogen by water.[101] However, a dramatic increase in luminescence intensity, referred to as the "light-switch" effect, with higher quantum yield was observed when complex **3** is bound to poly(dA-dT)$_2$.[102, 103,105] The quantum yield for *rac*-ΔΔ was measured to be 9%, which is approximately 7-8 times higher than that found for the *meso*-ΛΔ and *rac*-ΛΛ isomers with 1.3% and 1.1%, respectively. This suggests that the nitrogens of the bidppz ligand of the ΔΔ isomer may be shielded from protonation.[103] A similar variation in quantum yields was also observed for Δ-compared to Λ-[Ru(phen)$_2$(dppz)]$^{2+}$ due to a difference in location of the DPPZ ligand within the intercalation pocket. Interactions between closely bound complex ions may also play a role.[106] The final binding geometry studies of the three stereoisomers of complex **3** in poly(dA-dT)$_2$ suggested that the bidppz ligand is intercalated between the nucleobases in an *anti* conformation, with a small rotation around the central pivot bond. The complex intercalates asymmetrically, with one of the Ru(phen)$_2$ moieties deeply intercalated from the minor groove side.[103, 105]

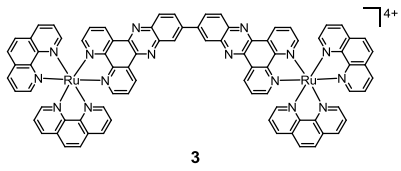

Fig. 4 The chemical structure of complex **3**.

2.1.2 Geometrical isomers

Cis–trans isomerism, also known as geometric isomerism or configurational isomerism, is a standard term in organic chemistry. For dinuclear complexes, *cis* indicates that the functional groups are on the same side of the two metal centers while

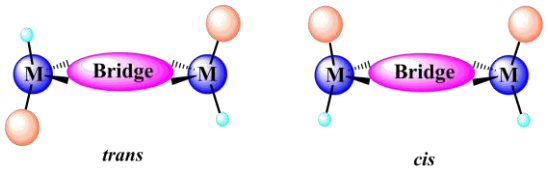

Fig. 5 Diagrammatic representation of the *trans* and *cis* forms of dinuclear transition metal complexes.

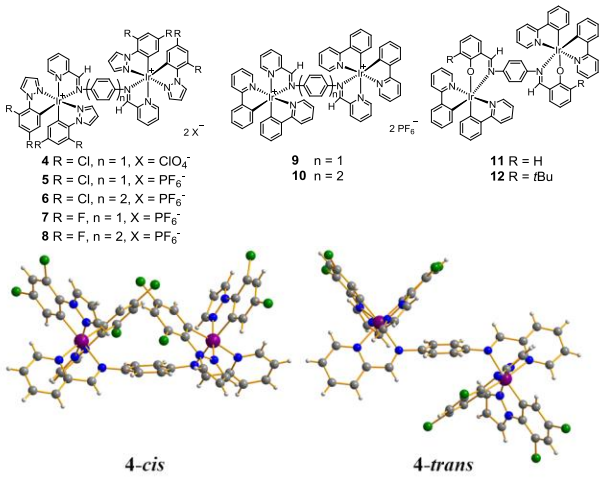

Fig. 6 Molecular structures of **4**–**12** (top) and X-ray crystal structures of **4-*cis*** and **4-*trans*** (bottom). The anions and solvent molecules are omitted for clarity.

trans conveys that they are on opposing sides (Fig. 5). Recently, we reported a series of aggregation induced phosphorescent emission (AIPE)-active dinuclear Ir(III) system with Schiff base bridging ligands, and their applications in anion detection, chemo/bio-sensors and information storage (Fig. 6).[50, 85, 109-111]

For ionic dinuclear Ir(III) complexes, *cis–trans* isomeric mixtures were found in the complexes **4**, **5**, **7** and **9** with phenyl in the bridging ligands. However, *cis–trans* isomerization was not observed in the complexes **6**, **8** and **10** with biphenyl in the bridging ligands. Indeed many studies had pointed out that the isomeric mixtures could be predicted by the conjugated bridging chain length in the dinuclear systems. A short conjugated bridging ligand could induce isomeric mixtures,[112-115] but this is not the case with a longer conjugated bridging ligand.[68, 116-118] Our work revealed no *cis–trans* mixtures in the neutral dinuclear Ir(III) complexes **11** and **12** with short conjugated bridging ligands; only the stable *trans* isomer was observed.[109, 110] Therefore, it seems that *cis–trans* isomerization is induced not only by the length of conjugated bridging chains, but also by a counter ion effect.

The *cis–trans* isomers in the complex **4** with ClO_4^- counter ions were separated by fractional crystallization and their crystal structures were obtained (Fig. 6). The ratio of *cis–trans* isomers in **4** was calculated as 2.58/1, which is higher than in the analogous complex **5** with PF_6^- counter ions. This result reveals that the isomer ratios are induced by the counter ions, and can be tuned by the counter ion exchange process. For instance, the ratio of *cis* isomer increased when ClO_4^- was

added to a solution of complex **5**·PF_6. Furthermore, **4**-*cis* isomer showed significantly higher PLQYs (31%) than the **4**-*trans* isomer (13%) in solution. The reason may be the distorted geometry in the **4**-*trans* isomer that would favour non-radiative processes, whereas the more planar geometry (**4**-*cis* isomer) would increase radiative processes, as observed previously.[119]

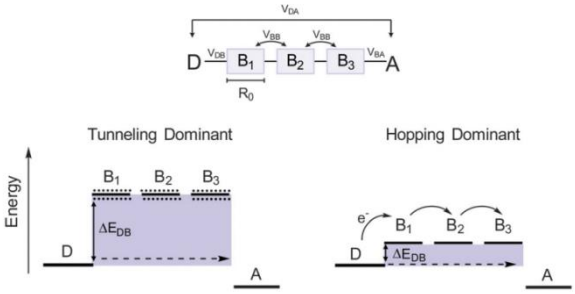

Fig. 7 Schematic comparison of the tunneling (left) and hopping (right) mechanisms of electron transfer in a D–B–A system. The McConnell superexchange model for electron tunneling through molecular structures is illustrated in the top drawing. For the tunneling model, the bridge virtual states are represented as dashed lines; while in the hopping model, the local bridge states are drawn as solid lines. ΔE_{DB} is the tunneling energy barrier for electron injection onto the bridge; V_{DA} represents the overall electronic coupling in a system, which depends on three distinct electronic couplings V_{DB}, V_{BB} and V_{BA}; R_0 represents the length of the individual bridging units. Reproduced with permission from ref. 65. Copyright 2015 The Royal Society of Chemistry.

2.2 Photoinduced electron and energy transfer in dinuclear metal complexes

Photoinduced electron and energy transfer processes commonly occur in dinuclear metal systems, such as Ru(II)−Rh(III),[120, 121] Ru(II)−Os(II),[122-128] Ru(II)−Ni(II),[129] Ru(II)−Zn(II),[130] Ru(II)−Cu(II),[131] Ru(II)−Ru(II),[64, 67] Ir(III)−Ru(II),[125, 132, 133] Ir(III)−Pt(II),[129] Ir(III)−Eu(III),[134] Ir(III)−Ir(III)[56]. Therefore, bimetallic complexes are popular choices as donor-bridge-acceptor (D-B-A) systems for investigations of photoinduced electron and energy transfer process. As shown in Fig. 7, the electron transfer usually occurs *via* two fundamentally different mechanisms: the coherent tunneling or incoherent hopping mechanism.[65, 135] The tunneling mechanism is often described by the superexchange model,[136] which requires the donor and acceptor at either ends of the bridge to be energetically well separated from the bridge states. In this situation the bridge is neither reduced nor oxidized but merely functions as a coupling medium for the transfer process. In contrast, the incoherent hopping mechanism involves real intermediate states that actively transport the electron or hole along the bridge. For energy transfer, through-space (Förster) or through-bond (Dexter) are the two main mechanisms (Fig. 8).[137] Thus, understanding the mechanism of photoinduced electron and energy transfer is crucial for further design of functional dinuclear metal complexes and their applications in optoelectronic devices. In this section, representative dinuclear complexes have been chosen to illustrate various approaches taken to investigate energy and electron transfer.

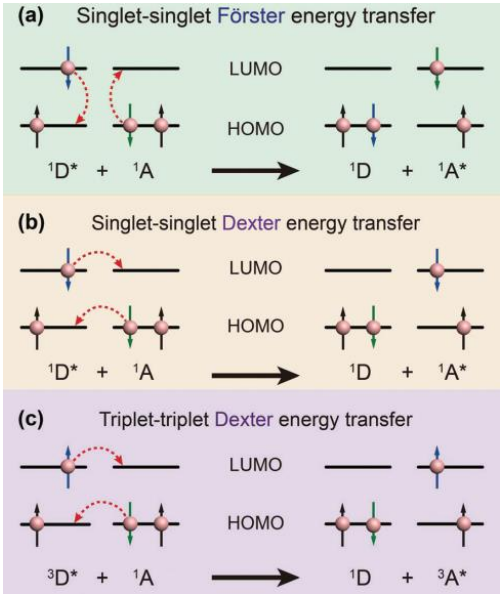

Fig. 8 Schematic diagrams of (a) Förster energy transfer and (b, c) Dexter energy transfer. D and A denote donor and acceptor, respectively. Reproduced with permission from ref. 137. Copyright 2014 The Royal Society of Chemistry.

2.2.1 Effects of the selection of bridge ligand on intramolecular electron transfer processes

In early work on electron and energy transfer, a Ru(II)−Rh(III) system was first studied by Scandola and coworkers.[120] The hetero-dinuclear complex **13** consists of two structurally similar components, namely, metal tris(po1ypyridine) complexes, linked by a flexible ethylene chain (Fig. 9). The Ru(II) component acts as the donor (D), and the Rh(III) component unit as the acceptor (A). A wide range of techniques such as picosecond laser spectroscopy, nanosecond single-photon counting (emission lifetimes), Raman spectroscopy and transient absorption measurements were applied to investigate the mechanism of electron and energy transfer between the two metal components. The cyclic voltammogram of **13** showed a Ru(II)/(III) oxidation potential at 1.13 V vs SCE, Rh(III)/(II) reduction potential at -0.92 V and two ligand-ligand' reduction potentials at -1.45 V and -1.66 V, respectively, which showed a superposition of the corresponding curves of the single Ru(II) component and the Rh(III) component. This result indicated that the interaction between the two polypyridyl centers is insignificant, thus metal-metal interaction takes place *via* a hole transfer through-bond superexchange process in the ground state (Fig. 10b).[138] The UV-vis absorption spectrum of **13** is an exact superposition of the spectra of the isolated mononuclear species, without a new band arising. Interestingly, although a weak intercomponent interaction was demonstrated by both UV-vis absorption and electrochemical results, the emission of **13** demonstrated 90%

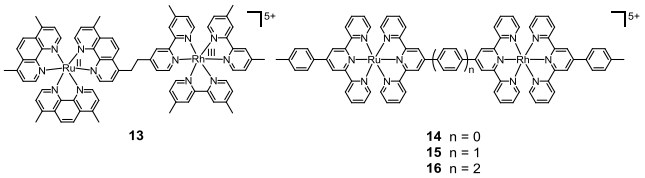

Fig. 9 Molecular structures of Ru(II)−Rh(III) complexes **13**–**16**.

quenching in comparison with the mononuclear Ru(II) complex. Based on the spectroscopic and redox data given above, both electron transfer to the Rh(III) moiety and energy transfer from the Ru(II) to the Rh(III) center are thermodynamically allowed and could be responsible for the quenching process. To further investigate the intercomponent quenching process, *i.e.* energy vs electron transfer, transient absorption

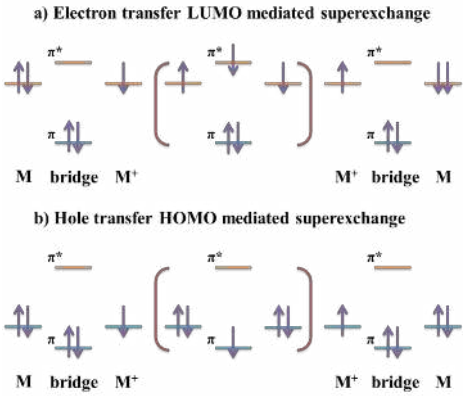

Fig. 10 a) Electron and b) hole transfer superexchange through bridging ligand π/π* orbitals. Reproduced with permission from ref. 138. Copyright 2005 The Royal Society of Chemistry.

spectroscopy was performed. The energy level diagram of **13** and the two individual mononuclear components is shown in Fig. 11. At room temperature, in acetonitrile solution, both ^{3}*Ru(II)−Rh(III) and ^{3}Ru(II)−*Rh(III) states could be quenched by the two electron-transfer processes, leading to a Ru(III)−Rh(II) state and subsequently to the ground Ru(II)-Rh(III) state. In theory, ^{3}Ru(II)−*Rh(III)→^{3}*Ru(II)−Rh(III) energy transfer could also occur (ΔG^o = -0.61 eV) at room temperature. However, the lack of observed energy transfer might be attributed to more efficient competition by the faster electron quenching process from ^{3}Ru(II)−*Rh(III)→Ru(III)−Rh(II). By contrast, at 77 K or in a more rigid environment, this energy transfer is favourable, where both electron transfer quenching processes are blocked as a consequence of restricted solvent repolarization.

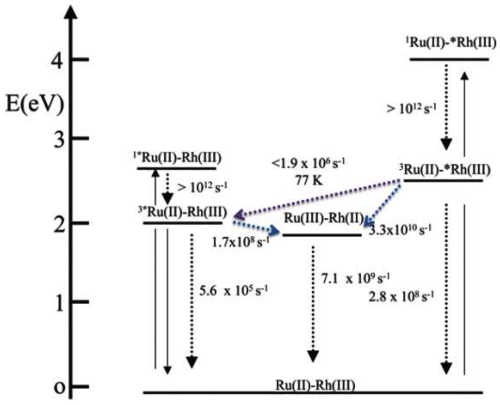

Fig. 11 Energy level diagram of complex **13** (Purple dot line represents energy transfer and blue dot lines represent electron transfer). Reprinted with permission from ref. 120. Copyright 1994 American Chemical Society.

The hetero-dinuclear Ru(II)-Rh(III) complexes **14**–**16** consisting of two terdentate ligands (based on 2,2′:6′,2″-terpyridine, tpy), bridged by the rigid phenylene spacers of differing lengths, which gives variable metal-metal distances (11, 15.5 and 20 Å for n = 0, 1 and 2, respectively) were reported by Sauvage and coworkers (Fig. 9).[121] The mechanisms of photoinduced electron and energy transfer in these complexes were discussed in detail. Interestingly, excited state ^{3}Ru(II)−*(MC) Rh(III)→^{3}*(MLCT) Ru(II)−Rh(III) energy transfer was found to be efficient for all the complexes at both 77 and 150 K. However, electron transfer quenching did not occur for all the complexes at 77 K which is in line with the previous opinion of Scandola *et al.*[120] Electron transfer quenching was observed at 150 K only in complex **14** (n = 0), and not in **15** and **16** (n = 1 and 2). This data indicates that electron transfer from excited Ru(II) to Rh(III) is efficient for **14** but not for the **15** and **16.** The following rate constants for electron transfer from excited Ru(II) to Rh(III) were obtained: **14**, 5 × 10^6 s^{-1}; **15**, 1 × 10^5 s^{-1}; **16**, 4 × 10^4 s^{-1}. These results were rationalized in terms of more favourable electronic factors and smaller reorganizational energies for **13**.

2.2.2 Förster energy transfer in phenylene bridged systems

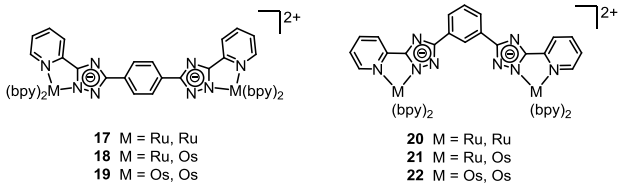

Fig. 12 Molecular structures of complexes **17**–**22**.

In 2004, Vos *et al.* reported a series of Ru−Ru, Ru−Os and Os−Os dinuclear complexes **17**–**22** with triazole-based bridging ligands and *m*- or *p*-phenylene substitution (Fig. 12).[123] The homo-dinuclear complexes **17**, **19**, **20** and **22** showed a similar redox potential corresponding to their mononuclear species. However, the hetro-dinuclear complexes **18** and **21** presented

an exact superposition of the redox potentials of the isolated mononuclear Ru and Os components. This result indicated that the electronic interaction is insignificant between the two metal centers. The most interesting observation is that both hetro-dinuclear complexes **18** and **21** present dual emission at 77 K corresponding to their Ru(II) and Os(II) components, respectively (Fig. 13). The Ru emission parts in **18** and **21** are only 6% of the intensity in their homo-dinuclear analogues **17** and **20**. The quenching of Ru(II) emission by the Os(II) center originates from the energy transfer mechanism. Excited state lifetime results revealed that both hetro-dinuclear complexes **18** and **21** showed much shorter lifetimes than the homo-dinuclear complexes. These results again demonstrated that energy transfer occurred from the Ru(II) component to the Os(II) component, consistent with the emission results above. An estimation of the energy transfer rate and the observation of temperature independent energy transfer rates for all complexes supported dipole-dipole (Förster) energy transfer as the dominant mechanism, rather than a through-bond Dexter mechanism *via* activated interligand hopping or superexchange which should show a strong temperature dependence. It is worth noting that the mechanism of energy transfer in protonated **18** (**18H**) at 293 K can be assigned to Dexter energy transfer because it is both protonated and *para*-substituted, which combine to enhance electronic coupling between the chromophores, favouring through-bond energy transfer.

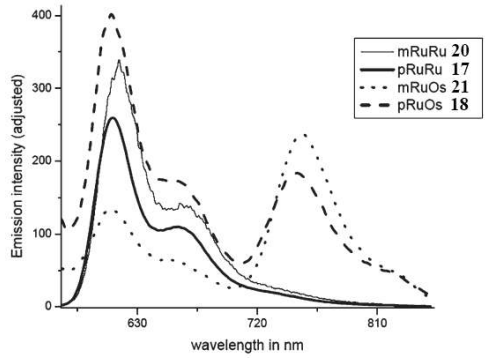

Fig. 13 Emission spectrum of dinuclear complexes at 77 K in basic ethanol/methanol 5/1 v/v. Reprinted with permission from ref. 123. Copyright 2004 American Chemical Society.

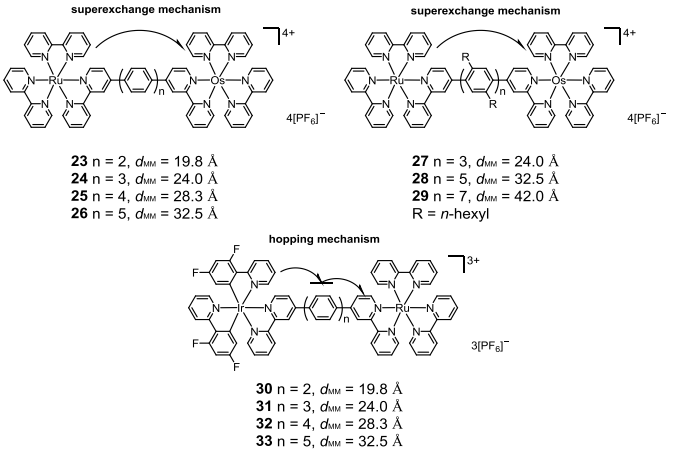

Fig. 14 Molecular structures of complexes **23**–**33** and corresponding Dexter energy transfer mechanisms.

2.2.3 Dexter energy transfer in phenylene bridged systems

To investigate the relationships between energy transfer and structural features a series of hetero-dinuclear Ru(II)−Os(II) complexes **23**–**26** (Fig. 14) connected by different conjugated lengths of *para*-phenylene bridging ligands (n = 2, 3, 4, 5) was reported by De Cola and coworkers in 2005.[127] Basic photophysical data revealed energy transfer between the higher energy Ru(II) and the lower energy Os(II) components in all the complexes, which is consistent with the previous results of similar Ru−Os complexes with *n*-hexyl substituted bridging ligands.[128] A schematic energy-level diagram for **23**–**26** is shown in Fig. 15a. The higher spin-allowed ^{1}MLCT excited state was estimated from the UV absorption bands, and the spin-forbidden ^{3}MLCT excited state was estimated from the 77 K emission for their mononuclear species. The triplet (^{3}MLCT) energies of the Ru and Os components are 2.10 and 1.73 eV, respectively, thus the energy transfer process can be induced by an exergonic $G = -0.37$ eV. Time-resolved emission and sub-picosecond transient absorption spectroscopy were performed. The emission of the Ru(II) component is strongly quenched by the Os(II) component due to a very efficient energy transfer process. The energy transfer rate constants can be calculated from eqn (1),

$$k_{\text{en}} = \left(\frac{1}{\tau}\right) - \left(\frac{1}{\tau^0}\right) \qquad (1)$$

where τ and τ^0 are the lifetimes of the quenched and unquenched ruthenium based luminescence, respectively. In order to establish the role of the bridging ligands in the energy transfer process, similarity structured Ru−Os complexes with *n*-hexyl substituted bridging ligands were selected for comparison.[128] The only difference in the two systems is that complexes **27**−**29** show an increased dihedral angle distortion of 65º, compared to 20º for **23**−**26**. Thus, the presence of the bulky alkyl chains increases the tilt angle between the phenyl rings and therefore reduces the electronic communication along the phenylene spacers between the donor and acceptor moieties. The energy transfer rate constants are shown in Table 1. The rates are dramatically influenced by the conjugated chain length (n) and minor geometrical changes. The rates decrease for both

dinuclear systems with the increased conjugated chain length (n). For n = 3, there is 90-fold increase for **24** with good planarization of the bridging ligand compared to **27**. The difference in the energy transfer rates became smaller with the longest spacer with 5 phenylene units, with only 50-fold increase for **26** compared to **28**. The above results indicated that the Dexter mechanism of energy transfer (superexchange mechanism between two chromophores). The observed faster energy transfer in **23**−**26** than in **27**−**30** can be attributed to the good co-planarity of the phenylenes in **23**−**26** since the distance between the chromophores is the same for both series of complexes.

Following the previous Ru−Os work, De Cola *et al*. reported a series of similarly structured hetero-dinuclear Ir(III)-Ru(II) complexes **30**–**33** (Fig. 14) with different conjugated length of *p*-phenylene bridging ligands (n = 2, 3, 4, 5).[133] The Ir(III) and Ru(II) components act as donor and acceptor, respectively, thus, the energy transfer was observed from the Ir(III) to the Ru(II) component in the photophysical results.

Table 1 Energy transfer rates[a]

	$[Ru{-}ph_n{-}Os]^{4+}$	$[Ru{-}ph_nR{-}Os]^{4+}$
	k_{en}	k_{en}
$[Ru{-}ph_2{-}Os]^{4+}$	2.5×10^{11}	—
$[Ru{-}ph_3{-}Os]^{4+}$	5.9×10^{10}	6.7×10^{8}
$[Ru{-}ph_4{-}Os]^{4+}$	4.1×10^{9}	—
$[Ru{-}ph_5{-}Os]^{4+}$	4.9×10^{8}	1.0×10^{7}
$[Ru{-}ph_7{-}Os]^{4+}$	—	1.3×10^{6}

[a] ph = *p*-C_6H_4-; R = *n*-hexyl. In aereated acetonitrile solution.

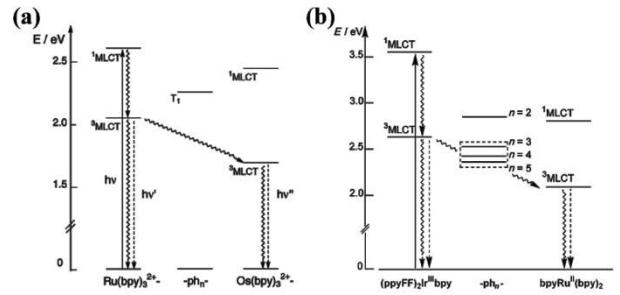

Fig. 15 Schematic energy-level diagrams for the energy transfer of the heterodinuclear complexes **23**–**26** (a); **30**–**33** (b). solid line: excitation; dashed line: luminescence; wavy line: radiationless decay. Reproduced with permission from ref. 127 (a) and 133 (b). Copyright 2005 Elsevier (a) and Copyright 2005 Wiley-VCH (b).

The energy-level diagrams for **23**–**26** and **30**–**33** shown in Fig. 15 reveal an energy transfer route from the higher excited ^{3}MLCT state of the Ir component to the lower excited ^{3}MLCT state of the Ru component. The emission of the Ir(III) component is strongly quenched by the Ru(II) component, and the emission intensity and lifetime of the Ru(II) component in all the complexes **30**–**33** are not affected by the different lengths of the bridging ligands. Time-resolved emission and sub-picosecond transient absorption spectroscopy probed the mechanism of energy transfer. The energy transfer rates decreased slightly as the bridging ligand's length increased, which showed a different trend compared with the previously reported Ru−Os series (Fig. 16). This result indicated an incoherent hopping mechanism (almost independent of the donor–acceptor distance) due to good orbital overlap between the donor and the phenylene chain. The authors envisaged that for the $[Ir{-}(C_6H_4)_n{-}Ru]^{3+}$ series, the triplet energy transfer is effective over a very long distance (*i.e*., > 20 nm) due to the long-lived excited state of such systems.

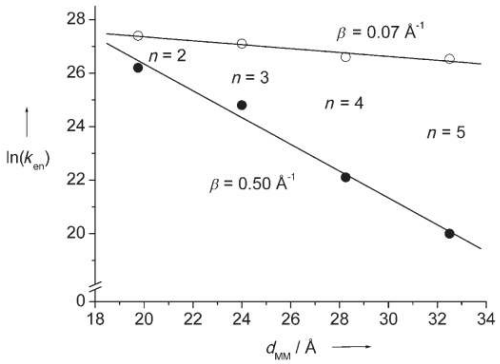

Fig. 16 Plot of ln(k_{en}) versus the metal–metal distance for the series $[Ir{-}ph_n{-}Ru]^{3+}$ (○) and $[Ru{-}ph_n{-}Os]^{4+}$ (●) (n = 2, 3, 4, 5, in both series) ph = *p*-C_6H_4-. Reproduced with permission from ref. 133. Copyright 2005 Wiley-VCH.

2.2.4 Intramolecular energy transfer in metal-center exchanged systems

Baitalik *et al*. reported two new hetro-dinuclear Ru(II)−Os(II) complexes **34** and **35** (Fig. 17)[126] in which the metals are exchanged in the two subunits. However, no Ru unit emission is observed in the complexes which revealed that the quenching originates from the Ru(II) to the Os(II) and is not controlled by the ligands. The excited state energies of the Os based component in **34** and **35** were calculated as 1.81 eV and 1.88 eV, respectively, estimated from the energies at the intersection point of the UV-vis absorption and emission spectra in acetonitrile solution at room temperature. The excited state energies of the Ru based component in **34** and **35** are 2.30 eV and 2.17 eV, estimated from the $E_{0\text{-}0}$ of their mononuclear complexes, respectively. Thus, the free energy change for energy transfer from the excited Ru-based component to the excited state of the Os-based component is -0.49 eV and -0.29 eV for **34** and **35**, respectively (Fig. 18) which makes the intramolecular energy transfer process ($*Ru^{II}Os^{II} \rightarrow Ru^{II}*Os^{II}$ and $Os^{II}Ru^{II}* \rightarrow Os^{II}*Ru^{II}$) thermodynamically favourable. Furthermore, the electronic quenching processes in both complexes were also considered. However, both photoinduced oxidative quenching ($*Ru^{II}Os^{II} \rightarrow Ru^{III}Os^{I}$) and reductive quenching ($*Ru^{II}Os^{II} \rightarrow Ru^{I}Os^{III}$) are thermodynamically unfavourable. In addition, experimental excited lifetime results indicated an efficient and very fast ($\sim 10^9$ s^{-1}) intramolecular energy transfer in both complexes.

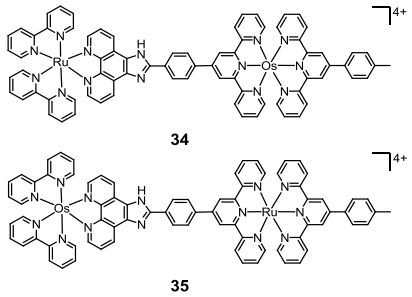

34

35

Fig. 17 Molecular structures of complexes **34** and **35**.

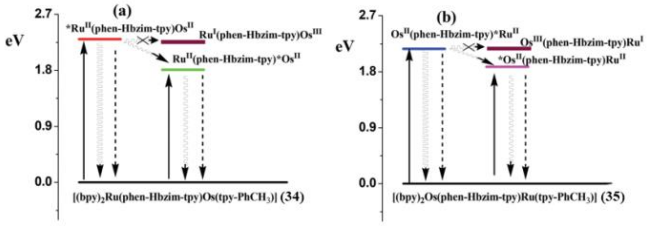

Fig. 18 Energy level diagrams showing the photoinduced energy transfer processes in (a) **34** and (b) **35**. Reproduced with permission from ref. 126. Copyright 2014 The Royal Society of Chemistry.

2.2.5 Intramolecular energy transfer through structuralmodification of the peripheral ligands

To investigate the energy transfer from ruthenium to osmium by substituent control, Constable *et al*. reported two structurally similar Ru_2−Os trinuclear complexes **36** and **37** (Fig. 19).[122] The pendant thienyl ligands on **37** enhance the lifetime of the ruthenium ^{3}MLCT state. For **36** and **37** the Ru and Os components are the donor and acceptor moieties, respectively. At room temperature, no energy transfer is observed for both complexes based on the emission spectra, which showed the signatures of the individual components. However, at 77 K, both complexes exhibited obvious energy transfer from Ru→Os; the Os unit emits strongly whereas the Ru unit emission was quenched to only 1% compared to its mononuclear complex. From time-resolved measurements the energy transfer rate constants were evaluated as 5.8×10^8 and 2.8×10^7 s^{-1} for **36** and **37**, respectively, *i.e.* 20-fold higher in **36** than **37**. Furthermore, temperature independent energy transfer revealed that the dipole–dipole Förster energy transfer mechanism was dominant for the Ru→Os energy transfer step within **36** and **37**, which is in accord with Vos's opinion.[123]

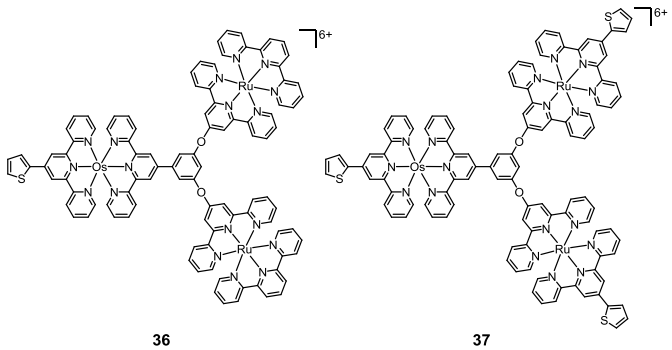

36 37

Fig. 19 Molecular structures of complexes **36** and **37**.

2.2.6 Conformational effect on electron transfer processes

How the torsion angle affects the extent of long-range electronic coupling in D–B–A systems was first studied by Harriman and co-workers.[139] As shown in Fig. 20, the complexes **38–41** are linked by an ethynylene-substituted biphenyl bridge that incorporates a constraining tether. The strap is intended to function as a ratchet giving access to a wide range of dihedral angles while keeping a fixed D–A distance. Triplet energy transfer rates were measured in a low temperature organic glass matrix to prevent any undesirable rotation from occurring. The results displayed a pronounced conformational dependence of the transfer rates between phenylene rings held at 0º and 90º. The electronic coupling was largest when the phenyl units were close to coplanar (φ = 30º). By contrast, at the largest dihedral angle (φ = 90º) the electronic coupling decreased drastically, resulting in a transfer rate that decreased by a factor of 80.

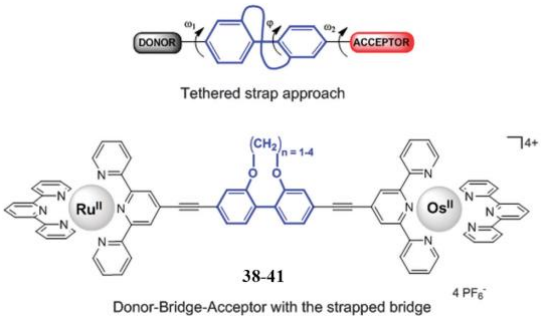

Fig. 20 Molecular structures of complexes **38–41**.

In conclusion, these representative examples have illustrated the role played by the bridge, metal centers and peripheral ligands in the photoinduced electron and energy transfer processes. It has been shown that the electron and energy transfer is stongly influenced by the triplet excited state energy of the individual components, the length of the bridge and the conformation of the bridge. However, it is still difficult to predict the charge transfer mechanism in a polynulcear complex based on current knowledge. For example, a hopping mechanism was confirmed in the Ir−Ru system, rather than a superexchange mechanism in the Ru−Os system which possesses the same bridging ligands. [127, 133] Careful design of molecular structure can afford precise control of distance, energy gap and conformational effects which can promote future investigations of the photoinduced electron and energy transfer processes and the development of molecular-based devices.[65]

3. Optoelectronic devices

3.1 OLEDs and LEECs

Organic lighting and display devices including organic light-emitting diodes (OLEDs)[2, 140-143] and light-emitting electrochemical cells (LEECs)[7, 144-147] have been exploited in

the emerging technologies of solid-state lighting and flat panel displays. Classical multilayer OLEDs and simpler LEEC structures are shown in Fig. 21. The operating principle of OLEDs is: 1) electrons and holes are injected from the cathode and anode, respectively, under an external electrical field, 2) electrons and holes transfer through an electron transfer layer (ETL) and a hole transfer layer (HTL) respectively, *via* a hopping mechanism and arrive at the interface of the emission layer (EML), 3) electron-hole pairs form when electrons and holes accumulate at the LUMO and HOMO of the emissive material, leading to exciton generation, charge recombination and emission. For the fabrication of the emission layer in OLEDs, several techniques are available, such as vacuum deposition,[148] conformal elastomeric masking,[149] cold welding,[150] thermal imaging,[151] organic vapor jet printing,[152] or solution processing.[153] In the case of LEECs, two operational models, namely the electrodynamic (ED) model[147, 154-156] and the electrochemical doping (EDC) model[157-160] have been proposed (Fig. 22). The fundamental difference is that the ED model assumes good carrier injection due to the accumulation of ions at the electrode interface, whereas the ECD model assumes carrier injection is promoted by the formation of a p–i–n junction upon doping of the organic semiconducting materials into the electrodes.[146, 161] For the fabrication of the emission layer in LEECs, solution processes (*e.g.*, spin-coating or inkjet-printing techniques) are commonly used.

Since Thompson and coworkers reported the first phosphorescent OLEDs (PHOLEDs) in 1998,[3] electroluminescent materials have mainly focused on transition metal complexes, especially iridium complexes, which utilize singlet and triplet excitons to realize nearly 100% internal quantum efficiency (IQE) in the device.[9, 162-165] In contrast to PHOLEDs, thermally activated delayed fluorescence (TADF) materials have recently emerged as new generation organo-electroluminescent materials for exciton harvesting in OLEDs.[166-170] OLEDs based on TADF materials have even shown superior performance compared to the traditional PHOLEDs.[1, 171-174] In this section, a series of luminescent dinuclear complexes and their applications in OLEDs and LEECs are summarized.

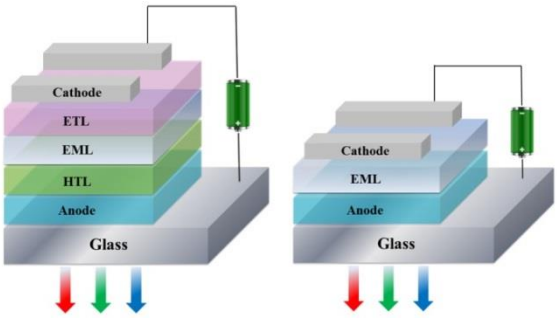

Fig. 21 Device structures of a typical multilayer OLED and a LEEC based on transition metal complexes as the emitter.

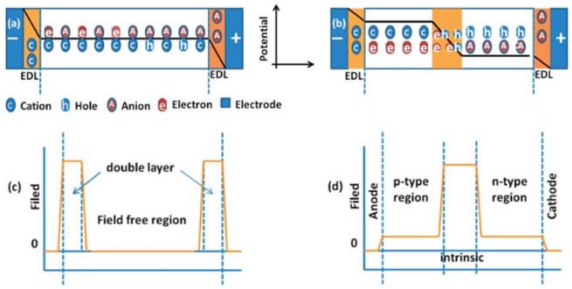

Fig. 22 Idealized electronic and ionic charge distribution, potential profiles and electric fields in light-emitting electrochemical cells modified from Matyba *et al.*[175] and Pingree *et al.*[176] Potential profiles, charge distributions and electric fields as predicted by (a), (c), the ED and (b), (d) the ECD. The thick black line in (a) and (b) represents the potential profile (in eV). Furthermore, the yellow line in (c) and (d) indicates the electric fields. Reproduced with permission from ref. 146. Copyright 2012 The Royal Society of Chemistry.

3.1.1 Phosphorescent Ir(III) complexes

Since the seminal work by Watts and Güdel in the 1980s,[177] phosphorescent cyclometalated Ir(III) complexes have attracted great interest due to their wide applications especially in the field of organo-electroluminescence. This is due to their extraordinary properties, namely: high phosphorescence quantum yields at room temperature from triplet metal-to-ligand charge-transfer (MLCT) states, suitable triplet state lifetime (in the order of μs), high thermal and photochemical stability for fabrication by vacuum deposition techniques, and a broad range of emission colors which can be tuned by modifying the structure of the ligands.[178-180] Since Forrest and coworkers reported the first PHOLEDs based on an Ir(III) complex emitter in 1999,[181] mononuclear Ir(III) complexes have received most attention due to their ease of synthesis and tuning of emission across the entire visible spectrum. Their structure-property relationships are now well understood.[5, 10, 182, 183]

In contrast to the rigorous development of mononuclear iridium complexes, the fundamental chemistry and applications of dinuclear iridium complexes are under-developed. However, the dinuclear complexes invariably present special photophysical properties and functions compared with mononuclear species through tuning the bridging ligands and the cyclometalated ligands. For example, in the solid state, highly efficient emission, with aggregation-induced emission and mechanochromic luminescence properties, can be simultaneously realized in a dinuclear iridium system *via* selection of a flexible Schiff base bridging ligand.[50, 109, 110] Furthermore, single-molecule white-light emission has been realized in a dinuclear iridium polymer through selection of two individual emitting color Ir(III) cores with a bulky conjugated bridging ligand.[184] Therefore, it is of great significance to develop novel dinuclear iridium complexes..

Recently, a series of luminescent dinuclear Ir(III) complexes and their applications in OLEDs and LEECs have

been reported.[72] The highest EQE of diiridium-based PHOLEDs is 27.6% with green electroluminescence.[78] The main challenge for diiridium-based OLEDs and LEECs is the to achieve efficient and stable blue and red electroluminescence, and to obtain white electroluminescence. Indeed, true-blue emissive diiridium complexes are very rare. In this section, representative luminescent Ir(III) complexes are presented with particular focus on their application in PHOLEDs. Furthermore, some guidelines for the future design of dinuclear Ir(III) complexes and their use in electroluminescent devices are provided based on more fundamental studies.

3.1.1.1 Sky blue/green-emitting dinuclear Ir(III) complexes. Obtaining a true-blue phosphor based on dinuclear Ir(III) complexes is still a huge challenge. A series of dinuclear Ir(III) complexes with sky-blue or green emission is shown in Fig. 23. Their photoluminescent and electroluminescent properties are listed in Table 2. A similar structural feature in all the complexes is the short conjugated bridging ligands that connect the two iridium centers which may increase the excited state energy gap to give the green or sky-blue emission.

Among these dinuclear Ir(III) complexes, N^O-type bridged derivatives commonly show bright green or sky-blue emission. In 2011, two neutral dinuclear Ir(III) complexes **42** and **43**, bridged by the versatile dianionic terpyridine dicarboxylate ligand were reported by Mazzanti and coworkers.[59] Both the solution ^{1}H NMR spectra and DFT calculations revealed that *ΛΔ* and *ΔΛ* enantiomers co-exist in both complexes **43** and **43**, whereas the *meso* form was not observed, which may be attributed to the interligand steric interactions. The UV absorption spectra of both complexes showed an intense absorption around 260 nm which was attributed to the spin-allowed ligand-centered (^{1}LC) transtions, whereas the weak absorption at > 400 nm was attributed to the singlet metal to ligand charge transfer (^{1}MLCT) transitions. The absorption tail between 400−500 nm arises from the formally spin-forbidden ^{3}MLCT transitions. Overall, both **42** and **43** showed absorption features that are similar to their analogous mononuclear species, which indicates a negligible contribution of the bridging ligand in the absorption process. Complexes **42** and **43** showed bright green or blue-green emission at room temperature with maximum emission wavelength at 538 and 477 nm, respectively. The photoluminescent quantum yields (PLQYs) of **42** and **43** are *Φ* 17.7% and 4.8%, respectively. The excited state lifetimes of **42** and **43** are 0.09 and 0.15 μs, respectively, which indicated the emission of both complexes is from ^{3}MLCT states. The significant blue-shift of **43** compared to **42** can be attributed to the introduction of the F-substituents, which increases the HOMO-LUMO energy gap by lowering the energy level of the HOMO.

In 2011, Hajra *et al*. reported a new dinuclear Ir(III) complex **44** containing a pyrazine dicarboxylate bridging ligand.[58] **44** showed bright green emission (PLQY = 38%) in dichloromethane solution at room temperature with maximum emission wavelength at 500 nm. DFT calculations showed that the HOMO of **44** is mainly centered on the cyclometallated ligands and metal *d* orbitals, whereas the LUMO is mainly centered on the bridging ligand. Thus, the emission of **44** can be attributed to the ^{3}MLCT state.

In 2013, Sünkel *et al*. reported a new dinuclear Ir(III) complex **45**, bridged by an oxamidato ligand.[61] The crystal structure analysis revealed only the *meso* diastereoisomer (*ΛΔ*), which is in contrast to most reported crystal structures of chloride- or methoxide-bridged dinuclear Ir(III) complexes where the enantiomeric pair (*ΛΛ* and *ΔΔ*) is observed. In the emission spectrum of **45** two peaks were observed at room temperature: the main emission peak at 523 nm can be attributed to the ^{3}MLCT, whereas the shoulder peak at around 560 nm can be attributed to the ^{3}LC. This structureless emission is more obvious at 77 K. The PLQY of **45** is as high as 60%, suggesting that this kind of dinuclear Ir(III) complex could be used in future optoelectronic devices.

Subsequently, M'hamedi *et al*. reported two new dinuclear Ir(III) complexes **46** and **47** with oxamidato-type bridging ligands and investigated their electroluminescent properties in OLEDs.[185] The ^{1}H and ^{13}C NMR spectra of **46** and **47** revealed that both the *meso* and *racemic* forms (two enantiomers, ΛΛ and ΔΔ) as a diastereomeric mixture (ratio = 3:2) exist in both complexes. Whereas the μ-dichloro-bridged precursor of **46** and **47**, showed only faint emission in solution, **46** and **47** are highly emissive (Φ_{PL} 73% and 63%) with short excited state lifetimes of τ_p 0.84 and 1.16 μs, respectively. Inspired by the superior photoluminescent properties, the electroluminescent properties of **46** and **47** were investigated. The PHOLED structures and energy levels of component materials are shown in Fig. 24. PEDOT:PSS is a hole-transport layer, poly(vinylcarbazole) (PVK) is the host material, OXD-7 and TPBi are electron transporting materials to optimize charge balance and confine excitons in the emitter layer. The electroluminescent performance is shown in Fig. 24 and Table 2. Very bright green electroluminescence was observed for both **46** (533 nm) and **47** (533 nm) with L_{max} > 25000 cd/m^2 which is among the brightest PHOLEDs fabricated using dinuclear Ir(III) complexes. The maximum EQEs of **46** and **47** are 2.95% and 3.46%, respectively.

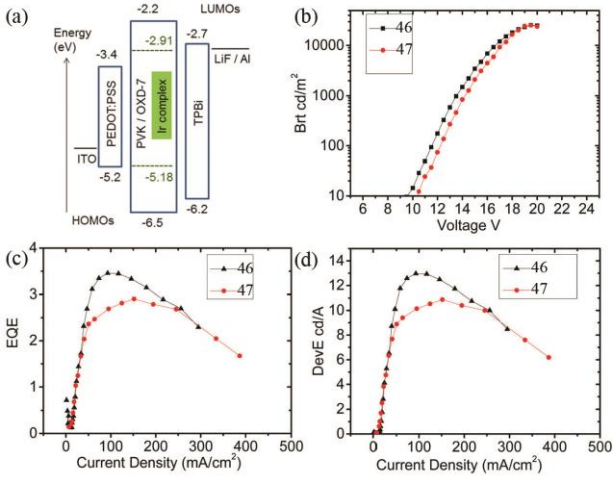

Fig. 24 (a) Energy level diagram for the devices of **46** and **47**. (b) Voltage-Brightness (V-B) curves of devices. (c) Plots of external quantum efficiency vs brightness for devices. (d) Plots of current efficiency vs current density for devices. Reproduced

with permission from ref. 185. Copyright 2017 The Royal Society of Chemistry.

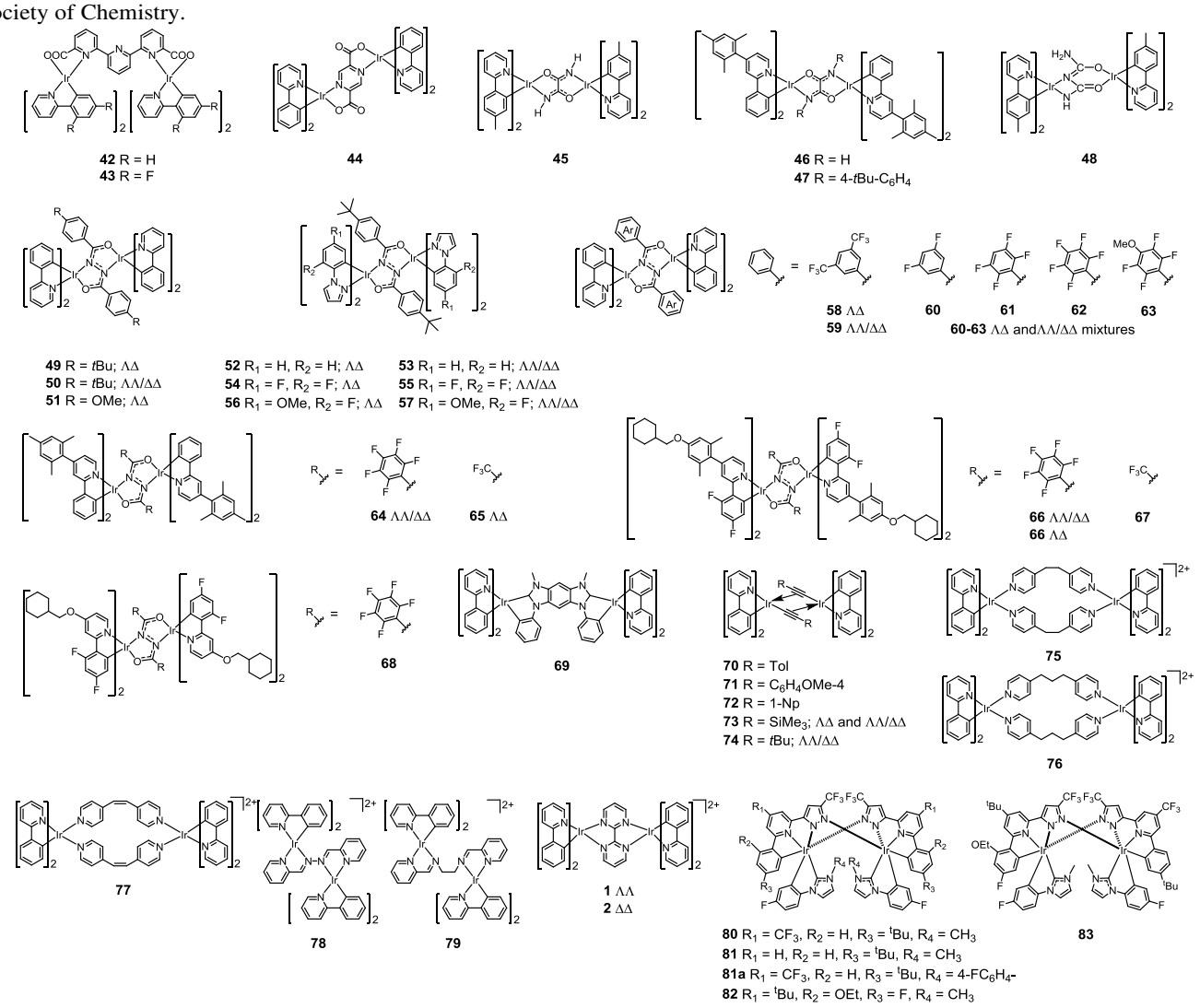

Fig. 23 Dinuclear Ir(III) complexes with green or blue-green emission.

Table 2 Photophysical properties and electroluminescence performance of sky-blue and green emitting dinuclear Ir(III) complexes

Complex	Photophysical properties			Device performance						
	$\lambda_{max,PL}$ (nm) [a]	PLQY (%) [a]	τ_p (μs) [a]	Turn-on voltage (V)	$\lambda_{max,EL}$ (nm)	Maximum brightness (cd m^{-2})	EQE (%)	CE (cd A^{-1})	PE (lm W^{-1})	Ref.
46	529	73	0.84	~10.5	533	25400	2.95	13	1.9	185
47	522	63	1.16	~9.5	533	25630	3.46	11	2.4	185
49	521	71	1.45	6.2	526	11000	7	24	7	96
50	523	88	1.44	5.5	526	7000	11	37	14	96
80	531	98	3.0	5.2	530	51772	18.3	67	41.2	78
81	487, 521, 559	95	4.58	3.6	489	28218	27.6	75.2	65.7	78

82	468, 500, 536	100	4.78	3.5	470	10031	14.2	29.7	24.6	78

[a] Measured in solution state.

In 2013, Graf *et al*. reported a new dinuclear complex **48** with an unprecedented N,N':O,O'-type bridging ligand.[186] The X-ray crystal structure revealed two N donor atoms coordinated with one iridium center in a four-membered chelate ring, whereas two O donor atoms coordinated with the other iridium center in a six-membered chelate ring. At room temperature, complex **48** exhibits bright green emission in both solution state and doped into poly(methy methacrylate) (PMMA) (Φ_{PL} 27% and 55%) with short excited lifetimes (0.7 μs and 1.5 μs) respectively.. These results indicated this kind of dinuclear Ir(III) complexes is promising for future applications in OLEDs.

In 2014, Zheng *et al*. reported three new dinuclear Ir(III) complexes **49**–**51**, bridged by diarylhydrazide ligands.[96] Similar to the previously reported dinuclear Ir(III) complexes, the *meso* (ΛΔ/ΔΛ) and *rac* (ΛΛ/ΔΔ) diastereomeric mixtures were found in this system. The diastereomers were readily separated by using their different solubilities to give pure **49** (ΛΔ/ΔΛ, 41% yield) and **50** (ΛΛ/ΔΔ, 30% yield). Both complexes **49** and **50** showed very bright green emission at room temperature with a peak at 521 nm and 523 nm, respectively, high PLQYs of 71% and 88%, and short excited lifetimes (1.45 μs and 1.44 μs) respectively. Solution-processed OLEDs were fabricated in the simple architecture ITO/ PEDOT : PSS (50 nm)/ PVK : PBD (40%) : Ir complex (5%) (90 nm)/ Ba (4 nm)/Al (100 nm). (PBD is an electron-transport material). The electroluminescent performance of complexes **49** and **50** is shown in Fig. 25 and Table 2. The parent Ir(III) dimers $[Ir_2(ppy)_4Cl_2]$ and $[Ir_2(flpy)_4Cl_2]$ were selected for comparison. Both complexes **49** and **50** showed obviously better electroluminescent properties than their parent Ir(III) dimers. The best device performance was for **50** with peak CE, PE and EQE of 37 cd A^{-1}, 14 lm W^{-1} and 11%, respectively. These superior data compared to **49** were attributed to the better solubility of **50** than **49**. It is worth noting that the electroluminescent performance of **49** and **50** is higher than the benchmark PHOLED based on the monuclear green $[Ir(ppy)_3]$ complex, using a solution processed emitter layer. This work proved that dinuclear Ir(III) complexes are a viable strategy to obtain highly efficient OLEDs.

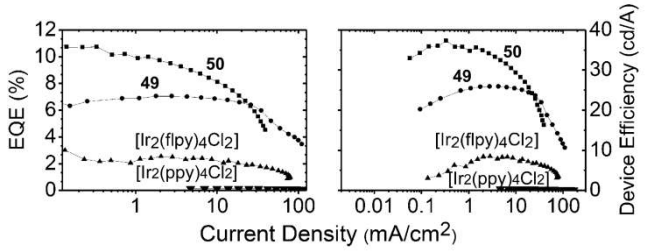

Fig. 25 Device performance of complexes $[Ir_2(ppy)_4Cl_2]$, $[Ir_2(flpy)_4Cl_2]$, **49** and **50** (fl = 9,9-dihexylfluorene) with a dopant concentration of 5% w/w. Reproduced with permission from ref. 96. Copyright 2014 Wiley-VCH.

Recently, a follow-up study on complexes **52**–**59** examined the effects of substitution on the bridging and cyclometalating ligands.[94] The diastereomers which formed in all these complexes were cleanly separated due to their different solubilities. Thus, their photophysical properties were investigated individually. Complexes **52**–**55** are almost non-emissive in both the solution state and in PMMA films at room temperature. However, the emission of both complexes can be detected at 77 K, thus the behaviour at room temperature can be explained by considering thermal population of low-lying non-emissive MC excited states.[187] Complexes **56**–**59** showed faint emission in the solution state, which was attributed to the non-radiative quenching through motion of the bridging unit. By contrast, they showed bright green emission with a peak at 493–515 nm, and PLQYs of 42%–68% in the PMMA state. Overall, it can be concluded that both the bridging and cyclometalating ligands play a significant role in the photophysical properties for all the complexes.

More recently, Congrave *et al*. developed a new series of diarylhydrazide-bridged diiridium complexes **60**–**68**[188] that showed highly efficient emission in the both solution and doped film states, high k_r, relatively short τ_p and in some cases notably sharp emission. Especially, complexes **66**–**68** exhibit sky-blue emission which is rare for diiridium complexes. A combination of X-ray molecular structures and computational studies revealed that the strong intramolecular π–π interactions (Fig. 26) between bridging ligand and cyclometalated ligand play a vital role in the observed excellent photophysical properties of the complexes. Furthermore, it was evident that the intramolecular π–π interactions are promoted by the introduction of fluorine substituents onto the phenyl rings of the bridging ligand. This work offers a new method for the future development of deeper blue emitting diiridium complexes.

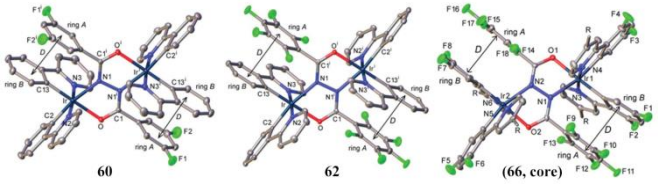

Fig. 26 X-ray molecular structures of *meso* **60**, *meso* **62** and the core part of *rac* **66** (*ΔΔ*) with the xylyl substituents (R) omitted. Thermal ellipsoids are drawn at 50% probability level. H atoms are omitted for clarity. Vector D identifies intramolecular π–π interactions, *meso* **60** = 3.32 Å, *meso* **62** = 3.24 Å, *rac* **66** = 3.27, 3.19 Å. Reprinted with permission from ref. 188. Copyright 2018 The Royal Society of Chemistry.

In 2009, Tennyson *et al*. reported a novel dinuclear complex **69**, bridged by an *N*-heterocyclic carbene ligand.[62] **69** displayed blue-green phosphorescence with a peak at 497 nm; the PLQY and excited state lifetimes were 11% and 0.79 μs, respectively. Solution electrochemistry revealed no observable electronic

communication between the two Ir units. Furthermore, the similar emission properties of **69** compared to its analogous mononuclear complex indicated that benzimidazolylidene coordination to an $[Ir(ppy)_2]$ fragment neither perturbs the emissive state nor facilitates interaction between the sub-units.

In 2015, Sánchez and coworkers reported a series of dinuclear Ir(III) complexes **70**–**74** with doubly alkynyl bridging ligands.[189] The structural characterization revealed that unique diastereoisomers (ΛΛ/ΔΔ) were observed in complexes **70**–**72** and **74**, whereas two diastereoisomer (ΔΛ and ΛΛ/ΔΔ) mixtures were obtained in **73**. All the complexes **70**–**74** were non-emissive in the solid state which can be attributed to the typical aggregation-caused quenching (ACQ), whereas they showed relatively stronger emission in the 505−515 nm region in degassed solutions. The PLQYs were in the range of 0.7 to 2.4%, which are higher than the parent chloride-bridged dimer due to the introduction of the strong-field alkynyl group. The low quantum yields for **70**–**74** in solution can be attributed to the relatively fast σ/π alkynyl exchange between the Ir centers which could favor an efficient radiationless decay pathway.

In 2012, a series of dinuclear Ir(III) complexes **75**–**79** with N^N-type bridging ligands were reported by Omary and coworkers.[190] Electrochemical studies revealed weak interaction between the two Ir units in complex **77**, bridged by ethylene-based ligands, which was shown by the appearance of two oxidation waves. In contrast the metal centers are electronically isolated in **75** and **76** in which the bridging ligands are based on ethane and propane linkers.

A one-electron reduced species located on the diimine-based bridging ligand was observed in **78** as revealed by the presence of two reversible reductions. No interaction was found in **79** where the electronic conduit is interupted by the ethylene spacer in the bridging ligand. The emission spectra of **75**–**79** in acetonitrile are shown in Fig. 27. Complexes **75** and **76** have similar structured emission at 480 and 510 nm with a shoulder at 548 nm, which can be attributed to the mixed ^{3}LC and ^{3}MLCT states. The PLQYs of **75** and **76** are 45% and 48%, respectively. By contrast, broad and unstructured emission was observed in the complexes **77**–**79**, which can be attributed to the mixed ^{3}MLCT and ^{3}LLCT states, supported by the DFT calculations. The PLQYs of **77**–**79** are 41%, 51% and 12%, respectively.

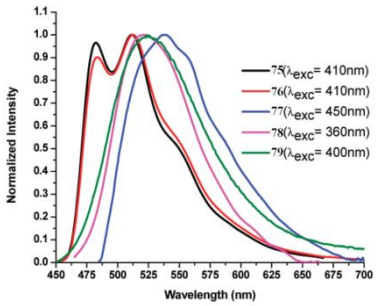

Fig. 27 Emission spectra of **75**–**79** in acetonitrile solution. Reproduced with permission from ref. 190. Copyright 2012 American Chemical Society.

In 2016, Ye *et al*. developed a useful tactic for avoiding the formation of diastereomeric mixtures in dinuclear Ir(III) complex *via* a chiral precursor strategy, using *L*- or *D*-proline as an auxiliary ligand.[95] Thus, the enantiomers **1** (ΛΛ) and **2** (ΔΔ) with a dipyrimidine bridging ligand were synthesized separately. The emission spectra of **1** and **2** were similar: both complexes showed structured blue emission with a peak at 436 nm and a shoulder at 465 nm in DCM solution. These two dinuclear complexes show the bluest emission of dinuclear Ir(III) complexes reported to date.

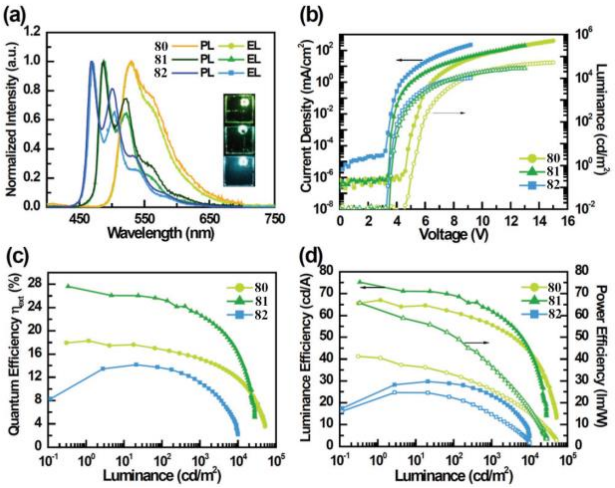

Fig. 28 EL characteristics of the OLEDs of **80**–**82**: a) normalized PL and EL spectra; b) current density–voltage–luminance (J–V–L) curves; c) external quantum effciency versus luminance; d) luminance effciency and power effciency data. Reproduced with permission from ref. 78. Copyright 2018 Wiley-VCH.

Recently a milestone study on a series of diiridium complexes **80**–**83** bearing novel 2-pyrazolyl-6-phenyl pyridine chelate and bidentate phenyl imidazolylidene chelate ligands was reported by Chi and co-workers.[78] All these complexes exhibited highly stable and efficient emission with near-unity PLQYs in both the solution and solid film states. In stark contrast to most of the previously reported solution-processed OLEDs based on diiridium complexes, the good volatility of complexes **80**–**83**, enabled their OLEDs to be fabricated by vacuum evaporation. The devices showed impressive performance (Fig. 28), especially the green emissive complex **81** gave a record high EQE for a diiridium complex of 27.6%. This value is also comparable to the top-tier green OLEDs using mononuclear Ir(III) dopants. However, further optimization of the device structures to avoid obvious roll-off at high luminance is desirable.

3.1.1.2 Yellow/orange-emitting dinuclear Ir(III) complexes. The archetypal parent iridium dimer, $[Ir(ppy)_2\mu\text{-}Cl]_2$ (**84**) has been widely used as a precursor in the synthesis of mono- and multinuclear iridium complexes, following the initial report by Watts *et al*. in 1993.[191] Ir(III) dimer **84** is a green emitter with λ_{max} at 517 nm, and a very low efficiency (Φ_{PL} = 0.5%) that limits its application in OLEDs. Following Watts' protocol, a

series of luminescent dinuclear Ir(III) dimers with atomic bridges were developed by other researchers, and they commonly showed yellow to orange emission (Fig. 29).

In 2012, a series of luminescent chloro-bridge Ir(III) dimers **85**–**89** developed by M'hamedi *et al*.[74] all showed brighter

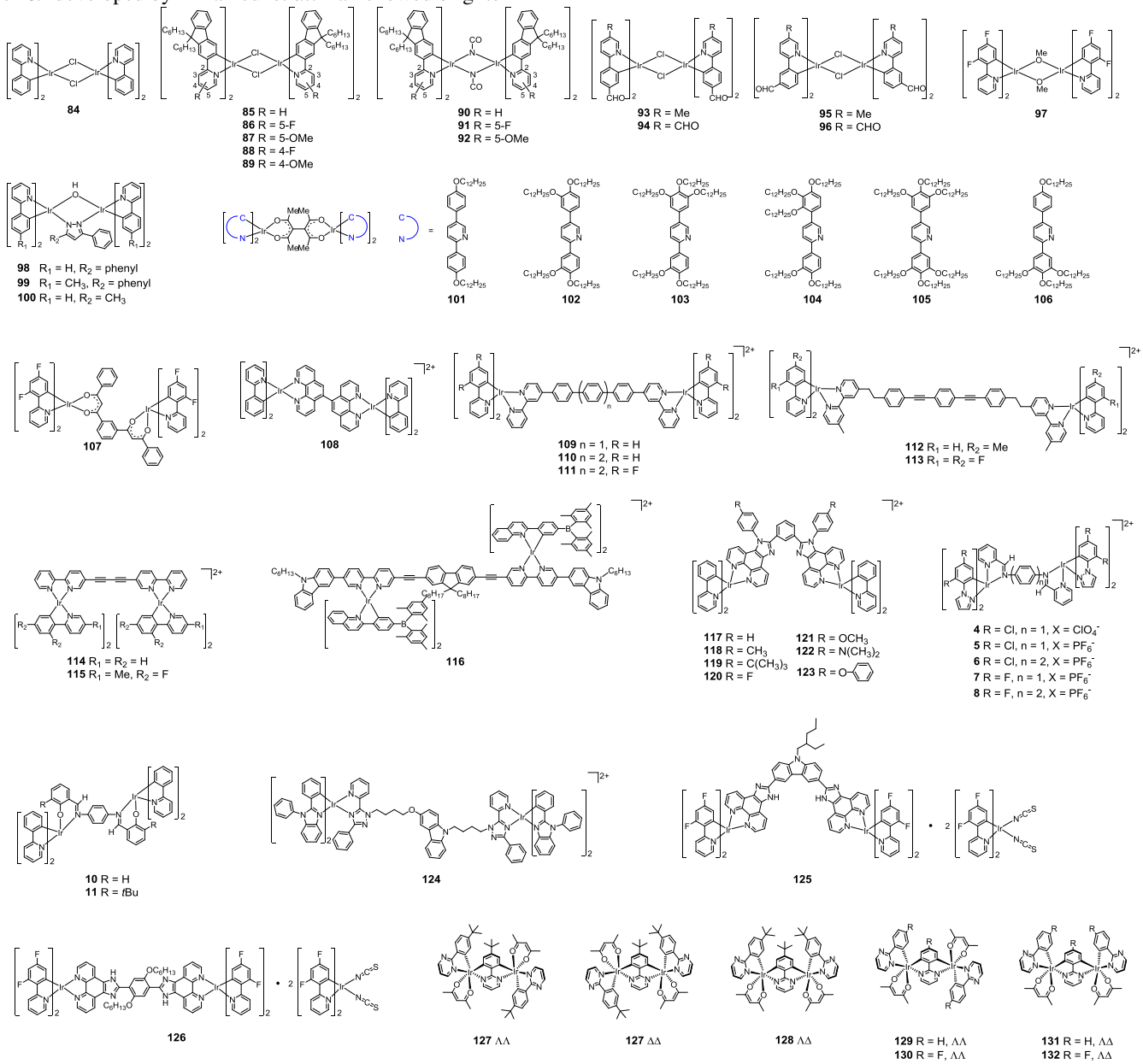

Fig. 29 Dinuclear Ir(III) complexes with yellow or orange emission.

yellow emission, compared to the parent dimer **84**. The PLQYs of **85**–**87** are in the range of 21%–41%, whereas the lower luminescence of **88** and **89** may be due to the different electronic structure induced by the position of the substituent group on the pyridine ligands (4-substitution in **88** and **89**). Devices were fabricated in the simple structure: ITO/PEDOT:PSS/PVK–PBD (40%)–complex (5%)/Ba/Al. The detailed photophysical and device performance data are shown in Table 3. The device based on complex **85** showed yellow electrophosphorescence with a maximum brightness of ~2200 cd/m^2 and EQE of 4%. These results further challenged the well-established view that dinuclear species are not viable as dopants for electrophosphorescent OLEDs. The follow-up studies used these chloro-bridged Ir(III) dimers as precursors to obtain a series of novel isocyanate-bridged Ir(III) dimers **90**–**92** and investigated their photophysical and electroluminescent properties (Table 3).[74] Their photoluminescent and electroluminescent spectra were consistent with their precursors **85**–**87** with bright yellow emission. However, the device performance based on **90**–**92** dopant showed obvious improvement with a maximum brightness and CE of ~3700 cd/m^2 and 10.3 cd/A, respectively.

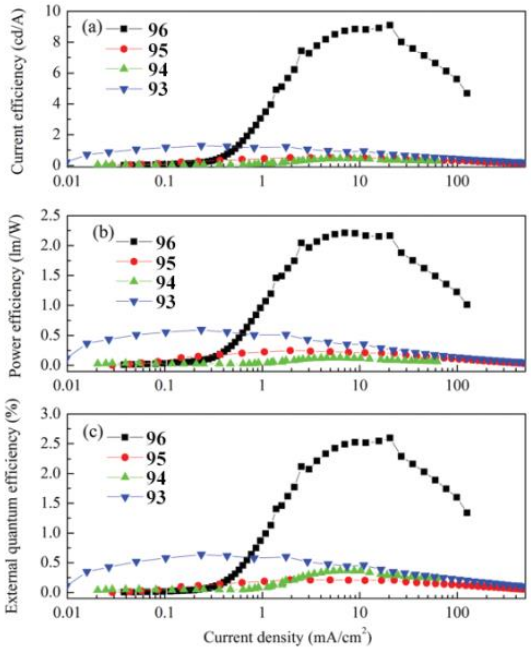

Fig. 30 (a) Current efficiency, (b) power efficiency and (c) external quantum efficiency vs. current density characteristics of the devices. Reproduced with permission from ref. 76. Copyright 2015 The Royal Society of Chemistry.

In 2015, four new luminescent chloro-bridged Ir(III) dimers **93**–**96** were reported by Zysman-Colman and coworkers.[76] Their photophysical properties were investigated in detail. The key findings were: i) Compared to the parent dimer **84**, a red-shift in emission for all complexes within the range of 563-611 nm can be attributed to the introduction of formyl groups into the structures. ii) A gradual increase of PLQY was observed as the numbers of formyl groups increased. This can be attributed to the more extensive hydrogen bonding interactions, which resulted in a large decrease in k_{nr}. OLEDs were fabricated with the structure: ITO/PEDOT:PSS/PVK/CBP:PBD:Ir complex (60:30:10, w/w)/B3PYMPM/Ca/Al. (B3PYMPM is an electron-transport material). The device based on **96** as dopant showed the best performance with maximum brightness of >6000, CE of 9.9 cd/A, PE of 2.16 lm/W^{-1} and EQE of 2.59% (Fig. 30 and Table 3). The poor device performances based on **93** and **95** dopants were suggested to originate from either incomplete host-to-guest energy transfer (**93**) or exciplex emission (**95**) (Fig. 31). For **94** and **96** the emission was nearly independent of the current density, demonstrating highly efficient host-to-guest energy transfer and no significant exciplex contribution.

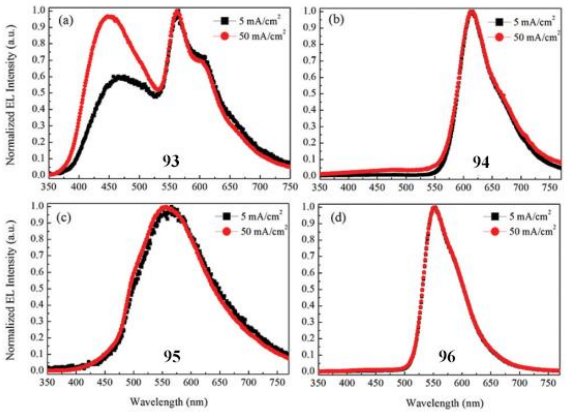

Fig. 31 The normalized EL spectra for the devices with the complexes **93** (a), **94** (b), **95** (c) and **96** (d) at current densities of 5 and 50 mA cm^{-2}. Reproduced with permission from ref. 76. Copyright 2015 The Royal Society of Chemistry.

In 2012, Ding *et al*. synthesized a novel methoxy-bridged Ir(III) dimer **97** by reacting chloride-bridged Ir(III) dimer with the mixtures of sodium methanolate and *N*-(2,6-diisopropylphenyl)methacrylamide ligand in DCM under dinitrogen atmosphere at room temperature for 48 h.[192] At room temperature in DCM, **97** showed strong emission with a peak at 539 nm and weak shoulders at 447 and 474 nm. However, upon storing the solution under visible light overnight the peak at 539 nm disappeared, whereas the two weak shoulders at 447 and 474 nm strengthen and dominate the spectrum. This data suggested that **97** has poor photostability.

In 2012, Chandrasekhar *et al*. reported three new heterobridged Ir(III) dimers **98**–**100** by reacting chloride-bridged Ir(III) dimer with mixtures of sodium methanolate and 3,5-diphenylpyrazole (Ph_2PzH) ligand.[193] Cyclic voltammetric studies indicated that **98**–**100** showed quasi-reversible redox process. For example, complex **98** showed two consecutive one-electron oxidation waves with the oxidation peaks at 0.62 and 0.95 V (Fig. 32), whereas no reduction process was observed. The two oxidation processes can be assigned to the stepwise oxidation of the two Ir(III) centers, *i.e*., Ir(III)–Ir(III)/Ir(III)–Ir(IV) and Ir(III)–Ir(IV)/Ir(IV)–Ir(IV) couples. The presence of two sequential redox waves clearly indicates electronic coupling between the two Ir centers which are effectively mediated by the hydroxyl bridge, supported by the DFT and TDDFT calculations. Photophysical studies demonstrated that **98**–**100** are phosphorescent emitters with λ_{max} at around 550 nm at room temperature in DCM solution. The PLQYs range from 11%–17%.

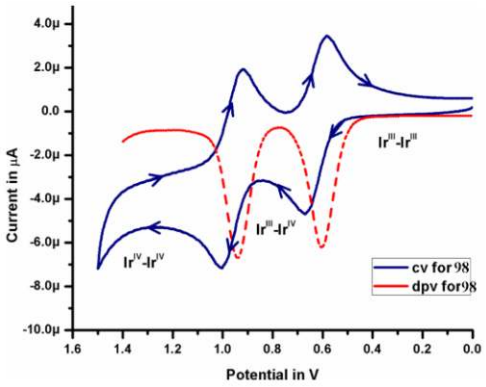

Fig. 32 Cyclic voltammogram (blue line) of **98** in DCM at a scan rate of 100 mV s^{-1}. The red line is the differential pulse voltammogram with a step potential of 5 mV and an amplitude of 50 mV. Reproduced with permission from ref. 193. Copyright 2012 American Chemical Society.

In 2012, Bruce, Williams *et al.* obtained a series of dinuclear Ir(III) complexes **101**–**106** bridged by the 1,1,2,2-tetraacetylethane (tae) ligand.[194] Two diastereomeric forms (*meso* and *rac*) were observed in all the complexes in ^{1}H NMR studies, and diastereomers of **101** and **104** were successfully separated by column chromatography, but no further structural characterization confirmed which isomer is which. All the complexes showed intense emission in the green-yellow to orange regions in DCM solution at room temperature. The PLQYs of all the complexes are *ca.* 50% which is even higher than typical Ir(III)-acac complexes with simple ppy ligands. Interestingly, complexes **102**, **104**, **105** and **106** (Table 4) are mesomorphic liquid-crystalline materials, showing a columnar hexagonal mesophase (Fig. 33), whereas **101** is not mesomorphic due to the low coverage of the dimer periphery by alkoxy chains. Furthermore, the morphology is a delicate function of the substitution position of the chains as **103** is not mesomorphic, wheras **104** is mesomorphic.

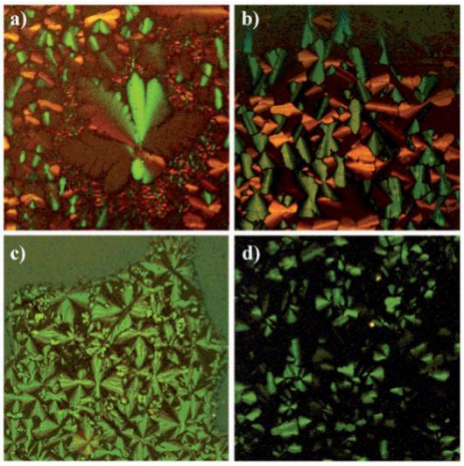

Fig. 33 Optical micrographs (on cooling) of **104** (isomer 1), 100 ºC (a), **104** (isomer 2), 60 ºC (b), **102**, mixture of diastereoisomers, 85 ºC (c), **106**, mixture of diastereoisomers, 133 ºC (d). Reproduced with permission from ref. 194. Copyright 2012 Wiley-VCH.

Table 4 Thermal behavior of the Ir(III)tae complexes **101**–**106**

	Transition and *T* [ºC]
101 (isomer 1)	Cr 153 Iso
101 (isomer 2)	Cr 157 Iso
102 (2:1)	Cr 74 Col_h 131 Iso
103 (2:1)	Cr 82 Iso
104 (isomer 1)	Cr 79 Col_h 126 Iso
104 (isomer 2)	Cr 63 Col_h 95 Iso
105 (4:3)	Cr 17 Col_h 61 Iso
106 (4:3)	Cr 130 Col_h 147 Iso

In 2010, a new neutral dinuclear Ir(III) complex **107** with a bis(β-diketonato) bridging ligand was reported by Do's group.[118] **107** showed a weak emission band at 615 nm with low quantum efficiency (Φ_{PL} = 2.3%) in degassed $CHCl_3$ solution, whereas bright orange emission with λ_{max} at 597 nm was observed in the solid state. This indicates that **107** may be aggregation-induced emission (AIE) active. X-ray crystal-packing analysis suggests that the AIE mechanism could derive from the strong π–π intermolecular interactions between adjacent pyridine rings of F_2ppy ligands.

N^N-type bridged Ir(III) complexes with long conjugated chains commonly show yellow to orange emission. In 2000, Campagna *et al.* developed a new synthetic approach by applying nickel-catalysed coupling reactions to a [Ir-$(ppy)_2$(Cl–phen)]$^+$ precursor to give the dinuclear Ir(III) complex **108**.[195] Cyclic voltammetric studies of **108** indicated two-electron reductions occurred in the two phenanthroline units of the bridging ligand which may be induced by the non-planar bridging structure, because of the strong steric constraints. Complex **108** showed orange-red emission with λ_{max} at 617 nm (Φ_{PL} = 12.3%, τ = 0.39 µs) in deaerated acetonitrile solution at room temperature, originating from the ^{3}MLCT state, supported by the electrochemical and UV absorption studies.

In 2003, De Cola and coworkers synthesized two oligo-*p*-phenylene bridged ionic dinuclear Ir(III) complexes **109** and **110** by a standard Suzuki coupling reaction.[196] At room temperature, both **109** and **110** exhibited orange-red emission with peaks at 608 and 606 nm and lifetimes of 72 and 75 ns, respectively, in equilibrated acetonitrile solution. The mononuclear species [Ir$(ppy)_2$bpy] which was studied for comparison (Fig. 34), gave an intense absorption band in the 400–550 nm region, with a weaker band at 650–800 nm. Such bands can be attributed to the population of the ^{3}MLCT state and showed a lifetime around 60 ns. However, for dinuclear complex **110**, a wide band that covered the entire 400–850 nm region was observed which can be assigned to the Ph_4 substituted bpy. This result indicated that the emission of complexes **109** and **110** originates from mixed ^{3}MLCT and ^{3}LC states. PHOLEDs showed a low efficiency with maximum CE and EQE values for **110** of 0.23 cd A^{-1} and 0.1%, respectively.[197]

The introduction of F atoms into the cyclometalating ligands induces a blue-shift in the emission with a peak at 546 nm for complex **111** compared to complexes **109** and **110**.[56] Similar transient absorption spectra of **111** to the complexes **109** and

110 again suggested that the emission is from mixed ^{3}LC and ^{3}MLCT excited states. A longer decay within ca. 86 µs measured by transient absorption spectra do not agree with the fluorescence lifetimes in this case, suggesting that the ^{3}LC excited state may be partly formed by direct excitation of the bridging ligand and a rapid intersystem crossing facilitated by the presence of the heavy atom.

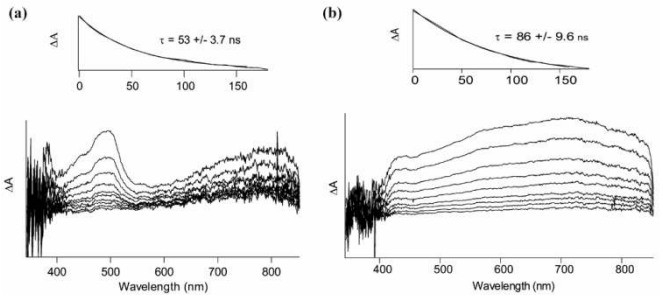

Fig. 34 Transient absorption spectra and decay kinetics in acetonitrile for [Ir(ppy)$_2$bpy] (a) and **110** (b). Reproduced with permission from ref. 197. Copyright 2003 The Royal Society of Chemistry.

In 2010, Bolink and Martín *et al*. reported two cationic dinuclear Ir(III) complexes **112** and **113** featuring an oligo-*p*-(phenyleneethynylene) bridge and ethylene units which break conjugation between the two Ir centers.[117] The PLQYs of both complexes were extremely low at around 9×10^{-3}. The detailed photophysical properties and theoretical calculations indicated that the lowest triplet excited state is located on the conjugated spacer (^{3}LC) which is below the ^{3}MLCT/^{3}LLCT emitting states and, therefore, favours a non-radiative transition. This unfavourable energy alignment explains the low PLQYs observed for dinuclear **112** and **113** with respect to the mononuclear complexes. Their electroluminescent properties were also investigated as the emitter in LEECs fabricated with the structure: ITO/PEDOT:PSS (100 nm)/complex **112** or **113**/ionic liquid (IL) (molar ratio = 1:1) (80 nm)/Al; ionic liquid (IL) is known to improve the performance of LEECs. Upon applying a bias of 3 V, the luminance and current density increased in a typical time-delayed response and reflected the mechanism of device operation for which the PF_6^- counter-ions have to reach the interface of the electrodes to enhance the charge-injection process (Fig. 35). The devices showed faint EL (< 10 cd m^{-2}) with λ_{max} at 596 nm and 540 nm, respectively for **112** and **113**. The maximum EQEs for **112** and **113** are very low at 0.16 and 0.13%, respectively. These values are close to the theoretical maxima of 0.20 and 0.16% estimated from the PLQY data, indicating that self-quenching in the devices had been minimized.

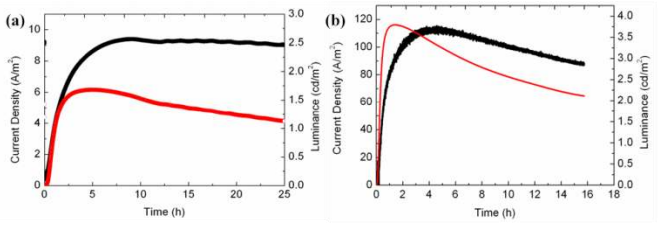

Fig. 35 Time-dependent current density (black) and luminance (red) curves of LEECs biased at 4.0 V with **112** (a) and **113** (b) as the active electroluminescent component. Reproduced with permission from ref. 117. Copyright 2010 Wiley-VCH.

In 2012, Harvey and coworkers reported two dinuclear Ir(III) complexes **114** and **115**, employing a diyne moiety at the 5-position of the bipyridyl bridged ligand.[113] ^{1}H NMR results indicated a diasteromeric mixture, which was not separated, in both **114** and **115**. At room temperature, complex **115** showed yellow emission with λ_{max} at 558 nm in 2-MeTHF solution which is significantly blue-shifted compared to **114** with λ_{max} at 647 nm due to the presence of the electron-withdrawing fluorine atoms on **115** which decreases the HOMO level and effectively increases the energy gap. A DFT and TDDFT study revealed that the emission process is dominated by mixed ^{3}MLCT/^{3}LLCT states.

In 2013, to realize two-photon-excited-phosphorescence (TPEP) probes for F^- ions, Zhao *et al*. designed and synthesized a new cationic dinuclear Ir(III) complex **116**, featuring a D–A–π–A–D conjugated oligomer as the bridging ligand and dimesitylboryl groups on the cyclometalated C^N ligands (Bpq).[198] **116** showed an optical absorption intensity twice that of the corresponding mononuclear analogue. Furthermore, complex **116** showed an intense absorption band at λ_{max} 448 nm with a molar extinction coefficient (ε) as high as 10^4, which is rare for Ir(III) complexes. Complex **116** showed an intense orange-red emission upon excitation at 400 nm with a peak at around 606 nm in DCM (Fig. 36a). The PLQY and lifetimes are 13% and 0.6 µs, respectively, indicating classical one-photon-excited-phosphorescence (OPEP). In consideration of the large conjugated structure and the charge-transfer properties of **116**, the TPEP properties were also investigated. As shown in Fig. 36a, upon femtosecond excitation at 800 nm, **116** showed emission features that are almost identical with the OPEP which was excited at 400 nm, revealing classical TPEP. The mechanisms of OPEP and TPEP are depicted in Fig. 36b. In view of the previously reported results that F^- ions can be recognized by arylborane ligands due to the strong B–F interaction, sensing of F^- ions was also investigated. As shown in Fig. 36c and 36d, upon excitation at 442 and 800 nm, respectively, the emission intensity of **116** gradually decreased with an increasing concentration of F^- ions, revealing that F^- can be efficiently detected by both OPEP and TPEP processes. It is worth noting that complex **116** was the first reported TPEP probe for F^- ions.

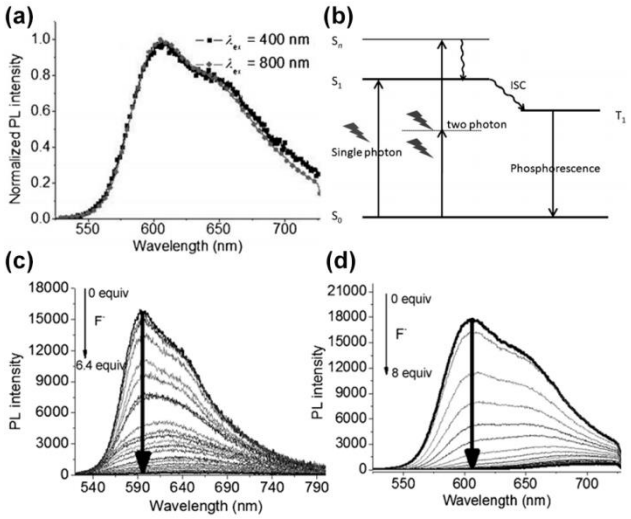

Fig. 36 (a) One-photon-induced luminescence spectra and two-photon-induced luminescence spectra (λ_{ex} = 800 nm) of complex **116** in THF. (b) Schematic representation of the one- and two-photon-excited photophysical processes in **116**. (c) Change in the one-photon-excited-phosphorescence spectra of **116** (100 μM) in THF with various amounts of F^- ions (λ_{ex} = 442 nm). (d) Change in the two-photon-excited-phosphorescence spectra of **116** (100 μM) in THF with various amounts of F^- ions (λ_{ex} = 800 nm). Reproduced with permission from ref. 198. Copyright 2013 Wiley-VCH.

In 2015, Chao's group reported a series of dinuclear complexes **117**–**123** with bright orange emission.[87] The PLQY and lifetimes of these complexes in DMSO/PBS solution were in the range of 9.8%–33.6% and 380–607 ns, respectively. In this work, **118**–**123** were firstly shown to serve as mitochondrial imaging dyes with low cytotoxicity and high resistance to the loss of the mitochondrial membrane potential characteristics. Furthermore, **119** and **122** were further developed for tracking mitochondrial morphological changes during the early stages of apoptosis.

In 2015, we developed a series of cationic dinuclear Ir(III) complexes **4**–**8**, featuring versatile Schiff base bridging ligands.[50, 85] They all showed faint emission in the solution state, whereas bright orange phosphorescence was observed in the aggregated state demonstrating classical AIPE behaviour. Furthermore, due to the good flexibility of the Schiff base bridging ligands, the molecular arrangements are relatively loose and can be easily destroyed by the force of manual grinding in a mortar and pestle, resulting in mechanochromic luminescence (MCL) with a change from orange to red emission clearly observed. Upon organic vapour treatment, or heating of the ground samples, the emission color reverted to the original orange, revealing reversible MCL. In summary, the flexible Schiff base bridging ligand plays an important role in achieving AIPE and MCL simultaneously. Benefiting from these combined properties, a perchlorate anion phosphorescent sensor and a phosphorescence re-writable data recording device were successfully fabricated.

In 2017, we disclosed two new neutral dinuclear Ir(III) complexes **11** and **12**, bearing two N^O-type Schiff base bridging ligands.[109, 110] **11** and **12** are bright yellow (587 nm, Φ_{PL} = 20%) and orange (608 nm, Φ_{PL} = 24%) emitters, respectively, in the solid state. As expected, both complexes showed AIPE and MCL simultaneously. In view of the highly efficient emission of both complexes in the solid state due to AIPE, an efficient second-level anti-counterfeit trademark and highly selective organic vapour sensors were fabricated using **11** and **12** as the active materials, respectively.

In 2017, a new cationic dinuclear Ir(III) complex **124**, bearing triazole–pyridine moieties linked with a flexible bridging chain was reported by our group.[86] Complex **124** showed faint emission (571 nm, Φ_{PL} = 6.2%) in pure acetonitrile solution, whereas stronger emission (550 nm, Φ_{PL} = 20%) was observed in CH_3CN/H_2O solution (v:v = 1:9) indicating the occurence of AIPE. A highly sensitive and selective "turn-off" sensor for 2,4,6-trinitrophenol (TNP) was fabricated using **124** as probe. The sensing mechanism was attributed to the efficient photoinduced electron transfer and strong electrostatic interaction between **124** and TNP.

In 2011, two Ir(III) soft salts formed from dinuclear cationic and mononuclear anionic complexes, bearing a carbazolyl (**125**) or *p*-phenylene bridge (**126**) were reported by Meyer and coworkers.[75] The photoluminescence peaks for **125** and **126** in the solid state are at 594 and 557 nm, respectively. OLEDs using soft salts as emitters were fabricated for the first time with the simple structure: ITO/PEDOT: PSS (40 nm)/PVK (20 nm)/**125** or **126**/Ca (300 nm)/Al (60 nm). The devices showed electroluminescence peaks at λ_{max} 570 and 621 nm, respectively. The highest CE and PE are 0.44 cd/A and 0.17 lm/W^{-1} for **125** and 0.06 cd/A and 0.03 lm/W^{-1} for **126**, respectively. The poor device performances for both complexes may be attributed to self-quenching effects, and/or to the electron/energy transfer to the conjugated bridging ligands. The higher device performance for **125** may be due to the better charge-carrier injection and transport ability of the carbazole moiety compared with the phenylene spacer in **126**.

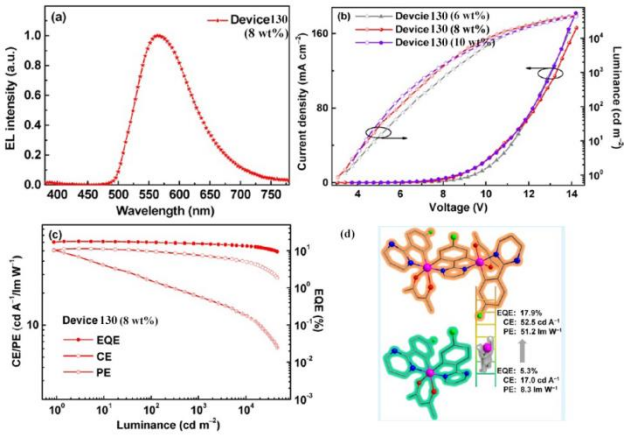

Fig. 37 (a) EL spectrum of device of complex **130** (8 wt%). (b) J–V–L relationships of devices of complex **130** (6, 8 and 10 wt%). (c) Efficiencies vs luminance curve of device of complex **130** (8 wt%). (d) The peak efficiencies of device based on

complex **130** and corresponding mononuclear analogue. Reproduced with permission from ref. 114. Copyright 2016 American Chemical Society.

In 2016, a series of C^N-type bridged Ir(III) dinuclear complexes **127**–**132** with short conjugated bridging ligands (2-phenylpyrimidine derivatives) were reported by Zhou and coworkers.[114, 115] The corresponding mononuclear complexes were also obtained. All the mono- and dinuclear complexes were successfully separated by column chromatography due to their different molecular dipole moments. The dinuclear complexes **127**–**132** showed intense orange phosphorescence (τ = 0.18–0.48 μs) red-shifted relative to the corresponding mononuclear analogues. The PLQYs of **127**–**132** are in the range of 36–68% in CH_2Cl_2 solution, which are high values for an orange-red diiridium complex. Solution-processed OLEDs based on all the dinuclear complexes were fabricated with a simple device structure. The detailed performance of the devices is summarized in Table 3. Complex **130** (8 wt%) gave outstanding electroluminescent performance (Fig. 37) with the peak luminance, EQE, CE and PE of 46 206 cd/m^{-2}, 17.9%, 52.5 cd/A and 51.2 lm/W, respectively.

Table 3 Photophysical properties and electroluminescence performance of yellow/orange emitting dinuclear Ir(III) complexes

	Photophysical properties				Device performance					
Complex	$\lambda_{max,PL}$ (nm)	PLQY (%)	τ_p (μs)	Turn-on voltage (V)	$\lambda_{max,EL}$ (nm)	Maximum brightness (cd m^{-2})	EQE (%)	CE (cd A^{-1})	PE (lm W^{-1})	Ref.
85	546, 590[a]	41[a]	5.3[b]	7.5	550, 594	770	4	12	3.53	74
86	545, 590[a]	28[a]	4.6[b]	4.2	550, 594	1900	0.9	3	1.06	74
87	550, 596[a]	21[a]	5.75[b]	4.5	554, 600	2120	2.55	8	2.05	74
88	544, 588[a]	—	—	8.2	—	780	0.55	1.7	0.40	74
89	542, 586[a]	—	—	9.2	—	892	1.4	4.2	0.81	74
90	548, 592[a]	38[a]	5[b]	6.6	553, 597	3700	3.2	10.3	2.61	74
91	549, 592[a]	29[a]	3[b]	4.8	554, 596	1860	1.4	4.6	1.61	74
92	552, 595[a]	28[a]	3.9[b]	6.2	554, 594	3600	2.6	8	1.87	74
93	563, 600[a]	2.5[a]	0.21[a]	6.5	447, 562	982	0.64	1.29	0.59	76
94	600[a]	—	—	5.7	612	630	0.21	0.51	0.25	76
95	611, 670[a]	15.7[a]	1.98[a]	8.1	557	178	0.37	0.44	0.13	76
96	556[a]	0.9[a]	0.6[a]	7.7	551	>6000	2.59	9.09	2.16	76
110	606[a]	17.5[a]	0.41[a]	5	n/a	n/a	0.1	0.23	n/a	195
112	588[a]	0.9[a]	0.4[a]	3	596	<10	0.16	n/a	n/a	117
113	521[a]	0.7[a]	1.2[a]	3	540	<10	0.13	n/a	n/a	117
125	594[c]	6.3[a]	n/a	6	670	1022	n/a	0.44	0.17	75
126	557[c]	14.9[a]	n/a	4	621	101	n/a	0.061	0.03	75
127	606[a]	61[a]	0.18[a]	3.1	598	18410	14.4	27.2	19.5	115
128	607[a]	49[a]	0.18[a]	3	598	16486	6.4	11.5	8.7	115
130	580[a]	68[a]	0.48[a]	3.2	564	46206	17.9	52.5	51.2	114

[a] Measured in solution state. [b] Measured in thin film. [c] Measured in solid state.

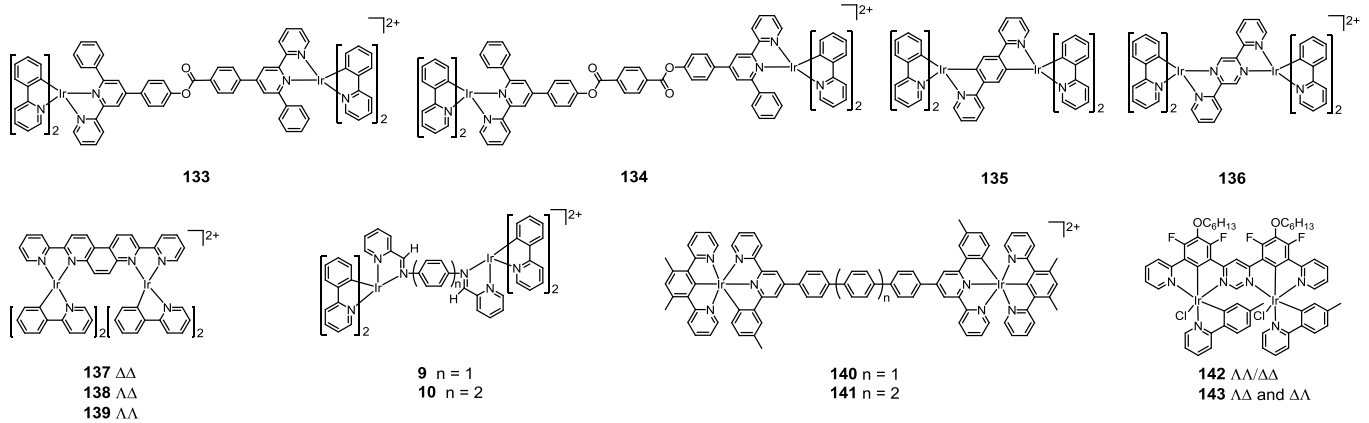

Fig. 38 Dinuclear Ir(III) complexes with red emission.

Chem Soc Rev

REVIEW ARTICLE

3.1.1.3 Red-emitting dinuclear Ir(III) complexes. Red-emitting Ir(III) complexes are important for achieving highly efficient multi-component white emission with good color purity. Generally, a small energy gap between the HOMO and LUMO levels is needed. Compared with mononuclear Ir(III) complexes, dinuclear Ir(III) complexes are more suitable candidates for red emitters by tuning the conjugation length of the bridging ligands or by attaching electron-withdrawing moieties onto the bridging ligands.

In 2001, two dinuclear Ir(III) complexes **133** and **134**, and their corresponding mononuclear analogues were reported by Campagna's group. [116] The UV-vis absorption spectra revealed that the MLCT band is significantly more intense in **133**, which features an asymmetric bridging ligand, compared with **134**. This suggests that the CT transition from the Ir center to the bridging L–C(O)O unit of **133** has a stronger oscillator strength than to the bridging L–OC(O) unit of **134**. Furthermore, the molar absorption coefficient of the MLCT band of **134** is almost twice that of the corresponding mononuclear complex. This indicates that the second metal center promotes light absorption. Both **133** and **134** showed red emission with λ_{max} at 638 and 620 nm, respectively, in CH_2Cl_2 solution. The corresponding PLQYs and excited lifetimes are 4%, 0.17 μs for **133**, and 4.5%, 0.19 μs for **134**. Compared with **134**, the significant red-shift of **133** can be attributed to the photo-induced intramolecular energy transfer from the MLCT (Ir→L–OC(O)) to MLCT (Ir→L–C(O)O) across the asymmetric bridging ligand.

In 2004, Tsuboyama *et al*. reported a neutral dinuclear Ir(III) complex **135** that exhibited red phosphorescence in both solution and solid states.[199] The emission λ_{max} is at 665 nm in 2-methyltetrahydrofuran; the corresponding PLQY and lifetimes are 4% and 2 μs, respectively. By contrast, no emission was observed for the cationic dinuclear Ir(III) complex **136**, which was reported by Zysman-Colman *et al*. in 2013.[60]

In 2007, Auffrant *et al.* reported three red emitters **137**–**139**.[69] Importantly, the three isomers were separated by using [*n*-Bu_4N][*Δ*-TRISPHAT] as a resolving agent. The tris(tetrachlorobenzenediolato)phosphate(V) anion (TRISPHAT) is well established as a powerful resolving agent for chiral cationic organometallic complexes. The luminescent properties of **137**–**139** are essentially identical to one another with weak emission in the red region (λ_{max} = 654 nm, Φ_{PL} ~ 0.6%, τ ~ 0.05 μs).

In 2014, two new ionic dinuclear Ir(III) Schiff base complexes **9** and **10** were reported by our group.[111] Both complexes showed faint emission in the solution state, whereas intense emission was observed in aggregated or solid state. Adding the poor solvent water into dilute solutions of the complexes, led to a remarkable increase in the emission intensity when the water fraction exceeded ca. 60% (Fig. 39a). These were the first examples of dinuclear ionic Ir(III) complexes that display aggregation-induced phosphorescent emission (AIPE). The mechanism of AIPE can be attributed to the restriction of intermolecular motion (RIM) through the intermolecular interactions (Fig. 39b), which are seen by X-ray crystal structure analysis and TD-DFT calculations. In a neat film state, both complexes **9** and **10** exhibited intense red emission with λ_{max} at 644 and 692 nm, respectively. Complex **10** is among the most red emissive ionic Ir(III) complex to date. The corresponding PLQYs are as high as 37% and 26% for **9** and **10**, respectively. These data indicate that highly efficient ionic transition metal complexes (iTMCs) can be realized by designing AIPE-active ionic dinuclear Ir(III) complexes.

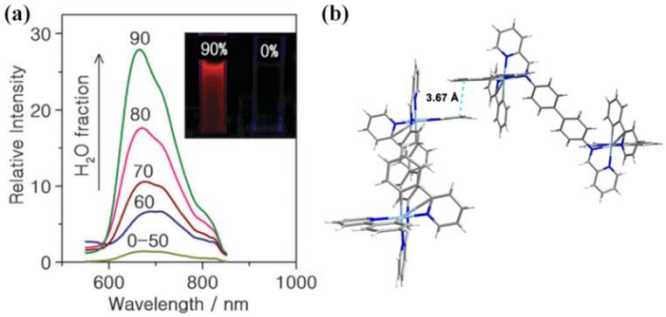

Fig. 39 (a) Emission spectra of complex **9** in CH_3CN–water mixtures with different water fractions (0–90% v/v) at room temperature. (b) Optimized geometry of complex **10** in the solid state. Reproduced with permission from ref. 112. Copyright 2014 The Royal Society of Chemistry.

In 2008, Williams *et al*. reported two dinuclear Ir(III) complexes **140** and **141** that feature two cyclometalating terdentate ligands in the structure.[68] In CH_3CN solution, both complexes showed similar emission properties (λ_{em} = 632 nm, Φ_{PL} ~ 2.7%, τ ~ 0.14 μs).

In 2014, two isomeric dinuclear Ir(III) complexes **142** and **143**, bridged by a terdentate N^C^N ligand were reported by Kozhevnikov and coworkers.[200] The luminescent properties of the two complexes are essentially identical to one another, with red phosphorescence at λ_{max} 625 nm in CH_2Cl_2 solution. The PLQYs are as high as 65%, which are amongst the best values for red phosphorescent emitters known to date. This work supported a new strategy for obtaining highly efficient diiridium complexes and further application in OLEDs. Moreover, this new class of complexes are also highly desirable candidates as sensitisers in both dye-sensitised solar cells and in

photocatalysed water splitting due to their strong absorption in the orange-to-red region.

In summary, highly efficient green and yellow/orange emitting OLEDs based on diiridium complexes emitters have been achieved in the past three years by both solution processing and vacuum evaporation, which challenges the previous misconception that dinuclear complexes are poor phosphors and usually show unsatisfactory performance in OLEDs. However, some challenges still remain in the future work: (i) Unlike their monoiridium analogues, highly stable and efficient deep-blue emissive diiridium complexes are still absent: further ingenious molecular design and a short conjugated bridge unit may solve this issue. (ii) Red emissive diiridium complexes can be easily designed by installing long conjugated bridging ligands between the iridium centers. However, highly efficient red emissive diiridium complexes are still rare. Modified designs that avoid intramolecular energy processes from MLCT to LC (bridging ligand center) states may enhance the emission. (iii) Further optimization of device structures to improve the EL performance with low roll-off is still needed. It is worth noting that the AIPE-active diiridium complexes which exhibit intense emission in the solid and pure film states are potential candidates in non-doped (neat film) OLEDs. Particularly, the first non-doped OLEDs based on AIPE-active mononuclear Ir(III) species with extremely simple device structures have been fabricated by Shan and co-workers, with a high current efficiency and EQE of 25.7 cd A^{-1} and 7.6%, respectively.[201]

3.1.2 TADF-active Cu(I) complexes

Thermally activated delayed fluorescence (TADF) materials, which utilize up-conversion of triplet excitons to the singlet excited state by reverse intersystem crossing (RISC) to efficiently harvest both singlet and triplet excitons (Fig. 40) have emerged as third-generation organic electroluminescent materials.[169, 202, 203] In 2009, Adachi *et al.* reported a Sn(IV)-porphyrin complex as a TADF material that utilized both singlet and triplet excitons in an OLED.[140] Since then, various TADF materials have been designed and synthesized, such as organic small molecules,[167, 203, 204] Cu(I) complexes,[168, 205, 206] Au(I) complexes,[1] organic exciplexes,[207] organic polymers,[202] quantum dots[208] and CDs@zeolite.[166] TADF-active Cu(I) complexes can exhibit advantages with respect to the other kinds of TADF materials,[205, 209, 210] such as: (i) Cu(I) complexes often have a small energy separation between the lowest singlet S_1 and triplet T_1 states due to the transitions of distinct metal-to-ligand charge transfer (MLCT) character; (ii) Cu(I) complexes can show pure TADF emission without a small amount of prompt fluorescence contributions due to the strong spin-orbit coupling (SOC), in contrast to the pure organic molecules; (iii) dual emission (TADF and phosphorescence) is usually observed in Cu(I) complexes, and this could effectively decrease transient singlet or triplet exciton concentrations and further restrict singlet–triplet and triplet–triplet annihilation (STA and TTA, respectively) which normally exist in PH and TADF-based OLEDs. Numerous TADF-active mononuclear Cu(I) complexes have been reported.[205] However, mononuclear Cu(I) complexes often suffer from the structural distortion in the excited state which reduces PL and EL efficiency. Accordingly, dinuclear Cu(I) complexes which possess more a rigid molecular conformation have attracted much attention in recent years.[211, 212] Dinuclear Cu(I) complexes show three advantages with respect to the mononuclear analogues:[205, 209, 211] (i) dinuclear Cu(I) complexes usually exhibit a smaller energy gap between S_1 and T_1 states, and a small ΔE_{ST} is regarded as the most important criterion for achieving high TADF efficiency; (ii) the more rigid conformation of dinuclear Cu(I) complexes can effectively restrict non-radiative channels and give high PL and EL efficiencies; (iii) introduction of another metal atom can effectively enhance the SOC and further realize phosphorescence and TADF dual emission. In this section, representative progress in TADF-active dinuclear Cu(I) complexes will be discussed.

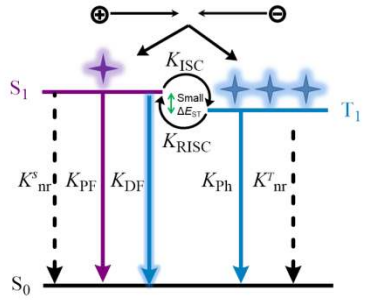

Fig. 40 The TADF mechanism that occurs during electroluminescence. PF = prompt fluorescence; DF = delayed fluorescence; ISC = intersystem crossing; RISC = reverse intersystem crossing; ΔE_{ST} = the energy difference between the first excited singlet and triplet states; nr = nonradiative.

3.1.2.1 TADF-active dinuclear Cu(I) complexes. Most investigations of dinuclear Cu(I) complexes are focused on halogenido-bridged systems because they usually show small ΔE_{ST}.[205] The ΔE_{ST} data of representative examples are summarized in Fig. 41 and Table 5. This kind of complex is usually synthesized *via* classical solution-based reactions or through the evaporation of the organic ligand together with CuI to further obtain CuI-based dunuclear complexes.[209]

In recent years, Yersin's group have extensively developed the photophysics of TADF-active Cu(I) complexes. In 2013, a series of halogenido-bridged Cu(I) complexes **144**–**148** with chelating ligands exhibiting N and P donors were synthesized.[213, 214] The emitting states of the complexes were attributed mainly to the singlet excited state corresponding to a TADF process at ambient temperature. It is worth noting that the complexes **146** and **147** exhibited rare blue emission among halogenido-bridged Cu(I) complexes with a maximum emission peak at 464 and 465 nm, respectively.

In 2014, the TADF mechanism of **149** was studied by Yersin *et al.*[211] At 77 K, **149** showed long-lived phosphorescence with a decay time of 2200 μs, whereas a short-lived decay time of 3 μs can be observed at room temperature. A small ΔE_{ST} of 600

cm^{-1} (74 meV) calculated from the emission spectra at 298 and 77 K indicated that the emission of **149** at room temperature originated from TADF. The short-lived TADF lifetime (~3 μs) showed that this kind of Cu(I) complex is promising for applications in OLEDs.

In 2015, three new Cu(I) complexes **150**–**152** with high PLQYs in the range of 52%–92% at room temperature were reported by Yersin's group.[206] The detailed photophysical investigations indicated that the emitting states for all complexes at room temperature originate from combined TADF and fast phosphorescence. For example, the ratio of TADF : phosphorescence for complex **150** is 80% : 20%. Thus, the overall emission decay time for the complex is reduced when compared with the pure TADF emission. This work represented a very promising way for engineering novel dual emissive Cu(I) complexes.

In 2016, Yersin *et al*. reported a Cu(I) complex **153**, bearing iodine bridges and an additional bidentate ligand (N^P), which exhibited the smallest ΔE_{ST} (270 cm^{-1}; 34 meV) so far reported in a Cu(I) complex (Fig. 41 and Table 5).[209] The small ΔE_{ST} facilitates highly efficient TADF with a short decay time of 5 μs. Introduction of an additional bidentate ligand (N^P) can not only significantly improve stability, but also induces a high PLQY (≈ 100%) by rigidifying the structure of the complex. All the above advantages favour this kind of Cu(I) complex as an emitter for highly efficient OLEDs.

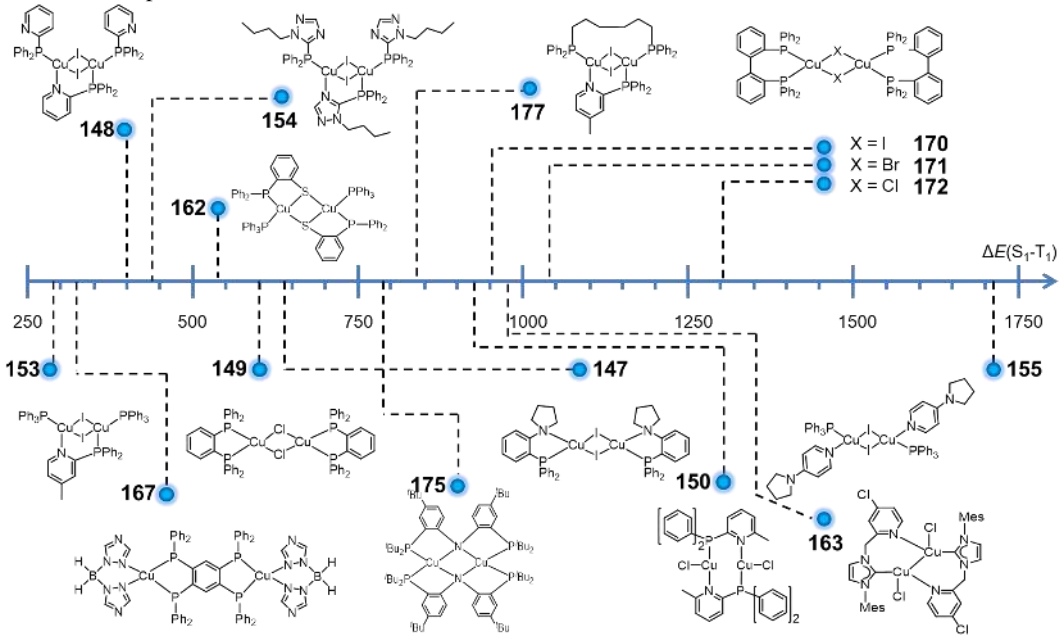

Fig. 41 Chemical structures of the TADF-active dinuclear Cu(I) complexes discussed in this contribution. They are arranged according to the energy separations between the lowest singlet S_1 and triplet T_1 state $\Delta E(S_1–T_1)$. The values of $\Delta E(S_1–T_1)$ are given in Table 5.

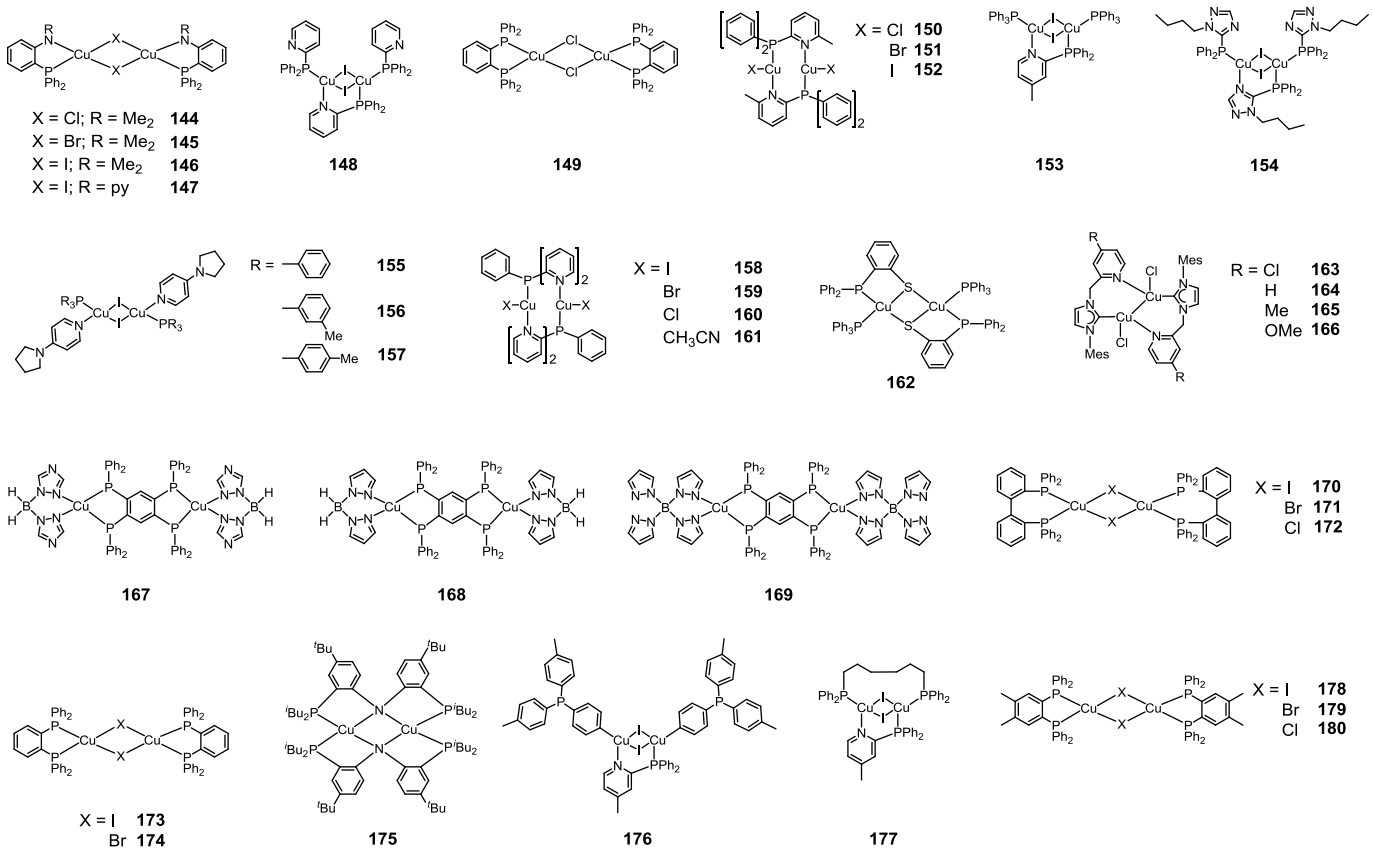

Fig. 42 Chemical structures of the TADF-active dinuclear Cu(I) complexes.

More recently, a new three-fold bridged dinuclear Cu(I) complex **154** that exhibits sky-blue emission peaking at 488 nm in the solid state at ambient temperature has been reported by Yersin's group.[215] Benefiting from the rigid molecular structure, high PLQY (≈ 85%) was observed for **154** in the solid state. In-depth photophysical studies explained the temperature-dependent luminescent behavior in the range of 1.3 K−300 K. As shown in Fig. 43a and b, below T ≈ 10 K, the steep decrease of the emission decay time with increasing temperature is a consequence of splitting of the T_1 state into substates and increasing the population of triplet substate III. Significant zero-field splitting (ZFS) energy of ΔE(III−II, I) ≈ 2.5 cm^{-1} will lead to an additional decay component that results from the direct effect of spin−lattice relaxation (SLR). The radiative rate k(III) is calculated to be 20 times higher than for the substates I and II. Thus, two decay components are observed. When focusing on the temperature range of ∼20 ≤ T ≤ ∼80 K, steady decay with an average decay time of 55 µs can be assigned to the transitions from the three triplet substates to the ground state. In the temperature range of ∼80 ≤ T ≤ 300 K, the decay time decreases obviously from 55 to 7 µs at room temperature. The ambient-temperature emission of **154** is assigned to the combined TADF (87%) and phosphorescence (13%). The combined emission shows a shorter decay time than the pure TADF emission (8 µs) (Fig. 43c). Accordingly, dual emissive Cu(I) complexes represent attractive candidates for highly efficient OLEDs by decreasing the population time of the excitons.

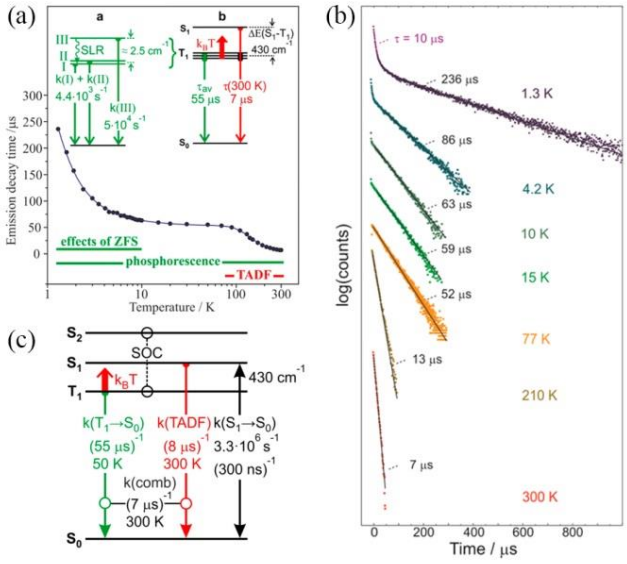

Fig. 43 (a) Temperature dependence of the emission decay time of complex **154** and fit curve. The insets show energy level diagrams displaying the ZFS of the T_1 state (a) and the singlet−triplet splitting (b) with state-related decay times/rates. SLR represents spin-lattice relaxation between triplet substate

III and the substates II/I. (b) Emission decay curves and decay times of complex powder at selected temperatures; λ_{exc} = 378 nm, λ_{det} = 490 nm, pulse width < 100 ps. (c) Simplified energy level diagram and decay times of complex powder. The ambient temperature emission represents combined TADF and phosphorescence. The S_2 state is displayed schematically to illustrate an effective SOC path. Reproduced with permission from ref. 215. Copyright 2018 American Chemical Society.

To obtain blue emission from a Cu(I) complex is still a big challenge. Recently, Kato's group synthesized a series of deep-blue emitting dinuclear Cu(I) complexes **155**–**157**, using both the traditional solution method and the recently developed solvent-free thermal method.[216] At room temperature, **155**–**157** showed bright emission in the range from 435 to 452 nm. These data represent the bluest emission in Cu(I) complex systems so far reported. The detailed TD-DFT investigations revealed all three complexes possess relatively small ΔE_{ST} in the range of 1500–1700 cm^{-1} (0.19–0.21 eV). The short decay times within 5 μs for all three complexes at room temperature indicated TADF in each complex. It is worth noting that the complex **155** showed the shortest decay time of 2.25 μs in TADF-active Cu(I) complexes reported so far.

Recently, a series of atypical dinuclear Cu(I) complexes **158**–**162** without halogenido-bridges has been synthesized by Kato and co-workers. TADF was identified as a plausible mechanism for luminescence with high PLQY of > 50% at room temperature, whereas at low temperatures phosphorescence was observed.[217, 218] Notably, **158**–**160** were synthesized *via* a novel solvent-assisted mechanochemical method which involved grinding complex **161** with halogenated potassium in the presence of a trace amount of water. Cu_4 and Cu_6 cluster structures were also obtained.[218]

In 2016, Steffen's group reported a series of dinuclear Cu(I) NHC–picolyl complexes **163**–**166** with high PLQYs of > 50%.[219] The detailed photophysical and TD-DFT investigations indicated complexes **163**–**165** are TADF materials, whereas complex **166** is a phosphorescent emitter. Cuprophilic interactions between two Cu centers supplies strong SOC to ensure highly efficient $T_1 \leftrightarrow S_1$ and $T_1 \rightarrow S_0$ processes, resulting in highly efficient emission, either by TADF or by fast phosphorescence.

In 2016, three tetraphosphane bridged dinuclear Cu(I) complexes **167**–**169**, terminally chelated by a borate diimine anion, were synthesized in good yields by Lu's group.[220] A small ΔE_{ST} (322 cm^{-1} – 644 cm^{-1}; 30–80 meV) observed in these complexes indicated TADF emission at ambient temperature. Slight blue-shifts in the emission were observed on cooling solid samples of **167**–**169** from 293 to 77 K. This observation is unusual for TADF emission which usually red-shifts on cooling. The blue shift was tentatively explained by a distortion from a tetrahedral ground-state to a more flattened excited state after MLCT excitation, leading to a larger energy gap.

In 2017, Chen *et al*. reported three halogenido-bridged Cu(I) complexes **170**–**172**[221] with emission colors from yellow to blue in the solid state at room temperature with low quantum yields (Φ <0.01%). The low PLQYs for all these complexes were attributed to the unfavourable rigid environment around the copper centers.

3.1.2.2 Dinuclear Cu(I) complex based OLEDs. OLEDs based on Cu(I) complexes are usually fabricated by the solution spin coating of the emitter layer due to the poor thermal stability of the Cu(I) complex. The detailed device performance data of dinuclear Cu(I) complexes are summarized in Table 6.

In 2007, Tsuboyama *et al*. reported three halogenido-bridged Cu(I) emitters **153**, **173** and **174**.[222] The solution-processed OLED using **173** as dopant showed a maximum EQE, PE and CE of ~4.8%, 4.2 lm/W and 10.4 cd/A, respectively. However, a possible TADF mechanism was not discussed.

In 2010, a highly emissive bis(phosphine)diarylamido dinuclear Cu(I) complex **175** was reported by Peters and co-workers.[223] The high PLQY can be attributed to the less distortion in the excited state of **175** which was established by a relatively small Stokes shift and TD-DFT calculations. Temperature dependent decay times combined with time-resolved spectra indicated complex **175** is a TADF material. Vapour-deposited OLEDs based on **175** as dopant gave remarkable EL performance with maximum external quantum efficiency (EQE) up to 16.1%. These data demonstrated that both singlet and triplet excitons originating from TADF can be harvested effectively in the device.

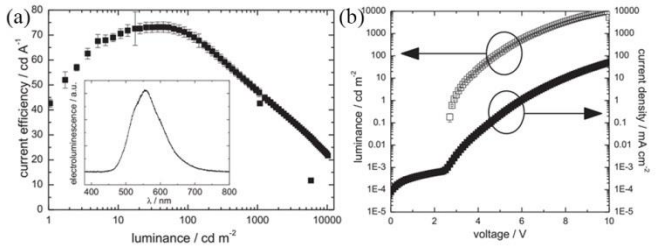

Fig. 44 (a) Current efficiency versus luminance of complex **177**; inset: electroluminescence spectrum of the device. (b) Luminance (left ordinate) and current density (right ordinate) versus bias voltage. Error bars were determined based on intrabatch variations from different pixels. Reproduced with permission from ref. 174. Copyright 2015 Wiley-VCH.

In 2013, Baumann and co-workers reported TADF-active Cu(I) complexes with N^P briding ligands and PPh_3 substituents on copper, represented by structure **176**[224]. Emission colors were tuned from yellow to blue by using electron-rich (*e.g.* imidazole, triazole) or electron-poor (*e.g.* pyridine, oxadiazole) heterocycles as part of the bridging ligand. **176** was tested in solution-processed OLEDs. The poor EL properties can be attributed to the nonoptimized device construction, resulting in leakage of an excess of holes/electrons or radical cations/anions at the emission layer.

To further optimize the OLED construction and obtain superior device performance, in 2015, Baumann and co-workers reported a green emissive dinuclear Cu(I) complex **177** which exhibited very high PLQY in both the solid state (≈ 88%) and host doped film (≈92%) at room temperature.[174] A small ΔE_{ST} of 830 cm^{-1} (0.10 eV) and temperature-dependent

decay profiles proved that the emission of complex **177** mainly originated from TADF. Solution-processed OLEDs based on **177** were fabricated. The detailed device structures are summarized in Table 6. 3TPYMB and PLEXCORE UT-314 were chosen to avoid quenching by energy transfer because of their high triplet energies. Benefiting from the efficient TADF, high EQE of 23% and CE of 73 cd A^{-1} were obtained for **177** devices. Moreover, the turn-on voltage was as low as 2.6 V. This is the best reported EL performance based on Cu(I) emitters and is even comparable with leading green phosphorescent OLEDs using iridium or platinum. The obvious "roll-off" phenomenon in the device (Fig. 44a) can be attributed to the loss of charge balance at high injection.

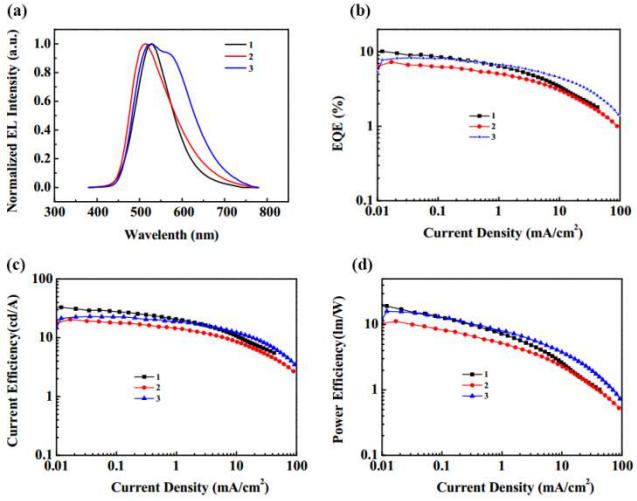

Fig. 45 (a) EL spectra of devices 1–3 using complex **178** EQE (b), CE (c) and PE (d) efficiencies vs current density curve of devices 1–3. Reproduced with permission from ref. 225. Copyright 2016 Elsevier.

In 2016, the EL properties of three TADF-active Cu(I) complexes **178**–**180** with blue-green emission were studied by Liu and co-workers.[225] The device structures are summarized in Table 6. The device A1 based on complex **178** achieved the best EL performance, with a maximum EQE of 10.1%, CE and PE efficiencies of 32.9 cd A^{-1} and 19.9 lm W^{-1}, respectively (Fig. 45). The device 3 exhibited a low turn-on voltage (3.9 V) and relatively low efficiency roll-off compared with devices 1 and 2, suggesting that holes and electrons were confined completely in the EML.

In summary, research on TADF-active dinuclear Cu(I) complexes has become increasingly significant due to their potential applications in electroluminescent devices. Especially, the strong SOC of Cu(I) complexes ensures highly efficient emission with short decay time, either by TADF or fast phosphorescence comparable with all-organic TADF molecules. Superior EL performance based on a dinuclear Cu(I) complex dopant has been realized with high EQE up to 23%. However, studies of OLEDs of Cu(I) complexes that usually show pure TADF or dual emission with short decay times are still at an initial stage. Further development of highly efficient blue and red emissive dinuclear Cu(I) complex and optimisation of device structures to achieve high EL performance are highly desired.

Table 5 Photophysical properties of dinuclear Cu(I) complexes

Complex	$\lambda_{max,PL}$ (nm) 300 K	$\lambda_{max,PL}$ (nm) 77 K	PLQY (%)	τ (µs) 298 K	τ (µs) 77 K	$\Delta(S_1\text{-}T_1)$ (cm^{-1})	Ref.
144	506	513	45	6.6	220	460	213
145	490	498	65	4.1	930	510	213
146	464	471	65	4.6	270	570	213
147	465	465	65	5.6	250	630	213
148	539	552	80	6.5	32	400	214
149	545	545	35	3.0	2200	600	211
150	485	510	92	8.3	44	930	206
151	501	526	52	12.4	84	950	206
152	484	511	76	7.3	51	1100	206
153	511	520	97	5.0	20	270	209
154	488	488	85	7	52	430	215
155	435	438	24	2.25	101.29	1715	216
156	452	463	31	2.55	99.76	1694	216
157	449	432	51	4.26	80.66	1592	216
158	530	542	74	32.9	87	—	217
159	518	540	50	11.6	46.1	—	217
160	528	537	23	5.01	31.1	—	217
161	470	484	2	—	—	—	217
162	484	482	52	1.66	200	547	218
163	550	559	49	11.0	101	960	219
164	520	530	59	11.0	97.6	630	219
165	523	536	68	9.2	32	670	219
166	538	544	67	15.3	18.7	> 1900	219

167	540	534	45	7.4	68.9	322	220
168	569	561	28	11.9	29.1	644	220
169	580	570	7	20.5	25.7	563	220
170	436,472,575	472,487,577	< 1	7.9	65.6	950	221
171	487	528	< 1	6.2	3163	1036	221
172	535	512	< 1	19.8	1834	1303	221
173	502	505	80	4.0,1.5	211,50	—	222
174	520	524	60	4.3,1.0	2300	—	222
175	512	523	57	11	336	790	223
177	519	558	88	24	109	830	174
178	498	500	32	2.5	103	966	225
179	511	517	28	12.5	714	966	225
180	527	532	29	4.8	818	1127	225

Table 6 Performance of devices fabricated from Cu(I) complexes

Complex	Device structure	$\lambda_{max,EL}$ (nm)	Maximum brightness (cd m^{-2})	EQE (%)	CE (cd A^{-1})	PE (lm W^{-1})	Ref.
173	ITO/PF01/CBP:Cu(10%)/Bphen/KF/Al	565	1700	4.8	10.4	4.2	222
175	ITO/CFx/TAPC/CBP:TAPC(25%)/CBP:TAPC (25%):Cu(0.2%)/CBP/BAlq-13/LiF/Al	515	—	16.1	—	—	223
176	ITO/PEDOT:PSS/poly-TPD/PVK:mCPy:CBP: Cu/TPBi/ LiF/Al	547	—	—	—	—	224
177	ITO/PEDOT:PSS/PLEXCORE UT-314/PYD2: Cu(30%)/3TPYMB/ LiF/Al	—	10000	23	73	—	174
178	ITO/MoO_3/TAPC/TCTA/mCP:Cu(10%)/TmPy PB/ LiF/Al	528	2339	10.1	32.9	19.9	225
179	Same as **173**	528	2399	7.3	20.4	11.2	225
180	Same as **173**	528	3256	8.3	22.9	16.0	225

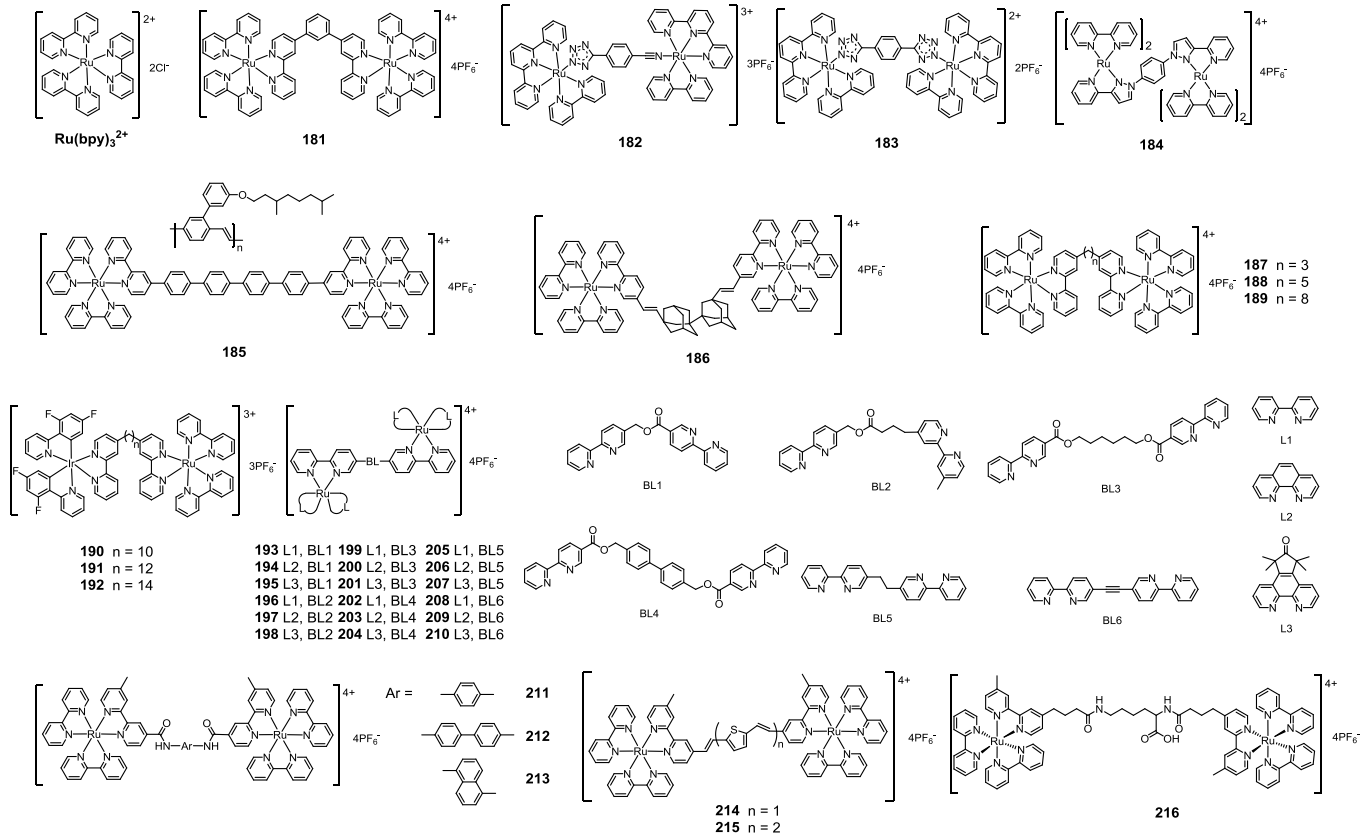

Fig. 46 Chemical structures of dinuclear Ru(II) complexes.

Chem Soc Rev

REVIEW ARTICLE

3.2 Electrochemical luminescence (ECL)

Electrochemiluminescence (ECL, also known as electrogenerated chemiluminescence) is a process whereby species generated at an electrode interface undergo electrochemical reactions to form an electronically excited state that emits light upon relaxation to a lower-level state. Specifically, as one of the most important bioanalytical detection methods, ECL has been widely used in clinical diagnostics and environmental assays due to its extremely low detection limit, high sensitivity and fast rate of sample analysis.[226] Generally, ECL can be produced through two dominant pathways, namely the annihilation and co-reactant pathways.[227] The most ubiquitous and famous ECL luminophore is the mononuclear species, $[Ru(bpy)_3]^{2+}$ (bpy = 2,2'-bipyridine) (Fig. 46) first reported in 1972 by Tokel and Bard.[228] Since then, many attempts have been made to decorate the ligands of Ru complexes so as to improve the ECL efficiency and sensitivity.[17] Alongside the well-studied mononuclear complexes, dinuclear or multinuclear Ru(II) complexes are considered to be a promising approach to enhance ECL properties because of their multiple redox centers.[229-231] Furthermore, ECL color switching can be tuned by application of a range of potentials in a binuclear heterometallic complex.[84] In this section, some representative ECL chromophores based on dinuclear or multinuclear Ru(II) complexes connected with different kinds of bridging ligands, such as benzene ring, alkyl chain, symmetrical aryl-diamide or oligothiophene rigid bridge, amino acid lysine (Lys), etc. will be discussed in detail.

In 1998, the ECL properties of dinuclear Ru(II) complex **181** with a 1,4-bis(4'-methyl-2,2'-bipyridin-4-yl)benzene (bphb) bridging ligand in acetonitrile (MeCN), 50:50 (v/v) MeCN/H_2O, and aqueous solutions were studied by Bard and co-workers.[232] As a reference, the corresponding mononuclear Ru(II) complex was also studied. The cyclic voltammetry traces of **181** in MeCN/0.1 M Bu_4NPF_6 are shown in Fig. 47. The two, one-electron, reduction processes at -1.051 V and -1.203 V can be assigned to stepwise one-electron reduction processes on the bridging ligand, as shown in equations (2) and (3).

$$[(bpy)_2Ru(bphb)Ru(bpy)_2]^{4+}+e^- \rightarrow [(bpy)_2Ru(bphb^-)Ru(bpy)_2]^{3+} \quad (2)$$

$$[(bpy)_2Ru(bphb^-)Ru(bpy)_2]^{3+}+e^- \rightarrow [(bpy)_2Ru(bphb^{2-})Ru(bpy)_2]^{2+} \quad (3)$$

Furthermore, a two-electron reduction process observed at -1.575 V (not shown in Fig. 47a) was proposed to occur at the bpy ligands. For the oxidation process, a two-electron oxidation wave at +1.573 V can be assigned to the two Ru(II→III) centers, and is consistent with negligible electronic coupling between the two Ru centers.

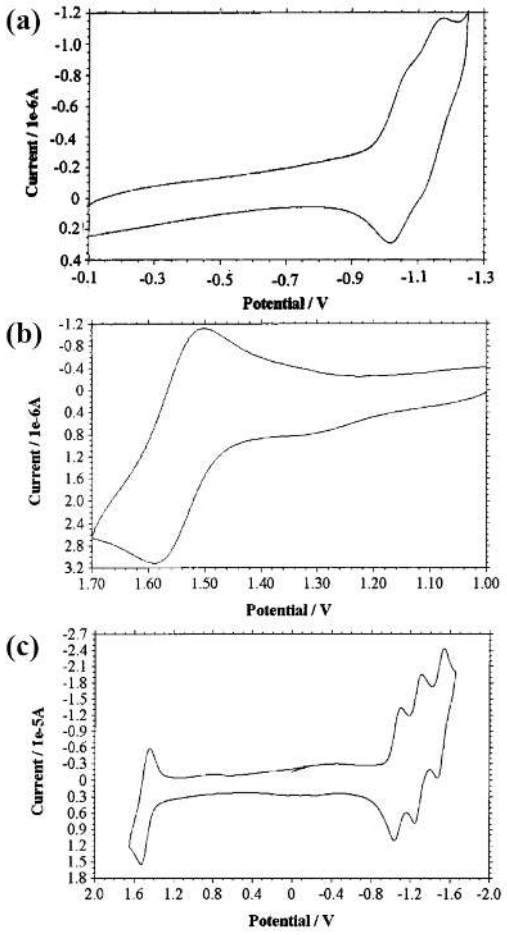

Fig. 47 (a) Reductive cyclic voltammogram of complex **181**. (b) Oxidative cyclic voltammogram of complex **181**. (c) Cyclic voltammogram of mononuclear $(bpy)_2Ru(bphb)^{2+}(2PF_6^-)$. Reproduced with permission from ref. 232. Copyright 1998 American Chemical Society.

For the corresponding mononuclear complex $(bpy)_2Ru(bphb)^{2+}$, as shown in Fig. 47c, three one-electron oxidation waves can be assigned to the first reduction on the bphb ligand (eqn 4) followed by sequential bpy-based

reductions (eqns 5 and 6). An oxidation process was assigned to Ru(II→III).

$$[(bpy)_2Ru(bphb)]^{2+}+e^-\rightarrow[(bpy)_2Ru(bphb^-)]^{1+} \quad (4)$$

$$[(bpy)_2Ru(bphb^-)]^{1+}+e^-\rightarrow[(bpy^-)(bpy)Ru(bphb^-)]^{0} \quad (5)$$

$$[(bpy^-)(bpy)Ru(bphb^-)]^{0}+e^-\rightarrow[(bpy^-)_2Ru(bphb^-)]^{1-} \quad (6)$$

Intense orange ECL was observed for both **181** and its mononuclear analogue with λ_{max} at 624 nm at the working electrode surface in MeCN solution. This emission is identical to that obtained upon photoexcitation, indicating that the ECL for both complexes can be attributed to the ^{3}MLCT state formed by the redox process. The ECL efficiency of **181** is as high as 0.16, which is comparable to its photoluminescent efficiency (0.158), revealing that the overall yield of excited states formed during the annihilation reaction is close to unity. Importantly, **181** exhibited much higher ECL efficiency than its mononuclear analogue (0.0006), and three times higher than the classic $Ru(bpy)_3^{2+}$ (0.05). Furthermore, the ECL properties for both **181** and $Ru(bpy)_3^{2+}$ through coreactant pathways in 50:50 (v/v) MeCN/H_2O and aqueous solution were investigated. The relative integrated ECL intensities of **181** with coreactant tripropylamine (TPrA) are 2.5–3 and 2 times that of the $Ru(bpy)_3^{2+}$/TPrA system in partially aqueous solution and purely aqueous solution, respectively. This work demonstrated that adding another metal center to form a dimetallic system is a promising way to improve the ECL efficiency in the both annihilation and coreactant pathways.

In 2006, ECL properties for two dinuclear Ru(II) complexes **182** and **183**, bearing an asymmetrical or a symmetrical tetrazole-based bridging ligand were studied by Bard and co-workers.[233] Electrochemical results showed two, one-electron, oxidation processes for asymmetrical **182** which were assigned to the two nonequivalent Ru centers mediated by the electronically asymmetric bridging ligand. In contrast, the single, two-electron, oxidation process for **183** was assigned to the two Ru(II → III) centers. UV-Vis-NIR spectroelectrochemistry for both complexes exhibited an obvious intervalence charge transfer (IVCT) band, indicating metal–metal electron coupling existed in the both complexes. The magnitude of the coupling energies for **182** and **183** are 500 and 313 cm^{-1}, respectively, according to the Hush model.[234] The ECL efficiencies of **182** and **183** are 150% and 40% relative to $Ru(bpy)_3^{2+}$, respectively, in 1 mM MeCN solutions and tetrabutylammonium hydroxide as supporting electrolyte.

In 2011, Wei *et al*. reported a new dinuclear Ru(II) complex **184** connected by a pyrazolyl-pyridyl-based bridging ligand.[235] The corresponding mononuclear analogue was studied as a reference. Both the mono- and dinuclear complexes exhibited intense orange emission (λ_{max} 603–608 nm) with lifetimes in the microsecond range in the solid state, revealing that the emission for both complexes can be attributed to the ^{3}MLCT state. Similar redox behaviour was observed for both complexes with one, two-electron, Ru(II → III) oxidation process and two, one-electron, reduction processes of the bipy ligands. The ECL efficiency of **184** is higher than its corresponding mononuclear complex, but both are lower than that of $Ru(bpy)_3^{2+}$ reference under identical experimental conditions. It is worth noting that the ECL intensity of **184** decreased significantly in the presence of diuretic furosemide, which provided a novel ECL method for the determination of diuretic furosemide with a low detection limit of 1.2×10^{-8} mol L^{-1}.

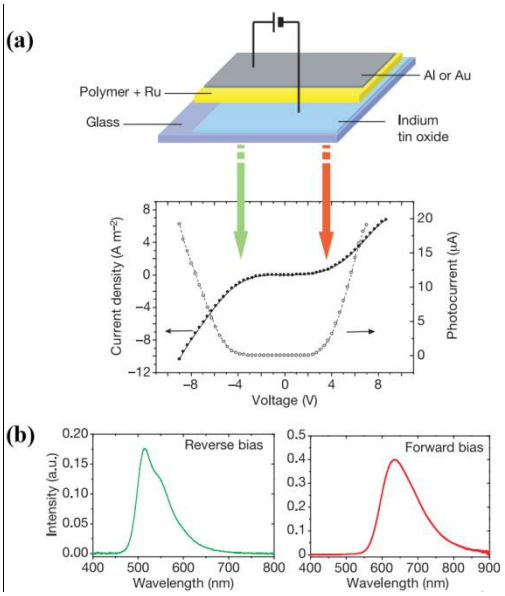

Fig. 48 (a) Schematic representation of the device structure (top), and plots of the current density (left) and photocurrent (right) versus voltage for the light-emitting cell. (b) Electroluminescence spectra at forward bias (right) and reverse bias (left) of a light-emitting cell comprising a dinuclear Ru complex and PPV host matrix (Ru/PPV mass ratio 1:5) as the emissive layer. Reproduced with permission from ref. 236. Copyright 2003 Nature Publishing Group.

In 2003, De Cola *et al*. reported an electroluminescent device with a doped emissive layer composed of a semiconducting poly(phenylenevinylene) (PPV) derivative and the dinuclear Ru(II) complex **185**.[236] The chemical structures are shown in Fig. 46. This device showed reversible color switching between red and green emission under forward and reverse biases, respectively (Fig. 48). Upon application of a low positive voltage (< 5 V), red emission originating from the excited state of **185** was observed due to the electroluminescent reaction between the oxidized and the reduced ruthenium complexes.

$$[Ru(ph)_4Ru]^{2+}+[Ru(ph)_4Ru]^{6+}\rightarrow*[Ru(ph)_4Ru]^{4+} + [Ru(ph)_4Ru]^{4+} \quad (7)$$

Interestingly, under reverse bias (-4 V), green emission originating from PPV was observed, and the proposed mechanism of light generation is presented in Fig. 49. At the ITO electrode, reduction of the ruthenium component is not centered on the metal units, but on the polyphenylene bridging ligand. The bipolaronic reduced species that is formed is

stabilized by the presence of the polyphenylene units and the Ru^{2+} cation in its proximity. Then, either the oxidized PPV accepts an electron from the reduced species to produce the excited state of the PPV, or PPV^{-} is formed by a stepwise electron transfer from the ruthenium component. With either mechanism, green light can be generated at reverse bias. It is worth noting that the reversible color switching was not observed in dinuclear ruthenium complex **186** under the same conditions. These results establish that the reversible color switching in electroluminescence is determined by the choice of bridging ligand.

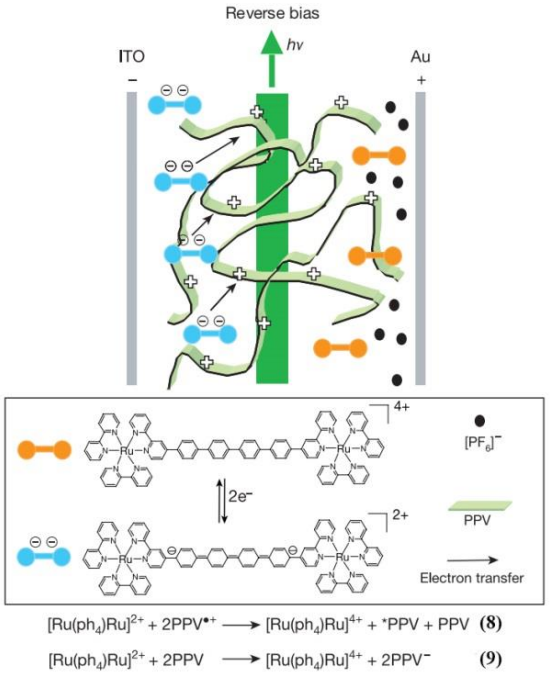

Fig. 49 Proposed mechanism for the emission of green light at reverse bias for **185**-PPV blend. Reproduced with permission from ref. 236. Copyright 2003 Nature Publishing Group.

In 2009, the ECL properties of a series of dinuclear Ru(II) complexes **187**–**189** brigded by alkyl chains of different length (n = 3, 5, 8) were studied by Peng's group.[229] The study was carried out in 0.1 M phosphate buffer with co-reactant TPrA or 2-(dibutylamino)ethanol (DBAE) at different working electrodes. The important findings are: 1) The ECL intensity increased with the increasing length of alkyl chain in the complex. Especially, in the presence of 5 mM TPrA or DBAE, complex **189** (n = 8) exhibited remarkable ECL enhancement (~25 times) at a Pt electrode when compared with $Ru(bpy)_3^{2+}$. 2) The log of ECL intensity exhibited a linear increase with increasing log of the concentration of **189** at a glassy carbon electrode with coreactant TPrA. The detection limit is as low as 0.1 fM, which is a remarkable increase in sensitivity compared to $Ru(bpy)_3^{2+}$ (200 fM). Furthermore, the TPrA needed with **189** is only 20% of that in the $[Ru(bpy)_3]^{2+}$/TPrA system.

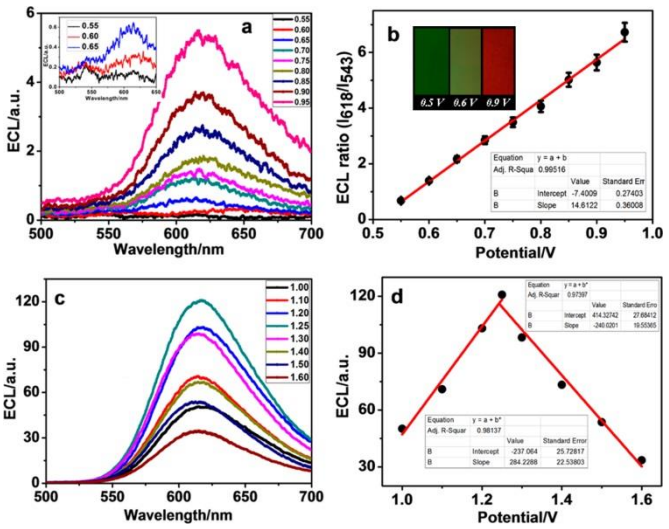

Fig. 50 (a) ECL spectra generated using an electrode potential swept from 0 to 0.95 V for 5×10^{-5} M **191** and 5 mM DBAE as co-reactant in phosphate buffer solution (0.1 M, pH 7.4). (b) Linearity of the ECL intensity ratio ($I_{618\ nm}/I_{543\ nm}$) and the scanning potential. (c) ECL spectra generated using an electrode potential swept from 0.95 to 1.60 V. (d) Linearity of the ECL intensity at 618 nm and the scanning potential. Reproduced with permission from ref. 84. Copyright 2015 American Chemical Society.

In 2015, Sun *et al.* reported three heterodinuclear Ir/Ru complexes linked by long alkyl chains (n = 10, 12, 14).[84] Interestingly, their electrochemiluminescence color can be tuned by scanning over a potential range from 0.55 to 1.6 V. As shown in Fig. 50a, for complex **191** a weak emission centered at 543 nm can be observed with an applied potential at 0.55 V. When the potential was increased to 0.95 V, a new emission peak centered at 618 nm appeared and the corresponding ECL intensity increased gradually, resulting in a linear response of the ECL intensity ratio ($I_{618\ nm}/I_{543\ nm}$) within the scanning potential range from 0.55 to 0.95 V (Fig. 50b). When the applied potential was further increased from 1.0 to 1.25 V, the $I_{618\ nm}$ from the ruthenium moiety increased sharply, while the $I_{543\ nm}$ from the iridium moiety was almost unchanged. Furthermore, the effective overlap between the peaks of the iridium and ruthenium moieties indicated that efficient resonance energy transfer occurs from the iridium to the ruthenium. Consequently in **191** the ECL intensity from ruthenium is higher than that of iridium. Upon further increasing the potential from 1.25 to 1.6 V, the ECL intensity from the ruthenium moiety decreased sharply, and exhibited a linear relationship (Figure 50d) between the ECL intensity and the scanning potential. Finally, this work developed a general methodology to control ECL color changes and on–off switching. This has potential bioanalytical applications by a ratiometric ECL detection method.

In 2009, Kim *et al.* reported a series of dinuclear Ru(II) complexes **193**–**204** with ester-bridged bis(bipyridine) ligands.[237] Their photophysical and ECL properties were studied, and the key findings are: 1) The maximum emission

wavelength of symmetrical dinuclear complexes **199**–**204** with symmetrical BL3 and BL4 ligands is in the range of 623–628 nm, while the complexes **193**–**198** with asymmetrical BL1 and BL2 ligands showed blue-shifted emission (586–598 nm). 2) The ECL intensity of asymmetrical complexes **195**–**198** showed a remarkable enhancement compared to the others. All the results indicated that the photophysical and ECL properties of dinuclear Ru(II) complexes can be tuned by the bridging ligands.

In 2013, Kim *et al*. designed two new bridging ligands, namely non-conjugated BL5 and conjugated BL6, coordinated with two ruthenium centers to form complexes **205**–**210**.[238] The ECL intensity for **208**–**210** bearing a conjugated bridging ligand was much higher than that of **205**–**207** containing a non-conjugated bridging ligand. It is worth noting that, similar to the previous work in 2009,[237] the complexes with a L3 ligand showed higher ECL intensity than that of complexes with L1 or L2 ligands.

In 2006, Sun *et al*. reported three dinuclear Ru(II) complexes **211**–**213** with symmetrical aryl-diamide bridging ligands.[239] ECL studies established that **211**–**213** showed emission with the peak at λ_{max} 570 nm, and with relative intensity much higher than the classical reference $Ru(bpy)_3^{2+}$. Especially, **213** showed the brightest emission with 11.5 times enhancement compared to $Ru(bpy)_3^{2+}$. The high efficiency of ECL was attributed to the combination of amide bonds and the central aromatic unit.

In 2008, Sun *et al*. reported two dinuclear Ru(II) complexes **214** and **215** bearing conjugated thienylenevinylene bridging ligands.[240] The ECL studies indicated that the ECL intensity of both complexes was lower than that of the reference $Ru(bpy)_3^{2+}$. The intensity decreased with the increasing number of thienylenevinylene units.

In 2003, a series of multinuclear Ru(II) complexes bridged by the amino acid lysine (Lys) ligand was reported by De Cola's group.[241] The ECL intensity of **216** and the corresponding trinuclear complex increased 30% with respect to the mononuclear reference complex. Heterogeneous ECL immunoassay studies indicated that the ECL signal can be proportionally enhanced upon increasing the number of ruthenium units bound to the dendritic structure that labels a biological molecule (*e.g*. antigen, antibody).

In summary, the key findings are: 1) Dinuclear Ru(II) complexes bearing asymmetrical bridging ligands usually show higher ECL intensity than symmetrical analogues. 2) Most dinuclear examples exhibited enhancement of ECL intensity compared to the corresponding mononuclear Ru(II) complexes and reference $Ru(bpy)_3^{2+}$. However, several challenges still remain for this system when used as ECL labels: 1) The poor water-solubility of most complexes of this type limits their use in bioanalytical detection. 2) Most examples suffer from the quenching of emission by dioxygen and by interactions with the environment. Recently, De Cola's group reported a water-soluble Pt complex, which showed highly efficient ECL efficiency in aqueous solution (72%) and procell (51%), respectively.[242] Aggregation-induced electrochemiluminescence (AIECL) of a Pt complex through the self-assembly process was considered as a reasonable strategy for higher ECL efficiency.[242] Therefore, this finding may promote highly efficient AIE-active dinuclear metal complexes for use as labels in future bioanalytical detection.

4. Photocatalysis

4.1 Photocatalytic water splitting

The development of renewable green energy sources is one of the most important challenges currently facing society. In this regard solar energy is widely considered to be highly promising for future economic and environmental development.[243] Water splitting with sunlight to produce H_2 and O_2 (eqn (10)) is of considerable importance as one way to solve energy shortfalls.[244] Photocatalytic water-splitting is a highly endothermic four-electron process, which can be divided into two half-reactions: water oxidation and reduction to produce O_2 (eqn (11)) and H_2 (eqn (12)).[245]

$$2H_2O \rightarrow 2H_2+O_2 \quad \Delta E^0=1.23\ V \tag{10}$$

$$2H_2O \rightarrow 4H^++4e^-+O_2 \quad E^0=+1.23\ V \text{ vs. NHE, pH 0} \tag{11}$$

$$4H^++4e^- \rightarrow 2H_2 \quad E^0=0\ V \text{ vs. NHE, pH 0} \tag{12}$$

At present, the photocatalytic performance of H_2 or O_2 generation is mainly evaluated by the turnover number (TON) and turnover frequency (TOF) values. A higher TON reflects a better durability of the photocatalytic system. A higher TOF value reflects a more active catalyst. In recent years, centermetal-free organic dyes and metal complex chromophores as photosensitizers (PSs) have been widely studied in the application of photocatalytic water splitting. However, both metal-free organic dyes and mononuclear metal complex chromophores typically suffer from short operational lifetime due to photodecomposition of the PSs.[44] Therefore, the development of novel supramolecular photocatalysts, comprising only one bi- or multi-metallic complex connected by the different metal components, that function as both a light absorber and catalytic center, has been a popular subject in the field of photocatalytic water splitting. In this section, some representative bi- or multi-metallic photocatalysts and their photocatalytic performance will be discussed.

4.1.1 H_2 generation

Hydrogen produced from photocatalytic water splitting is a desirable process to replace fossil fuels in society.[246] The general requirements for the design and construction of efficient metal complex chromophores for solar H_2 generation are as follows. (i) Metal complex chromophores should exhibit a high molar extinction coefficient (ε) with a very broad absorption range, especially in the visible light region. (ii) Suitable redox potentials of chromophores are needed for the efficient electron transfer from the sacrificial reductant to the catalyst. (iii) Metal complex chromophores should exhibit an excited state lifetime in the millisecond regime to ensure the

charge transfer reaction. (iv) The photostability of the metal complex chromophores should be sufficiently high to guarantee long-term operation in the solar H_2 generation.[44] In consideration of the above requirements, Ru(II) complexes show particular advantages in solar H_2 generation in comparison with alternatives such as Ir(III), Pt(II), Cu(I), Co(II) complex chromophores.

The key components of photocatalytic H_2-generating systems are shown in Fig. 51. In contrast to the typical two-component systems (Fig. 51a) for H_2 production which consist of a sacrificial reductant (SR), a PS (*e.g.* metal-free organic dyes or mononuclear metal complex chromophore), and a water reduction catalyst (WRC), a dinuclear or multinuclear supramolecular photocatalyst which acts as both light absorber and catalytic center is an alternative system (Fig. 51b) due to its good photostability. Furthermore, electron or energy transfer between the photoactivated center and the catalytic center can be easily controlled by decorating the peripheral ligands or the bridging ligands, to give hydrogen in high yields.[44]

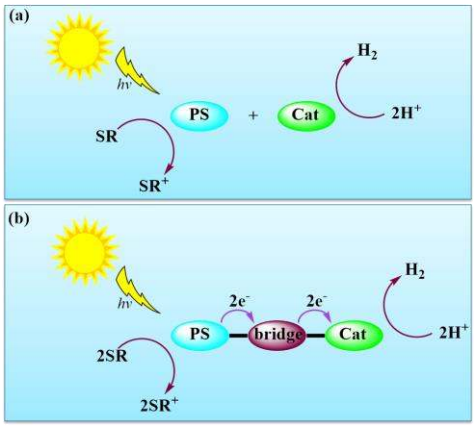

Fig. 51 Photocatalytic H_2 production systems: (a) a two-component photocatalytic system; (b) a supramolecular photocatalytic system. Sacrificial reagent (SR), photosensitizers (PS) and catalyst (Cat).

4.1.1.1 Ru–M supramolecular photocatalysts. Most investigations of supramolecular photocatalysts are based on a Ru–M system: some representative Ru–Pt/Pd/Rh/Co photocatalysts are shown in Fig. 52. In 2006, Sakai's group first studied a supramolecular photocatalyst for H_2 production using the Ru–Pt dinuclear complex **217**.[247] Upon irradiation with visible-light after 10 h in the presence of EDTA as the sacrificial reductant, a relatively low TON of 4.8 was observed. No hydrogen was formed in the multi-component system consisting of $[Ru(bpy)_3]^{2+}$ and K_2PtCl_4. Furthermore, no colloidal platinum dispersion formed, based on *in situ* dynamic light scattering measurements during the H_2 production reactions. These data suggest that the Ru–Pt photocatalyst acting as both photosensitizer (Ru component) and the catalyst (Pt component) is essential for the observed photocatalytic H_2 production. Subsequently, it was shown that three new Ru–Pt complexes **218**–**220**[248] do not behave as photocatalysts for H_2 production, indicating that good intramolecular electron transfer from the ^{3}MLCT excited state of the Ru component to the Pt component maybe a crucial factor for the formation of H_2 from the reduction of water.

Recently, Huijser and co-workers focused on the effect of peripheral ligands on the photocatalysts. A series of Ru–Pt or Ru–Pd di- or multi-nuclear complexes **221**–**226** (Fig. 52),[249] and their photocatalytic performance are summarized in Table 7. The key findings are: 1) Introduction of carboxyethyl ester units on the peripheral ligands of the light-harvesting Ru center leads to a huge increase of both the TON and TOF values. A TOF value of 200 h^{-1} obtained in this work is the highest reported for a supramolecular photocatalytic system. 2) No obvious change in the photocatalytic performance was observerd when the Pt center was replaced by Pd.

Chem Soc Rev

REVIEW ARTICLE

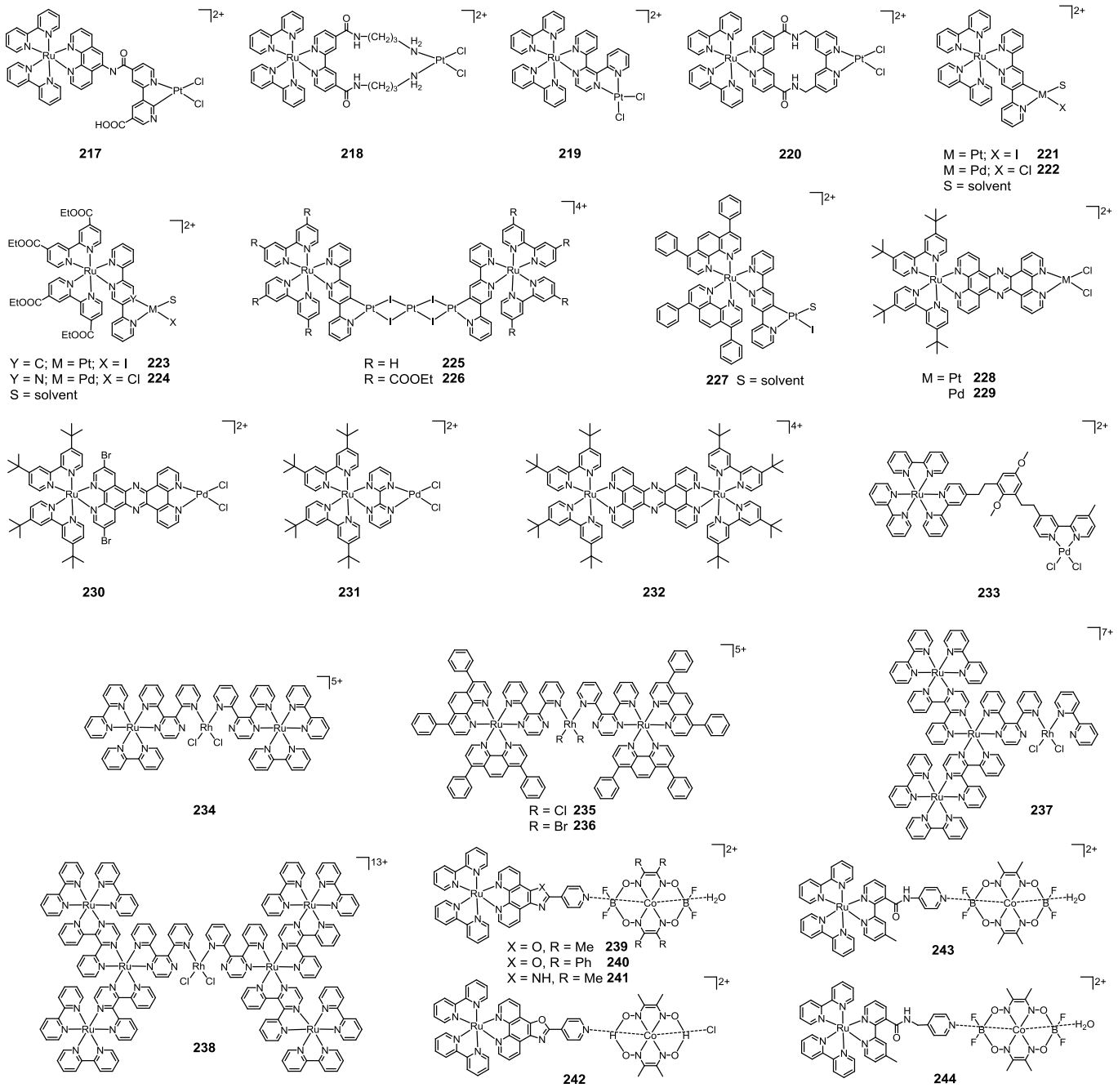

Fig. 52 The chemical structures of bi- and multi-metallic Ru-Metal photocatalysts for H_2 production.

More recently, the dinuclear photocatalyst **227** with more bulky ligands was reported by Pryce's group.[250] The relatively higher TOFs of **227** when compared with **221** bearing dipyridyl ligands can be attributed to an extended excited state lifetime of **227** Furthermore, the modest photocatalytic performance may be due to the absence of an excited state equilibrium of the complex which is supported by transient absorption (TA) and excited state absorption (ESA) data.

Recently, a series of Ru–Pd/Pt/Ru complexes **228**–**232** was reported by Rau and co-workers. Among these complexes, only

228,[251] **229**[252] and **230**[253] exhibited modest photocatalytic performance, whereas **231** and **232**[254] exhibited very poor performance. The relatively high catalytic efficiency of **228** using a Pt component as the catalytic center with a TON value of 7 was explained by its superior photostability. However, the higher TON value observed from **229** using a Pd component as the catalytic center was attributed to the formation of Pd colloids under the catalytic conditions. This alternative mechanism of H_2 production was also proposed by Johansson's group.[255] Upon illumination, Pd is released from the complex **233** as evidenced by XPS and TEM measurements, and the appearance of Pd^0/colloids strongly correlates with the formation of H_2.

In 2007, the first multi-nuclear Ru-Rh photocatalyst **234** for H_2 production was reported by Brewer's group.[256] The Rh(III) species **234** does not directly produce H_2. However, upon LED lamp irradiation, the newly formed Rh(I) species $[\{(bpy)_2Ru(dpp)\}_2Rh]^{5+}$ (dpp = 2,3-bis(2-pyridyl)pyrazine) is the key intermediate for H_2 production, this active species is obtained through photoinitiated electron collection by $[\{(bpy)_2Ru(dpp)\}_2RhCl_2]^{5+}$ in the presence of dimethylaniline (DMA) as the electron donor. Furthermore, the excellent stability of the Ru–Rh photocatalyst in this system was proved by the good linear relationship between the volume of of H_2 production and irradiation time. To further improve the photocatalytic performance, the new Ru-Rh photocatalysts **235** and **236** were synthesized with the peripheral bipy ligands of **234** replaced by the more sterically bulky Ph_2phen ligands.[257] **235** and **236** exhibited TON values of 150 and 610, respectively, significantly outperforming related Ru–Rh–Ru photocatalysts such as **234** (TON 30) and single-component systems.

More recently, two new photocatalysts **237** and **238** have been studied by Brewer and co-workers.[258] Heptametallic **238** exhibited better photocatalytic performance with a TON value of 300 when compared with tetrametallic **237** that has a TON value of 40. This difference in photocatalytic activity was attributed to the differences in the electrochemical and photophysical properties. The LUMO of **237** is mainly localized on the bridging ligand. However, for **238**, the LUMO is predominantly on the Rh center. The transient absorption experiments suggested that heptametallic **238** undergoes excited state electron transfer, whereas this transfer does not happen in tetrametallic **237**. The facile reduction of the Rh center in the excited state of **238** is clearly advantageous for the photocatalytic ability.

In 2008, the first Ru–Co photocatalysts **239**–**242** were reported by Artero *et al*.[259] **241** exhibited the best performance with a TON value of 104 in the presence of TEA as the sacrificial reductant and $[Et_3NH][BF_4]$ as the proton source. The data are comparable with previously reported TON values using Ru–Pt or Ru–Pd species.

In 2009, two new Ru–Co photocatalysts **243** and **244**, bearing a conjugated and non-conjugated bridging ligand, respectively, were reported by Sun's group.[260] The better photocatalytic performance of **244** with a TON value of 48 was attributed to the restricted back electron-transfer reaction that was controlled by the non-conjugating methylene group in the bridging ligand.

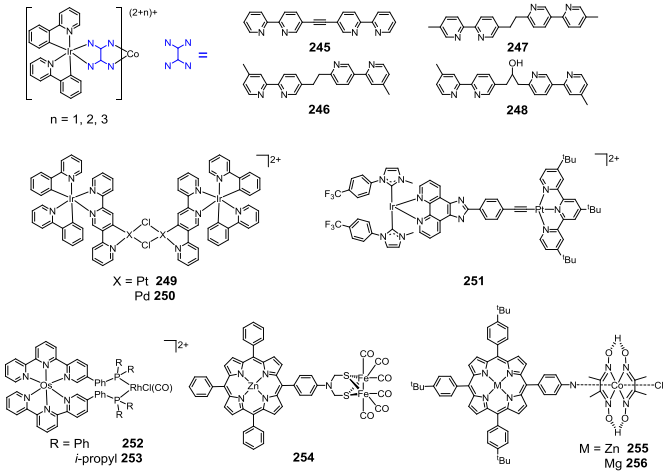

Fig. 53 The chemical structures of bi- or multi-metallic photocatalysts for H_2 production.

4.1.1.2 Other supramolecular photocatalysts. In 2010, self-assembled Ir–Co species **245**–**248** (Fig. 53) for H_2 production in the presence of TEOA as the sacrificial reductant in CH_3CN:H_2O (1:1) were first studied by Otsuki and co-workers.[261] In particular, complex **246** exhibited higher photocatalytic performance (TON = 20) when compared with the corresponding multi-component counterpart with the identical component concentrations. This work initiated a new way for the photocatalytic H_2 production by using a self-assembled supramolecular photocatalyst.

In 2012, photocatalytic H_2 production using the new Ir–Pt and Ir–Pd photocatalysts **249** and **250** (Fig. 53) in the presence of TEA as the sacrificial reductant were studied by Vos's group.[262] Under 350 nm light irradiation, the relatively low TONs of 65 and 16 were obtained for **249** and **250**, respectively. In comparison, higher TONs of 308 and 254 were observed with irradiation at 470 nm. Furthermore, the relatively low photocatalytic efficiency of the Pd catalytic center in comparison with the Pt analogue was attributed to unwanted electronic transitions from the Pd center to the bridging ligand in the 350 nm region, which inhibits the formation of H_2.

In 2015, Yu *et al*. reported that the Ir–Pt complex **251** (Fig. 53) is a highly efficient photocatalyst for H_2 production with a high TON of 1672 after 60 h of visible-light irradiation.[79] The good linear relationship between H_2 generation and irradiation time indicated excellent photostability of **251**. However, the catalytic mechanism for this process was unclear.

In 2009, the Os–Rh photocatalysts **252** and **253** (Fig. 53) bearing a light harvesting Os center and a catalytic Rh center were studied by Nishibayashi's group.[263] Both **252** and **253** exhibited high activity and stability during photocatalytic H_2 production. In particular, upon visible-light irradiation in a 1 : 1 CH_3CN–H_2O solution for 240 h, **252** exhibited a high TON of 594.

Noble-metal-free complexes have been studied by Song's group (**254**)[264] and Sun's group (**255** and **256**),[265] respectively (Fig. 53). All of these complexes exhibited poor ability for photocatalytic H_2 production. However, the development of

cheap photocatalysts using earth-abundant metals is a promising topic for future studies.

In summary, research on supramolecular photocatalysts for H_2 production is still at a fundamental stage, and the complicated photocatalytic mechanism is not fully clear. However, it is clear that H_2 production performance is influenced by several factors, such as redox potential, excited-state lifetime of the light absorber, molar absorptivity and luminescence properties. Further investigations of supramolecular structure-performance relationships are needed. New noble-metal-free photocatalysts for efficient H_2 production is a promising topic of research.

Table 7 Representative supramolecular photocatalysts for photocatalytic H_2 production

Supramolecular photocatalyst	Solvents	Light source	SR[a]	TON[b]	TOF (h^{-1})[c]	Ref.
217	NaAc–HAc buffer solution	350 W Xe lamp, $\lambda > 350$ nm	EDTA	4.8	0.48	247
221	6:1 $CH_3CN–H_2O$	40-50 mW LED lamp 470 nm	TEA	80	15	249
222	6:1 $CH_3CN–H_2O$	LED lamp 470 nm	TEA	120	20	249
223	6:1 $CH_3CN–H_2O$	LED lamp 470 nm	TEA	650	200	249
224	6:1 $CH_3CN–H_2O$	LED lamp 470 nm	TEA	400	66.67	249
225	6:1 $CH_3CN–H_2O$	LED lamp 470 nm	TEA	99	15	249
226	6:1 $CH_3CN–H_2O$	LED lamp 470 nm	TEA	650	200	249
227	6:1 $CH_3CN–H_2O$	LED lamp 470 nm	TEA	54	24	250
228	6:1 $CH_3CN–H_2O$	40±5 mW LED lamp 470 nm	TEA	7	0.7	251
229	6.25:1 $CH_3CN–H_2O$	Argon ion laser 476 nm	TEA	146.2	14.6	252
230	6:1 $CH_3CN–H_2O$	LED lamp 470 nm	TEA	67.3	3.74	253
231	CH_3CN	LED lamp 470 nm	TEA	0	0	254
232	CH_3CN	LED lamp 470 nm	TEA	0.56	< 0.1	254
233	CH_3CN	Tungsten filament lamp, $\lambda > 475$ nm	TEA	30	6	255
234	3 : 1 $CH_3CN–H_2O$	5 W LED lamp, 470 nm	DMA	30	7.5	256
235	CH_3CN	LED lamp, 470 nm	DMA	150	7.5	257
236	DMF	LED lamp, 470 nm	DMA	610	30.5	257
237	DMF	LED lamp, 470 nm	DMA	40	2	258
238	CH_3CN	LED lamp, 470 nm	DMA	300	15	258
239	Acetone	150 W CdI-doped Hg lamp	TEA	85	8	259
240	Acetone	150 W CdI-doped Hg lamp	TEA	12	3	259
241	Acetone	150 W CdI-doped Hg lamp	TEA	104	6.93	259
242	Acetone	150 W CdI-doped Hg lamp	TEA	17	4.25	259
243	Acetone	500 W Xe lamp, $\lambda > 400$ nm	TEA	38	4.75	260
244	Acetone	500 W Xe lamp, $\lambda > 400$ nm	TEA	48	6	260
245	1 : 1 $CH_3CN–H_2O$	100 W Xe lamp, $\lambda > 400$ nm	TEOA	2.5	0.31	261
246	1 : 1 $CH_3CN–H_2O$	100 W Xe lamp, $\lambda > 400$ nm	TEOA	20	2.5	261
247	1 : 1 $CH_3CN–H_2O$	100 W Xe lamp, $\lambda > 400$ nm	TEOA	3.9	0.49	261
248	1 : 1 $CH_3CN–H_2O$	100 W Xe lamp, $\lambda > 400$ nm	TEOA	8	1	261
249	9 : 1 $CH_3CN–H_2O$	500 mW LED lamp, 470 nm	TEA	308	17.11	262
250	9 : 1 $CH_3CN–H_2O$	500 mW LED lamp, 470 nm	TEA	254	14.44	262
251	9 : 1 Acetone–H_2O	300 W Xe lamp, $\lambda > 420$ nm	TEA	1672	27.86	79
252	1 : 1 $CH_3CN–H_2O$	250 W Hg lamp, $\lambda > 380$ nm	NaHA	594	2.48	263
253	1 : 1 $CH_3CN–H_2O$	250 W Hg lamp, $\lambda > 380$ nm	NaHA	52	2.88	263
254	CH_2Cl_2	500 W Hg lamp, $\lambda > 400$ nm	EtSH[d]	0.31	0.31	264
255	4 : 1 THF–H_2O	300 W Xe lamp, $\lambda > 400$ nm	TEA	22	4.4	265
256	4 : 1 THF–H_2O	300 W Xe lamp, $\lambda > 400$ nm	TEA	3	0.6	265

[a] SR = sacrificial reductant. EDTA: ethylenediaminetetraacetic acid disodium salt; DMA: dimethylaniline; TEA: trimethylamine; TEOA: triethanolamine; NaHA: sodium ascorbate; EtSH: ethanethiol. [b] TON = product (mol)/photocatalyst (mol). [c] TOF = TON/t, t is the reaction time.

4.1.2 O_2 generation

Water splitting to produce O_2 is a challenge due to the high thermodynamic and kinetic demands of the process (eqn (11)). Many studies have addressed the development of efficient water oxidation catalysts (WOCs) to conquer this bottleneck, mainly including metal oxides[266, 267] and transition metal complexes.[268, 269] Over the past three decades, a series of Ru complexes has been successfully exploited as WOCs for O_2 production.[270-278] since the pioneering example reported by Meyer *et al.* in 1982.[279] It is extremely important that the ligands used to bind the metal center

are kinetically robust with regard to oxidation, otherwise the ligand will degrade.[271] Generally, a robust water oxidation catalyst can be generated by self-assembly from two mononuclear complexes to yield a dinuclear species during the catalytic process, or by directl design and synthesis of a dinuclear species.[269, 276]Over the past few years, a few successful examples of di- and multi-nuclear Ru catalysts for photocatalytic O_2 production have been reported. Two different photocatalytic strategies are presented: 1) Two-component systems, including a supramolecular photocatalyst (acting as both photosensitizer and catalyst) and a sacrificial electron acceptor (SEA). 2) Three-component systems, including a PS, a molecular catalyst and a sacrificial electron acceptor. The catalytic mechanism can be attributed to the intra- or intermolecular O–O bond formation that can occur *via* the so-called water nucleophilic attack (WNA) or interaction of two M–O units (I2M) mechanism.[271, 280, 281]

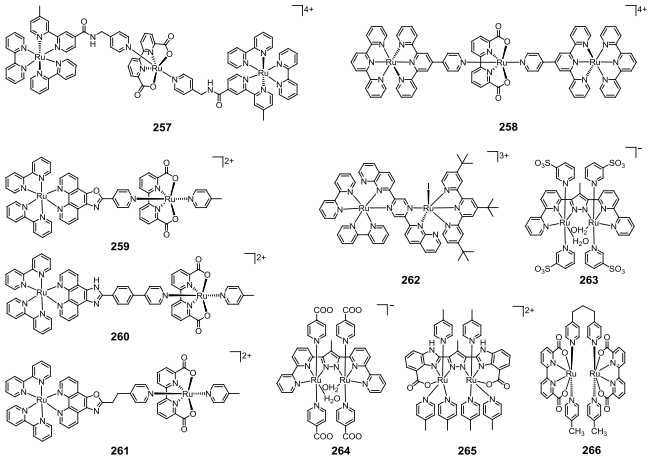

Fig. 54 The chemical structures of photocatalysts for O_2 production.

4.1.2.1 Two-component systems. In 2012, two trinuclear Ru supramolecular photocatalysts **257** and **258** with two light-harvesting sites and one catalytic site for water oxidation in the presence of $Na_2S_2O_8$ as SEA were studied by Sun's group.[282] Complex **257** displayed enhanced photocatalytic activity (TON = 38, TOF = 4.71 min^{-1}) after 70 min compared with a conventional multicomponent system (TON = 8) consisting of $[Ru\text{-}(bpy)_3]^{2+}$ as photosensitizer and $[RuL(pic)_2]$ as catalyst. The superior activity for **257** was attributed to the expected intramolecular electron transfer between the $[Ru(bpy)_3]^{3+}$ units and the catalytic center that are generated through the oxidative quenching of the excited state $[Ru(bpy)_3]^{2+}$* by $S_2O_8^{2-}$. In contrast to **257**, no O_2 generation was detected in the system containing **258**, and the O_2 formation was observed only upon addition of $[Ru(bpy)_3]^{2+}$. This difference indicated poor electron transfer between the photosensitizer unit $[Ru(tpy)_2]^{2+}$ and the SEA, since the lifetime of the $[Ru(tpy)_2]^{2+}$ excited state is significantly shorter compared to that of $[Ru(bpy)_3]^{2+}$.

In 2014, three new supramolecular photocatalysts **259**–**261** based on dinuclear Ru complexes connected by different linkages were reported by Sun's group.[283] The photocatalytic water oxidation performance of **259**–**261** follows the order **261** > **260** > **259** (Table 8). The enhanced photocatalytic ability of **261** with a flexible linkage was explained by the beneficial electron transfer and charge separation induced by adjusting the distance between the catalytic unit and the PS unit. Furthermore, an electrochemical study indicated that the higher oxidation potential of the PS unit (ca. 1.3 V vs. NHE) than the onset potential of the water oxidation catalytic unit (ca. 0.95 V vs. NHE) could provide a driving force for the water oxidation.

In 2012, Thummel's group reported a new supramolecular photocatalyst **262** for water oxidation.[284] **262** exhibited effective catalytic ability with a TON of 134 after irradiation for 6 h, and 22 times higher than its mononuclear analogous (TON = 6) in the presence of photosensitizer $[Ru(bpy)_3]^{2+}$. Interestingly, in the absence of light, a small amount of O_2 was also formed in the presence of **262** and the strong oxidant $Na_2S_2O_8$. However, an explanation for this was not presented.

4.1.2.2 Three-component systems. In 2015, Llobet's group reported two new molecular catalysts **263** and **264** for water oxidation in the presence of a photosensitizer and a SEA.[80] **263** exhibited very high TONs and TOFs of 5300 and 11.1 s^{-1}, respectively, after three successive catalytic runs. This result represents a new benchmark for homogeneous light-driven water oxidation. Based upon detailed electrochemical and photophysical investigations, an integrated photocatalytic mechanism in this three-component system was proposed (Fig. 55).

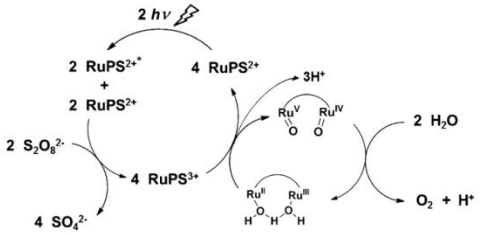

Fig. 55 General scheme for the processes that occur during photodriven water oxidation. Reproduced with permission from ref. 80. Copyright 2015 Wiley-VCH.

In 2015, Laine *et al*. investigated a new dinuclear catalyst **265**.[285] at pH = 7.2 and 6.2. The results indicated that **265** exhibited better catalytic ability at pH = 6.2 with a TON of 890 than at pH = 7.2 (TON = 500). This can be attributed to the photosensitizer decomposition at higher pH. The high catalytic ability of **265** was ascribed to the negatively charged ligands that stabilize the metal centers in high-valent redox states.

Sun's group had stated that **266** is a highly efficient catalyst for water oxidation with Ce^{IV} as an oxidant in their previous work.[286] More recently, light-driven water oxidation in a three-component system including a PS, **266** and a SEA was explored.[287] Interestingly, the catalytic ability of **266** obviously enhanced with an increase of CH_3CN content in the buffer solution from 20% (TON = 57) to 60% (TON = 215). Furthermore, the corresponding photocatalytic rate increased from 0.07 to 0.33 s^{-1}. This result indicated that CH_3CN not only promoted the O_2 production, but also accelerated the photocatalytic rate. Finally, in optimised conditions, **266** exhibited highly efficient O_2 production with a TON of 638.

In summary, a series of multinuclear Ru(II) complexes as supramolecular photocatalysts or molecular catalysts have been studied for O_2 production. At present the three-component systems show consistently enhanced photocatalytic ability over the two-component systems. However, further design of new supramolecular photocatalysts for the highly efficient production of

O_2 is desired due to the better durability of photocatalysis when compared with combined PS and molecular catalyst systems.

Table 8 Representative molecular catalyst for photocatalytic O_2 production

catalyst	Solvents	Light source	PS[a]	SEA[b]	TON	TOF	Ref.
257	1 : 9 $CH_3CN–H_2O$	500 W Xe lamp, λ > 400 nm	—	$Na_2S_2O_8$	38	4.71 min^{-1}	282
258	1 : 9 $CH_3CN–H_2O$	500 W Xe lamp, λ > 400 nm	—	$Na_2S_2O_8$	0	0	282
259	1 : 9 $CH_3CN–H_2O$	500 W Xe lamp, λ > 400 nm	—	$Na_2S_2O_8$	20	0.89 min^{-1}	283
260	1 : 9 $CH_3CN–H_2O$	500 W Xe lamp, λ > 400 nm	—	$Na_2S_2O_8$	18	0.8 min^{-1}	283
261	1 : 9 $CH_3CN–H_2O$	500 W Xe lamp, λ > 400 nm	—	$Na_2S_2O_8$	34	1.51 min^{-1}	283
262	1 : 100 $CH_3CN–H_2O$	LED lamp 472 nm	—	$Na_2S_2O_8$	134	0.37 min^{-1}	284
263	H_2O	150 W Xe lamp, λ = 400 nm	$[Ru(bpy)(becb)_2]^{2+}$	$Na_2S_2O_8$	2373 (5300)[c]	11.1 s^{-1}	80
264	H_2O	150 W Xe lamp, λ = 400 nm	$[Ru(bpy)(becb)_2]^{2+}$	$Na_2S_2O_8$	2362	9.2 s^{-1}	80
265	H_2O	missing	$[Ru(bpy)_2(deep)]^{2+}$	$Na_2S_2O_8$	890	—	285
266	3 : 2 $CH_3CN–H_2O$	300 W Xe lamp, λ > 400 nm	$[Ru(bpy)_3]^{2+}$	$Na_2S_2O_8$	638	0.33 s^{-1}	287

[a] PS: photosensitizer. becb: 4,4-bis(ethoxycarbonyl)-2,2-bipyridine; deeb: diethyl (2,20-bipyridine)-4,40-dicarboxylate. [b] SEA: sacrificial electron acceptor. [c] In parentheses, total O_2 production and TON after three cycles, the reaction mixture was only degassed with N_2 between cycles.

4.2 CO_2 reduction

Reduction of CO_2 into energy-rich compounds is an important topic that can simultaneously tackle the shortage of fossil-fuel resources and global warming.[36, 40, 42, 288] Photocatalytic CO_2 reduction utilizing solar light as an energy source has been widely investigated as a key technology for the conversion ofabundant solar energy to chemical energy, so-called artificial photosynthesis. Rhenium polypyridine complexes are known to act as photocatalysts and electrocatalysts for reducing CO_2 to CO.[289] A major problem with these photocatalysts is the lack of an extended absorption into the visible region. The present approach is to fabricate supramolecular photocatalysts, similar to the photocatalytic H_2 or O_2 production systems. Supramolecular photocatalysts used in the reduction of CO_2 act as both the light absorbing center and the catalytic center. Two distinct reaction mechanisms that use supramolecular photocatalysts for the reduction of CO_2, are oxidative quenching (OQ) and reductive quenching (RQ).[290] As shown in Fig. 56, for both mechanisms, the reduction of CO_2 proceeds via the reduced form of the catalyst. Since the first supramolecular Ru-Ni complex used for the photochemical reduction of CO_2 was reported by Kimura *et al.* in 1992,[291] huge efforts had been devoted to the design of new bi- or multi-metallic analogues. Ishitani's group have recently described the development of supramolecular photocatalysts for the photochemical reduction of CO_2,[290] including Ru(II)–Re(I), Ru(II)–Ru(II), Ru(II)–Ni(II), Ru(II)–Co(III), Ir(III)–Re(I), Os(II)–Re(I), Pd(II)–Re(I), Zn(II)–Re(I), Fe(III)–Re(I), Co(II)–Re(I) and Cu(II)–Re(I) systems. Their chemical structures and photocatalytic CO_2 reduction performance are presented in Fig. 57 and 58, and Tables 9 and 10. Therefore, in this section, we will mainly focus on the latest development of novel asymmetrical trinuclear supramolecular photocatalysts and their performance to supplement the recent review.[290]

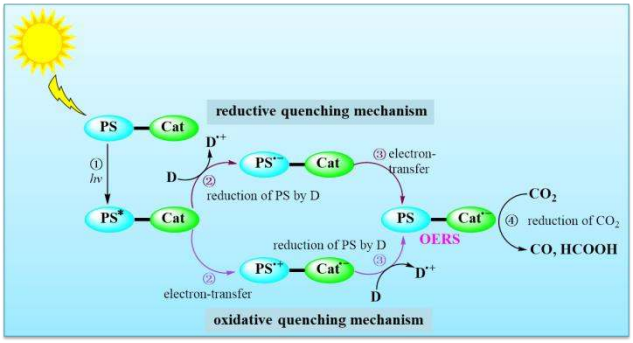

Fig. 56 The mechanisms for the photochemical generation of the one-electron reduced species (OERS) of the supramolecular photocatalysts. Sacrificial electron donor (D), photosensitizers (PS) and catalyst (Cat).

Chem Soc Rev

REVIEW ARTICLE

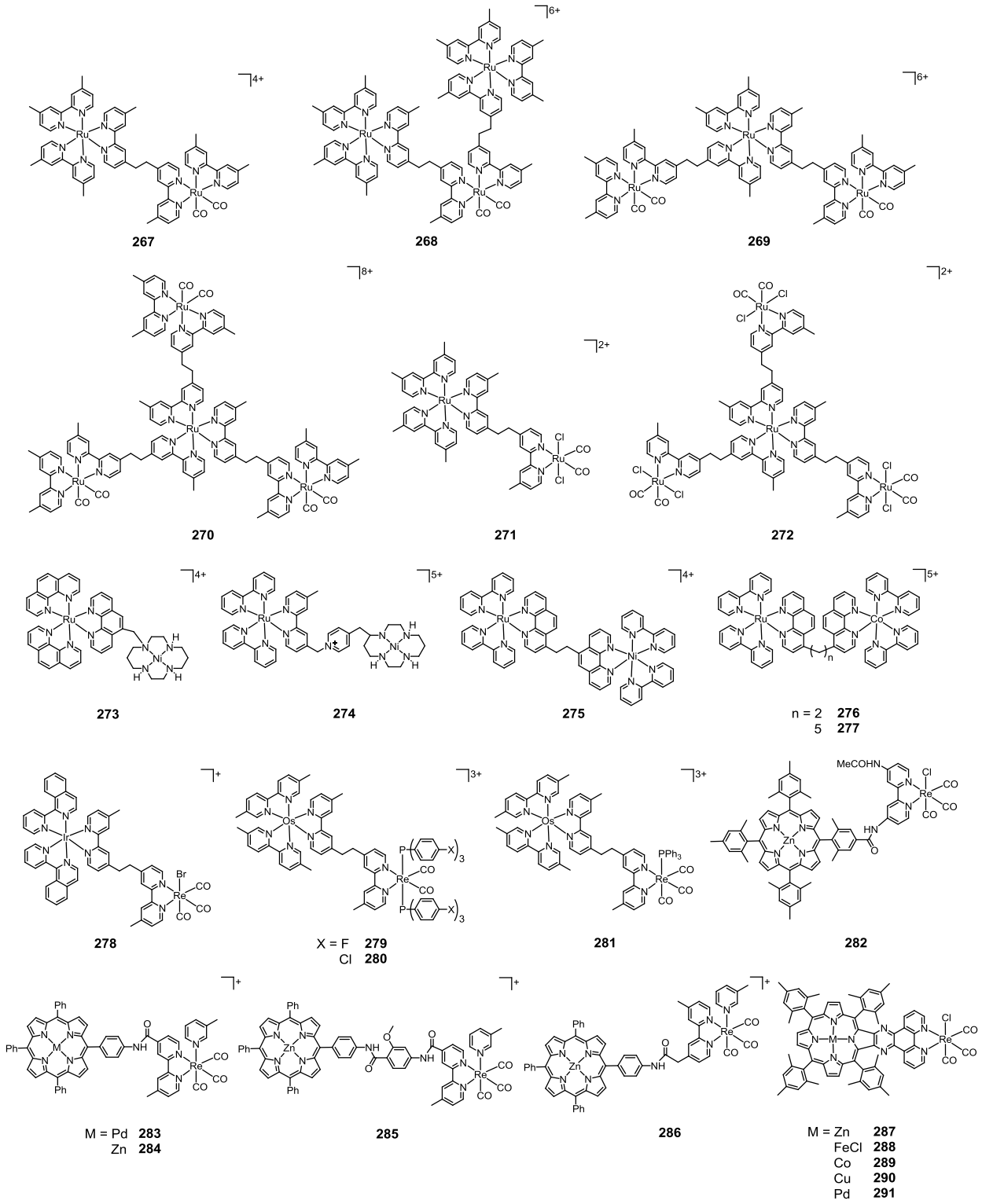

Fig. 57 The chemical structures of di- and multi-nuclear supramolecular photocatalysts.

Table 9 Photocatalytic CO_2 reduction performance of supramolecular photocatalysts

	Solvent	Light source	Donor[a]	Product (Φ)[b]	Γ (%)[c]	TON	TOF (min^{-1})	Ref.
267	4 : 1 DMF–TEOA	High-pressure Hg lamp, $\lambda \geq 500$ nm	BNAH	HCOOH (0.038)[d]	90	315		292
268	4 : 1 DMF–TEOA	High-pressure Hg lamp, $\lambda \geq 500$ nm	BNAH	HCOOH (0.041)[d]	91	562	7.8	292
	4 : 1 DMF–TEOA	High-pressure Hg lamp, $\lambda \geq 500$ nm	MEO-BNAH	HCOOH (0.061)[d]	89	671	11.6	292
	4 : 1 DMF–TEOA	High-pressure Hg lamp, $\lambda > 500$ nm	BI(OH)H	HCOOH (0.46)[d]	87	2766	44.9	293
	4 : 1 DMF–TEOA	High-pressure Hg lamp, $\lambda > 500$ nm	BIH	HCOOH (0.18)[d]	72	641	10.2	293
269	4 : 1 DMF–TEOA	High-pressure Hg lamp, $\lambda \geq 500$ nm	BNAH	HCOOH (0.030)[d]	77	353		292
270	4 : 1 DMF–TEOA	High-pressure Hg lamp, $\lambda \geq 500$ nm	BNAH	HCOOH (0.017)[d]	70	234		292
271	5 : 1 DMF–TEOA	High-pressure Hg lamp, $\lambda \geq 500$ nm	BNAH	HCOOH	91	337		290
272	5 : 1 DMF–TEOA	High-pressure Hg lamp, $\lambda \geq 500$ nm	BNAH	CO	98	40		290
273	ascorbate buffer solution	500W Xe lamp, $\lambda = 350$ nm	AscH	CO	72	< 1		291
274	ascorbate buffer solution	500 W Xe lamp, $\lambda = 350$ nm	AscH	CO	11	< 1		294
275	3 : 1 : 1 DMF–H_2O–TEOA	500 W Xe lamp, $\lambda < 400$ nm	TEOA	CO	50	2		295
276	3 : 1 : 1 DMF–H_2O–TEOA	500 W Xe lamp, $\lambda < 400$ nm	TEOA	CO	73	3		295
277	3 : 1 : 1 DMF–H_2O–TEOA	500 W Xe lamp, $\lambda < 400$ nm	TEOA	CO	79	5		295
278	5:1 DMA–TEOA	High-pressure Hg lamp, $\lambda \geq 500$ nm	BNAH	CO (0.21)	> 99	130		296
	5:1 DMA–TEOA	High-pressure Hg lamp, $\lambda \geq 500$ nm	BIH	CO (0.41)	> 99	1700		296
279	5 : 1 DMF–TEOA	500 W Xe lamp, $\lambda > 620$ nm	BIH	CO (0.10)	> 99	762	1.6	297
280	5 : 1 DMF–TEOA	500 W Xe lamp, $\lambda > 620$ nm	BIH	CO (0.12)	> 99	1138	3.3	297
281	5 : 1 DMF–TEOA	High-pressure Hg lamp, $\lambda \geq 500$ nm	BNAH	CO	> 99	973		290
282	Unown	Unknown light source	TEA	CO (0.0064)				298
283	5 : 1 DMF–TEA	Unknown light source, $\lambda > 420$ nm	TEA	CO		2		299
284	5 : 1 DMF–TEOA	Unknown light source, $\lambda > 520$ nm	TEOA	CO		14		300
285	5 : 1 DMF–TEOA	Unknown light source, $\lambda > 450$ nm	TEOA	CO		32		300
286	5 : 1 DMF–TEOA	Xe lamp, $\lambda > 520$ nm	TEOA	CO		332		301
287	19 : 1 DMF–TEA	High-pressure Hg lamp, $\lambda \geq 375$ nm	TEA	CO		13		302
288	19 : 1 DMF–TEA	High-pressure Hg lamp, $\lambda \geq 305$ nm	TEA	CO		< 1		302
289	19 : 1 DMF–TEA	High-pressure Hg lamp, $\lambda \geq 305$ nm	TEA	CO		< 1		302
290	19 : 1 DMF–TEA	High-pressure Hg lamp, $\lambda \geq 305$ nm	TEA	CO		< 1		302
291	19 : 1 DMF–TEA	High-pressure Hg lamp, $\lambda \geq 305$ nm	TEA	CO		< 1		302

[a] BNAH: 1-benzyl-1,4-dihydronicotinamide; MEO-BNAH: 1-(4-methoxybenzyl)-1,4-dihydronicotinamide; BI(OH)H: 1,3-dimethyl-2-(*o*-hydroxyphenyl)-2,3-dihydro-1*H*-benzo[d]imidazole; BIH: 1,3-dimethyl-2-phenyl-2,3-dihydro-1*H*-benzo[d]imidazole; AscH: ascorbic acid. [b] = product [product (mol)]/[absorbed photons (einstein)]. [c] Γ = [target product (mol)]/[reduced compounds (mol)]. [d] 500 W Xe lamp, $\lambda = 480$ nm. Reproduced with permission from ref. 290. Copyright 2017 American Chemical Society.

Chem Soc Rev

REVIEW ARTICLE

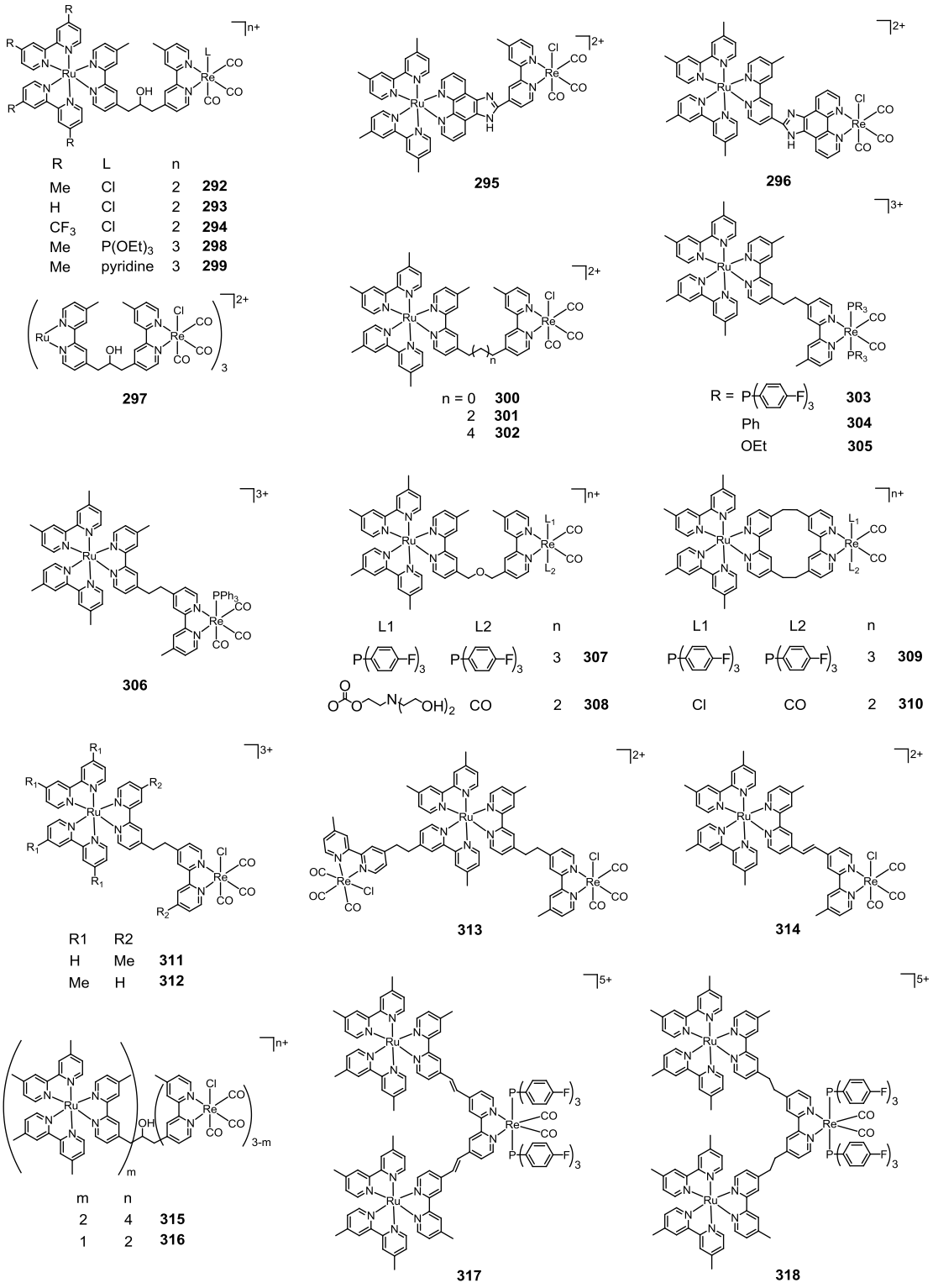

Fig. 58 The chemical structures of Ru–Re supramolecular photocatalysts.

Table 10 Photocatalytic CO_2 reduction performance of Ru–Re supramolecular photocatalysts

	Solvent	Light source	Donor[a]	Product (Φ)	Γ (%)	TON	TOF (min^{-1})	Ref.
292	5 : 1 DMF–TEOA	High-pressure Hg lamp, $\lambda \geq 500$ nm	BNAH	CO (0.12)	96	170		303
293	5 : 1 DMF–TEOA	High-pressure Hg lamp, $\lambda \geq 500$ nm	BNAH	CO		50		303
294	5 : 1 DMF–TEOA	High-pressure Hg lamp, $\lambda \geq 500$ nm	BNAH	CO		3		303
295	5 : 1 DMF–TEOA	High-pressure Hg lamp, $\lambda \geq 500$ nm	BNAH	CO		14		303
296	5 : 1 DMF–TEOA	High-pressure Hg lamp, $\lambda \geq 500$ nm	BNAH	CO		28		303
297	5 : 1 DMF–TEOA	High-pressure Hg lamp, $\lambda \geq 500$ nm	BNAH	CO (0.093)		240		303
298	5 : 1 DMF–TEOA	High-pressure Hg lamp, $\lambda \geq 500$ nm	BNAH	CO (0.16)	97	232		304
299	5 : 1 DMF–TEOA	High-pressure Hg lamp, $\lambda \geq 500$ nm	BNAH	CO	96	97		304
300	5 : 1 DMF–TEOA	High-pressure Hg lamp, $\lambda \geq 500$ nm	BNAH	CO (0.13)	76	180		305
301	5 : 1 DMF–TEOA	High-pressure Hg lamp, $\lambda \geq 500$ nm	BNAH	CO (0.11)		120		305
302	5 : 1 DMF–TEOA	High-pressure Hg lamp, $\lambda \geq 500$ nm	BNAH	CO (0.11)		120		305
303	5 : 1 DMF–TEOA	High-pressure Hg lamp, $\lambda \geq 500$ nm	BNAH	CO (0.15)	94	207	4.7	306
	5 : 1 DMF–TEOA	High-pressure Hg lamp, $\lambda \geq 500$ nm	BIH	CO (0.45)	> 99	3029	35.7	82
304	5 : 1 DMF–TEOA	High-pressure Hg lamp, $\lambda \geq 500$ nm	BNAH	CO (0.10)	91	144		306
305	5 : 1 DMF–TEOA	High-pressure Hg lamp, $\lambda \geq 500$ nm	BNAH	CO (0.10)	73	27		306
306	5 : 1 DMF–TEOA	High-pressure Hg lamp, $\lambda \geq 500$ nm	BNAH	CO (0.13)	98	233		290
	5 : 1 DMF–TEOA	High-pressure Hg lamp, $\lambda \geq 500$ nm	BNAH	CO (0.54)	> 99	2915		290
307	5 : 1 DMF–TEOA	High-pressure Hg lamp, $\lambda \geq 500$ nm	BNAH	CO (0.18)	95	253		307
308	5 : 1 DMF–TEOA	High-pressure Hg lamp, $\lambda \geq 500$ nm	BNAH	CO (0.12)				307
	5 : 1 DMF–TEOA	High-pressure Hg lamp, $\lambda \geq 500$ nm	BIH	CO (0.50)	> 99	> 1000		308
309	5 : 1 DMF–TEOA	High-pressure Hg lamp, $\lambda \geq 500$ nm	BNAH	CO (0.09)		123		309
310	5 : 1 DMF–TEOA	High-pressure Hg lamp, $\lambda \geq 500$ nm	BNAH	CO (0.16)		204		309
311	5 : 1 DMF–TEOA	High-pressure Hg lamp, $\lambda \geq 500$ nm	AscNa	HCOOH (0.002)	81	25		310
312	5 : 1 DMF–TEOA	High-pressure Hg lamp, $\lambda \geq 500$ nm	BI(CO_2H)H	CO (0.13)	81	130		311
313	DMF–TEOA	LED lamp, $\lambda = 520$ nm	BNAH	CO		315	4.2	312
314	5 : 1 DMF–TEOA	Xe lamp, $\lambda \geq 500$ nm	BNAH	CO		50		313
315	5 : 1 DMF–TEOA	High-pressure Hg lamp, $\lambda \geq 500$ nm	BNAH	CO		110		314
316	5 : 1 DMF–TEOA	High-pressure Hg lamp, $\lambda \geq 500$ nm	BNAH	CO		190		314
317	5 : 1 DMF–TEOA	High-pressure Hg lamp, $\lambda \geq 500$ nm	BNAH	CO	69	283	2.3	315
318	5 : 1 DMF–TEOA	High-pressure Hg lamp, $\lambda \geq 500$ nm	BNAH	CO	75	313	2.8	315
319	5 : 1 DMF–TEOA	High-pressure Hg lamp, $\lambda \geq 500$ nm	BIH	CO		3552 ± 461	4.67	316
320	5 : 1 DMF–TEOA	High-pressure Hg lamp, $\lambda \geq 500$ nm	BIH	CO		4347 ± 421	4.68	316

[a] AscNa: sodium ascorbate; BI(CO_2H)H: 2-(1,3-dimethyl-2,3-dihydro-1*H*-benzimidazol-2-yl)benzoic acid. Reproduced with permission from ref. 290. Copyright 2017 American Chemical Society.

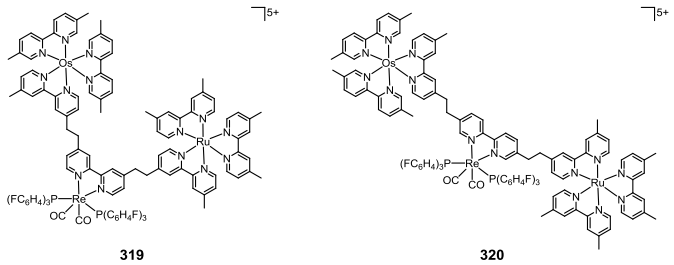

Fig. 59 The chemical structures of Ru–Re supramolecular photocatalysts **319** and **320**.

Recently, Ishitani's group synthesized two trinuclear supramolecular photocatalysts **319** and **320** (Fig. 59) containing three different metal centers Os(II)–Re(I)–Ru(II) for the first time[316] *via* stepwise Mizoroki–Heck reactions. The energy transfer processes in these complexes were studied in detail. The key findings are: 1) Highly efficient intramolecular energy transfer from an excited Re unit to an excited Ru unit was observed for both complexes, and the emission occurs mainly from excited Ru and Os units. 2) The faster energy transfer rate observed from the Re to the Ru unit, compared with from the Ru or Re to the Os unit, can be attributed to the different energy transfer mechanisms. For example, Furue *et al*. had reported that the intramolecular excited energy transfer in a Ru–Os dinuclear complex proceeds by a Förster mechanism,[317] whereas the excited Re→Ru energy transfer proceeds *via* a Dexter mechanism.[318] 3) In contrast to **319**, the intramolecular

excited Ru→Os energy transfer in **320** proceeded very slowly or did not occur, which can be attributed to the longer distance between the Ru and Os units in **320**. Refering to supramolecular photocatalysts,[290] dinuclear Ru–Re or Os–Re systems exhibit the best photocatalytic CO_2 reduction performance reported to date for bimetallic systems. Inspired by this, two trinuclear complexes **319** and **320** were compared with their dinuclear Ru–Re and Os–Re analogues. As shown in Fig. 60a, both **319** and **320** can be used as supramolecular photocatalysts for the highly selective formation of CO. Importantly, both **319** and **320** exhibited superior catalytic ability and great durability in the CO_2 reduction process. The TONs for **319** and **320** reached 3552 ± 461 and 4347 ± 421, respectively, after 35 h irradiation, which are higher than the summation of their parent dinuclear Ru–Re and Os–Re complexes. These two trinuclear complexes exhibit the highest TON_{CO} for all reported photocatalytic reactions. The reason for this outstanding performance has been investigated by UV absorption measurements. As shown in Fig. 60b, upon irradiation at $\lambda > 500$ nm for 1 h, the spectrum of **319** showed a slight decrease in the band at *ca.* 420 to 500 nm. The spectral shape was maintained for 6 h. On the contrary, in the case of the Ru–Re analogue, the absorption band at 460 nm sharply decreased in intensity with continuous irradiation (Fig. 60c), which mainly reflects the decomposition of the Ru unit. The corresponding time courses of the absorbance changes at 460 nm for **319** and for dinuclear Ru–Re are shown in Fig. 60d. The change in the absorption intensity matched well with the time courses of photocatalytic CO formation for both catalysts (Fig. 60a). Therefore, this result indicated that the photocatalytic stability can be effectively improved by the introduction of the Os unit into the Ru–Re system.

In summary, introduction of an additional photosensitising Os unit into Ru–Re systems to give trinuclear complexes **319** and **320** has two main advantages in comparison with the parent dinuclear complexes: 1) A wider range of visible light up to 730 nm can be strongly captured by the trinuclear complexes. 2) Photocatalytic durability of **319** and **320** is improved by 27% and 55%, respectively, compared with their parent dinuclear complexes.

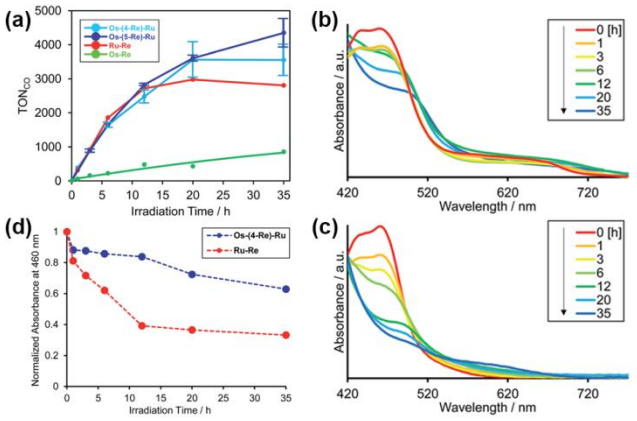

Fig. 60 (a) Time courses of the TON of CO formation during photocatalytic reactions. Absorption spectral changes of reaction solutions of (b) Os–(4-Re)–Ru (**319**) and (c) Ru–Re after irradiation. (d) Time courses of the absorbance changes at 460 nm in (b) and (c). Reproduced with permission from ref. 316. Copyright 2018 The Royal Society of Chemistry.

4.3 Dye-sensitized photoelectrochemical/photoelectrosynthesis cells (DSPECs)

Photoelectrochemical cells (PECs) assembled with an n-type semiconductor TiO_2 single-crystal electrode for the photoassisted (under UV irradiation) electrochemical water oxidation were first reported by Honda and Fujishima in the 1970s.[319] Since then, inorganic semiconductor materials have been widely studied as photoanodes for water splitting.[320, 321] However, this kind of photoanode still suffers from a lack of broad wavelength light absorption due to its wide band-gap. For example, only 5% of the solar energy (predominantly UV light) can be absorbed by TiO_2 photoanodes, which leads to a very low energy transfer efficiency.[321] Additional challenges arise from rapid electron−hole recombination which reduces efficiencies.[46] Inspired by dye-sensitized solar cells (DSSCs),[322] the development of dye-sensitized photoelectrochemical/photoelectrosynthesis cells (DSPECs) is a promising strategy for water-splitting and carbon dioxide reduction.[83, 323-326] As shown in Fig. 61a, solar-driven water oxidation occurs at the photoanode, and proton or water reduction occurs at the cathode. The photoanode usually comprises nanocrystalline films of TiO_2 derivatized by adsorption of a chromophore that is capable of absorbing solar energy, and a catalyst for water oxidation, or chromophore–catalyst supramolecular photocatalysts.[323] Fig. 61b shows photocathodes in tandem cells for CO_2 reduction. The two electrode compartments are separated by a proton exchange membrane (PEM) which allows for proton diffusion and charge balance.[323] The working mechanism of a DSPEC can be summarized as follows: (1) Light absorption to produce an excited state of the chromophore; (2) electron or hole injection into electrodes; (3) electron transport to a transparent conducting oxide (TCO) electrode for ohmic delivery to a cathode or photocathode; (4) catalyst activation, catalytic water oxidation or water/CO_2 reduction.

The first DSPEC reported by Meyer's group in 1999 was used for dehydrogenation of *iso*-propanol to acetone.[327] In 2009, Mallouk and co-workers first reported a DSPEC with nanoparticles of IrO_2 as the water oxidation catalyst for water splitting.[328] In 2016, Ishitani's group developed a DSPEC for CO_2 reduction using a photocathode comprising a Ru(II)–Re(I) supramolecular photocatalyst and a NiO electrode.[83] Although DSPECs are far less developed than semiconductor-based PECs, significant progress has been achieved in recent years. In this section, some representative DSPECs based on di- or multi-nuclear supramolecular photocatalysts for water-splitting and carbon dioxide reduction will be discussed.

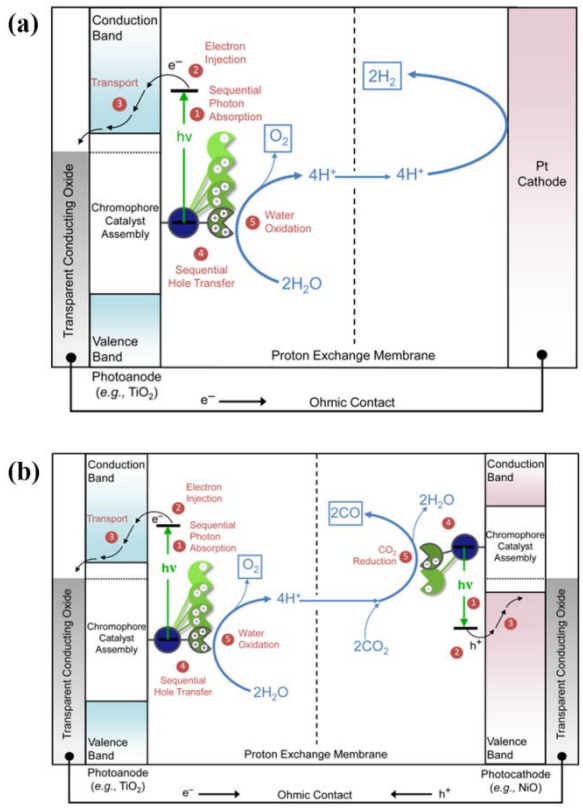

Fig. 61 (a) Schematic diagram of a DSPEC for water splitting into hydrogen and oxygen. (b) Schematic diagram of a tandem DSPEC for solar-driven CO_2 splitting into CO and O_2. Reproduced with permission from ref. 323. Copyright 2015 American Chemical Society. https://pubs.acs.org/doi/10.1021/acs.chemrev.5b00229.

4.3.1 DSPECs for water-splitting

How to assemble chromophores and catalysts onto a semiconductor surface is a prime consideration in the construction of a DSPEC. Multiple strategies have been explored, including co-deposition,[329] "layer-by-layer" deposition assemblies with Zr(IV)-phosphate bridges,[330] electroassembly by reductive vinyl coupling,[331] and adsorbing pre-synthesized covalently-linked chromophore–catalyst systems by a simple solution-soaking procedure.[332] For the selection of supramolecular photocatalysts, inspired by DSSCs, carboxylic acid (−COOH) derivatives have been initially studied to bind onto metal oxide films in DSPECs. However, carboxylates typically hydrolyze and desorb from the surface in water, especially at high pHs. The most widely reported supramolecular photocatalysts are phosphonic acid derivatives ($-PO_3H_2$) which bind with higher stability than carboxylates in aqueous solution,[323] as shown in Fig. 62. In this section, some representative supramolecular photocatalysts as photoanodes for water spliting will be discussed in detail.

Meyer's previous work had demonstrated electrocatalytic water oxidation by a surface-bound mononuclear Ru(II) complex on ITO.[333] The mechanism is a stepwise process: 1) proton-coupled electron transfer (PCET) activation to $Ru^{IV}{=}O^{2+}$, 2) further oxidation to $Ru^{V}{=}O^{3+}$, 3) O-atom attack on water to give an intermediate peroxide, and 4) finally further oxidation to release O_2. In 2011, possible photoinduced generation of catalytically active species (Ru^{IV} and Ru^{V}) at the remote Ru_b site in a supramolecular photocatalyst **321** in a DSPEC was studied.[334] **321** was adsorbed on TiO_2 in methanol solution through a soaking procedure. The maximum coverage of **321** on the TiO_2 interface was $\sim 7.2 \times 10^{-8}$ mol cm^{-2} in a film of ~6 μm thickness. The electrochemical properties of the TiO_2 surface-attached **321** are shown in Fig. 63. Stepwise oxidation from ITO–Ru_a^{II}–Ru_b^{II}–OH_2^{2+} to ITO–Ru_a^{II}–Ru_b^{III}–OH_2^{3+} ($E_{1/2}$ = 0.82 V), to ITO–Ru_a^{II}–$Ru_b^{IV}{=}O^{2+}$ ($E_{1/2}$ = 1.26 V), and to ITO–Ru_a^{III}–$Ru_b^{IV}{=}O^{3+}$ ($E_{1/2}$ = 1.65 V) was observed. Transient absorption spectra provided evidence for the generation of TiO_2 (e^-) with a long-lived, positive absorption feature at 950 nm. Upon 532 nm laser excitation, the electron injection from surface-bound **321** to TiO_2 is mainly dominated by two processes: 1) The remote $d\pi(Ru_b^{II}) \rightarrow \pi^*(BL)$ transition, and further electron injection to the TiO_2 surface (eqn (13)). However, the large spatial separation and weak electronic coupling between $\pi^*(BL^{-\bullet})$ and the TiO_2 interface may induce a low injection rate from this excited state. The previous work had identified ultrafast injection rates and high efficiencies from surface-bound MLCT excited states, whereas low injection rates and efficiencies were observed from remote states.[335] 2) Injection from surface-bound $Ru_a^{III} \rightarrow$ 4,4'-$(HOOC)_2bpy^{-\bullet}$ MLCT excited states (eqn (14)), which is known to occur rapidly and with high efficiency. Furthermore, electron injection by ITO–Ru_a^{II}–Ru_b^{III}–OH_2^{3+} that is generated on the surface by electrolysis at E_{app} = 1.1 V (vs NHE) was also investigated. In this case, Ru_a^{II} is the only intense light absorber, which shows a combination of $d\pi(Ru_a^{II}) \rightarrow \pi^*(BL)$ and $d\pi(Ru_a^{II}) \rightarrow \pi^*$(4,4'-$(COOH)_2$bpy) transitions. The 532 nm laser excitation would result in predominantly bridging ligand-based excited states, followed by intramolecular PCET to form $-Ru_b^{IV}{=}O^{2+}$ at the remote site (eqn (15)).

Chem Soc Rev

REVIEW ARTICLE

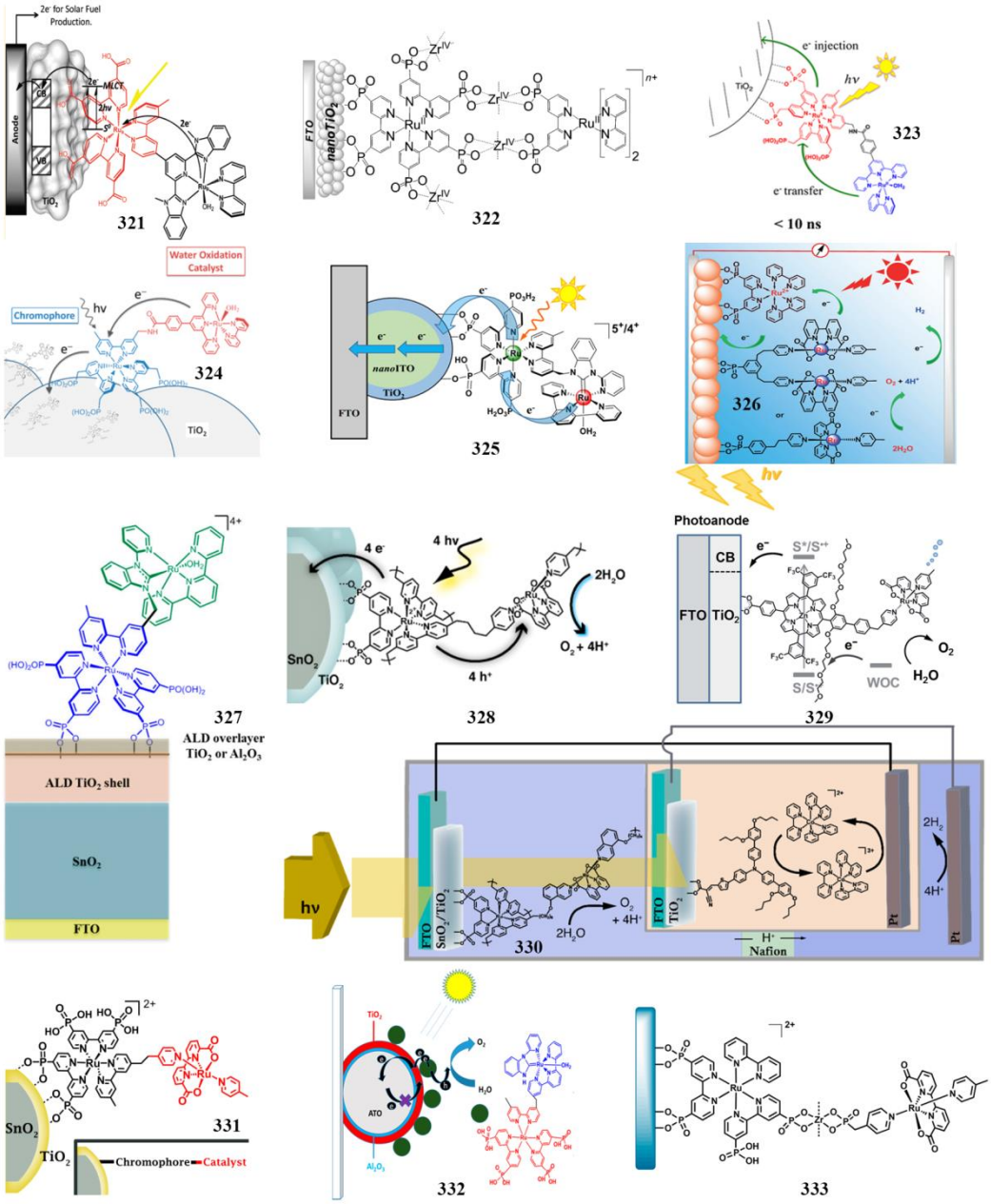

Fig. 62 Representative photoanodes in DSPECs for solar water splitting. Reproduced with permission from ref. 334. Copyright 2011 American Chemical Society for **321**; Reproduced with permission from ref. 330. Copyright 2012 Wiley-VCH for **322**; Reproduced with permission from ref. 336. Copyright 2012 American Chemical Society for **323**; Reproduced with permission from ref. 337. Copyright 2013 American Chemical Society for **324**; Reproduced with permission from ref. 338. Copyright 2013 Proceedings of the National Academy of Sciences, USA for **325**; Reproduced with permission from ref. 339. Copyright 2014 Wiley-VCH for **326**; Reproduced with permission from ref. 46. Copyright 2016 American Chemical Society for **327**; Reproduced with permission from ref. 331. Copyright 2015 American Chemical Society for **328**; Reproduced with permission from ref. 340. Copyright 2016 The Royal Society of Chemistry for **329**; Reproduced with permission from ref. 341. Copyright 2016 American Chemical Society for **330**. https://pubs.acs.org/doi/10.1021/jacs.6b10699; Reproduced with permission from ref. 342. Copyright

2016 American Chemical Society for **331**; Reproduced with permission from ref. 343. Copyright 2017 American Chemical Society for **332**; Reproduced with permission from ref. 344. Copyright 2018 American Chemical Society for **333**.

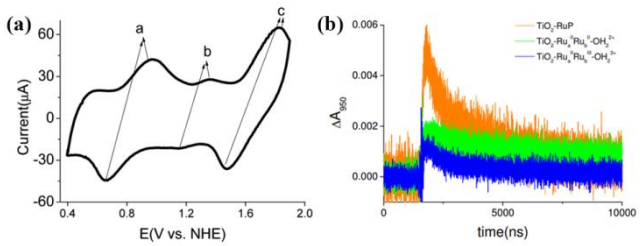

Fig. 63 (a) Cyclic voltammogram of **321** on nanoITO (10 mV/s). Surface coverage (Γ) was 9×10^{-9} mol cm^{-2}, 22 ± 2 °C. (b) Transient absorption decay at 950 nm for $TiO_2(e^-)$ in TiO_2–$Ru(bpy_2)(4,4'\text{-}(PO_3H_2)_2bpy)^{2+}$ (RuP, orange, $\Gamma = 2 \times 10^{-7}$ mol cm^{-2}), TiO_2–Ru_a^{II}–Ru_b^{II}–OH_2^{2+} (green) and TiO_2–Ru_a^{II}–Ru_b^{III}–OH_2^{3+} (blue) ($\Gamma = 5 \times 10^{-8}$ mol cm^{-2}) with 532 nm laser excitation. Reproduced with permission from ref. 334. Copyright 2011 American Chemical Society.

$$TiO_2\text{—}Ru_a^{II}(BL)Ru_b^{II}OH_2^{2+} \xrightarrow{h\nu} TiO_2\text{—}Ru_a^{II}(BL^{-\bullet})Ru_b^{III}OH_2^{2+*} \xrightarrow{\text{injection}} TiO_2(e^-)\text{—}Ru_a^{II}(BL)Ru_b^{III}OH_2^{3+} \quad (13)$$

$$TiO_2\text{—}OOC(bpy)Ru_a^{II}(BL)Ru_b^{II}OH_2^{2+} \xrightarrow{h\nu} TiO_2\text{—}OOC(bpy^{-\bullet})Ru_a^{III*}(BL)Ru_b^{II}OH_2^{2+} \xrightarrow{\text{injection}} TiO_2(e^-)\text{—}Ru_a^{III}(BL)Ru_b^{II}OH_2^{2+} \xrightarrow{\text{rapid ET}} TiO_2(e^-)\text{—}Ru_a^{II}(BL)Ru_b^{III}OH_2^{3+} \quad (14)$$

$$TiO_2\text{—}Ru_a^{II}(BL)Ru_b^{III}OH_2^{3+} \xrightarrow{h\nu} TiO_2\text{—}Ru_a^{III}(BL^{-\bullet})Ru_b^{III}OH_2^{3+} \xrightarrow{\text{injection}} TiO_2(e^-)\text{—}Ru_a^{III}(BL)Ru_b^{III}OH_2^{3+} \xrightarrow{\text{rapid ET}} TiO_2(e^-)\text{—}Ru_a^{II}(BL)Ru_b^{IV}{=}O^{2+} + 2H^+ \quad (15)$$

It is worth noting that the injection efficiencies for both forms of the assembly are lower than those for $[Ru(bpy)_2(4,4'\text{-}(PO_3H_2)_2bpy)]^{2+}$ bound to TiO_2 (TiO_2–Ru^{2+}), whereas the back electron transfer rates, $TiO_2(e^{-1}) \rightarrow Ru_b^{III}$–$OH_2^{3+}$ and $TiO_2(e^{-1}) \rightarrow Ru_b^{IV}$–$O^{2+}$, are significantly decreased when compared with $TiO_2(e^{-1}) \rightarrow Ru^{3+}$ back electron transfer.

In 2012, Hanson *et al.* reported a layer-by-layer self-assembly strategy for the preparation of the chromophore-catalyst **322** on nanostructured metal oxide substrates by immersing nanocrystalline TiO_2 films in three separate aqueous solutions of $HClO_4$ with chromophore Ru unit, $ZrOCl_2$, and the catalytic Ru unit.[330] The resulting structures showed rapid intralayer energy and electron transfer.

In 2012, a new di-Ru photocatalyst **323** bearing a synthetically flexible saturated bridging ligand was reported by Ashford *et al.*[336] The key findings are: 1) Electron injection efficiencies are wavelength dependent. For example, a higher injection efficiency of ~30% was observed for **323** when excited at 440 nm, and $[Ru_a^{II}–]^{4+}$ dominates the absorption. A decreased injection yield of ~12% was observed when excited at 532 nm with the major light absorber being $[–Ru_b^{II}–OH_2]^{4+}$. Rapid electron injection occurs on the subnanosecond time-scale. 2) Back electron transfer from $TiO_2(e^-)$ to the oxidized Ru(III) site was dependent on pH, increasing from 6 μs (pH = 1) to 35 μs (pH = 4.5).

In 2013, Wang *et al.* examined by femtosecond transient absorption spectroscopy the ultrafast dynamics of the initial photoactivation step in a supramolecular photocatalyst **324** anchored to TiO_2.[337] The key findings are: 1) Ultrafast electron injection from the light absorbing $–Ru_a^{II}–$ site to TiO_2 was observed with a time scale ranging from ~100 fs to several 100 ps. The injection efficiency is as high as 95%. 2) Following the ultrafast electron injection into TiO_2, the electron transfer from catalyst $[–Ru_b^{II}–OH_2]^{2+}$ to the chromophore $[–Ru_a^{III}]^{3+}$ occurs on the time scale of 145 ps. 3) Back-electron transfer $TiO_2 \rightarrow$ oxidized $[Ru_a^{II}–Ru_b^{III}–OH_2]^{5+}$ was observed on a microsecond-millesecond time scale.

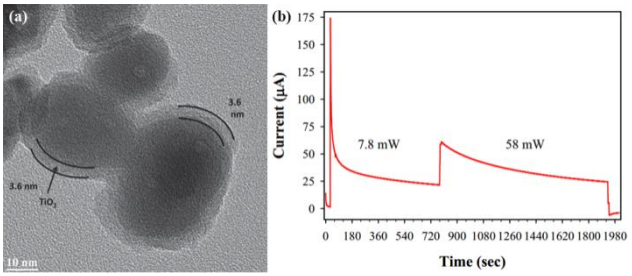

Fig. 64 (a) TEM image of a "core–shell" nanostructure with a 3.6 nm layer of TiO_2 shell. (b) Photocurrent measured during H_2 production experiment in the DSPEC. Reproduced with permission from ref. 338. Copyright 2013 Proceedings of the National Academy of Sciences, USA.

In 2013, Alibabaei *et al.* first reported photocatalyst **325** bound to the surface of a "core–shell" nanoparticle, as a photoanode for photoelectrochemical water splitting.[338] The core structure consists of a nanoparticle film of either tin-doped indium oxide (nanoITO) or antimony-doped tin oxide (nanoATO) (generically transparent conducting oxides (TCO)), deposited on a fluoride-doped tin oxide (FTO) glass substrate. The shell consists of a conformal TiO_2 nanolayer applied by atomic layer deposition (ALD). The "core–shell" nanostructure was proved by TEM experiments, which showed a thin TiO_2 shell with a thickness of 3.6 nm (Fig. 64a). In this configuration, effective excitation and rapid electron injection into the nanostructured TCO on the nanosecond timescale was observed. H_2 evolution and photocurrent measurements using this photoanode and a Pt cathode were carried out. As shown in Fig. 64b, upon weak light irradiation (7.8 mW) at 445 nm and applied voltage bias (0.2 V vs. NHE) in aqueous pH 4.6 solution (20 mM acetate/acetic acid buffer, 0.5 M $LiClO_4$) at 22 ± 1 °C, the current decreased from 175 to 20 μA. The decrease in photocurrent with time was attributed to the unstable TiO_2–$[Ru_a^{III}–]^{3+}$ assembly. The photon conversion efficiency

was 4.4% at the peak photocurrent. The Faradaic efficiency for H_2 production was estimated as ~86%. The observed photocurrent provided evidence for O_2 production. However, a quantitative investigation was not reported in this work.

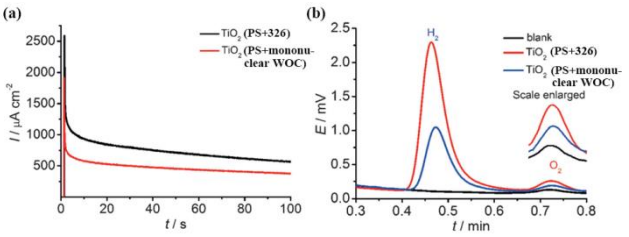

Fig. 65 (a) The photocurrent changes of the TiO_2–(PS+**326**) and TiO_2–(PS+mononuclear Ru catalyst) under sustained light illumination (300 mW cm^{-2}), an applied external bias of 0.2 V vs NHE, and in 0.1 M aqueous Na_2SO_4. (b) GC data of gases generated by the DSPECs after light illumination (300 mW cm^{-2}), with the photoanodes TiO_2–(PS+**326**) and TiO_2–(PS+mononuclear Ru catalyst), an applied external bias of 0.2 V vs NHE, and in 0.1 M aqueous Na_2SO_4. Reproduced with permission from ref. 339. Copyright 2014 Wiley-VCH.

In 2014 photoanodes consisting of a mononuclear Ru complex (PS) and dinuclear Ru complex **326** with a planar "bda" ligand (bda is 2,2'-bipyridine-6,6'-dicarboxylate) or mononuclear Ru complex (WOCs), bound to TiO_2 were presented by Sun's group for light-driven water splitting.[339] The changes of photocurrent density with longer-term light irradiation (100 s) are shown in Fig. 65a. Photocurrent density of TiO_2–(PS+**326**) exhibited a sharp peak and then decays slowly from 1.1 mA cm^{-2} to 0.7 mA cm^{-2}. By comparison, photocurrent density of TiO_2–(PS+mononuclear Ru catalyst) displayed a similar trend, but with lower decays from 0.6 mA cm^{-2} to 0.45 mA cm^{-2}. Water-splitting performances of DSPECs with the photoanode TiO_2–(PS+**326**) or TiO_2–(PS+mononuclear Ru catalyst) are shown in Fig. 65b. Gas chromatography (GC) results indicated that H_2 and O_2 can be produced in both the DSPECs. The amount of hydrogen generated by TiO_2–(PS+**326**) is 1.41 μmol, which is higher than that by TiO_2–(PS+mononuclear Ru catalyst) with 0.85 μmol. The corresponding Faradaic efficiencies were calculated to be 80% and 72%, respectively. Similar to the trend observed in hydrogen generation, the higher oxygen generation of 0.66 μmol was observed in TiO_2–(PS+**326**) compared with that of TiO_2–(PS+mononuclear Ru catalyst) with 0.40 μmol. The corresponding Faradaic efficiencies were measured to be 75% and 68%, respectively. All of the results in this work indicated that the dinuclear WOC shows better catalytic performance than the mononuclear WOC for the light-driven water splitting.

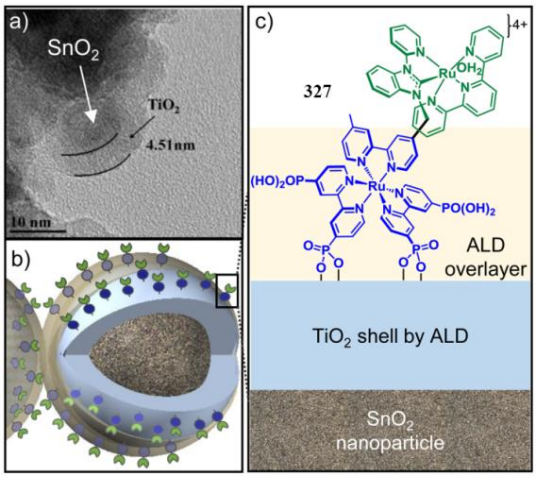

Fig. 66 (a) TEM image of multi-layers photoanode. (b) Depiction of core/shell nanoparticle along with a surface-stabilizing overlayer of TiO_2 or Al_2O_3 added by atomic layer deposition (ALD). (c) Zoomed-in view highlighting the structure of assembly **327** on the core/shell surface stabilized by an ALD oxide overlayer. Reproduced with permission from ref. 46. Copyright 2016 American Chemical Society.

In 2015, based on the previous report of a "core–shell" photoanode, Alibabaei *et al*. proposed a new strategy for the stabilization of binding to a photoanode surface by adding an inert oxide overlayer of TiO_2 or Al_2O_3 by ALD.[81] Fig. 66 shows the TEM results for the resulting multi-layered photoanode, the corresponding cross-section image of the photoanode, and the chemical structure of the supramolecular photocatalyst **327**. Upon irradiation (15.1 mW cm^{-2}) at 455 nm, this new configuration of the photoanode showed an obvious improvement for the photocurrent density (0.79 mA cm^{-2}) compared with that of the simple "core–shell" ITO–TiO_2 (0.1 mA cm^{-2}) or SnO_2–TiO_2 (0.48 mA cm^{-2}) photoanodes. The experiments used a Pt counter-electrode at 200 mV vs. NHE (0 V vs. Ag/AgCl) bias at pH 4.6 in 0.5 M $LiClO_4$ with 20 mM acetate/acetic acid buffer. With optimization of the thickness of the Al_2O_3 overlayers (0.55 nm), the photocurrent reached 1.97 mA cm^{-2}. Furthermore, the DSPEC based on SnO_2/TiO_2 (4.5 nm)–**327** (0.3 nm Al_2O_3) photoanode operated at pH 7 in phosphate buffers at room temperature, with an applied bias of 600 mV vs NHE, and illumination at 455 nm. The Faradaic efficiencies for H_2 and O_2 generation after 100 s were 57% and 41%, respectively.

In 2015, Sherman *et al*. reported a novel electrochemical procedure for the photosensitizer–catalyst assemblies on oxide electrode surfaces. The supramolecular photocatalyst **328** attached on core/shell SnO_2/TiO_2 nanoparticle surfaces was obtained by reductive vinyl coupling to form the central C-C link in the bridge.[331] The photoanode produced O_2 with a Faradaic efficiency of 22% after illumination with 100 mW cm^{-2} white light with a 400 nm cutoff filter from 60 to 960 s for 5 min in 0.1 M $H_2PO_4^-$/HPO_4^{2-} at pH 7, with an applied bias of 0.4 V vs SCE. Furthermore, upon LED (14 mW cm^{-2}) illumination at 450 nm for 10 min, the solar efficiency for DSPEC production of hydrogen was ~0.3%.

In 2016, Yamamoto *et al*. reported a Zn–Ru dinuclear supramolecular photocatalyst **329** assembled on a TiO_2 electrode for visible-light driven water oxidation.[340] Because of the Zn-porphyrin component, DSPEC with **329** showed a broader wavelength absorption response (up to 620 nm) compared to conventional ruthenium-based sensitizers. Water oxidation efficiency using **329** was higher than the reference systems with co-adsorption of the individual Zn–porphyrin and Ru units. Initial incident photon-to-current efficiencies (IPCE) of 18% and 6.4% were observed under monochromatic illumination at 424 nm and 564 nm, respectively.

In 2016, Sherman *et al*. reported a tandem DSPEC (based on a TiO_2–**330** photoanode) with a dye-sensitized solar cell (DSSC) for water splitting.[341] The versatility of this novel DSPEC–DSSC assembly offers significant advantages for applications in solar driven water splitting: 1) The solar absorption spectrum can be easily tuned by the two light-absorbing electrodes, enabling much higher efficiencies for oxygen and hydrogen production compared to single-absorber systems. 2) The achieved photocurrent can be tuned by easy modification of the dye, or the redox mediator, and by selection of the semiconductor support.

In 2017, a covalently linked photosensitizer–catalyst assembly **331** was reported for solar water splitting by Concepcion and co-workers.[342] With illumination by a 100 mW cm^{-2} white light source for 30 s, a maximum photocurrent of ~0.85 mA cm^{-2} was achieved for the core–shell electrodes in a 0.1 M acetate buffer, 0.5 M in $NaClO_4$ at pH 5.7. The Faradaic efficiency for O_2 generation after 5 min illumination was 74%.

In 2017, Wang *et al*. reported a new core–shell photoanode configuration by the introduction of an Al_2O_3 layer between the antimony-doped tin oxide Sb:SnO_2 (ATO) and TiO_2 layers, to control internal electron transfer within the core–shell structure.[343] The generated photocurrent density of **332** was improved up to 300% when the thickness of the Al_2O_3 blocking layer was changed from 0 (27 μA cm^{-2}) to 0.55 nm (76 μA cm^{-2}). However, further increase in the thickness of Al_2O_3 above 0.55 nm led to a decrease of photocurrent densities.

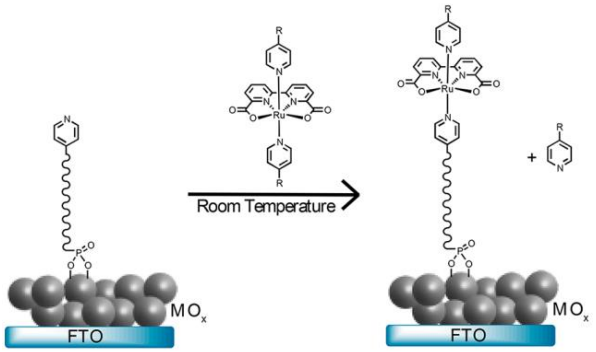

Fig. 67 Attachment procedure for Ru(bda)(L)(L') catalysts on metal oxide (MO_x) surfaces by surface ligand exchange. Reproduced with permission from ref. 344. Copyright 2018 American Chemical Society.

More recently, Wang *et al*. devised a novel "bottom-up" surface-ligand exchange strategy for immobilizing pyridyl-substituted Ru(II) catalysts at the surface of a photoanode (Fig. 67).[344] Surface-bound pyridine can be exchanged by immersion for 12 h in a methanol solution of the pyridyl-substituted Ru complex. Based on this approach, a series of pyridyl-substituted Ru complexes with a planar "bda" ligand that usually shows lower overpotentials for driving water oxidation, were easily stabilized at the surface of the photoanode. Furthermore, this strategy allows for rapid screening of layer-by-layer surface-bound assemblies, for example, **333** prepared by the immersion of a TiO_2–Ru–Zr(IV)–pyridine electrode in a 1 mM solution of the Ru catalyst solution for 4 h. After 10 min photolysis periods, the photocurrent density and Faradaic efficiencies are 103 μA cm^{-2} and 61%, respectively, by using the resulting photoanode of the DSPEC.

In summary, research on DSPECs for water splitting is still in its infancy. There are some key challenges to be overcome. 1) To develop a DSPEC that can be used in light driven water splitting with a high photocurrent density by applying a small external bias, or even no bias. 2) To enhance electron injection efficiency by expanding the light absorption wavelength into the IR or NIR regions. 3) To achieve a DSPEC for water splitting with long-term stability.

4.3.2 DSPECs for CO_2 reduction

A schematic diagram of a tandem DSPEC for light driven CO_2 splitting into CO and O_2 is presented in Fig. 61b. The photocathode plays a key role for the CO_2 reduction. Generally, water reduction of CO_2 to CO is driven at −0.12 V (vs NHE) and E_{CB} (TiO_2) ≈ −0.1 V at pH 0. The absence of a suitable p-type oxide photocathode has greatly limited progress in implementing DSPECs.[323] In 2015, Ishitani's group reported a novel hybrid photocathode consisting of a Ru(II)–Re(I) supramolecular photocatalyst and a NiO electrode for photoelectrochemical CO_2 reduction in a nonaqueous solution.[345] However, light driven photoelectrochemical CO_2 reduction using water as a reductant became a prime target. Consequently, in 2016, a tandem DSPEC with a NiO–RuRe (**334**) hybrid photocathode and a CoO_x/TaON photoanode was reported by Ishitani's group.[83] Upon irradiation at λ = 460 nm, a photocathodic response was clearly observed starting at approximately −0.1 V vs Ag/AgCl in a CO_2-purged aqueous solution containing 50 mM $NaHCO_3$ (pH = 6.6). This photoresponse can be attributed to the electron transfer process from the valence band of the NiO electrode to the excited Ru photosensitizer unit in RuRe. Therefore, photoelectrochemical CO_2 reduction in the aqueous solution occurs at the NiO–RuRe photocathode.

Photoelectrochemical CO_2 reduction data obtained using various electrodes under different applied biases are summarized in Table 11. It can be seen that the formation of CO occurs only when using a NiO–RuRe photocathode with an applied bias. Small amounts of H_2 formation are derived from photocatalysis of the degraded product of the Ru photosensitizer, due to the similar results observed in the NiO–Ru system. Water oxidation at a CoO_x/TaON photoanode

was also investigated in a $NaHCO_3$ aqueous solution (pH = 8.3) under an Ar atmosphere. The photocurrent was observed at −0.7 V vs Ag/AgCl under irradiation at λ = 400 nm; O_2 formation was also observed in the liquid phase under these reaction conditions. The Faraday efficiency after 5 min of irradiation was 89%. Subsequently, the authors studied a tandem DSPEC consisting of a NiO−RuRe cathode and a CoO_x/TaON photoanode for the CO_2 reduction using water as a reductant. The photoanode and photocathode were separated by a Nafion membrane. As shown in Fig. 68, upon irradiation at λ > 400 nm, the transmitted light was received by the CoO_x/TaON photoanode through the backside of the NiO−RuRe photocathode and the Nafion membrane. To accelerate the reaction, a bias of −0.3 V vs CoOx/TaON was applied to NiO−RuRe. Furthermore, a chemical bias of 0.10 V was simultaneously generated from the pH difference between the two electrodes. Finally, this tandem DSPEC showed activity for visible-light-driven catalytic reduction of CO_2 in the aqueous solution to generate CO and O_2 for the first time. The formed O_2 was detected in the liquid phase in the CoOx/TaON photoanode with a Faradaic efficiency of 68% after 60 min of irradiation. Simultaneously, the formed CO was also captured in the gas phase in the NiO−RuRe photocathode chamber with a TON_{CO} of 17. The low catalytic performance of the system was suggested mainly to arise from the photocathode. The NiO cathode suffers from slow hole transport and unfavorable interfacial kinetics, resulting in poor catalytic ability and durability in the system. Therefore, further improvements in catalytic ability of NiO photocathodes and exploring new semiconductor oxides are necessary for achieving highly efficient photoelectrochemical CO_2 reduction.

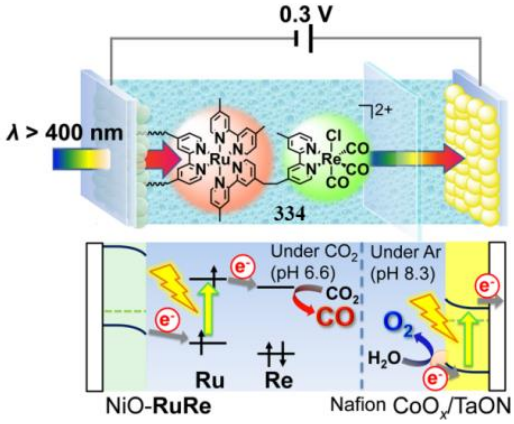

Fig. 68 A Schematic image of hybrid photoelectrochemical cell based on complex **334**. Reproduced with permission from ref. 83. Copyright 2016 American Chemical Society. https://pubs.acs.org/doi/10.1021/jacs.6b09212.

Table 11 Photoelectrochemical CO_2 reduction with various electrodes[a]

sample	Complex/nmol	Potential/V[b]	CO/nmol (TON_{CO})	H_2/nmol	*F*red/%[c]
NiO−**334**	11.2	−0.7	241(22)	13	59
NiO−**334**	10.3	−0.3	111(11)	10	45
NiO−**334**	9.6	0	n.d.	n.d.	
NiO−Ru	11.5	−0.7	n.d.	21	21
NiO−Re	15.9	−0.7	n.d.	n.d.	
NiO−**334**[d]	10.2	−0.7	n.d.	n.d.	
NiO−**334**[e]	9.4	−0.7	n.d.	11	56

[a] Electrode was irradiated at λ > 460 nm for 5 h in 50 mM $NaHCO_3$ aq solution under a CO_2 atmosphere. [b] Versus Ag/AgCl (sat. KCl). [c] Faradaic efficiency for CO_2 reduction. [d] In the dark. [e] Under an Ar atmosphere.

5. Chemo/bio-sensors and photodynamic therapy

5.1 Chemosensors

Luminescent chemosensors are of great importance due to their applications in numerous fields, such as chemistry, biology, environmental monitoring and national and personal security.[21, 346-348] In comparison with conventional fluorescent sensor systems, phosphorescent sensors based on transition metal complexes such as Ir(III), Ru(II), Pt(II) and Au(I) offer advantages such as large Stokes shifts, high chemical- and photo-stability and longer excited state lifetimes (*ca.* microseconds). Their relatively long lifetimes can be easily distinguished from fluorescent backgrounds (*ca.* nanoseconds), resulting in higher signal-to-noise ratios in the sensing process.[23] Furthermore, the photophysical properties of phosphorescent materials can be fine-tuned *via* rational modification of the ligand structures and the metal centers.[23] Review articles have summarized numerous mononuclear metal complexes for the sensing of different kinds of analytes.[23, 349-351] However, the development of phosphorescent sensors based on dinuclear metal complexes is still overlooked and will be discussed in this section. Moreover, some key advantages of dinuclear metal complexes will be summarized in comparison with mononuclear counterparts.

Chem Soc Rev

REVIEW ARTICLE

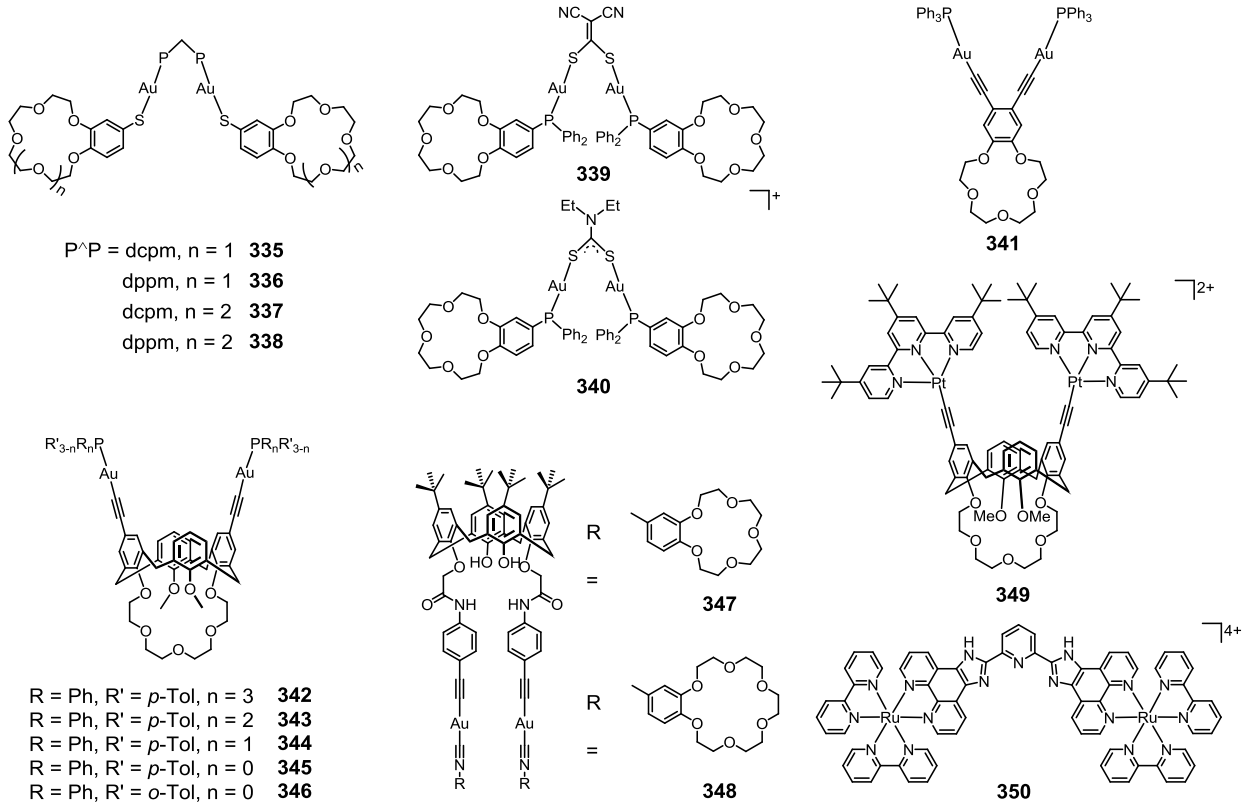

Fig. 69 The chemical structures of dinuclear metal complexes for the sensing of cations.

5.1.1 Phosphorescent chemosensors for metal cations

Metal cations play important roles in biological, environmental and life processes. Consequently, great effort has been devoted to the development of effective chemosensors for the detection of various metal cations.[348, 352] In this context, representative dinuclear metal complexes are shown in Fig. 69. As a classical strategy, host–guest chemistry of crown ethers has been used to sense guest cations *via* the formation of non-covalent interactions.[353, 354] Yam's group have pioneered dinuclear Au(I) complexes for these applications. In 1998 complexes **335–338** with bridging diphosphines (dppm = bis(diphenylphosphanyl)methane; dcpm = bis(dicyclohexylphosphanyl)methane) and benzocrown ether functionalized thiolate ligands were reported.[355, 356] All these complexes showed bright emission in the range of 492–580 nm in dichloromethane solution at room temperature, originating from a S→Au ligand-to-metal charge transfer (LMCT) excited state. These complexes served as luminescent sensors for metal cations, with specificity depending on the size of the crown ether pendants. For example, **335** and **336** with the smaller crown ether sense K^+, whereas **337** and **338** with the larger crown ether sense Cs^+. Upon addition of metal cations into a solution of **336**, the emission at λ_{max} 520 nm dropped in intensity and a new band appeared at 720 nm (Fig. 70). This new band was suggested to originate from a thiolate ligand-to-metal-metal charge transfer (LMMCT) excited state due to the enhanced intramolecular Au···Au interaction in the cation complex.

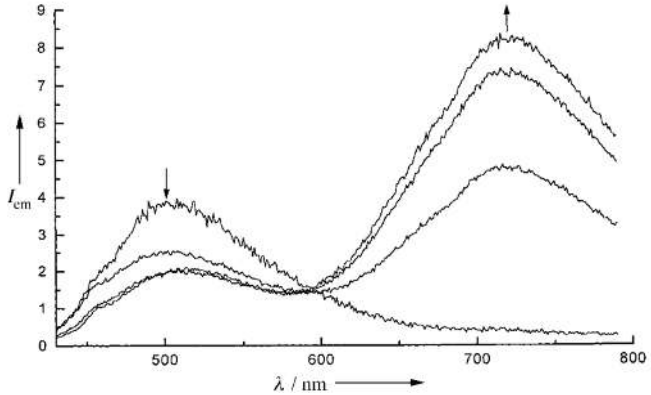

Fig. 70 Emission spectral changes of **336** (1.7×10^{-3} mol L^{-1}) upon addition of various concentrations of potassium ions in

CH_2Cl_2–MeOH (1:1, v/v; 0.1 M nBu$_4$NPF$_6$). Reproduced with permission from ref. 355. Copyright 1998 Wiley-VCH.

As an extension of this work, Yam *et al*. reported two new Au(I) complexes **339** and **340** with different bridging dithiolate ligands.[357] Upon addition of various metal cations, UV-vis absorption results indicated that both complexes exhibited preferential binding towards K^+ over Na^+. The X-ray crystal structure of **340**–Na (Fig. 71) showed an intramolecular sandwich binding of the Na cation and the two crown ether units with a 1:1 stoichiometry, in agreement with ESI–mass spectrometry results. Furthermore, the intramolecular Au···Au distance was only 3.0825 Å.

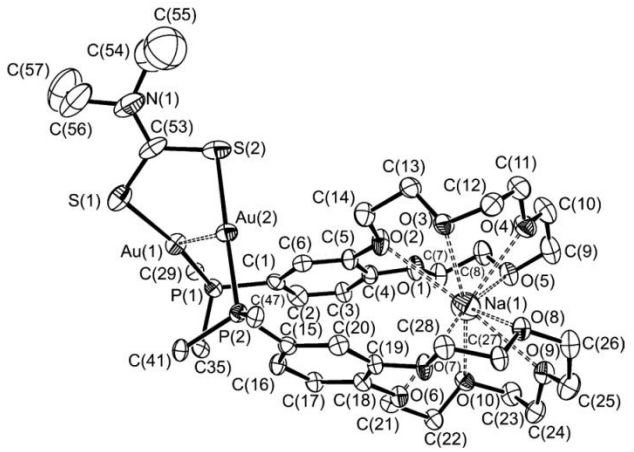

Fig. 71 The crystal structure of **340**–Na. Reproduced with permission from ref. 357. Copyright 2005 Elsevier.

In 2004, a new dinuclear Au(I) complex **341** connected by a benzocrown ether functionalized ethynyl bridge was synthesized by Yam's group.[358] This complex showed intense phosphorescence in both the solid and solution states, which originates from the [σ(Au–P)→π*(C≡C)] or metal-perturbed [π→π*(C≡C)] IL excited states. UV-vis absorption results indicated that **341** specifically recognizes Na^+ in CH_2Cl_2-MeOH (1:1 v/v) at room temperature.

As another sensing strategy, calixarene crown ethers have been widely studied as ion receptors that can hold smaller molecules or ions.[359, 360] In 2003, a series of luminescent dinuclear Au(I) alkynylcalix[4]crown-5 complexes **342**–**346** was synthesized by Yam *et al*.[361] All the complexes exhibited orange emission in dichloromethane solution with a band at 578–585 nm originating from metal-perturbed IL or [σ(Au–P)→π*(phosphine)] triplet excited states. All the complexes showed a binding response to K^+ and Na^+ in the order **345** > **346** ≥ **343** ≥ **342** > **344** and **346** ≥ **342** > **343** > **344** > **345**. This order was attributed to the different calixcrown cavity size that was induced by the subtle steric effects of the substituents on the phosphine ligand. For example, smaller-sized **345** represented the largest binding constant for Na^+ and the smallest binding constant for K^+. Furthermore, the K^+/Na^+ selectivities of complexes **342**–**345** are 3×10^5, 1.8×10^2, 1.9×10^2 and 13, respectively.

In 2009, He *et al.* reported the dinuclear Au(I) complexes **347** and **348**.[362] Both complexes showed bright emission with bands centerd at ca. 448–478 nm in dichloromethane solution at room temperature, assigned to mixed metal-pertubed intraligand (IL) and alkynyl-to-aryl isocyanide (LLCT) excited states. Upon addition of various metal cations, the complexes showed specific binding ability for K^+ and Cs^+, respectively. A new emission band at 600 nm was attributed to a Au···Au interaction induced *via* a sandwiched binding mode (Fig. 72), resulting in a reduced HOMO–LUMO energy gap.

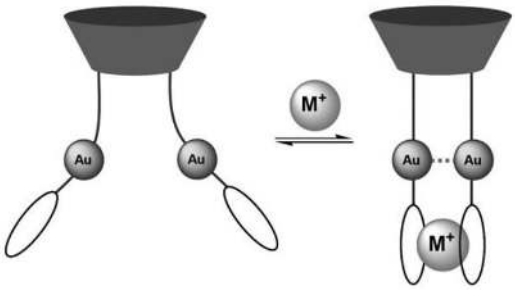

Fig. 72 Schematic diagram showing the proposed formation of a Au···Au interaction upon the sandwich binding of metal ion to **347** and **348**. Reproduced with permission from ref. 362. Copyright 2009 Wiley-VCH.

In 2006, a novel dinuclear Pt(II) alkynylcalixcrown complex **349** was studied for the specific recognition of metal cations by Lo *et al*.[363] Upon excitation, **349** showed a faint emission band at 738 nm, accompanied by a long-lived phosphorescent lifetime in the microsecond range in acetonitrile solution. The emission of **349** originated predominantly from ^{3}MLCT [dπ(Pt)→π*(t-Bu$_3$-tpy)], and probably mixed with some ^{3}LLCT [π(C≡C)→π*(t-Bu$_3$-tpy)] transitions. The weak emission of **349** was ascribed probably to quenching of the emissive ^{3}MLCT excited state by photoinduced electron transfer (PET) from the electron-rich alkoxy-substituted calixcrown moiety to the platinum terpyridyl unit. Interestingly, as shown in Fig. 73, upon addition of various metal cations, complex **349** showed a specific turn-on response for K^+, with selectivities of 10^2–10^4-fold greater than for other cations.

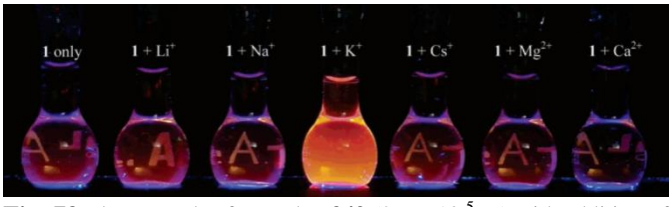

Fig. 73 Photograph of complex **349** (3.7×10^{-5} M) with addition of various cations in CH_3CN (0.1 M nBu$_4$NPF$_6$) solution. Reproduced with permission from ref. 363. Copyright 2006 American Chemical Society.

In 2013, Chao's group proposed a new strategy for the highly selective and sensitive sensing of Cu^{2+} ion in aqueous media, *in vivo* and *in vitro* by a dinuclear Ru(II) complex **350**.[364] As shown in Fig. 74, upon addition of various cations, complex **350** exhibited an almost complete quenching response to Cu^{2+}, whereas almost no quenching was observed for other cations. The detection limit for Cu^{2+} was as low as 3.33×10^{-8} M. Interestingly, **350** showed

two-photon luminescence with a significant two-photon absorption cross section (400 GM). Two-photon detection of Cu^{2+} was also realized by complex **350** when two-photon excitation at 850 nm was applied. Furthermore, as shown in Fig. 75, one-photon or two-photon detection of Cu^{2+} was also realized in living cells with low cytotoxicity, good water solubility, and good membrane permeability.

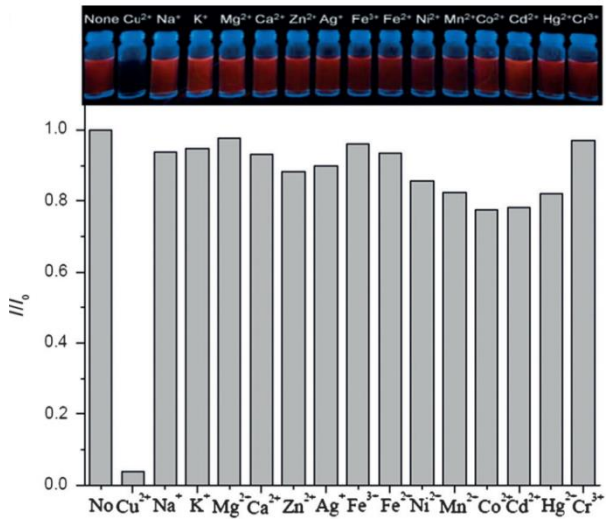

Fig. 74 Photograph of complex **350** (20 μM) with addition of various cations. Reproduced with permission from ref. 364. Copyright 2013 Wiley-VCH.

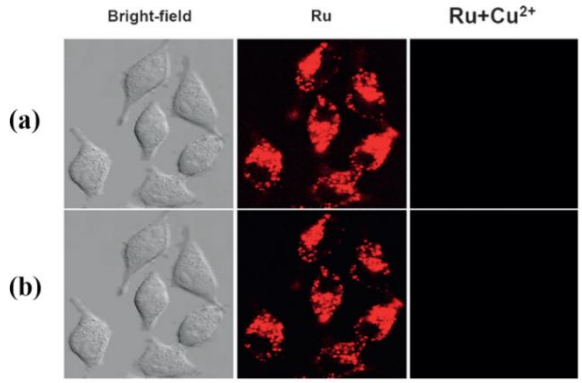

Fig. 75 (a) One-photon fluorescence microscopy and (b) two-photon fluorescence microscopy images of HeLa cells incubated with **350** (10 μm) before and after the exogenous Cu source treatment. Reproduced with permission from ref. 364. Copyright 2013 Wiley-VCH.

5.1.2 Phosphorescent chemosensors for anions

The selective detection of anions is vital because of their important roles in various chemical, biological, and environmental processes.[346, 365, 366] Ye's group reported in 2012 that complex **350** not only demonstrates a specific response towards Cu^{2+} cations, but also is an effective probe for CN^- anions in water.[367] Upon addition of various anions, the emission of **350** was quenched in a specific response to CN^-. Moreover, the response to CN^- was also observed in mixtures of CN^- and other anions. The detection limit for CN^- was determined to be 5 μM. The specificity for CN^- was attributed to hydrogen bonding to CN^- of N−H and phenyl C−H bonds of complex **350** based on heteronuclear multiple bond correlation (HMBC) spectra.

In 2010, two dcpm-containing Au(I) thiolate dinuclear complexes **351** and **352** (Fig. 76) with different urea receptors were synthesized by Yam's group.[368] Complex **351** showed high selectivity and sensitivity for F^-. As shown in Fig. 77, upon addition of 0–1 equivalents of F^-, the absorption band at 358 nm decreased gradually in intensity, while two new bands at ~288 nm and ~370 nm appeared, demonstrating the formation of hydrogen-bonding interactions between F^- and **351**. With addition of more F^-, a new band at ~490 nm grew in intensity, with two isosbestic points at 314 and 428 nm, and accompanied by a color change from yellow to red, attributed to the deprotonation of **351**. UV-vis absorption and ^1H NMR results indicated a 1:1 binding stoichiometry between F^- and **351**. Furthermore, complex **351** exhibited higher binding affinity for anions compared with that of complex **352**, probably because of the higher acidity of the urea moieties as a result of the introduction of the NO_2 group in **351**.

Chem Soc Rev

REVIEW ARTICLE

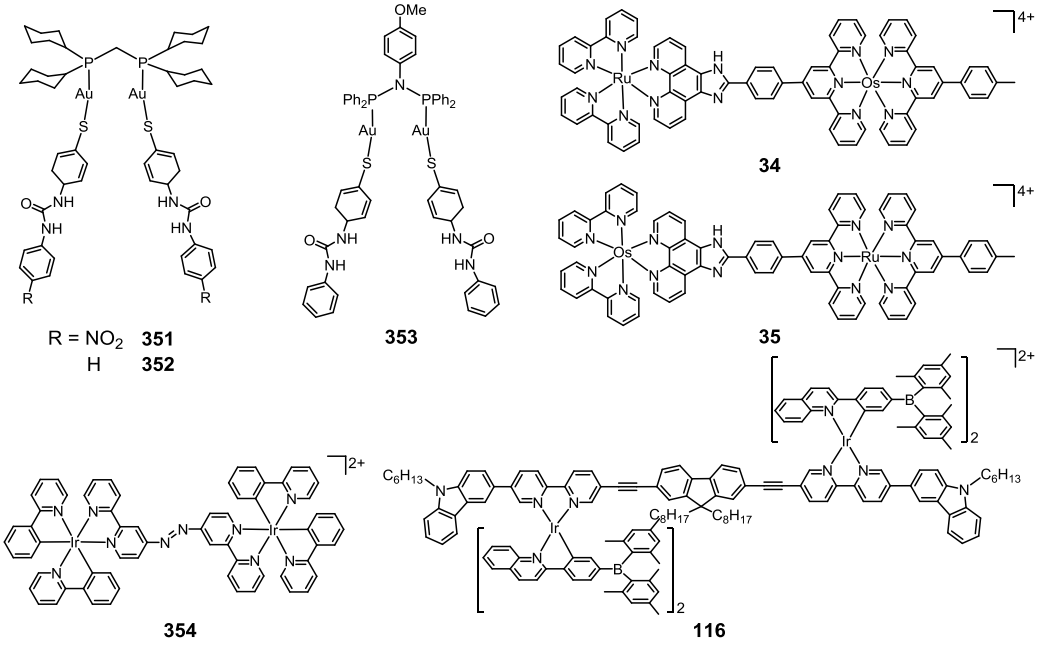

Fig. 76 The chemical structures of dinuclear metal complexes for the sensing of anions.

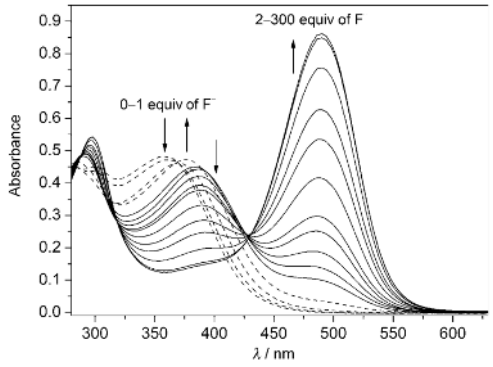

Fig. 77 UV/Vis spectral changes of complex **351** (1.17×10^{-5} M) in DMSO (0.1 M nBu$_4$NPF$_6$) upon addition of F^-. Reproduced with permission from ref. 368. Copyright 2010 Wiley-VCH.

Subsequently, a new urea-containing Au(I) thiolate dinuclear complex **353** demonstrated highly selective detection of F^-, evidenced by decolorization of the yellow solution, and drastic changes of emission and NMR spectra[369] Interestingly, the sensing mechanism was attributed not to H-bonding interactions (as occurs in **351** and **352**) but instead to irreversible P–N bond hydrolysis, which was confirmed by the ESI-MS spectra (Fig. 78). Cl^- was shown to bind to the urea moiety of **353** and not to cleave the molecule.

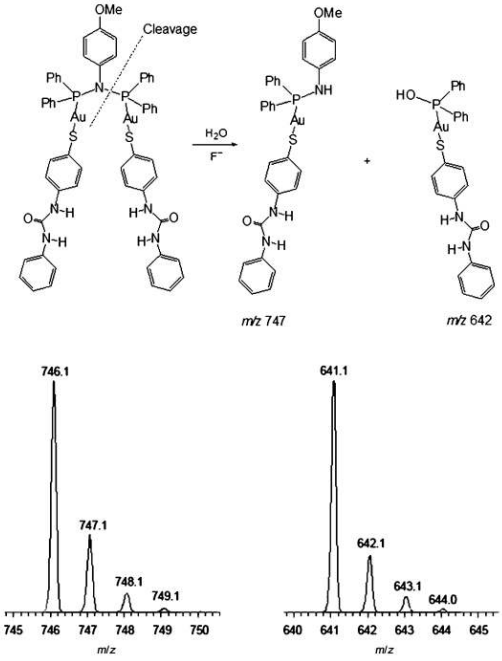

Fig. 78 Top) Scheme showing the proposed decomposition pathway of complex **353** with the cleavage of the P–N bond. Bottom) Ion clusters at m/z= 746 and 641, expanded from the negative ESI-MS spectra of a CH_2Cl_2 solution of complex **353** and 1 equiv of F^-. Reproduced with permission from ref. 369. Copyright 2015 Wiley-VCH.

In 2013, Chao's group reported dinuclear iridium(III) complex **354** for the highly selective and sensitive turn-on detection of sulphite/bisulphite in both living cells and *in vitro*.[370] Complex **354** is non-emissive due to the electron-withdrawing azo bridge quenching the MLCT excited state. However, as shown in Fig. 79, a remarkable enhancement of phosphorescent intensity was observed when **354** was treated with sulfite or bisulfite (26-fold and 27-fold enhancement, respectively). Almost no change was observed when **354** was treated with other anions. The detection limits were determined to be 0.24 mM for sulphite and 0.14 mM for bisulphite. Mass spectrometric analysis revealed that the sensing mechanism can be attributed to a reaction at the azo group, resulting in the formation of a **354**–HSO_3^- adduct.

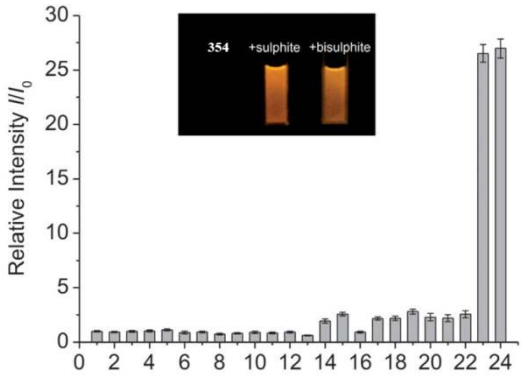

Fig. 79 Relative emission intensity of **354** (10 μM) treated with different anions in a mixed solution of DMSO : HEPES buffer (3 : 7, 10 mM, pH 7.5), λ_{ex} = 405 nm, λ_{em} = 600 nm. Bar (1) control, (2) Cl^-, (3) I^-, (4) CN^-, (5) SCN^-, (6) CO_3^{2-},(7) NO_2^-, (8) NO_3^-, (9) citrate, (10) EDTA, (11) boric acid, (12) OH^-, (13) PO_4^{3-},(14) $S_2O_3^{2-}$, (15) S^{2-}, (16) H_2O_2, (17) ascorbic acid, (18) Cys, (19) Hcy, (20) GSH, (21) DTT, (22) BME, (23) SO_3^{2-} and (24) HSO_3^-. Reproduced with permission from ref. 370. Copyright 2013 The Royal Society of Chemistry.

Intramolecular energy transfer in the hetro-dinuclear Ru(II)−Os(II) complexes **34** and **35** has been discussed in section **2.2.4**. It is also worth noting that both these complexes can be used as a probe for sensing F^-, CN^- and AcO^- anions.[126] The UV-vis absorption and the emission spectra of **34** and **35** red-shift in the presence of F^-, CN^- and AcO^-. Spectrophotometric titrations suggested that these anions induce deprotonation of the imidazole NH group, which is consistent with ^{1}H NMR results showing that the intensity of the NH signal gradually decreased with the addition of F^-.

As discussed in section **3.1.1.2**, dinuclear Ir(III) complex **116** showed a specific response towards F^- *via* both OPEP and TPEP processes.[198]

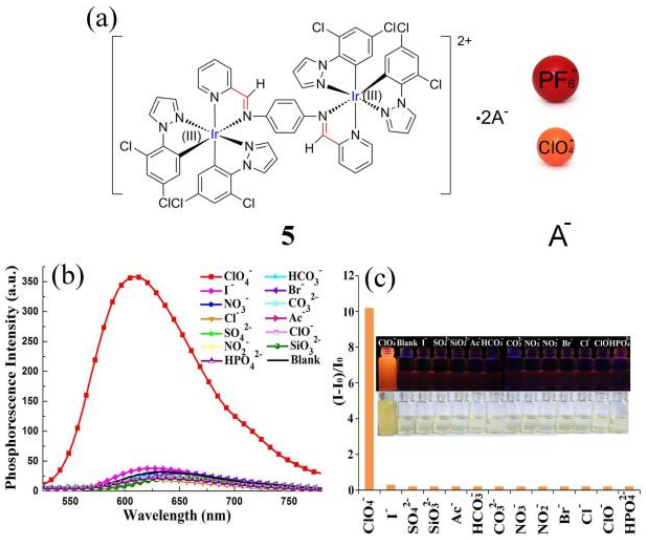

Fig. 80 (a) Chemical structure of complexes **5**·2PF_6 and **5**·2ClO_4; (b) phosphorescence spectra of **5**·2PF_6 (10 μM) in the presence of different anions (15 equiv.) in 10 mM HEPES buffer (CH_3CN : H_2O, 1 : 4, v/v); (c) the corresponding phosphorescence variations of **5**·2PF_6. Inset: Photographs of **5**·2PF_6 with different anions (15 equiv.) under UV lamp irradiation (top) and sunlight (bottom). Reproduced with permission from ref. 85. Copyright 2015 The Royal Society of Chemistry.

In 2015, we reported a rapid, highly selective ''turn-on'' phosphorescent probe for sensing ClO_4^- anions in aqueous media and living cells by using a novel AIPE-active dinuclear Ir(III) complex **5**•2PF_6.[85] As shown in Fig. 80, complex **5**•2PF_6 essentially showed faint emission in the HEPES buffer (10 mM in CH_3CN/H_2O, 1:4, v/v, pH 7.4) with a short decay time (0.02 μs). However, upon addition of different anions and shaking the sample by hand for a few seconds, complex **5**•2PF_6 responds specifically toward ClO_4^- with turn-on phosphorescence with a long decay time (0.24 μs) under UV excitation. The detection limit for ClO_4^- was as low as 0.05 ppm. Importantly, under sunlight, the change in the solution from clear to turbid can be easily observed by naked eyes in a few seconds, which provides a convenient strategy for the sensing of anions. Transmission electron microscopy (TEM) results revealed that nanoaggregates gradually increased in size with the addition of more ClO_4^- (Fig. 81). ^{1}H NMR and MALDI-TOF negative-ion mass spectra indicated that partial anion exchange has occurred from PF_6^- to ClO_4^-. X-ray crystal structure analysis revealed that **5**•2ClO_4 has a more rigid structure compared with **5**•2PF_6 which may affect the solubility of the complexes, and induce aggregation in the solvent. Also the increased rigidity of **5**•2ClO_4 is responsible for the enhanced phosphorescence. To the best of our knowledge, this represented the first example of anion sensing based on AIPE. Further work is needed to determine if this "anion-exchange induced AIPE" process is a general strategy for the selective phosphorescence-based detection of anions.

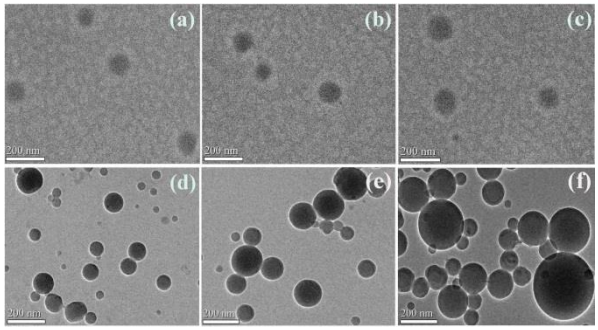

Fig. 81 TEM images of nanoparticles obtained from anion titration experiments of **5**•2PF_6 (10 μM) with (a) blank; (b) 10 equiv. HPO_4^{2-}; (c) 10 equiv. I^-; (d) 3 equiv. ClO_4^-; (e) 5 equiv. ClO_4^-; (f) 10 equiv. ClO_4^- in 10 mM HEPES buffer (CH_3CN:H_2O, 1:4, v/v). Reproduced with permission from ref. 85. Copyright 2015 The Royal Society of Chemistry.

5.1.3 Phosphorescent chemosensors for explosives

In the 21st century, the security of human society has been seriously threatened by an increased frequency of terrorist bomb attacks and the use of land-mines. Consequently, rapid and highly effective detection of explosives has become an issue of paramount importance.[371-374] Photoluminescence detection of explosives by using organic fluorescent molecules[375-377] and phosphorescent transition metal complexes[378, 379] has attracted considerable attention owing to their rapid response time, low cost, and high selectivity and sensitivity. However, both fluorescent and phosphorescent materials usually suffer from ACQ, which limits their practical applications at high concentrations or in aggregated states. Therefore, AIE or AIEE-active phosphorescent materials with highly efficient emission in the aggregated and solid states are ideal candidates for the detection of explosives, in comparison with ACQ-active chromophores.

In 2017, two di- and trinuclear AIEE-active cationic Ir(III) complexes **355** and **356** (Fig. 82a) were synthesized by our group for the rapid, highly selective and sensitive sensing of 2,4,6-trinitrophenol (TNP) which shows enhanced explosive power compared with that of well-known 2,4,6-trinitrotoluene (TNT).[86] Indeed, the selective sensing of TNP among other nitro-aromatic explosives is a challenge owing to their similar electron affinities.[380] Both complexes **355** and **356** showed an emission peak at around 571 nm in the pure CH_3CN solution (Fig. 82b) with low PLQYs of 0.062 and 0.041, respectively. However, the obviously enhanced emission which was observed in mixed CH_3CN/H_2O solution (v/v = 1:9) with higher PLQYs of 0.20 and 0.088, respectively, identified both complexes are AIEE materials. Taking advantage of this AIEE behaviour in aqueous solution, both complexes exhibited a specific response to TNP with phosphorescence quenching, whereas no quenching was observed upon the addition of other nitro-explosives. The Stern–Volmer (SV) plots (Fig. 83) were used to analyze the luminescence quenching efficiency, and the estimated K_{sv} values for **355** and **356** are 49749 M^{-1} and 96178 M^{-1}, respectively, which are among the highest values reported for luminescent sensors.[375, 379, 381, 382] The detection limits for **355** and **356** as phosphorescent sensors for TNP are 0.51 and 0.39 μM, respectively. All the above results demonstrated that AIEE-active complexes can be highly selective and sensitive detectors of TNP in aqueous solution. Since the LUMO energy of **355** and **356** (−2.43 eV) is higher than that of TNP (−3.89 eV), the electron transfer may occur from the higher energy LUMOs of **355** and **356** to the lower energy LUMO of TNP. It is worth noting that compared to the reported AIE- or AIEE-active mononuclear phosphorescence Ir(III) complexes used for detection of TNP,[379, 381, 382] dinuclear complexes **355** and trinuclear **356** exhibit lower LUMO levels due to their more conjugated structures. This reduced LUMO level is closer to the LUMO level of TNP, but is lower than other nitroaromatic explosives, which may facilitate highly efficient selectivity for the detection of TNP. Furthermore, in aqueous media, strong electrostatic interactions can be formed between ionized TNP with a negative charge and cationic complexes **355** and **356**. Therefore, the quenching mechanism of these complexes towards TNP is due to a combination of strong electrostatic interactions and efficient electron transfer processes.

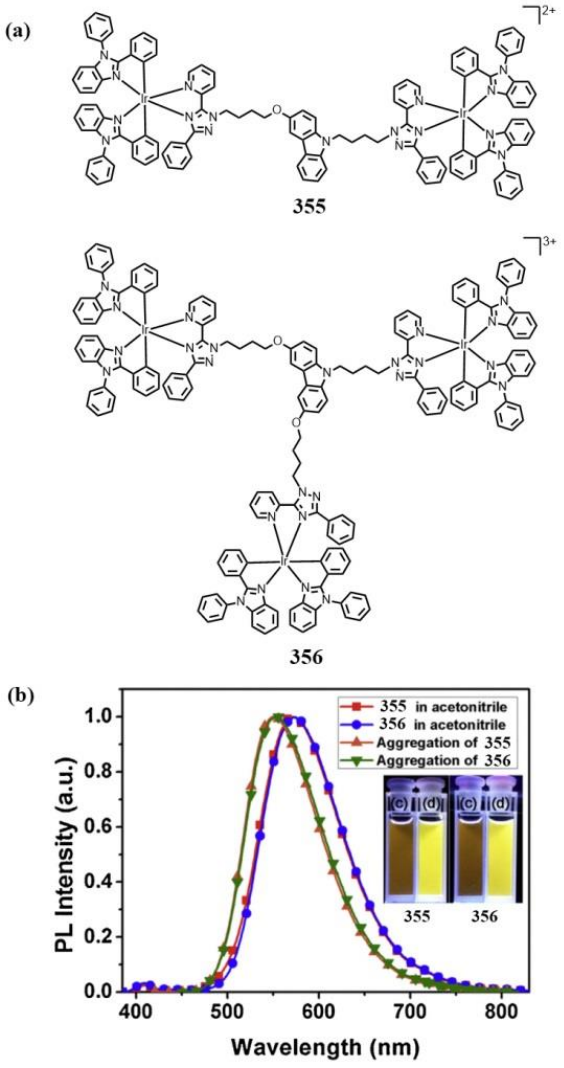

Fig. 82 (a) The chemical structures of complexes **355** and **356**. (b) The emission spectra of **355** and **356** in CH_3CN and CH_3CN/H_2O mixtures (v/v = 1:9). Inset: emission images of

355 (left) and **356** (right) in (c) CH_3CN and (d) CH_3CN/H_2O mixtures (v/v = 1:9). Reproduced with permission from ref. 86. Copyright 2017 Elsevier.

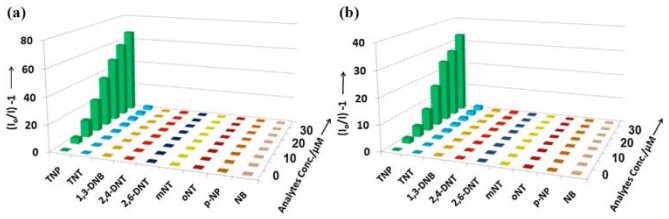

Fig. 83 Stern-Volmer plots of nitro compounds on the emission intensity of (a) **355** and (b) **356** in CH_3CN/H_2O mixtures (v/v = 1:9). Reproduced with permission from ref. 86. Copyright 2017 Elsevier.

In summary, phosphorescent sensors based on di- or multi-nuclear transition metal complexes have significant potential advantages over mononuclear complexes, such as: 1) Deep-red emission is easily obtained by introduction of a longer conjugated bridging ligand in the bimetallic complexes;[72] this is a great advantage in biological sensing. 2) "Turn-off" sensors usually suffer from limited sensitivity due to competing luminescence quenching by heavy metal ions.[383] Therefore, "turn-on" sensors are highly desired. Dinuclear metal complexes are good candidates in this regard, because most dinuclear complexes have lower emission efficiency due to the intramolecular energy transfer from the luminescent ^{3}MLCT state to the bridging ligand-centerd excited state which is less emissive.[72] However, upon addition of analytes, enhanced emission may be observed due to the new electronic structure of the complex that is induced by a strong interaction between the bridging ligand and the analyte. 3) Highly efficient detection of analytes in aqueous solution or solid state, rather than in organic solvent, is highly desired. Recently, luminescent detection of analytes by AIE or AIEE materials has become popular because of their highly efficient luminescence in aqueous solution, and even in the solid state through the formation of aggregates.[373, 381, 382, 384] In principle, AIE or AIEE materials can be easily obtained by designing new di- or multi-nuclear complexes bearing Schiff-base or flexible chain-type bridging ligands.[50, 85, 86, 109-111]

5.2 Biosensors

Luminescent imaging or sensing of biomolecules and living cells is of great significance in facilitating the study of biological processes in real time.[385, 386] Phosphorescent transition metal complexes have attracted much attention in applications such as O_2 sensing, mitochondrial imaging and tracking, and DNA imaging and sensing,[349, 387-390] due to the excellent photophysical properties of the complexes, such as: 1) Large Stokes shifts that reduce the excitation beam and inner filter effects. 2) Long excited lifetimes that can effectively discriminate the long-lived imaging signals from the short-lived background autofluorescence. 3) Synthetic versatility to optimise photochemical and physicochemical stability. 4) Inherent triplet excited state phosphorescent emission could provide excellent sensitivity to molecular dioxygen, enabling hypoxia imaging.[391-393] In this section, the key advances in phosphorescent biosensors by employing dinuclear transition metal complexes are introduced.

5.2.1 O_2 probes

The quantitative determination of oxygen concentration is of critical value for life sciences and environmental sciences.[394-396] The basis of oxygen sensing is *via* phosphorescence quenching which occurs by energy transfer from the triplet excited state of the phosphorescent chromophore to the triplet ground state of molecular O_2.[390, 397, 398] Phosphorescent complexes such as Ir(III), Ru(II), Pt(II) and Pd(II) have been widely studied for O_2 sensing due to their high quantum yield (Φ), long decay lifetime, good solubility, and high stability.[395, 396] However, studies on bimetallic complexes for the sensing of O_2 are very rare. This is surprising as compared with mononuclear complexes, bimetallic systems have a great advantage for O_2 sensing in living cells due to the relative ease of obtaining deep-red emission.[72] It is well known that the lower energy deep-red or near-infrared emission is highly desirable in biological applications for minimizing photodamage to biological samples.[399]

Recently, Zhao's group synthesized the red-emitting dinuclear Ir(III) complex **357** bearing a 2-pyrimidine-benzimidazole bridging ligand (Fig. 84a).[400] The mono-cationic structure of **357** is beneficial for enhanced emission, compared to the low quantum yields of most dicationic Ir complexes. Complex **357** showed red phosphorescence in dichloromethane solution with peaks at 619 and 659 nm, which are red-shifted by 85 nm relative to the corresponding monoiridium complex. DFT calculations indicated that the emission of **357** originated mainly from the ^{3}ILCT state located on the bridging ligand. Ir(III) complexes with ^{3}ILCT character are known to possess longer phosphorescent lifetimes and better oxygen sensitivity than those with ^{3}MLCT character.[401] As shown in Fig. 84b, the emission intensity as well as the lifetime of **357** gradually decreased with the incremental increase of O_2 concentrations. The Stern–Volmer plots with excitation at 405 nm showed a linear relationship between O_2 concentration and I_0/I (I = the emission intensity, and I_0 = emission intensity without oxygen) indicating that **357** can be used as a phosphorescent probe for the quantitative determination of oxygen. Importantly, intracellular O_2 levels in HeLa cells were successfully detected by the probe signals based on both emission intensity and phosphorescence lifetime using time-resolved luminescence imaging (TRLI) techniques. As shown in Fig. 85, the phosphorescence intensity of **357** gradually increased as the O_2 concentration dropped from 21 to 2.5%, and was accompanied by an enhanced lifetime. These results suggest that new red-emitting dinuclear Ir(III) complexes are a a promising strategy for obtaining efficient oxygen probes.

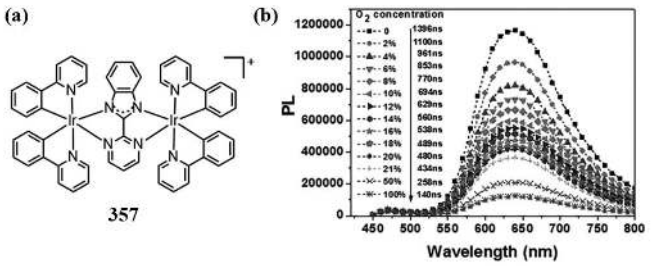

Fig. 84 (a) The chemical structure of complex **357**. (b) Emission spectra of **357** (10 mM) at different oxygen concentrations in DMSO (λ_{ex} = 365 nm). Reproduced with permission from ref. 400. Copyright 2018 Wiley-VCH.

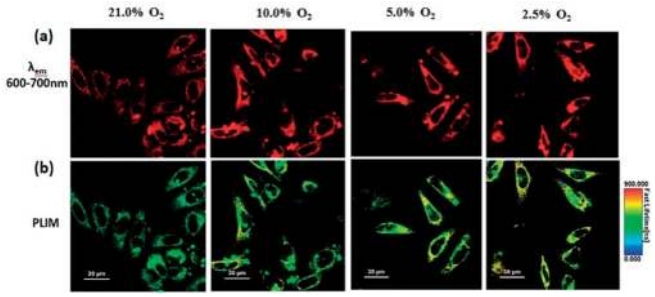

Fig. 85 (a) Confocal luminescence images and (b) photoluminescence-lifetime images of HeLa cells incubated with **357** (10 μM) at different oxygen concentrations. (b) Reproduced with permission from ref. 400. Copyright 2018 Wiley-VCH.

Most reports of O_2 sensing in living cells are focused on probes in the cytoplasm. There is a strong need for probes which can function in the key organelles.[398, 402, 403] For example, mitochondria are one of the prime targets for O_2 sensing as they are the centers of oxygen metabolism, which directly reflect the cell's health. In 2014, a binuclear Ru(II) probe **358** which is bridged across a mitochondrial penetrating peptide (MPP) (Fig. 86) was developed by Keyes's group.[404] Complex **358** exhibited excellent cell permeability with rapid, irreversible uptake, and accumulation in the mitochondria. The cytotoxicity of **358** is moderate in the dark, and more than 40% of cells remain viable over 24 h under conditions used for imaging. As expected, the change in O_2 concentration within live HeLa cells was successfully monitored by complex **358**.

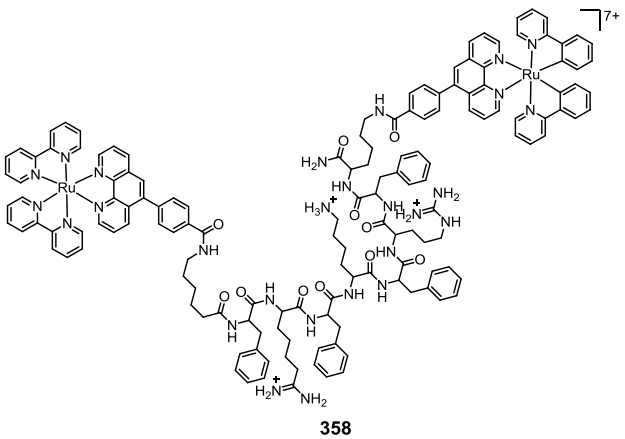

Fig. 86 The chemical structure of complex **358**.

5.2.2 Mitochondrial probes

Mitochondria are well known as the powerhouses of the cell. Tracking mitochondrial dynamics is critical for understanding their physiological and pathological processes.[405-407] Commercial mitochondrial fluorescent dyes are not suitable for this purpose because due to their poor photostabilities they are unable to monitor life processes over a long time-frame.[408] Development of phosphorescent dyes is thus highly desired. In this context complex **358** (see section **5.2.1** can be used for mitochondrial imaging. Complexes **359**–**364** (Fig. 87) reported by Pisani *et al.* in 2010 provided the first examples of dinuclear species acting as delocalised lipophilic cations that preferentially accumulated in the mitochondria.[409] The lipophilicity of the complexes was found to increase with the increasing number of methylene groups, thereby allowing greater cellular accumulation. Concomitantly, the cytotoxicity of the complexes increased with the increasing number of methylene groups.

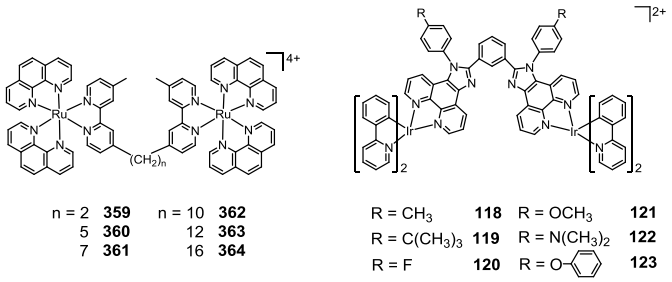

Fig. 87 The chemical structures of complexes **359**–**364** (left) and **118**–**123** (right).

As mentioned in **3.1.1.2**, the dinuclear complexes **118**–**123** serve as mitochondrial imaging dyes *via* a clathrin-mediated endocytotic pathway, without requiring prior membrane permeabilization or replacement of the culture medium.[87] More importantly, **119** and **122** were further developed for tracking mitochondrial morphological changes during the early stages of apoptosis. As shown in Fig. 88, upon exposure to cyanide *m*-chlorophenylhydrazone (CCCP), the reticulum-like mitochondria were gradually transformed to small and dispersed fragments, which is consistent with previous reports. CCCP acts as an uncoupler that causes rapid acidification of mitochondria and reduces the ability of ATP synthase, resulting in the decrease of the mitochondrial membrane potential.

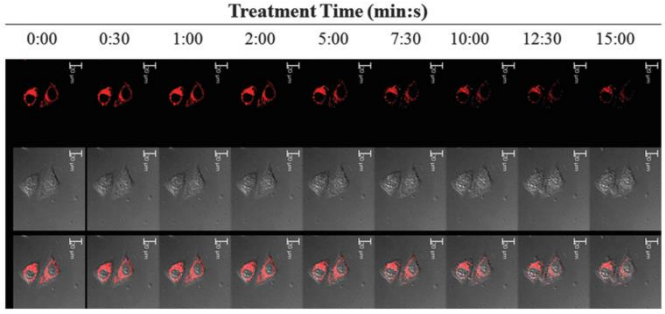

Fig. 88 Phosphorescence images of CCCP (20 mM) treated living HeLa cells stained with 5 μM of **119**, with increasing scan times (the scan time is shown in the upper panel). The

upper panel is the luminescence images of **119**. The middle panels are images of the bright field. The lower panels are the merged images. Excitation wavelength: 405 nm; emission filter: 580 ± 10 nm. Reproduced with permission from ref. 87. Copyright 2015 The Royal Society of Chemistry.

5.2.3 DNA probes

The development of optical probes for DNA within the cell nucleus is of great importance for understanding the role of DNA in genetic disease and tumorgenesis.[410, 411] In 1990, Barton *et al*. reported the first case of a mononuclear Ru(II) complex **365** (Fig. 89) as a molecular "light switch" for DNA structures *in vitro*. No photoluminescence was observed in aqueous solution at ambient temperatures, but emission was dramatically enhanced in the presence of DNA, referred to as the "light-switch" effect, owing to intercalation between the Ru(II) complex and DNA.[412] Since then, numerous charged mononuclear Ru(II) complexes have been developed to display excellent water solubility and to bind to DNA with high affinities through an intercalative mechanism.[383, 413--417] In 1993, Carson *et al*. reported the first cases of dinuclear Ru(II) complexes with high binding affinity for DNA: they also described that the binding affinity can be highly dependent on the ancillary ligands of the metal centers.[415] Since then, much effort has been devoted in the development of dinuclear Ru(II) complex systems for DNA binding.[101-108, 418, 419] Interestingly, in contrary to the mononuclear Ru(II) complex system, most dinuclear Ru(II) complexes bind to DNA *via* a groove binding mechanism: an initial groove-bound and a final intercalated geometry.[24] For example, Lincoln and Nordén found that the complex **3** rearranges from a groove-binding to an intercalative geometry that is reached by threading one of the $Ru(phen)_2$ moieties through the DNA duplex, thereby intercalating one of the bridging dppz ligands between the DNA base pairs and thus placing one metal center in each groove.[102] Lincoln, Nordén and colleagues also reported a novel type of chiral bis-intercalating Ru(II) complex **366** with extremely high binding affinity ($K>10^8$ M^{-1}) for DNA *via* a remarkable bis-intercalative binding mode, that is around two orders of magnitude higher than that of the mononuclear complex **367**.[413, 417] The binding ability with duplex and quadruplex DNA of dinuclear Ru(II) complexes **368**–**370** (Fig. 90) was firstly investigated by Thomas' group in 2006.[420] Interestingly, both complexes **368** and **369** exhibited enhanced binding ability for quadruplex compared to duplex DNA, which is accompanied by a distinctive "quadruplex light-switch" effect: *i.e*., highly enhanced and sufficiently blue-shifted emission away from the normal duplex phenomenon. This system showed unique advantages as *in vivo* quadruplex probes. In 2008, Lutterman *et al.* showed that intercalation was not required for **369** to act as a molecular "light switch" for DNA based on relative viscosity measurements.[421]

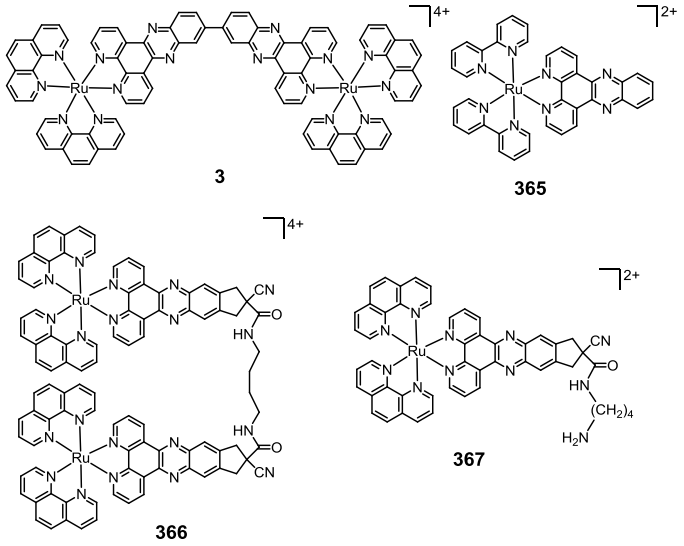

Fig. 89 The chemical structures of complexes **3**, **365**–**367**.

Although numerous probes for DNA have been developed *in vitro*, studies involving direct imaging of DNA in living cells are still rare, and are limited by the poor membrane permeability of probe molecules.[403, 422, 423] In 2009, dinuclear complex **368** was used for directly imaging nuclear DNA of living cells by Gill and co-workers.[424] The inherent hydrophilicity and high charge of **368** would imply that the molecule will not freely diffuse across the cell membrane. Therefore, the mechanism of cellular uptake of the complex was investigated by transmission electron microscopy. As shown in Fig. 91a, after incubating MCF-7 cells with solutions of **368**, it was found that **368** mainly located within the nucleus of the MCF-7 cells with high concentration. A relatively lower concentration of **368** is located throughout the cell cytosol. Remarkably, as highlighted in Fig. 91b, the absence of **368** from endosomal and lysosomal compartments confirmed that cellular uptake of **368** is *via* active transport rather than an endocytotic pathway. **368** has been investigated as a luminescent probe for DNA. As shown in Fig. 91c, **368** enables visualization of characteristic structural changes in nuclear DNA as cells progress through the cell cycle.

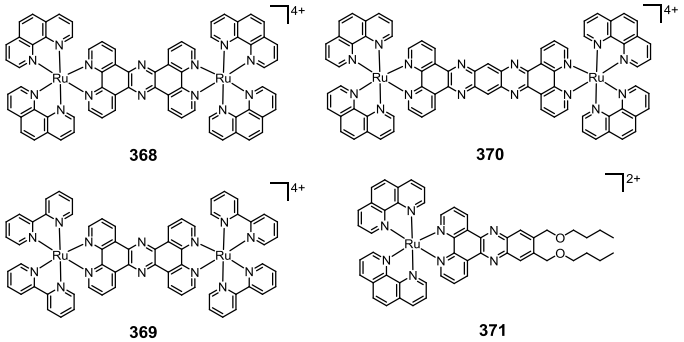

Fig. 90 The chemical structures of complexes **368**–**371**.

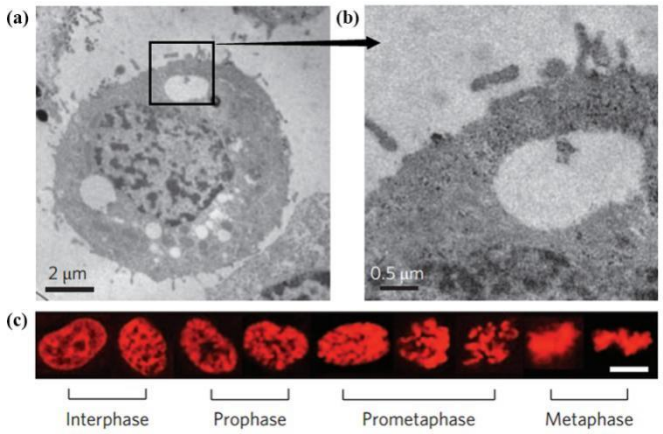

Fig. 91 (a) TEM micrograph showing the cellular uptake of **368** by MCF-7 cells (500 mM, 1 h). (b) The absence of **368** within an intracellular vesicle (large scale). (c) Asynchronous cell imaging shows mitotic cells stained by **368** visualizing chromosome aggregation through progression of mitosis. Reproduced with permission from ref. 424. Copyright 2009 Nature Publishing Group.

As emerging "functional imaging" techniques, fluorescence (FLIM) and phosphorescence (PLIM) lifetime imaging microscopy make it possible to monitor the changes of some specific biologically relevant microenvironmental parameters and DNA transformations characteristic of different cell cycle stages *via* reporting of lifetime.[425] Particularly, PLIM presents the key advantage over FLIM of a dramatic increase in contrast and probe selectivity due to the possibility of rejecting scattered excitation light and short-lived autofluorescence *via* long-lived luminescent labeling ($\tau > 100$ ns).[426] By far the majority of studies in this field involve PLIM for sensing of parameters such as pH and biological oxygen, however, the sensing of biologically important molecules (such as DNA and RNA) is still very rare.[427] In 2011, the Δ- and Λ-enantiomers of mononuclear Ru(II) complex **371** (Fig. 90) wer presented to investigate the diastereomeric interaction inside the cell and cell nucleus in fixed and live CHO cells by confocal laser scanning microscopy (CLSM) and PLIM techniques by Svensson *et al.*[428] CLSM images indicated that the Δ-enantiomer showed brighter emission in the nucleus and weaker emission in the nucleolus than the Λ-enantiomer. Since both enantiomers exhibited similar affinity to DNA, such a significant difference in the cell staining patterns was attributed to the higher quantum yield of the Δ-enantiomer over that of the Λ-enantiomer when bound to DNA. Live cell PLIM and intense imaging indicated that the cell membrane was impermeable to both enantiomers unless photoactivation aided the uptake. Upon photoactivated internalization, the Δ-enantiomer exhibited the most intense emission with the longest lifetime in the nuclei, while the Λ-enantiomer showed more intense emission in the cytoplasm but longer emission lifetime in the nuclei.

In 2014, PLIM technology was exploited for DNA targeting by Thomas's group.[88] This process is independent of probe concentration, whilst providing information on the micro-environment of the probe itself. Furthermore, the large timescale of PLIM, within hundreds of nanoseconds to microseconds, can avoid common problems of biomolecular autofluorescence. In this work, dinuclear complexes **369** and **370** were found to show two-photon absorption for the first time. It is well known that the lower energy two-photon absorption can facilitate luminescence-based deep tissue imaging. Thus, by combining the advantages of longer phosphorescent lifetime and two-photon absorption **369** and **370** were exploited as probes for cellular DNA. As shown in Fig. 92, 2P-PLIM images presented luminescence decay kinetics from live MCF-7 cells labeled with **369**. The emission predominantly originated from the cell nuclei with a lifetime of 165 ± 16 ns (left). A similar emission lifetime from the nucleus (176 ± 11 ns) was observed when focusing upon a single cell (right). The capability of **369** and **370** to act as high-resolution 2P-PLIM DNA stains was further studied. Fig. 93 shows 2P-PLIM (left) and confocal (right) imaging of HeLa metaphase spreads labeled with **369**. Similar PLIM intensity and lifetime images of the chromosomes are observed from both the metaphase and interphase nuclei (182 ± 12 ns and 182 ± 4 ns, respectively). Furthermore, the observed small region of short-lived emission (Fig. 93, location c) was attributed to a precipitate of **369**. This work indicates that 2P-PLIM for DNA targeting may be a promising probe for specific sub-cellular targets even in deep tissue in the future.

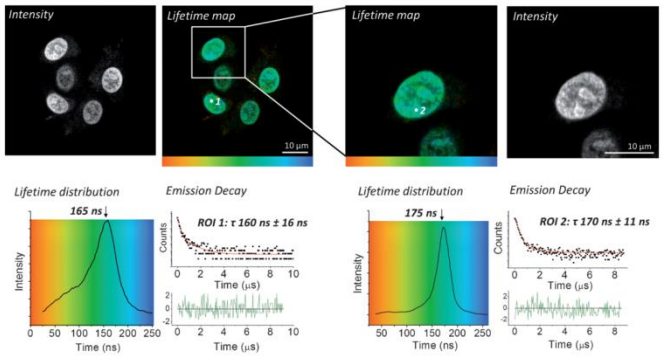

Fig. 92 PLIM imaging of live MCF-7 cells pretreated with complex **369** (500 mm, 1 h, serum-free media). Reproduced with permission from ref. 88. Copyright 2014 Wiley-VCH.

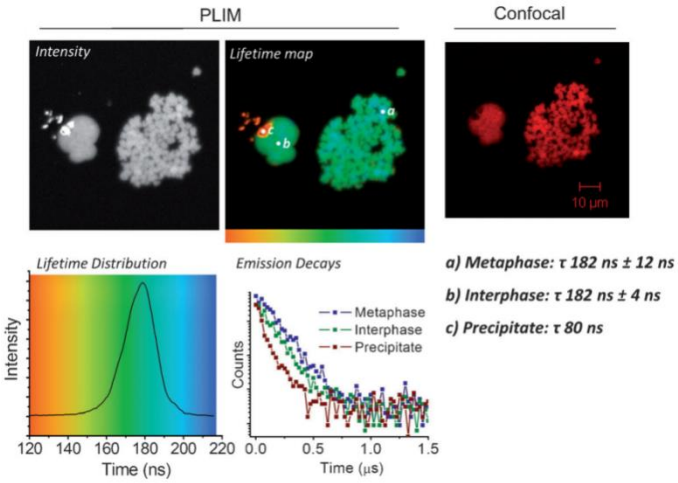

Fig. 93 2P-PLIM (left) and confocal (right) imaging of HeLa metaphase spreads labeled with **369**. Reproduced with permission from ref. 88. Copyright 2014 Wiley-VCH.

In 2014, two new dinuclear Ir(III)–Ru(II) complexes **372** and **373** (Fig. 94) which function as luminescent nuclear DNA-imaging agents for confocal microscopy were presented by Thomas's group.[429] Complexes **372** and **373** showed unstructured emission with peaks at 660 and 675 nm, respectively in acetonitrile solution, which arise from a Ru(II)-based ^{3}MLCT state. Cellular-imaging experiments using **372** and **373** were carried out. The key findings are: 1) Both complexes exhibited superior cellular uptake properties in comparison with Ru(II)–Ru(II) analogues, which is due to the lower charge of the Ir(III)–Ru(II) system, and hence increased lipophilicity. 2) Fluorinated derivative **373** exhibited rapid and enhanced nuclear staining in HeLa cells compared to **372** (Fig. 95). This indicates that fluorination can promote cellular uptake of transition-metal bioprobes.

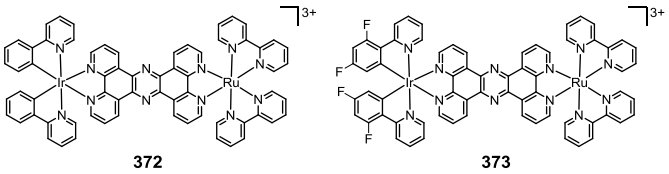

Fig. 94 The chemical structures of complexes **372** and **373**.

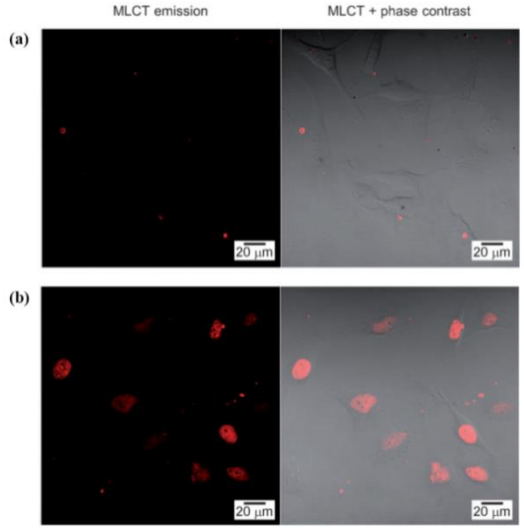

Fig. 95 Relative rate of cellular uptake of **372** (a) and **373** (b) (10 mm, 80 m in serum-free media) by HeLa cells, as assessed by MLCT emission. Reproduced with permission from ref. 429. Copyright 2014 Wiley-VCH.

In 2017, two new dinuclear Ir(III) complexes **374** and **375** (Fig. 96) were reported by Kim's group.[430] Both complexes exhibited an appreciable affinity for single-stranded DNA and double-stranded DNA *in vitro*. Specifically, **374** displayed a unique G-quadruplex DNA binding affinity with larger enhancement of emission, but **375** did not. The reason was attributed to the more extended planar structure in **374** that more easily intercalates into G-quadruplexes. However, cellular imaging experiments indicated that cell nucleus stains were not observed for both complexes, which were localized only in the cytosol of HeLa cells.

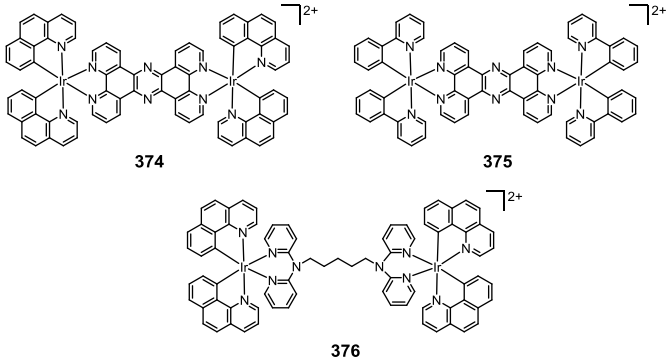

Fig. 96 The chemical structures of complexes **374**–**376**.

In contrast to the rigid, planar and hydrophobic linker in **374** and **375**, Liu *et al*. reported the dinuclear Ir(III) complex **376** (Fig. 96) with a flexible pentamethylene linker. **376** showed specific binding to G-quadruplex DNA *in vitro* due to the strong electrostatic interaction between the complex and G-quadruplex DNA.[431]

Specific recognition of mismatched DNA is of great importance for cancer diagnosis and therapy, since DNA mismatches are associated with oncogenic transformation.[432-434] In 2016, Che's group reported a series of luminescent mono- and dinuclear Pt(II) complexes with out-of-plane bulky ancillary ligands. These complexes showed a specific binding affinity towards intracellular mismatched DNA.[387] As shown in Fig. 97, dinuclear Pt(II) complex **377** showed faint emission in the presence of well-matched DNA of HCT116 cells, whereas greatly enhanced emission was observed in the presence of mismatched DNA of HCT116N cells. This difference was attributed to the specific binding between the complex and mismatched DNA *via* cooperative π-stacking and a groove binding interaction (Fig. 97a), since the mismatched sites possess larger binding pockets. Pt(II) complexes with out-of-plane bulky ancillary ligands are, therefore, promising candidates for cancer diagnosis *via* simple emission spectroscopy measurements.

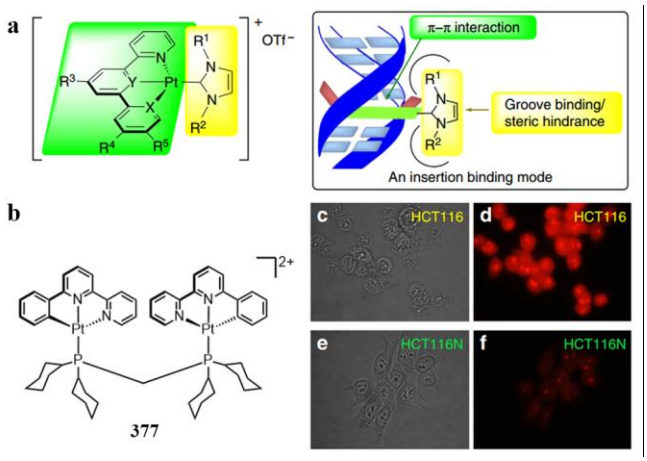

Fig. 97 (a) Illustration of a Pt(II) complex for binding mismatched DNA. (b) The chemical structure of complex **377**. Fluorescence microscopy images of HCT116 (d) and HCT116N (f) cells pretreated with digitonin and stained with 10 μM **377**. (c, e) Bright-field images of HCT116 and HCT116N cells, respectively. Reproduced with permission from ref. 387. Copyright 2016 Nature Publishing Group.

In summary, the study of phosphorescent probes for dynamic imaging and monitoring of biomolecules, especially in living cells, is a new research field that is gaining momentum. Generally, the cellular uptake is influenced by the overall charge, size, hydrophobicity and structure of the conjugated moiety of the complex. Dinuclear metal complexes as biosensors show several advantages over their mononuclear counterparts, such as: 1) Ease of obtaining deep-red emission by introduction of a longer conjugated bridging ligand. Red emitters are important for biological sensing in living cells and in deep tissue. 2) Dinuclear complexes usually exhibit better photostability when compared with mononuclear analogues *via* introduction of a bulky conjugated bridge to enhance the coordination strength between the metal center atoms and the bridging ligand. High stability is beneficial for long-time imaging and tracking. 3) Dinuclear metal complexes have been used as a selective probe for DNA by the rational design of symmetric/asymmetric chemical structures of dinuclear complexes to control the different modes of groove binding. Therefore, further developments of new biosensors based on dinuclear complexes are expected.

5.3 Photodynamic therapy

Photodynamic therapy (PDT) is a non-invasive medical technique comprising a photoactivated process to destroy malignant cells *via* the generation of excessive reactive oxygen species (ROS) while sparing the normal tissues. Singlet oxygen ($^1O_2$) as a primary toxic ROS is produced by energy transfer from the triplet excited state of photosensitizers to the ground state of O_2.[435-438] Series of fluorescent porphyrin-based[439] and BODIPY-based[440] photosensitizers have been developed to generate $^1O_2$ for the treatment of cancer cells. However, these kinds of photosensitizers usually suffer from the poor conversion rate of singlet oxygen, and need a long irradiation time which can result in harmful side-effects on human skin. Phosphorescent photosensitizers based on transition metals, such as Ru(II) and Ir(III), are promising candidates for PDT, and they show several advantages compared with fluorescent photosensitizers,[441, 442] such as: 1) Rapid and efficient triplet excited state generation owing to the strong SOC of the complex, which can promote the formation of $^1O_2$. 2) The longer triplet excited lifetimes of complexes is beneficial to the efficient production of $^1O_2$. 3) Deeper tissue-penetrating near-infrared (NIR) light can be obtained *via* specific functionalisation of the chelating ligands and the bridge that surround the metal atoms. Currently, most reported phosphorescent photosensitizers for PDT are focused on mononuclear metal complexes, with only rare examples of dinuclear species.

Recently, a series of dinuclear complexes **378**–**382** (Fig. 98) acting as PDT photosensitizers toward human SK-MEL-28 melanoma cells *in vitro* was reported by Sun's group.[443] The rigid π-conjugated linkers of the complexes served to expand the visible absorption region and to enhance the molar extinction coefficients. The octyl chains were attached to the central fluorene unit to enhance the penetrability of the cell membrane. **378**–**382** exhibited orange−red emission with λ_{max} 580−620 nm. The transient absorption spectra and DFT calculations indicated that triplet states were predominantly $^3\pi,\pi^*$ (centered at the terpyridyl bridging ligand) for **378** (τ = 3.1 μs) and **381** (τ = 48 μs), and ^{3}CT for **379**, **380**, and **382** (τ = 1.7−2.7 μs). The significantly enhanced lifetime of **381** compared to **378** was attributed to the stronger ligand field of the C^N^N ligand that contains the stronger σ-donating 6-phenyl ring, resulting in a large energy separation between shorter lifetime ^{3}CT and longer lifetime $^3\pi,\pi^*$ states. Before studying the PDT effect of **378**–**382** for human SK-MEL-28 melanoma cells, the dark toxicity was investigated. Complexes **379** and **381** exhibited greater dark toxicity than complexes **378**, **380** and **382**. The PDT effects of all the complexes under different visible and red light sources were evaluated. Upon irradiation with red light (625 nm), the photocytotoxicities of all the complexes are very weak and showed no obvious change compared with the cytotoxicity in the dark. However, under visible light all the complexes showed an obvious PDT effect *via* $^1O_2$ generation: The PDT efficiency is in the order **380** > **378** > **381** > **382** > **379**. Thus, **380** with nanomolar photocytotoxicity and the highest phototherapeutic index (PI) of 288 is the most promising photosensitizer for PDT. Cellular imaging experiments of all the complexes, with or without light treatment, were performed to probe the cellular uptake by SK-MEL-28 melanoma cells. As shown in Fig. 99, in the dark only **378** appeared to be readily taken up into the cells. However, upon treatment with visible light (50 J cm^{-2}) excitation, the observed phosphorescence from all five complexes suggested photoactivated cellular uptake. **379** and **381** were located at the cytoplasm and multiple nucleoli; **380** and **382** were distributed throughout the cell, whereas only cellular debris was observed for **378**.

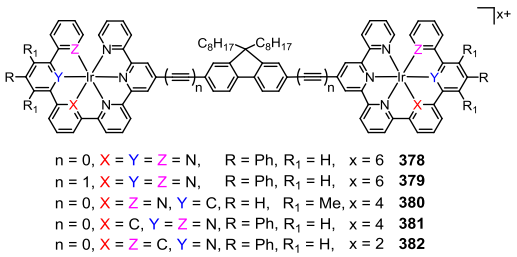

Fig. 98 The chemical structures of complexes **378**–**382**.

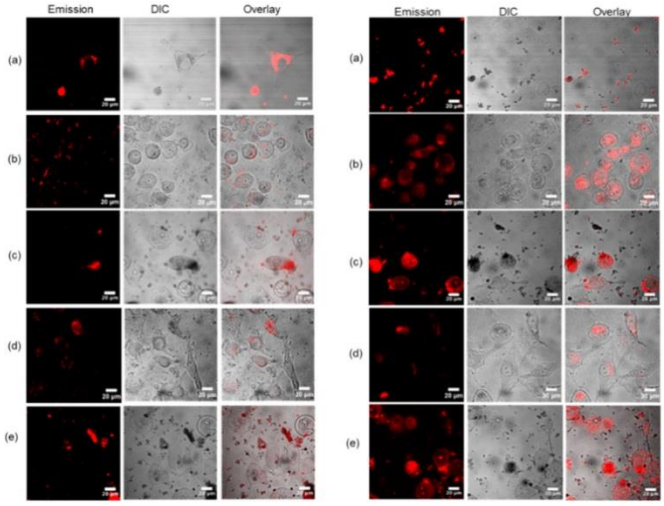

Fig. 99 Confocal luminescence images of SK-MEL-28 cells dosed with **378**–**382** (a–e, 50 μM) in the dark (left) and with visible light (50 J cm^{-2}) (right). Reproduced with permission from ref. 443. Copyright 2018 American Chemical Society.

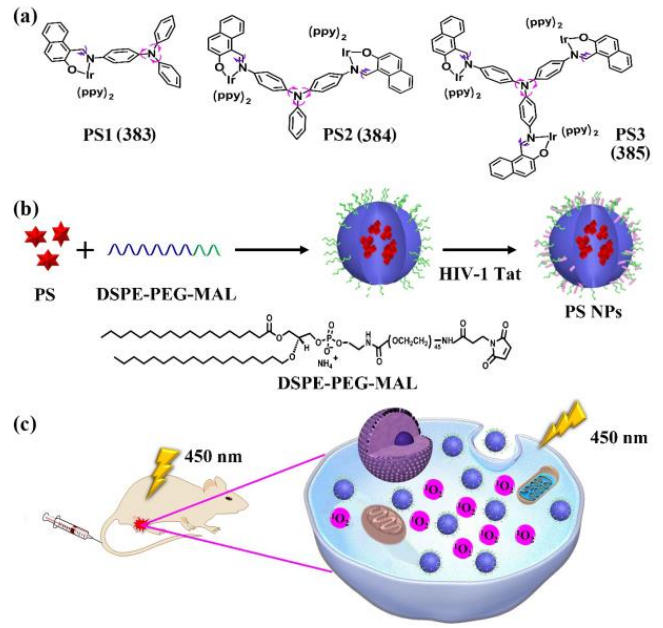

Fig. 100 (a) The chemical structures of PS1 (**383**), PS2 (**384**) and PS3 (**385**). (b) The assembly of NPs; C) Schematic illustration of PS3 NPs as PSs for PDT. Reproduced with permission from ref. 90. Copyright 2018 Wiley-VCH.

More recently, a series of deep-red emissive Ir(III) complexes **383**–**385** with different numbers of iridium centers, and the corresponding nanoparticles (NPs) (Fig. 100a) have been studied as photosensitizers for PDT *in vitro* and *in vivo* by our group.[90] The assembly of NPs is shown in Fig. 100b, comprising the iridium complexes as the core which were encapsulated by a biocompatible 1,2-distearoyl-sn-glycero-3-phosphoethanolamine-*N*-[maleimide(poly(ethyleneglycol))-2000] (DSPE-PEG-MAL), and with the HIV-1 transactivator (RKKRRQRRRC) as the surface functionalization group. HIV-1 Tat is the cell penetrating peptide, which can effectively enhance the cell penetrability of the NPs. Complexes **383**–**385** are AIE materials, which show enhanced emission in water-THF mixtures compared to that in pure THF solutions. In contrast to the relatively weak emission observed from complexes **383**–**385** with PLQYs in the water-THF mixtures of only 11%, 5% and 8%, respectively, their corresponding NPs (NP1-3) showed a remarkable enhancement with PLQYs of 33%, 15% and 35%, respectively, in water solution. The NPs are deep-red emitters with λ_{max} 652 nm, 671 nm and 690 nm, respectively. The $^1O_2$ generation ability was found to increase with the increasing of numbers of Ir centers for both the PSs and the NPs; this was evaluated by measuring the absorbance of indocyanine green (ICG) upon light irradiation. The PDT effect of the PSs **383**–**385** and their derived NPs for HeLa cells *in vitro* were investigated. As shown in Fig. 101A–D, all the NPs showed negligible dark cytotoxicity. However, as expected, all NPs showed strong photocytotoxicity under light irradiation (20 mW cm^{-2}) for 30 min. The photocytotoxicity increased incrementally with the numbers of Ir centers, with NP3 exhibiting the best PDT performance. In contrast to the impressive PDT properties of the NPs, all the PSs exhibited a poor PDT effect. Cellular uptake experiments indicated that NP3 showed significantly stronger emission in comparison with PS3 which was located at the cytoplasm of HeLa cells. Tumor inhibition experiments using NP3 with or without light were carried out *in vivo*. As shown in Fig. 101E and F, in the groups 1, 2 and 3 without either light or NP3, the relative tumor volume increased 8–9 times after 14 days of feeding. In sharp contrast to the groups 1–3, in the group 4, treated with both light and NP3 simultaneously, the tumor volume was significantly reduced, indicating that NP3 is a promising photosensitizer for PDT *in vivo*.

In summary, the development of photosensitizers based on dinuclear or multinuclear complexes for PDT is still a largely unexplored topic. However, this kind of photosensitizer has exhibited better PDT performance compared with their corresponding mononuclear complexes, with clearly increased $^1O_2$ generation ability. The reasons may be attributed to the wider absorption range of multinuclear complexes in the visible light region, and the greater production of triplet excitons which is induced by the increased numbers of Ir centers, accompanied by enhanced spin-orbit coupling.

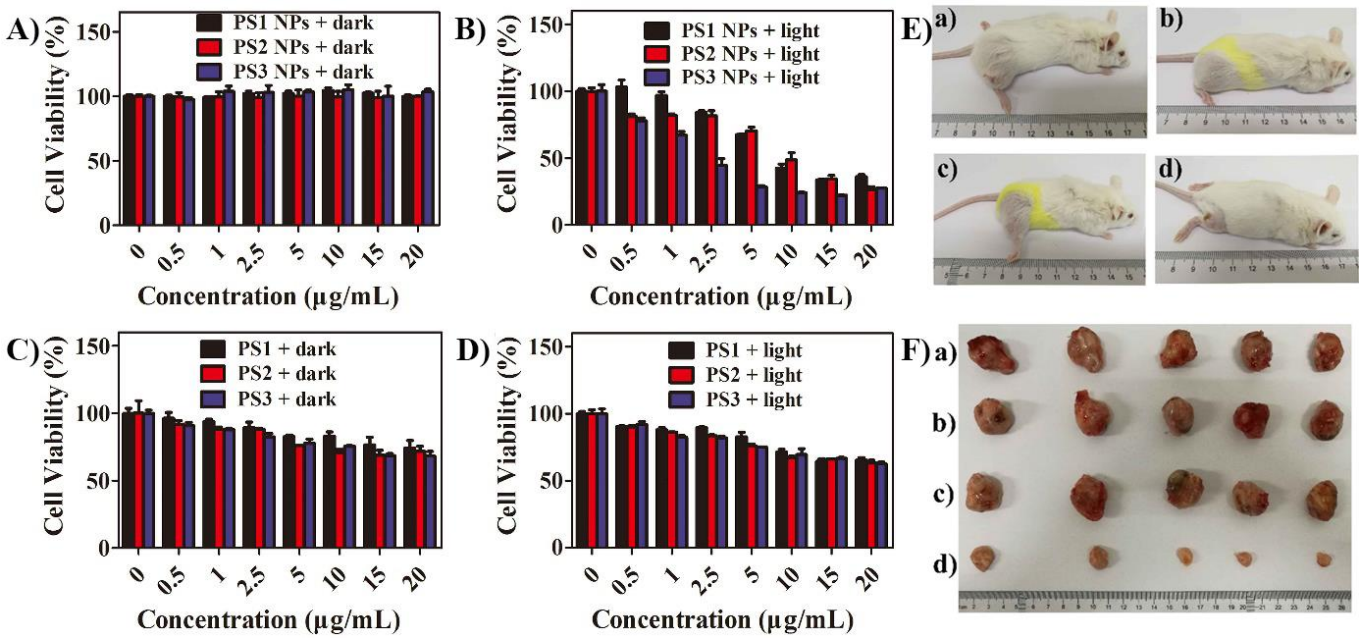

Fig. 101 Cell viability upon treatment with PSs against HeLa cells A, C) under dark and B, D) under light (450 nm, 20 mW cm^{-2}, 30 min). E) Representative images of mice and F) harvested tumors, various groups treated with a) with saline, b) with saline and light, c) with NP3, d) with NP3 and light (100 mg mL^{-1}, 100 μL), light irradiation (450 nm, 200 mW cm^{-2}, 20 min). Reproduced with permission from ref. 90. Copyright 2018 Wiley-VCH.

6. Smart materials

Mechanochromic luminescent (MCL) materials are a class of "smart" materials whose emission colors can be changed when an external force (such as grinding, crushing, rubbing, or extrusion) is applied, leading to either a chemical or a physical structural change.[444, 445] The physical mechanisms of MCL are mainly ascribed to the phase transformations from a crystalline state to a different crystalline state, or from a crystalline state to an amorphous state. These transformations are accompanied by a change in the mode of molecular packing and molecular conformation, which affects the HOMO–LUMO energy levels and consequently alters the luminescent properties. Generally, this force-triggered luminescent change can be reversed and the original emission is restored *via* a recrystallization process when the treated material is heated or exposed to organic solvent/vapour. A variety of MCL materials have been developed, including organic small-molecules,[446-448] metal clusters,[449-451] metal complexes,[54, 452, 453] carbon dots,[454] polymers,[455-457] metal-organic frameworks (MOFs)[53, 458] and perovskites.[459, 460] There is huge potential for MCL materials in applications such as sensors, memory chips and security inks. The development of metal complexes in this context is a significant topic due to their excellent phosphorescent properties. The MCL mechanism in metal complexes is considered to originate from intramolecular conformational folding or twisting, as well as from variations in intermolecular π–π, C–H···π, metal–metal, or hydrogen-bonding interactions.[461-465] In this section, recent advances in mechanochromic dinuclear metal complexes will be discussed.

6.1 Au(I) complexes

In recent years, Ito's group, Liu's group and others have investigated mono- and dinuclear Au(I) complexes with MCL properties.[51, 462, 466-472] The MCL mechanism is mainly attributed to changes in the intra- or intermolecular Au···Au interactions upon application of external force stimuli.

Chem Soc Rev

REVIEW ARTICLE

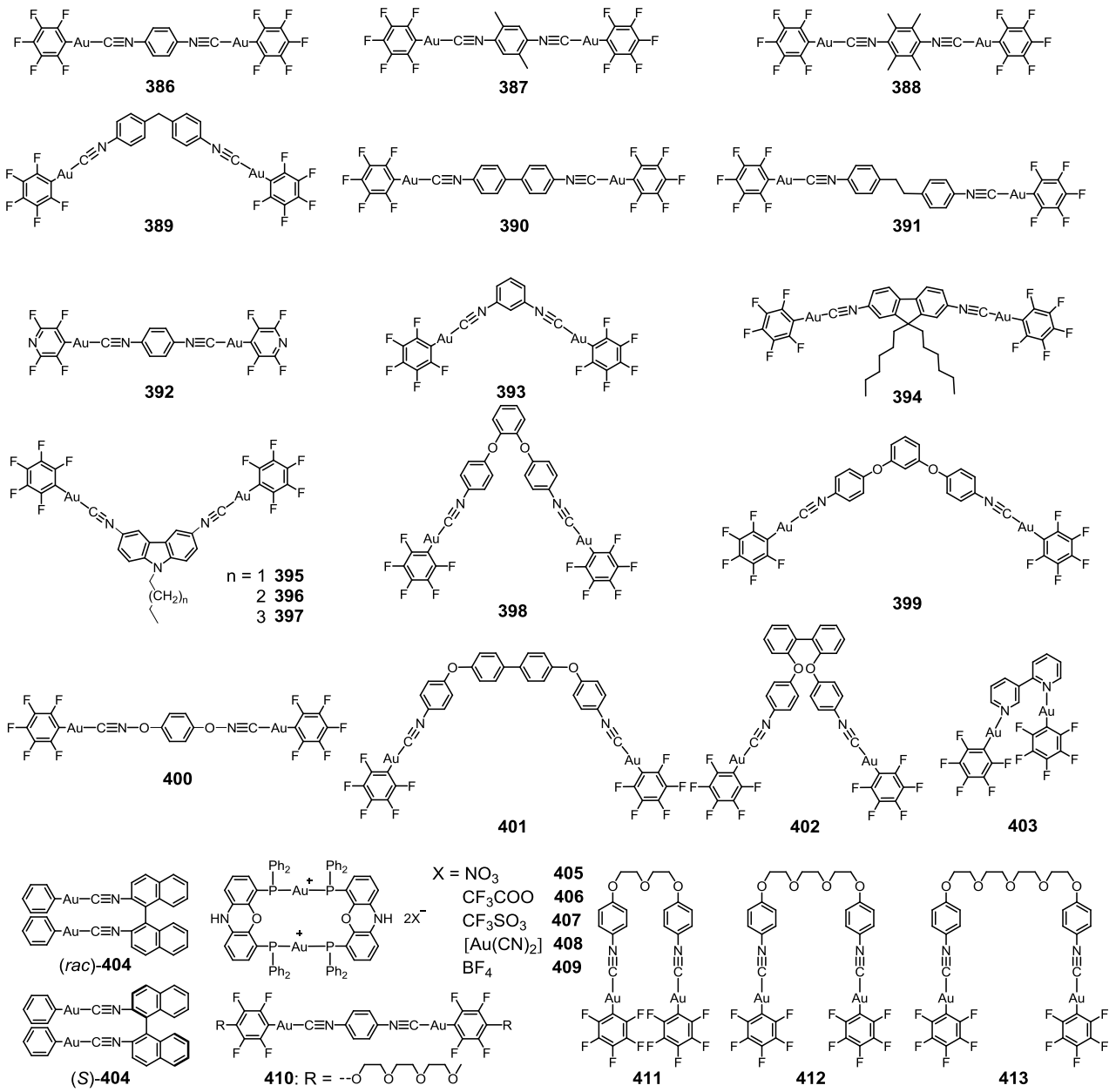

Fig. 102 The chemical structures of dinuclear Au(I) complexes.

In 2008, Ito *et al.* reported a dinuclear Au(I) complex $[(C_6F_5Au)_2(\mu$-1,4-diisocyanobenzene)] (**386**) which showed intense blue emission in the solid state.[473] As shown in Fig. 103, upon gentle grinding of **386**, the emission color changed to yellow. After treatment of the ground **386** with drops of dichloromethane, the emission reverted to the original blue color, demonstrating reversible MCL behaviour. XRD results (Fig. 104b) indicated that **386** undergoes a phase transformation from a microcrystalline state to a metastable amorphous state during the grinding process. The IR spectrum (Fig. 104a) indicated that upon grinding obvious changes occur in the coordination mode of the isocyanide ligand to the Au(I) atom, giving rise to the red-shifted emission. The crystalline structure of **386** is shown in Fig. 104c; the shortest Au···Au distance of

5.19 Å is far beyond the range of significant aurophilic bonding (2.7 Å to 3.3 Å). However, upon grinding, it was considered that the aurophilic interaction is enhanced *via* rearrangement to molecular stacking in the amorphous phase, leading to the observed yellow emission.

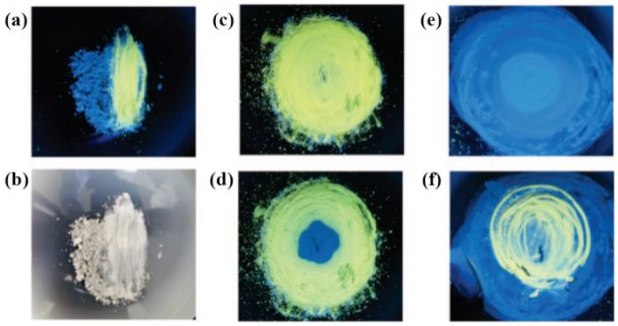

Fig. 103 Photographs showing **386** on an agate mortar under UV irradiation with black light (365 nm): (a) after grinding the right-half with a pestle, (b) the same sample under ambient light, (c) entirely ground powder of **386**, (d) partial reversion to the blue luminescence by dropwise treatment using dichloromethane onto the center of the ground powder, (e) powder after treatment with dichloromethane, and (f) repetition of the yellow emission by scratching the powder with a pestle. Reproduced with permission from ref. 473. Copyright 2008 American Chemical Society.

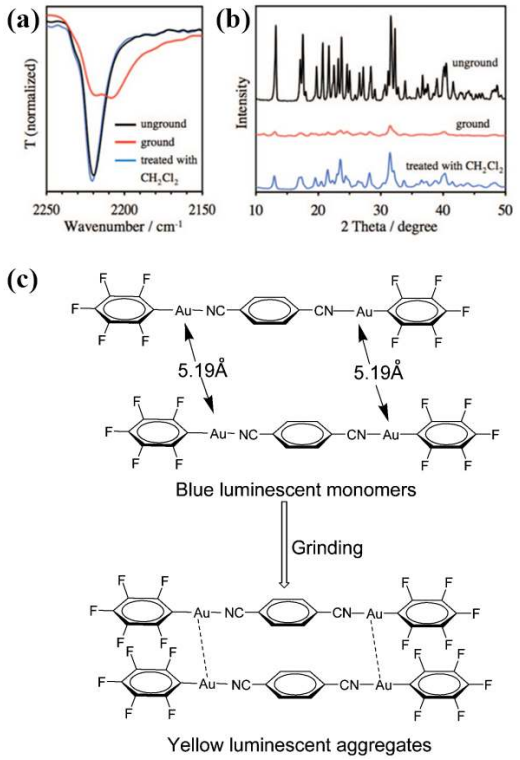

Fig. 104 IR spectra (a) and XRD pattern (b) of **386** in various states. (c) Structural changes accompanying the luminescence changes of **386**. Reproduced with permission from ref. 473. Copyright 2008 American Chemical Society.

In 2013, Reber and Raithby *et al.* investigated the MCL mechanism of **386** *via* applied hydrostatic pressure on the molecule.[474] Contrary to the previous conclusion of Ito *et al.*,[473] crystallinity was retained throughout, and the absence of obvious intermolecular interactions indicated that the MCL mechanism of **386** is due to the altered molecular geometry and crystal packing under hydrostatic pressure, with rotation of the central phenyl rings out of the plane of the terminal pentafluorophenyl rings, rather than enhanced aurophilic interactions.[474] These different mechanisms may be attributed to the different nature of the applied external stimuli, for which hydrostatic pressure is unidirectional, whereas grinding is multidirectional.

In 2012, Liang *et al.* reported a series of dinuclear Au(I) complexes **387–391** with various aromatic bridging ligands.[475] Upon grinding, complexes **387** and **388** exhibited a redshifted (~100 nm) emission from blue to green color. In contrast, complex **389** exhibited a relatively smaller redshifted (~25 nm) emission. No MCL behaviour was observed for **390** and **391**. XRD results indicated that, upon grinding, a phase transformation from crystalline to metastable amorphous state was observed for **387–389**, whereas no phase transformation was observed for **390** and **391**. This work demonstrated that the MCL properties of these complexes are significantly affected by the bridging ligand structures.

In 2015, Seki *et al.* reported that the dinuclear Au(I) isocyanide complex **392** with pyridyl end groups exhibited interconvertible tetracolored emission.[476] As shown in Fig. 105a, **392** exhibited four individual solid state emissions (blue, green, yellow and orange) from the samples named as 2B, 2G, 2Y and 2O, respectively. The as-synthesized solid sample of **392** is 2Y. Soaking 2Y in acetone solution (step i in Fig. 105c) lead to the blue-emitting solid sample 2B which immediately transforms to a green-emitting sample 2G upon drying in the air (step ii in Fig. 105c). No further color change was observed even under reduced pressure for weeks. When 2G was mechanically ground in a ball-mill at 4600 rpm for 10 min (step iii in Fig. 105c), the yellow emission of 2Y was recovered. After grinding for an additional 5 min (step iv in Fig. 105c), orange emission was observed, corresponding to the formation of 2O. PXRD patterns showed obvious crystalline states of 2B, 2G and 2Y, whereas the ground 2O was amorphous. Single crystal and PXRD analyses indicated that aurophilic interactions were not present in 2B and 2G, but were present in 2Y. The amorphous 2O phase is suggested to contain aurophilic interactions with the shortest Au···Au distance.

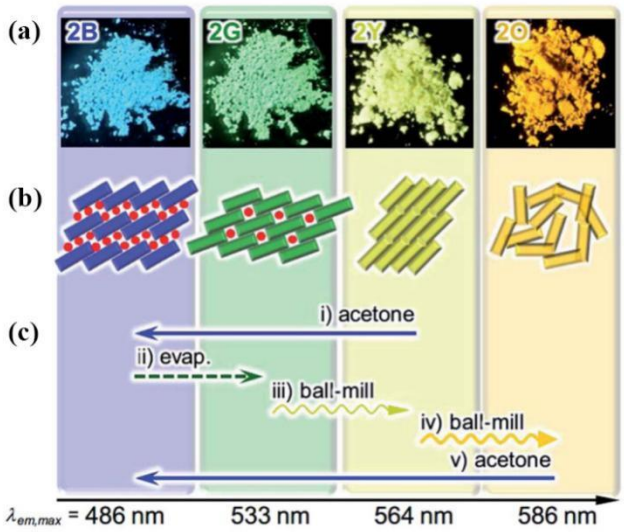

Fig. 105 (a) Photographs of the powder forms of **392** showing different photoluminescence under UV light at 365 nm. (b) Schematic representation of the solid state molecular arrangements of **392**, in which a molecule of **392** is denoted as a rectangle, with the colors of the corresponding emission. Solvent molecules are denoted as red circles. (c) Specific procedures for the interconversion of the four emitting states of **392**. Reproduced with permission from ref. 476. Copyright 2015 The Royal Society of Chemistry.

More recently, Seki *et al*. reported that **393**, which is a *meta*-substituted isomer of **386**, exhibits pseudopolymorphs with different emission properties *via* different solvent crystallization procedures.[466] The correspondingemission peaks are in the range of λ_{max} 488–519 nm. XRD results indicated that distinct crystal structures are responsible for the different emission properties. Upon grinding, all samples underwent redshifted emission with a new peak at λ_{max} 540 nm upon formation of an amorphous state. This phase transformation was reversible *via* heat treatment of the ground samples.

In 2015, Chen *et al*. reported a fluorene-based dinuclear Au(I) complex **394**, which showed AIE and MCL simultaneously.[477] As shown in Fig. 106, complex **394** is faintly emissive in pure DMF solution, whereas intense yellow emission is observed when a large ratio of H_2O was added into the mixtures, indicating that **394** is AIE active. Upon grinding, **394** exhibited obvious MCL properties with green emission changing to yellow. This change was reversed to the original green emission upon treatment of the ground sample with dichloromethane or heating at 100 °C for 30 s. XRD results attributed the reversible MCL behaviour of **394** to a phase transformation between the crystalline and amorphous states.

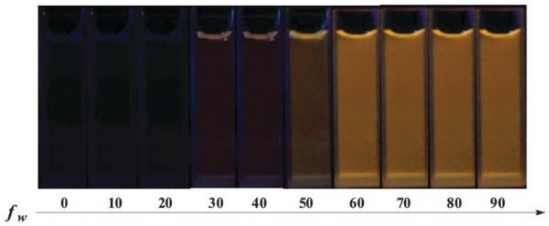

Fig. 106 Fluorescence images of **394** (concentration: 2.0 10^{-5} mol L^{-1}) in diverse DMF–H_2O mixtures with different f_w values under 365 nm UV light. Reproduced with permission from ref. 477. Copyright 2015 The Royal Society of Chemistry.

Subsequently, Chen *et al*. reported a series of carbazole-based dinuclear Au(I) complexes **395**–**397** which showed AIE and MCL properties simultaneously.[478] XRD results indicated that the MCL mechanism of all complexes was due to a phase transformation from a crystalline state to an amorphous state. Interestingly, upon grinding, complex **395** showed reversible MCL behaviour, while irreversible MCL behaviour was observed for complexes **396** and **397**. The X-ray crystal structure analysis revealed strong intermolecular aurophilic interactions in **397**, with the shortest Au···Au distances of 3.040 Å. Upon grinding, the intermolecular aurophilic interactions may be further enhanced, making it difficult to revert to the original state.

To study the effect of *o*-, *m*- and *p*- isomerization on MCL properties, complexes **398**–**400** were synthesized.[479] All these complexes exhibited AIE activity. The *o*-isomer **398** exhibited reversible MCL behaviour; the *m*-isomer **399** displayed reversible mechanical force-induced luminescence enhancement behaviour; whereas no MCL behaviour was observed for *p*-isomer **400**. Furthermore, two new *m*-substituted complexes **401** and **402** also showed reversible mechanical force-induced luminescence enhancement, which is consistent with the data for **399**.[480]

More recently, Chen *et al*. reported a new bipyridine-bridged dinuclear Au(I) complex **403**, which showed AIE and MCL properties simultaneously.[481] An SEM image (Fig. 107) revealed rod-shaped aggregates due to the self-assembly of **403** in the DMF : H_2O (1 : 9 v/v) mixture. Synergistic effects of intermolecular Au···Au interactions and restricted intramolecular rotation were suggested as the cause of self-assembly of **403**. Aggregated **403** exhibited high emission efficiency (Φ 56%, λ_{max} 553 nm) in DMF : H_2O (1 : 9) mixture. Reversible high-contrast phosphorescent mechanochromism was observed for solid samples of **403**.

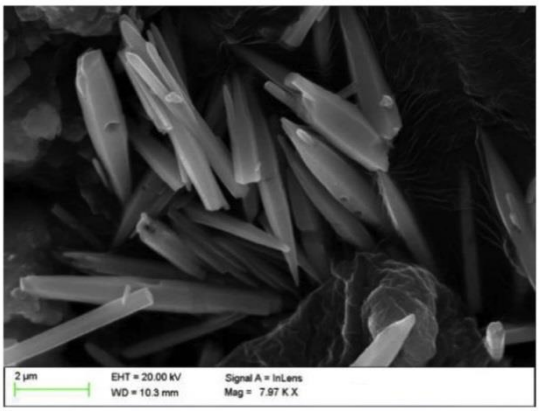

Fig. 107 SEM image of complex **403** (2.0×10^{-5} mol L^{-1}) formed from DMF/water mixture (f_w = 90%). Reproduced with permission from ref. 481. Copyright 2018 Elsevier.

In 2016, 2,2'-binaphthyl-bridged dinuclear Au(I) complex **404** was synthesized by Ito's group.[482] As shown in Fig. 108, crystals of

racemic [(*rac*)-**404**] and homochiral [(*S*)-**404**] exhibited distinct emission colors with different crystal packing arrangements. Upon grinding, both crystals transform into amorphous powders with essentially the same red-shifted emission spectra and enhanced PLQYs, compared to the parent crystals.

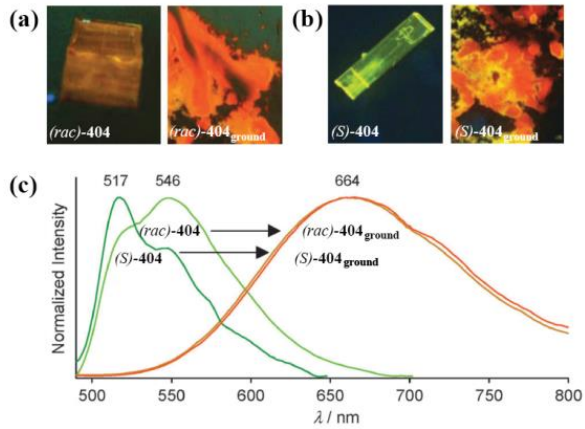

Fig. 108 Photographs of (a) (*rac*)-**404** and (*rac*)-**404** ground and (b) (*S*)-**404** and (*S*)-**404** ground taken under ultraviolet irradiation (λ_{ex} = 365 nm). (c) Emission spectral changes from crystals to the ground samples. Reproduced with permission from ref. 482. Copyright 2016 The Royal Society of Chemistry.

In 2015, a series of dicationic dinuclear Au(I) cyclophane complexes **405**–**409** with various counteranions (X^-) was reported by Deák *et al*.[483] Interestingly, the emission colors varied from yellow to red, depending on the different counteranions. All the complexes exhibited reversible thermochromic (room temperature to 77 K) and MCL properties. XRD results indicated a crystalline-to-amorphous phase transformation occurred during the grinding process. The authors proposed that N–H···X interactions played a significant role in the observed MCL properties, while the intermolecular Au···Au interaction was effectually precluded by the introduction of the bulky diphosphine ligands. The dicationic structure could also disfavour Au···Au interactions due to Coulombic repulsion, although the authors do not comment on this.

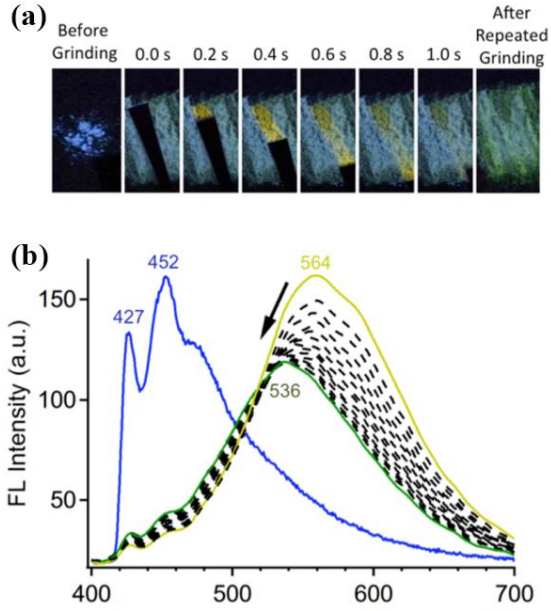

Fig. 109 (a) Photographs showing the luminescent color change of **410** upon grinding. (b) The corresponding time-resolved emission spectra of **410**. Reproduced with permission from ref. 484. Copyright 2016 American Chemical Society.

In 2016, Yagai *et al*. reported the new complex **410** with flexible triethylene glycol (TEG) side chains.[484] As shown in Fig. 109, before grinding complex **410** exhibited structured emission peaks at 427 and 452 nm. Upon grinding of **410** for only 1 s, yellow emission with λ_{max} at 564 nm appeared. Further repeated grinding of **410** gave green emission with λ_{max} at 536 nm. Polarized optical microscopy (POM) revealed three different phases of **410** during the grinding process. As shown in Fig. 110, the green-emitting and blue-emitting phases were found in a birefringence crystalline domain, which is characteristic of a crystalline state. However, no birefringence was presented in the yellow-emitting phase, indicating an amorphous state. These results indicated that the MCL mechanism of **410** was attributed to a rare crystal-to-crystal transformation mediated by a transient amorphous state.

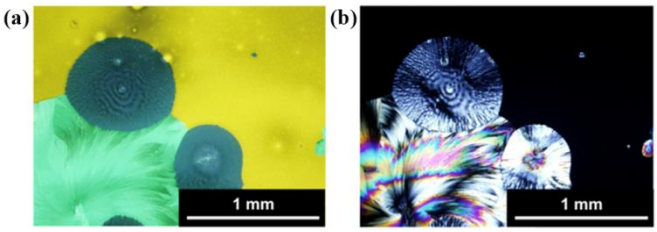

Fig. 110 (a) Emission (excitation at 365 nm) and (b) polarized optical micrographs of a polymorphic thin film of **410** prepared from its 1,2-dichlorobenzene solution. Reproduced with permission from ref. 484. Copyright 2016 American Chemical Society.

In 2014, three dinuclear Au(I) complexes **411**–**413** bearing glycol bridges of different lengths were reported by Liang *et al*.[485] All complexes showed obvious AIE properties in different solvent–water mixtures. However, in the solid state, **411**–**413**

showed very low PLQYs of < 1% with emission at λ_{max} 485 nm for **411** and 480 nm for **412** and **413**, respectively. Upon grinding, the emission for all the complexes showed a dramatic increase of intensity accompanied with a red shift in the emission spectra of > 15 nm. The PLQYs of ground **411**–**413** are 67.5%, 44.9% and 31%, respectively. The MCL mechanism was attributed to the formation of aurophilic interactions and the changes in multiple intermolecular interactions, such as C–H···F, C···F and weak π–π.

6.2 Ir(III) complexes

The first example of an Ir(III) complex with MCL properties was reported by our group in 2012.[453] Since then, various mono- and dinuclear Ir(III) complexes with MCL have been developed.[50, 109, 110, 463, 486-493] Interestingly, in most of the cases, AIE and MCL activity are observed simultaneously. This is consistent with the opinion first expressed by Chi's group, that AIE materials may be a key treasure source for mechanochromic luminescence.[445] There are four different types of MCL Ir(III) complexes based on the structure of the ancillary ligand, including alkyl chains,[486-491] dendrimer-like,[492] Schiff base[50, 109, 110] and rigid aromatic ring.[463, 493]

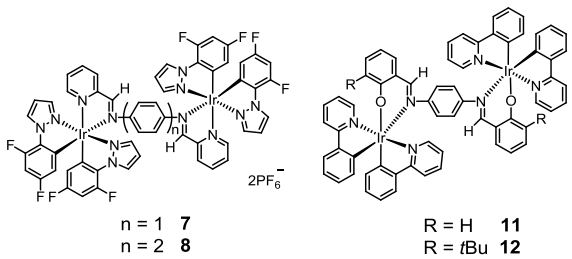

Fig. 111 The chemical structures of dinuclear Ir(III) complexes.

In contrast to mononuclear Ir(III) complexes, dinuclear Ir(III) analogues with MCL properties are very rare. Only four examples are known, namely complexes **7**, **8**, **11** and **12**, all with Schiff base bridging ligands, reported by our group (Figure 111).[50, 109, 110] The ionic complexes **7** and **8** show faint emission in dilute solution, while bright orange emission with λ_{max} at 612 nm and 627 nm, respectively, was observed in the solid state,[50] indicating their AIE nature. Upon grinding, both **7** and **8** exhibited obvious MCL behaviour with a red-shift of the emission by *ca*. 20 nm to λ_{max} 635 nm and 648 nm, respectively. This emission change can be rapidly reversed to the original emission by exposure of the ground samples to CH_2Cl_2 vapour due to the vapour-induced recrystallization. Based on detailed single-crystal structure analysis and XRD measurements, it was proposed that phase transformations from the crystalline to the amorphous state occurred in the grinding process and the flexible imine units of the bridging ligand play key a role in achieving simultaneous AIE and MCL properties. Taking advantage of the AIE and reversible MCL of complex **8**, a rapidly re-writable phosphorescence data recording device was successfully constructed (Fig. 112).

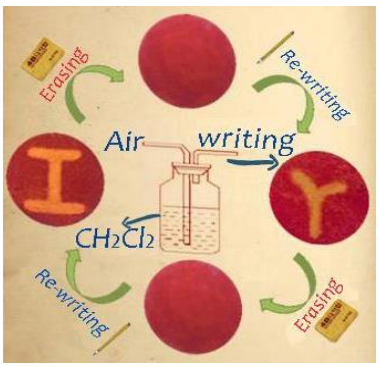

Fig. 112 A phosphorescence re-writable data recording device based on mechanochromic and vapochromic phosphorescence of complex **8**. Reproduced with permission from ref. 50. Copyright 2015 The Royal Society of Chemistry.

In 2017, two new neutral dinuclear Ir(III) complexes **11** and **12** were presented by our group.[109, 110] Similar to the previous ionic complexes **7** and **8**, both **11** and **12** exhibit AIE and MCL properties simultaneously. These combined properties of **11** were exploited in the design of a simple, convenient and efficient technology for optical data encryption and decryption. As shown in Fig. 113a, in the encryption stage, the characters 'NENU' were written on a filter paper with an orange-emitting fluorescent material selected from the literature as MASK. Next a sample of ground **11** (abbreviated as G) that showed a similar emission color to the Mask was carefully spread on the paper with the letters 'AIPE'. Under UV irradiation, the emission from G was hidden by the Mask with an identified orange emission. In the decryption stage, when DCM solvent was sprayed onto the as-prepared letters 'NENU', the intense yellow security letters 'AIPE' appeared, originating from the emission of unground complex **11**. This reversible encryption and decryption cycle was performed several times. This work suggested that AIE and MCL-active Ir(III) complexes are promising candidates in the practical applications of anti-counterfeit and optical data encryption.

Furthermore, taking advantages of mechanochromic and vapochromic properties of complex **12**, a device for detecting volatile organic compounds (VOCs) was fabricated. As shown in Fig. 113b, the ground complex **12** gave no obvious response to low polarity organic vapors, showing only faint emission. However, remarkably enhanced emission was observed when **12** was treated with various low polarity organic vapors. The device can be reversibly switched between the ON or OFF states *via* organic vapor fumigation and grinding processes, due to the phase transformations between the crystalline and amorphous states.

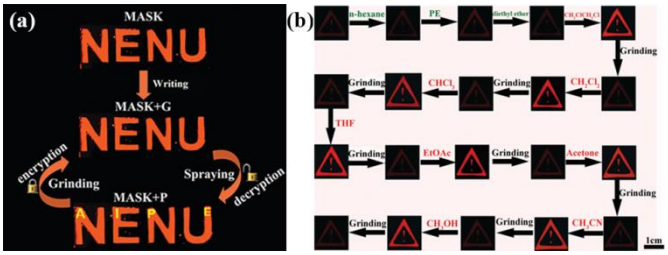

Fig. 113 (a) Optical information encryption and decryption devices based on complex **11** as the active material. (b) Photographic images of the monitoring of VOCs by **12** after exposure to different VOCs and grinding under UV irradiation. The letters 'NENU' denote North East Normal University, Changchun, where the experiment was performed. Reproduced with permission from ref. 109 and 110, respectively. Copyright 2017 The Royal Society of Chemistry.

6.3 Other metal complexes

In 2015, a Zn(II)-salen helical complex **414** (Fig. 114a) was reported by Mizukami *et al*.[494] As shown in Fig. 114b, the crystals of **414** exhibited intense green emission, while light-blue emission was observed after crushing the crystals into a powder (Fig. 114c). This MCL behaviour was assumed to be the result of a crystal phase transition with the blue-shifted emission attributed to weakened intermolecular π–π interactions.

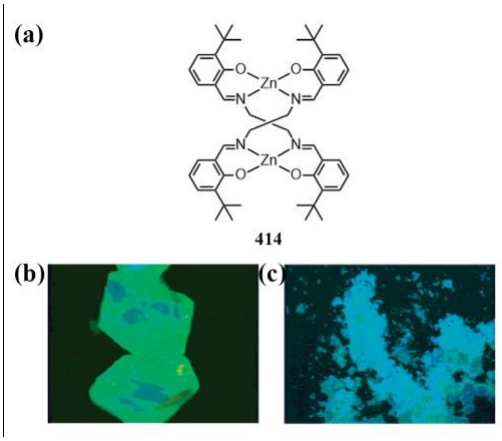

Fig. 114 (a) The chemical structure of dinuclear Zn(II) complex **414**. Fluorescence microscope images of (b) single crystals, (c) crushed crystals (powder). Reproduced with permission from ref. 494. Copyright 2005 American Chemical Society.

In 2016, a dinuclear Pt(II) complex **415** with bis-salen ligands and an isobutenylene linker (Fig. 115) was reported by Achira *et al*.[495] The crystals of **415** exhibited intense yellow emission (Fig. 115d) which is similar to its mononuclear analogue (Fig. 115a). Upon crushing, crystals of both mono and dinuclear complexes showed enhanced intensity of emission, but without any color change (Fig. 115b and e). However, when the crushed microcrystals were smeared into thin films on a glass slide, complex **415** exhibited an obvious color change from yellow to orange (Fig. 115f) whereas no change in emission was observed for its mononuclear analogue (Fig. 115c). These data indicate that dinuclear complex **415** exhibits enhanced pressure sensitivity which the authors suggest to arises from the introduction of the semiflexible linker, which contributes to the fragility of the molecular packing in the crystals of **415** under shear stress.[495]

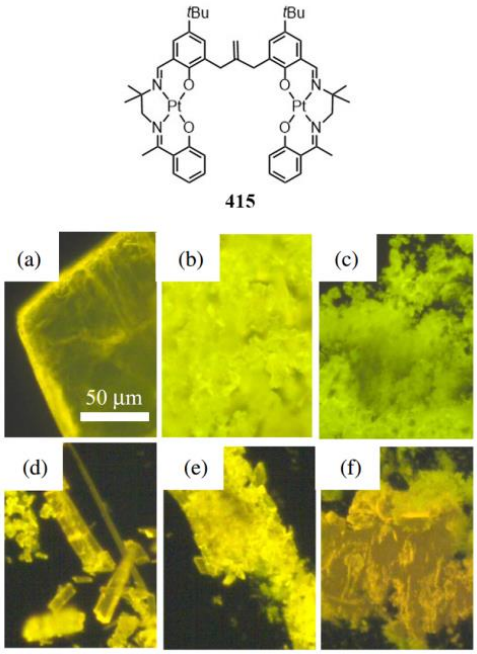

Fig. 115 The chemical structure of dinuclear Pt(II) complex **415** (top). Microscopic fluorescence images of mononuclear analogue of **415** (a–c) and **415** (d–f). (a, d) Microscale single crystals, (b, e) crushed microcrystals, and (c, f) samples smeared on a glass slide. Reproduced with permission from ref. 495. Copyright 2016 Elsevier.

Recently, Lu *et al*. reported four dinuclear Cu(I) complexes **416–419** bearing hexadentate macrocyclic *N*-heterocyclic carbene (NHC) ligands (Fig. 116).[496] Crystal structure analysis revealed a co-crystal comprising two molecules of **417a** and one molecule of **417b**. The crystals of the acetonitrile-free complexes **418** and **419** were obtained by slow vapor diffusion of diethyl ether into a solution of heated **416** and **417** in a mixed solvent (CH_3OH/acetone and CH_3OH/ether, respectively). The as-prepared **418** showed a red-shifted emission spectrum with a higher PLQY of 93%, when compared with **416**, **417** and **419**. These properties were attributed to the strong intramolecular cuprophilic interaction of **418** in the triplet excited states. Upon grinding (Fig. 117), **416–419** exhibited an obvious color change (with a red-shift of the emission of 20–28 nm). XRD results indicated that a phase transformation from the crystalline to the amorphous state occurred in the grinding process. The mechanism of MCL was attributed to strong intramolecular cuprophilic interactions with a short Cu···Cu distance induced by grinding.

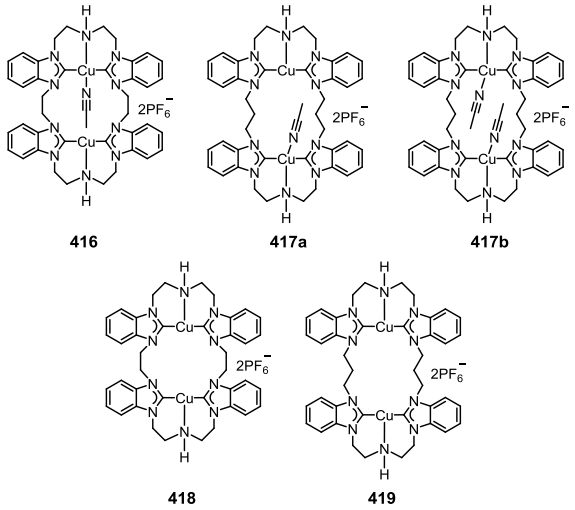

Fig. 116 The chemical structures of dinuclear Cu(I) complexes **416**–**419**.

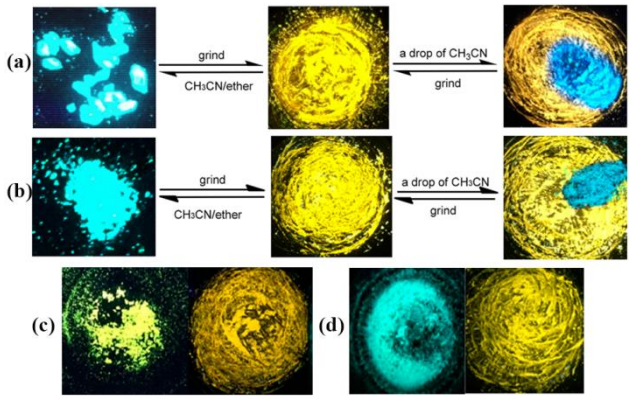

Fig. 117 Photographic images of reversible mechanochromic process of **416** (a) and **417** (b) taken under 365 nm illumination. Photographic images of **418** (c) and **419** (d) taken under 365 nm illumination before and after grinding. Reproduced with permission from ref. 496. Copyright 2018 American Chemical Society.

In summary, a range of MCL-active dinuclear metal complexes including Au(I), Ir(III), Zn(II), Pt(II) and Cu(I) complexes has been presented. The structure–property relationships as well as the MCL mechanisms have been discussed. In the bimetallic systems, MCL behaviour can be obtained *via* introduction of flexible bridging ligands between the two metal centers. The MCL mechanisms are widely assigned to variations in intermolecular π–π, C–H···π, intra- or intermolecular metal–metal, or hydrogen-bonding interactions.[54, 445] However, there is still scope for further insights into the detailed MCL mechanisms. Dinuclear metal complexes with MCL properties are still very rare. Further design and synthesis of new families of MCL-active dinuclear metal complexes remains a very active topic. Tang et al. stated that the restriction of intramolecular motions (RIMs) in AIEgens plays an essential role in their mechanochromic effects.[497] When a stimulus is applied to RIM-dominated AIEgens which have relative loose packing modes, the weak inter- or intramolecular interactions (*e.g.* π–π, C–H···π, metal–metal, or hydrogen-bonding interactions) can be modified or destroyed, resulting in MCL. Furthermore, Chi et al. have stated that the existence of a relatively stable crystalline state is a prerequisite for mechanochromism. AIE compounds with strong crystallizability or non-crystallizability are generally unsuitable as mechanochromic luminescent materials.[445] Notably, series of AIE-active dinuclear Au(I) and Ir(III) complexes have been shown to exhibit MCL behaviour, therefore, AIE-active metal complexes are expected to become a rich source of MCL complexes.

7. Conclusions and outlook

In this review, we have summarized recent advances in dinuclear metal complexes and their applications. Many of the studies have been motivated by exploring their fundamental structural and optoelectronic properties. Early work focussed on dinuclear analogues of the paradigmatic Ru(II) complex $[Ru(bpy)_3]^{2+}$. Research then extended to a wide range of other metals, such as Re(I), Rh(III), Ir(III), Pt(II), Au(I), Os(II), Ni(II) and Zn(II) in combination with a vast array of tailored ligands. Importantly, as a result of judicious molecular design (and some serendipity) many bimetallic complexes are now known to display specific photophysical properties and enhanced device performance exceeding that of their mononuclear metal complexes. These recent exciting findings should encourage chemists to further explore bimetallic chemistry. Moreover, this review article has systematically discussed the relationships between electronic structures and luminescent properties, which provide insights into the excited state character and intramolecular electron or energy transfer process in these complexes. However, it remains difficult to predict the charge transfer mechanism in a di- or poly-nuclear complex based on current knowledge. There is still no universal rule to explain the accurate structure-property relationships of different kinds of dinuclear metal complexes in all their diverse applications. Ongoing systematic variation of molecular structures allows the detailed investigation of the effects of bridge distance, energy gap and conformation on electronic coupling. These factors will promote future investigations into the photoinduced electron and energy transfer processes, and the development of molecular-based devices. Thus, the field is wide open for the rational design of new luminescent bimetallic systems with fine-tuned and desirable physical and chemical properties. Further breakthroughs can be anticipated in the fields of OLEDs, photocatalytic water splitting and CO_2 reduction, DSPEC, chemosensors, biosensors, PDT and smart materials.

It is well known that organic luminescent materials usually suffer from the notorious ACQ phenomenon, which can greatly limit their practical applications. However, the anti-ACQ property of AIE can overcome these difficulties. Recently, numerous AIE-active organic molecules have been developed and they show particular advantages when compared with ACQ-active materials in various optoelectronic applications such as non-doped OLEDs, real-time pressure mapping,

high-level security devices, biological probes and photodynamic therapy.[497-502] By contrast, AIE-active metal complexes have been less studied. We anticipate significant developments of novel AIE-active bimetallic complexes, which will impact the future of optoelectronic technology. For practical applications we particularly highlight the following two areas which are at the forefront of exciting advances in dinuclear metal complexes.

(i) Non-doped organic light-emitting diodes (OLEDs). While OLEDs based on transition metal emitters *via* host–guest doping methods have been extensively exploited, the development of non-doped OLEDs is still highly desired due to their easier preparation, superior reproducibility of manufacture, lack of unwanted host-guest interactions and potentially enhanced device stability. The combined advantages of AIE and excellent phosphorescent/TADF properties from dinuclear metal complexes, should lead to highly efficient and stable non-doped OLEDs. In contrast to mononuclear metal complexes, the larger size of di- or multinuclear metal complexes not only reduces intermolecular triplet-triplet annihilation, but also retards the attack ofnucleophiles on the complex, which is believed to be the reason for the higher stability of the devices.[503, 504] In addition, design and synthesis of new AIE-acitve dinuclear metal complexes with bipolar characters *via* decoration of cyclometalated ligands or bridging ligands may further facilitate improved device efficiency.

(ii) Photodynamic therapy (PDT) under hypoxia. Currently, PDT investigations are mainly performed under normoxia conditions where oxygen supply is sufficient, which is the opposite to hypoxic solid tumor cells.[441] Therefore, development of new photosensitizers for efficient PDT under hypoxia is of great significance. Because of the strong SOC accompanied with good ability to generate triplet excitons, transition metal complexes possess superior oxygen sensitivity. However, most luminescent transition metal complexes usually suffer from ACQ in the aggregated state, which greatly limits the production of triplet excitons. Therefore, AIE-active materials are ideal candidates. In contrast to the mononuclear species, di- or multi-nuclear AIE-active transition metal complexes may be a better choice due to their enhanced SOC and triplet exciton generation derived from the introduction of another metal atom in the molecule. Furthermore, easily obtained long wavelength emission in dinuclear species has great potential applications in deep tissue imaging therapy.

Conflicts of interest

There are no conflicts to declare.

Acknowledgements

The work was funded by NSFC (No.51473028), the key scientific and technological project of Jilin province (20160307016GX), the Development and Reform Commission of Jilin province (20160058). The project was supported by Open Research Fund of State Key Laboratory of Polymer Physics and Chemistry, Changchun Institute of Applied Chemistry, Chinese Academy of Sciences. M. R. B. thanks EPSRC grant EL/L02621X/1 for funding.

References

1 D. Di, A. S. Romanov, L. Yang, J. M. Richter, J. P. H. Rivett, S. Jones, T. H. Thomas, M. A. Jalebi, R. H. Friend, M. Linnolahti, M. Bochmann and D. Credgington, *Science*, 2017, **356**, 159-163.

2 A. K. Chan, M. Ng, Y. C. Wong, M. Y. Chan, W. T. Wong and V. W. Yam, *J. Am. Chem. Soc.*, 2017, **139**, 10750-10761.

3 M. A. Baldo, D. F. O'Brien, Y. You, A. Shoustikov, S. Sibley, M. E. Thompson and S. R. Forrest, *Nature*, 1998, **395**, 151-154.

4 Y. Ma, H. Zhang, J. Shen, C. Che, *Synth. Met.*, 1998, **94**, 245-248.

5 M. J. Jurow, C. Mayr, T. D. Schmidt, T. Lampe, P. I. Djurovich, W. Brütting and M. E. Thompson, *Nat. Mater.*, 2015, **5**, 85-91.

6 K. T. Kamtekar, A. P. Monkman and M. R. Bryce, *Adv. Mater*, 2010, **22**, 572-582.

7 J. D. Slinker, A. A. Gorodetsky, M. S. Lowry, J. Wang, S. Parker, R. Rohl, S. Bernhard and G. G. Malliaras, *J. Am. Chem. Soc.*, 2004, **126**, 2763-2767.

8 A. Asadpoordarvish, A. Sandström, C. Larsen, R. Bollström, M. Toivakka, R. Österbacka and L. Edman, *Adv. Funct. Mater.*, 2015, **25**, 3238-3245.

9 C. D. Ertl, C. Momblona, A. Pertegas, J. M. Junquera-Hernandez, M. G. La-Placa, A. Prescimone, E. Orti, C. E. Housecroft, E. C. Constable and H. J. Bolink, *J. Am. Chem. Soc.*, 2017, **139**, 3237-3248.

10 D. Ma, T. Tsuboi, Y. Qiu and L. Duan, *Adv. Mater.*, 2017, **29**, 1603253.

11 S. Tang, A. Sandstrom, P. Lundberg, T. Lanz, C. Larsen, S. van Reenen, M. Kemerink and L. Edman, *Nat. Commun.*, 2017, **8**, 1190.

12 J. Zhang, L. Zhou, H. A. Al-Attar, K. Shao, L. Wang, D. Zhu, Z. Su, M. R. Bryce and A. P. Monkman, *Adv. Funct. Mater.*, 2013, **23**, 4667-4677.

13 J. I. Kim, I.-S. Shin, H. Kim and J.-K. Lee, *J. Am. Chem. Soc.*, 2005, **127**, 1614-1615.

14 S. Zanarini, E. Rampazzo, S. Bonacchi, R. Juris, M. Marcaccio, M. Montalti, F. Paolucci and L. Prodi, *J. Am. Chem. Soc.*, 2009, **131**, 14208-14209.

15 G. J. Barbante, E. H. Doeven, E. Kerr, T. U. Connell, P. S. Donnelly, J. M. White, T. Lopes, S. Laird, D. J. Wilson, P. J. Barnard, C. F. Hogan and P. S. Francis, *Chem. Eur. J.*, 2014, **20**, 3322-3332.

16 M. B. Herbert, V. M. Marx, R. L. Pederson and R. H. Grubbs, *Angew. Chem. Int. Ed.*, 2013, **52**, 310-314.

17 Z. Liu, W. Qi and G. Xu, *Chem. Soc. Rev.*, 2015, **44**, 3117-3142.

18 E. Puodziukynaite, J. L. Oberst, A. L. Dyer and J. R. Reynolds, *J. Am. Chem. Soc.*, 2012, **134**, 968-978.

19 J. Liu, Y. Liu, Q. Liu, C. Li, L. Sun and F. Li, *J. Am. Chem. Soc.*, 2011, **133**, 15276-15279.

20 H. Woo, S. Cho, Y. Han, W. S. Chae, D. R. Ahn, Y. You and W. Nam, *J. Am. Chem. Soc.*, 2013, **135**, 4771-4787.

21 Y. Yang, Q. Zhao, W. Feng and F. Li, *Chem. Rev.*, 2013, **113**, 192-270.

22 Y. You, Y. Han, Y. M. Lee, S. Y. Park, W. Nam and S. J. Lippard, *J. Am. Chem. Soc.*, 2011, **133**, 11488-11491.

23 Q. Zhao, F. Li and C. Huang, *Chem. Soc. Rev.*, 2010, **39**, 3007-3030.
24 M. R. Gill and J. A. Thomas, *Chem. Soc. Rev.*, 2012, **41**, 3179-3192.
25 K. K. Lo, K. Y. Zhang, S. K. Leung and M. C. Tang, *Angew. Chem. Int. Ed.*, 2008, **47**, 2213-2216.
26 H. Song, J. T. Kaiser and J. K. Barton, *Nat. Chem.*, 2012, **4**, 615-620.
27 Y. Yuan, R. T. Kwok, B. Z. Tang and B. Liu, *J. Am. Chem. Soc.*, 2014, **136**, 2546-2554.
28 T. Zou, C. T. Lum, C. N. Lok, W. P. To, K. H. Low and C. M. Che, *Angew. Chem. Int. Ed.*, 2014, **53**, 5810-5814.
29 F. Schmitt, P. Govindaswamy, G. Süss-Fink, W. H. Ang, P. J. Dyson, L. Juillerat-Jeanneret and B. Therrien, *J. Med. Chem.*, 2008, **51**, 1811-1816.
30 B. S. Howerton, D. K. Heidary and E. C. Glazer, *J. Am. Chem. Soc.*, 2012, **134**, 8324-8327.
31 A. Levina, A. Mitra and P. A. Lay, *Metallomics*, 2009, **1**, 458-470.
32 C. Mari, V. Pierroz, S. Ferrari and G. Gasser, *Chem. Sci.*, 2015, **6**, 2660-2686.
33 E. Wachter, D. K. Heidary, B. S. Howerton, S. Parkin and E. C. Glazer, *Chem. Commun.*, 2012, **48**, 9649-9651.
34 J. I. Goldsmith, W. R. Hudson, M. S. Lowry, T. H. Anderson and S. Bernhard, *J. Am. Chem. Soc.*, 2005, **127**, 7502-7510.
35 H. Takeda, K. Koike, H. Inoue and O. Ishitani, *J. Am. Chem. Soc.*, 2008, **130**, 2023-2031.
36 A. J. Morris, G. J. Meyer and E. Fujita, *Acc. Chem. Res.*, 2009, **42**, 1983-1994.
37 J. Bonin, M. Robert and M. Routier, *J. Am. Chem. Soc.*, 2014, **136**, 16768-16771.
38 H.-C. Chen, D. G. H. Hetterscheid, R. M. Williams, J. I. van der Vlugt, J. N. H. Reek and A. M. Brouwer, *Energ. Environ. Sci.*, 2015, **8**, 975-982.
39 G. Menendez Rodriguez, A. Bucci, R. Hutchinson, G. Bellachioma, C. Zuccaccia, S. Giovagnoli, H. Idriss and A. Macchioni, *ACS Energ. Lett.*, 2016, **2**, 105-110.
40 H. Rao, L. C. Schmidt, J. Bonin and M. Robert, *Nature*, 2017, **548**, 74-77.
41 D. W. Shaffer, Y. Xie, D. J. Szalda and J. J. Concepcion, *J. Am. Chem. Soc.*, 2017, **139**, 15347-15355.
42 C. Wang, Z. Xie, K. E. deKrafft and W. Lin, *J. Am. Chem. Soc.*, 2011, **133**, 13445-13454.
43 D. R. Whang, K. Sakai and S. Y. Park, *Angew. Chem. Int. Ed.*, 2013, **52**, 11612-11615.
44 Y. J. Yuan, Z. T. Yu, D. Q. Chen and Z. G. Zou, *Chem. Soc. Rev.*, 2017, **46**, 603-631.
45 D. L. Ashford, B. D. Sherman, R. A. Binstead, J. L. Templeton and T. J. Meyer, *Angew. Chem. Int. Ed.*, 2015, **54**, 4778-4781.
46 M. K. Brennaman, R. J. Dillon, L. Alibabaei, M. K. Gish, C. J. Dares, D. L. Ashford, R. L. House, G. J. Meyer, J. M. Papanikolas and T. J. Meyer, *J. Am. Chem. Soc.*, 2016, **138**, 13085-13102.
47 W. Song, Z. Chen, M. K. Brennaman, J. J. Concepcion, A. O. T. Patrocinio, N. Y. Murakami Iha and T. J. Meyer, *Pure Appl. Chem.*, 2011, **83**, 749-768.
48 D. Wang, M. V. Sheridan, B. Shan, B. H. Farnum, S. L. Marquard, B. D. Sherman, M. S. Eberhart, A. Nayak, C. J. Dares, A. K. Das, R. M. Bullock and T. J. Meyer, *J. Am. Chem. Soc.*, 2017, **139**, 14518-14525.
49 D. Wang, B. D. Sherman, B. H. Farnum, M. V. Sheridan, S. L. Marquard, M. S. Eberhart, C. J. Dares and T. J. Meyer, *Proc. Natl. Acad. Sci. U S A*, 2017, **114**, 9809-9813.
50 G. Li, X. Ren, G. Shan, W. Che, D. Zhu, L. Yan, Z. Su and M. R. Bryce, *Chem. Commun.*, 2015, **51**, 13036-13039.
51 T. Seki, N. Tokodai, S. Omagari, T. Nakanishi, Y. Hasegawa, T. Iwasa, T. Taketsugu and H. Ito, *J. Am. Chem. Soc.*, 2017, **139**, 6514-6517.
52 H. Sun, S. Liu, W. Lin, K. Y. Zhang, W. Lv, X. Huang, F. Huo, H. Yang, G. Jenkins, Q. Zhao and W. Huang, *Nat. Commun.*, 2014, **5**, 3601.
53 Q. Zhang, J. Su, D. Feng, Z. Wei, X. Zou and H. C. Zhou, *J. Am. Chem. Soc.*, 2015, **137**, 10064-10067.
54 X. Zhang, Z. Chi, Y. Zhang, S. Liu and J. Xu, *J. Mater. Chem. C*, 2013, **1**, 3376-3390.
55 M. A. Esteruelas, A. M. López, E. Oñate, A. San-Torcuato, J.-Y. Tsai and C. Xia, *Organometallics*, 2017, **36**, 699-707.
56 F. Lafolet, S. Welter, Z. Popović and L. D. Cola, *J. Mater. Chem.*, 2005, **15**, 2820-2828.
57 G. Turnbull, J. A. G. Williams and V. N. Kozhevnikov, *Chem. Commun.*, 2017, **53**, 2729-2732.
58 T. Hajra, J. K. Bera and V. Chandrasekhar, *Aust. J. Chem.*, 2011, **64**, 561-566.
59 E. S. Andreiadis, D. Imbert, J. Pecaut, A. Calborean, I. Ciofini, C. Adamo, R. Demadrille and M. Mazzanti, *Inorg. Chem.*, 2011, **50**, 8197-8206.
60 L. Donato, C. E. McCusker, F. N. Castellano and E. Zysman-Colman, *Inorg. Chem.*, 2013, **52**, 8495-8504.
61 M. Graf, R. Czerwieniec and K. Sünkel, *Z. Anorg. Allg. Chem.*, 2013, **639**, 1090-1094.
62 A. G. Tennyson, E. L. Rosen, M. S. Collins, V. M. Lynch and C. W. Bielawski, *Inorg. Chem.*, 2009, **48**, 6924-6933.
63 K. D. Demadis, C. M. Hartshorn and T. J. Meyer, *Chem. Rev.*, 2001, **101**, 2655-2685.
64 D. M. D'Alessandro, P. H. Dinolfo, J. T. Hupp, P. C. Junk and F. R. Keene, *Eur. J. Inorg. Chem.*, 2006, 772-783.
65 M. Gilbert and B. Albinsson, *Chem. Soc. Rev.*, 2015, **44**, 845-862.
66 S. Kanti Seth, P. Gupta and P. Purkayastha, *New J. Chem.*, 2017, **41**, 6540-6545.
67 J. Otsuki, T. Akasaka and K. Araki, *Coor. Chem. Rev.*, 2008, **252**, 32-56.
68 V. L. Whittle and J. A. G. Williams, *Inorg. Chem.*, 2008, **47**, 6596-6607.
69 A. Auffrant, A. Barbieri, F. Barigelletti, J. Lacour, P. Mobian, J.-P. Collin, J.-P. Sauvage, and B. Ventura, *Inorg. Chem.*, 2007, **46**, 6911-6919.
70 E. A. Plummer, J. W. Hofstraat and L. De Cola, *Dalton Trans.*, 2003, 2080-2084.
71 A. Santoro, A. M. Prokhorov, V. N. Kozhevnikov, A. C. Whitwood, B. Donnio, J. A. Williams and D. W. Bruce, *J. Am. Chem. Soc.*, 2011, **133**, 5248-5251.
72 G. Li, D. G. Congrave, D. Zhu, Z. Su and M. R. Bryce, *Polyhedron*, 2018, **140**, 146-157.
73 S. Bettington, M. Tavasli, M. R. Bryce, A. S. Batsanov, A. L. Thompson, H. A. Al-Attar, F. B. Dias and A. P. Monkman, *J. Mater. Chem.*, 2006, **16**, 1046-1052.
74 A. M'Hamedi, A. S. Batsanov, M. A. Fox, M. R. Bryce, K. Abdullah, H. A. Al-Attar and A. P. Monkman, *J. Mater. Chem.*, 2012, **22**, 13529-13540.
75 G. Nasr, A. Guerlin, F. Dumur, L. Beouch, E. Dumas, G. Clavier, F. Miomandre, F. Goubard, D. Gigmes, D. Bertin, G. Wantz and C. R. Mayer, *Chem. Commun.*, 2011, **47**, 10698-10700.
76 M. Y. Wong, G. Xie, C. Tourbillon, M. Sandroni, D. B. Cordes, A. M. Slawin, I. D. Samuel and E. Zysman-Colman, *Dalton Trans.*, 2015, **44**, 8419-8432.

77 X. Yang, X. Yan, H. Guo, B. Liu, J. Zhao, G. Zhou, Y. Wu, Z. Wu and W.-Y. Wong, *Dyes and Pigments*, 2017, **143**, 151-164.

78 J.-L. Liao, P. Rajakannu, P. Gnanasekaran, S.-R. Tsai, C.-H. Lin, S.-H. Liu, C.-H. Chang, G.-H. Lee, P.-T. Chou, Z.-N. Chen and Y. Chi, *Adv. Opt. Mater.*, 2018, **6**, 1800083.

79 Z. T. Yu, Y. J. Yuan, X. Chen, J. G. Cai and Z. G. Zou, *Chem. Eur. J.*, 2015, **21**, 10003-10007.

80 S. Berardi, L. Francas, S. Neudeck, S. Maji, J. Benet-Buchholz, F. Meyer and A. Llobet, *ChemSusChem*, 2015, **8**, 3688-3696.

81 L. Alibabaei, B. D. Sherman, M. R. Norris, M. K. Brennaman and T. J. Meyer, *Proc. Natl. Acad. Sci. U S A*, 2015, **112**, 5899-5902.

82 Y. Tamaki, K. Koike, T. Morimoto and O. Ishitani, *J. Catalysis*, 2013, **304**, 22-28.

83 G. Sahara, H. Kumagai, K. Maeda, N. Kaeffer, V. Artero, M. Higashi, R. Abe and O. Ishitani, *J. Am. Chem. Soc.*, 2016, **138**, 14152-14158.

84 W. Sun, S. Sun, N. Jiang, H. Wang and X. Peng, *Organometallics*, 2015, **34**, 3385-3389.

85 G. Li, W. Guan, S. Du, D. Zhu, G. Shan, X. Zhu, L. Yan, Z. Su, M. R. Bryce and A. P. Monkman, *Chem. Commun.*, 2015, **51**, 16924-16927.

86 Y. Cui, L.-L. Wen, G.-G. Shan, H.-Z. Sun, H.-T. Mao, M. Zhang and Z.-M. Su, *Sens. Actuators B: Chem.*, 2017, **244**, 314-322.

87 Y. Chen, W. Xu, J. Zuo, L. Ji and H. Chao, *J. Mater. Chem. B*, 2015, **3**, 3306-3314.

88 E. Baggaley, M. R. Gill, N. H. Green, D. Turton, I. V. Sazanovich, S. W. Botchway, C. Smythe, J. W. Haycock, J. A. Weinstein and J. A. Thomas, *Angew. Chem. Int. Ed.*, 2014, **53**, 3367-3371.

89 H. Ito, T. Saito, N. Oshima, N. Kitamura, S. Ishizaka, Y. Hinatsu, M. Wakeshima, M. Kato, K. Tsuge and M. Sawamura, *J. Am. Chem. Soc.*, 2008, **130**, 10044-10045.

90 L. Zhang, Y. Li, W. Che, D. Zhu, G. Li, Z. Xie, N. Song, S. Liu, B. Z. Tang, X. Liu, Z. Su and M. R. Bryce. *Adv. Sci.*, 2019, **6**, 1802050.

91 X. Hua and A. von Zelewsky, *Inorg. Chem.*, 1995, **34**, 5791-5797.

92 L. S. Kelso, D. A. Reitsma and F. R. Keene, *Inorg. Chem.*, 1996, **35**, 5144-5153.

93 F. R. Keene, *Chem. Soc. Rev.*, 1998, **27**, 185-193.

94 D. G. Congrave, Y.-t. Hsu, A. S. Batsanov, A. Beeby and M. R. Bryce, *Organometallics*, 2017, **36**, 981-993.

95 S. Y. Yao, Y. L. Ou and B. H. Ye, *Inorg. Chem.*, 2016, **55**, 6018-6026.

96 Y. Zheng, A. S. Batsanov, M. A. Fox, H. A. Al-Attar, K. Abdullah, V. Jankus, M. R. Bryce and A. P. Monkman, *Angew. Chem. Int. Ed.*, 2014, **53**, 11616-11619.

97 V. E. Pritchard, D. Rota Martir, S. Oldknow, S. Kai, S. Hiraoka, N. J. Cookson, E. Zysman-Colman and M. J. Hardie, *Chem. Eur. J.*, 2017, **23**, 6290-6294.

98 D. Rota Martir, D. Escudero, D. Jacquemin, D. B. Cordes, A. M. Z. Slawin, H. A. Fruchtl, S. L. Warriner and E. Zysman-Colman, *Chem. Eur. J.*, 2017, **23**, 14358-14366.

99 F. O. Garces, K. A. King, and R. J. Watts, *Inorg. Chem.*, 1988, 27, 3464-3471.

100 F. O. Garces, K. Dedeian, N. L. Keder and R. J. Watts, *Acta Cryst.*, 1993, **C49**, 1117-1120.

101 P. Lincoln and B. Nordén, *Chem. Commun.*, 1996, 2145-2146.

102 L. M. Wilhelmsson, F. Westerlund, P. Lincoln and B. Nordén, *J. Am. Chem. Soc.*, 2002, **124**, 12092-12093.

103 L. M. Wilhelmsson, E. K. Esbjörner, F. Westerlund, B. Nordén and P. Lincoln, *J. Phys. Chem. B*, 2003, **107**, 11784-11793.

104 P. Nordell and P. Lincoln, *J. Am. Chem. Soc.*, 2005, **127**, 9670-9671.

105 F. Westerlund, M. P. Eng, M. U. Winters and P. Lincoln, *J. Phys. Chem. B*, 2007, **111**, 310-317.

106 J. Andersson, M. Li and P. Lincoln, *Chem. Eur. J.*, 2010, **16**, 11037-11046.

107 A. A. Almaqwashi, J. Andersson, P. Lincoln, I. Rouzina, F. Westerlund and M. C. Williams, *Biophysical*, 2016, **110**, 1255-1263.

108 A. G. Clark, M. N. Naufer, F. Westerlund, P. Lincoln, I. Rouzina, T. Paramanathan and M. C. Williams, *Biochemistry*, 2018, **57**, 614-619.

109 Y. Jiang, G. Li, W. Che, Y. Liu, B. Xu, G. Shan, D. Zhu, Z. Su and M. R. Bryce, *Chem. Commun.*, 2017, **53**, 3022-3025.

110 Y. Jiang, G. Li, D. Zhu, Z. Su and M. R. Bryce, *J. Mater. Chem. C*, 2017, **5**, 12189-12193.

111 G. Li, Y. Wu, G. Shan, W. Che, D. Zhu, B. Song, L. Yan, Z. Su and M. R. Bryce, *Chem. Commun.*, 2014, **50**, 6977-6980.

112 R. E. Daniels, S. Culham, M. Hunter, M. C. Durrant, M. R. Probert, W. Clegg, J. A. Williams and V. N. Kozhevnikov, *Dalton Trans.*, 2016, **45**, 6949-6962.

113 A. M. Soliman, D. Fortin, P. D. Harvey and E. Zysman-Colman, *Dalton Trans.*, 2012, **41**, 9382-9393.

114 X. Yang, Z. Feng, J. Zhao, J. S. Dang, B. Liu, K. Zhang and G. Zhou, *ACS Appl. Mater. Interfaces*, 2016, **8**, 33874-33887.

115 X. Yang, X. Xu, J. S. Dang, G. Zhou, C. L. Ho and W. Y. Wong, *Inorg. Chem.*, 2016, **55**, 1720-1727.

116 V. L. Whittle and J. A. G. Williams, *Inorg. Chem.*, 2008, **47**, 6596-6607.

117 R. D. Costa, G. Fernandez, L. Sanchez, N. Martin, E. Orti and H. J. Bolink, *Chem. Eur. J.*, 2010, **16**, 9855-9863.

118 C. H. Shin, J. O. Huh, S. J. Baek, S. K. Kim, M. H. Lee and Y. Do, *Eur. J. Inorg. Chem.*, 2010, 3642-3651.

119 B.-K. An, S.-K. Kwon, S.-D. Jung and S. Y. Park, *J. Am. Chem. Soc.*, 2002, **124**, 14410-14415.

120 M. T. Indelli, C. A. Bignozzi, A. Harriman, J. R. Schoonover and F. Scandola, *J. Am. Chem. Soc.*, 1994, **116**, 3768-3779.

121 M. T. Indelli, F. Scandola, J.-P. Collin, J.-P. Sauvage and A. Sour, *Inorg. Chem.*, 1996, **35**, 303-312.

122 E. C. Constable, R. W. Handel, C. E. Housecroft, A. F. Morales, L. Flamigni and F. Barigelletti, *Dalton Trans.*, 2003, 1220–1222.

123 F. Weldon, L. Hammarstro1m, E. Mukhtar, R. Hage, E. Gunneweg, J G. Haasnoot, J. Reedijk, W. R. Browne, A. L. Guckian. and J. G. Vos, *Inorg. Chem.*, 2004, **43**, 4471-4481.

124 W. R. Browne, F. Weldon, A. Guckian and J. G. Vos, *Collec. Czech. Chem. Commun.*, 2003, **68**, 1467-1487.

125 J. M. Haider, R. M. Williams, L. De Cola and Z. Pikramenou, *Angew. Chem. Int. Ed.*, 2003, **42**, 1830-1833.

126 D. Maity, C. Bhaumik, D. Mondal and S. Baitalik, *Dalton Trans.*, 2014, **43**, 1829-1845.

127 S. Welter, N. Salluce, P. Belser, M. Groeneveld and L. De Cola, *Coord. Chem. Rev.*, 2005, **249**, 1360-1371.

128 B. Schlicke, P. Belser, L. De Cola, E. Sabbioni and V. Balzani, *J. Am. Chem. Soc.*, 1999, **121**, 4207-4214.

129 D. Schallenberg, A. Neubauer, E. Erdmann, M. Tanzler, A. Villinger, S. Lochbrunner and W. W. Seidel, *Inorg. Chem.*, 2014, **53**, 8859-8873.

130 L. Flamigni, F. Barigelletti, N. Armaroli, J.-P. Collin, I. M. Dixon, J.-P. Sauvage and J. A. G. Williams, *Coord. Chem. Rev.*, 1999, 671-682.
131 N. Isoda, Y. Torii, T. Okada, M. Misoo, H. Yokoyama, N. Ikeda, M. Nojiri, S. Suzuki and K. Yamaguchi, *Dalton Trans*, 2009, 10175-10177.
132 K. Barthelmes, M. Jager, J. Kubel, C. Friebe, A. Winter, M. Wachtler, B. Dietzek and U. S. Schubert, *Inorg. Chem.*, 2016, **55**, 5152-5167.
133 S. Welter, F. Lafolet, E. Cecchetto, F. Vergeer and L. De Cola, *Chemphyschem*, 2005, **6**, 2417-2427.
134 P. Coppo, M. Duati, V. N. Kozhevnikov, J. W. Hofstraat and L. De Cola, *Angew. Chem. Int. Ed.*, 2005, **117**, 1840-1844.
135 O. S. Wenger, *Acc. Chem. Res*., 2011, **44**, 25-35.
136 H. M. McConnell, *J. Chem. Phys*., 1961, **35**, 508-515.
137 H. Xu, R. Chen, Q. Sun, W. Lai, Q. Su, W. Huang and X. Liu, *Chem. Soc. Rev.*, 2014, **43**, 3259-3302.
138 W. R. Browne, N. M. O'Boyle, J. J. McGarvey and J. G. Vos, *Chem. Soc. Rev.*, 2005, **34**, 641-663.
139 A. C. Benniston, A. Harriman, P. Li, P. V. Patel and C. A. Sams, *Phys.Chem.Chem.Phys*., 2005, **7**, 3677-3679.
140 A. Endo, M. Ogasawara, A. Takahashi, D. Yokoyama, Y. Kato and C. Adachi, *Adv. Mater.*, 2009, **21**, 4802-4806.
141 D. Y. Kondakov, T. D. Pawlik, T. K. Hatwar and J. P. Spindler, *J. Appl. Phys.*, 2009, **106**, 124510.
142 H. Sasabe and J. Kido, *J. Mater. Chem. C*, 2013, **1**,1699-1707.
143 C. W. Tang and S. A. VanSlyke, *Appl. Phys. Lett.*, 1987, **51**, 913-915.
144 Q. Pei, G. Yu, C. Zhang, Y. Yang and A. J. Heeger, *Science*, 1995, **269**, 1086-1088.
145 E. Fresta and R. D. Costa, *J. Mater. Chem. C*, 2017, **5**, 5643-5675.
146 T. Hu, L. He, L. Duan and Y. Qiu, *J. Mater. Chem.*, 2012, **22**, 4206-4215.
147 J. D. Slinker, J. Rivnay, J. S. Moskowitz, J. B. Parker, S. Bernhard, H. D. Abruña and G. G. Malliaras, *J. Mater. Chem.*, 2007, **17**, 2976-2988.
148 C. W. Tang, S. A. VanSlyke and C. H. Chen, *J. Appl. Phys.*, 1989, **65**, 3610-3616.
149 T. W. Lee, S. Jeon, J. Maria, J. Zaumseil, J. W. P. Hsu and J. A. Rogers, *Adv. Funct. Mater.*, 2005, **15**, 1435-1439.
150 C. Kim and S. R. Forrest, *Adv. Mater.*, 2003, **15**, 541-544.
151 S. Lamansky, T. R. Hoffend Jr., H. Le, V. Jones, M. B. Wolk and W. A. Tolbert, *Organic Light-Emitting Materials and Devices IX*, edited by Z. H. Kafafi, P. A. Lane, Proc. of SPIE, 2005, **5937**, 593702.
152 M. S. Arnold, G. J. McGraw, S. R. Forrest and R. R. Lunt, *Appl. Phys. Lett.*, 2008, **92**, 053301.
153 C. L. Ho, W. Y. Wong, G. J. Zhou, B. Yao, Z. Xie and L. Wang, *Adv. Funct. Mater.*, 2007, **17**, 2925-2936.
154 J. C. deMello, N. Tessler, S. C. Graham and R. H. Friend, *Phys. Rev. B*, 1998, **57**, 12951-12963.
155 J. C. deMello, J. J. M. Halls, S. C. Graham, N. Tessler and R. H. Friend, *Phys. Rev. Lett.*, 2000, **85**, 421-424.
156 J. D. Slinker, J. A. DeFranco, M. J. Jaquith, W. R. Silveira, Y. W. Zhong, J. M. Moran-Mirabal, H. G. Craighead, H. D. Abruna, J. A. Marohn and G. G. Malliaras, *Nat. Mater.*, 2007, **6**, 894-899.
157 Q. Pei, Y. Yang, G. Yu, C. Zhang and Alan J. Heeger, *J. Am. Chem. Soc.*, 1996, **118**, 3922-3929.
158 Q. Pei and A. J. Heeger, *Nat. Mater.*, 2008, **7**, 167-168.
159 L. Edman, *Electrochimica Acta*, 2005, **50**, 3878-3885.
160 N. D. Robinson, J.-H. Shin, M. Berggren and L. Edman, *Phys. Rev. B*, 2006, **74**, 155210.
161 M. Lenes, G. Garcia-Belmonte, D. Tordera, A. Pertegás, J. Bisquert and H. J. Bolink, *Adv. Funct. Mater.*, 2011, **21**, 1581-1586.
162 M. Du, Y. Feng, D. Zhu, T. Peng, Y. Liu, Y. Wang and M. R. Bryce, *Adv. Mater.*, 2016, **28**, 5963-5968.
163 K. Udagawa, H. Sasabe, C. Cai and J. Kido, *Adv. Mater.*, 2014, **26**, 5062-5066.
164 D. Zhang, J. Qiao, D. Zhang and L. Duan, *Adv. Mater.*, 2017, **29**, 1702847.
165 J. Zou, H. Wu, C. S. Lam, C. Wang, J. Zhu, C. Zhong, S. Hu, C. L. Ho, G. J. Zhou, H. Wu, W. C. Choy, J. Peng, Y. Cao and W. Y. Wong, *Adv. Mater.*, 2011, **23**, 2976-2980.
166 J. Liu, N. Wang, Y. Yu, Y. Yan, H. Zhang, J. Li and J. Yu, *Sci. Adv*., 2017, **3**, e1603171.
167 M. K. Etherington, F. Franchello, J. Gibson, T. Northey, J. Santos, J. S. Ward, H. F. Higginbotham, P. Data, A. Kurowska, P. L. Dos Santos, D. R. Graves, A. S. Batsanov, F. B. Dias, M. R. Bryce, T. J. Penfold and A. P. Monkman, *Nat. Commun.*, 2017, **8**, 14987.
168 M. J. Leitl, V. A. Krylova, P. I. Djurovich, M. E. Thompson and H. Yersin, *J. Am. Chem. Soc.*, 2014, **136**, 16032-16038.
169 H. Uoyama, K. Goushi, K. Shizu, H. Nomura and C. Adachi, *Nature*, 2012, **492**, 234-238.
170 M. Y. Wong and E. Zysman-Colman, *Adv. Mater.*, 2017, **29**, 1605444.
171 X. L. Chen, J. H. Jia, R. Yu, J. Z. Liao, M. X. Yang and C. Z. Lu, *Angew. Chem. Int. Ed.*, 2017, **56**, 15006-15009.
172 L. S. Cui, H. Nomura, Y. Geng, J. U. Kim, H. Nakanotani and C. Adachi, *Angew. Chem. Int. Ed.*, 2017, **56**, 1571-1575.
173 C. Li, R. Duan, B. Liang, G. Han, S. Wang, K. Ye, Y. Liu, Y. Yi and Y. Wang, *Angew. Chem. Int. Ed.*, 2017, **56**, 11525-11529.
174 D. Volz, Y. Chen, M. Wallesch, R. Liu, C. Flechon, D. M. Zink, J. Friedrichs, H. Flugge, R. Steininger, J. Gottlicher, C. Heske, L. Weinhardt, S. Brase, F. So and T. Baumann, *Adv. Mater.*, 2015, **27**, 2538-2543.
175 P. Matyba, K. Maturova, M. Kemerink, N. D. Robinson and L. Edman, *Nat. Mater.*, 2009, **8**, 672-676.
176 L. S. C. Pingree, D. B. Rodovsky, D. C. Coffey, G. P. Bartholomew and D. S. Ginger, *J. Am. Chem. Soc.*, 2007, **129**, 15903-15910.
177 S. Sprouse, K. A. King, P. J. Spellane and R. J. Watts, *J. Am. Chem. Soc.*, 1984, **106**, 6647-6653.
178 S. Lamansky, P. Djurovich, D. Murphy, F. Abdel-Razzaq, H.-E. Lee, C. Adachi, P. E. Burrows, S. R. Forrest and M. E. Thompson, *J. Am. Chem. Soc.*, 2001, **123**, 4304-4312.
179 E. Holder, B. M. W. Langeveld and U. S. Schubert, *Adv. Mater.*, 2005, **17**, 1109-1121.
180 L. Xiao, Z. Chen, B. Qu, J. Luo, S. Kong, Q. Gong and J. Kido, *Adv. Mater.*, 2011, **23**, 926-952.
181 M. A. Baldo, S. Lamansky, P. E. Burrows, M. E. Thompson and S. R. Forrest, *Appl. Phys. Lett.*, 1999, **75**, 4-6.
182 C. Adachi, M. A. Baldo, M. E. Thompson and S. R. Forrest, *J. Appl. Phys.*, 2001, **90**, 5048-5051.
183 Y. Kawamura, K. Goushi, J. Brooks, J. J. Brown, H. Sasabe and C. Adachi, *Appl. Phys. Lett.*, 2005, **86**, 071104.
184 D. A. Poulsen, B. J. Kim, B. Ma, C. S. Zonte and J. M. J. Frećhet, *Adv. Mater*., 2010, **22**, 77-82.185 A. M'hamedi, M. A. Fox, A. S. Batsanov, H. A. Al-Attar, A. P. Monkman and M. R. Bryce, *J. Mater. Chem. C*, 2017, **5**, 6777-6789.
186 M. Graf, K. Sünkel, R. Czerwieniec and H.-C. Böttcher, *J. Organomet. Chem.*, 2013, **745-746**, 341-346.

187 T. Sajoto, P. I. Djurovich, A. Tamayo, M. Yousufuddin, R. Bau and M. E. Thompson, *Inorg. Chem.*, 2005, **44**, 7992-8003.
188 D. G. Congrave, Y. T. Hsu, A. S. Batsanov, A. Beeby and M. R. Bryce, *Dalton Trans.*, 2018, **47**, 2086-2098.
189 J. Fernández-Cestau, N. Giménez, E. Lalinde, P. Montaño, M. T. Moreno and S. Sánchez, *Organometallics*, 2015, **34**, 1766-1778.
190 V. Chandrasekhar, T. Hajra, J. K. Bera, S. M. Rahaman, N. Satumtira, O. Elbjeirami and M. A. Omary, *Inorg. Chem*, 2012, **51**, 1319-1329.
191 G. A. Carlson, P. I. Djurovich and R. J. Watts, *Inorg. Chem*, 1993, **32**, 4483-4484.
192 X. Yuan, S. Zhang and Y. Ding, *Inorg. Chem. Commun.*, 2012, **17**, 26-29.
193 V. Chandrasekhar, B. Mahanti, P. Bandipalli and K. Bhanuprakash, *Inorg. Chem*, 2012, **51**, 10536-10547.
194 A. M. Prokhorov, A. Santoro, J. A. Williams and D. W. Bruce, *Angew. Chem. Int. Ed.*, 2012, **51**, 95-98.
195 P. M. Griffiths, F. Loiseau, F. Puntoriero, S. Serroni and S. Campagna, *Chem. Commun.*, 2000, 2297-2298.
196 E. A. Plummer, J. W. Hofstraat and L. De Cola, *Dalton Trans.*, 2003, 2080-2084.
197 E. A. Plummer, A. van Dijken, J. W. Hofstraat, L. De Cola and K. Brunner, *Adv. Funct. Mater.*, 2005, **15**, 281-289.
198 W. J. Xu, S. J. Liu, X. Zhao, N. Zhao, Z. Q. Liu, H. Xu, H. Liang, Q. Zhao, X. Q. Yu and W. Huang, *Chem. Eur. J.*, 2013, **19**, 621-629.
199 A. Tsuboyama, T. Takiguchi, S. Okada, M. Osawa and K. Ueno, *Dalton Trans*., 2004, 1115-1116.
200 P. H. Lanoe, C. M. Tong, R. W. Harrington, M. R. Probert, W. Clegg, J. A. Williams and V. N. Kozhevnikov, *Chem. Commun.*, 2014, **50**, 6831-6834.
201 P. Li, Q.-Y. Zeng, H.-Z. Sun, M. Akhtar, G.-G. Shan, X.-G. Hou, F.-S. Li and Z.-M. Su, *J. Mater. Chem. C*, 2016, **4**, 10464-10470.
202 Y. Liu, C. Li, Z. Ren, S. Yan and M. R. Bryce, *Nat. Rev. Mater.*, 2018, **3**, 18020.
203 Z. Yang, Z. Mao, Z. Xie, Y. Zhang, S. Liu, J. Zhao, J. Xu, Z. Chi and M. P. Aldred, *Chem. Soc. Rev.*, 2017, **46**, 915-1016.
204 H. Tsujimoto, D. G. Ha, G. Markopoulos, H. S. Chae, M. A. Baldo and T. M. Swager, *J. Am. Chem. Soc.*, 2017, **139**, 4894-4900.
205 R. Czerwieniec, M. J. Leitl, H. H. H. Homeier and H. Yersin, *Coord. Chem. Rev.*, 2016, **325**, 2-28.
206 T. Hofbeck, U. Monkowius and H. Yersin, *J. Am. Chem. Soc.*, 2015, **137**, 399-404.
207 K. Goushi, K. Yoshida, K. Sato and C. Adachi, *Nat. Photon.*, 2012, **6**, 253-258.
208 C. Mongin, P. Moroz, M. Zamkov and F. N. Castellano, *Nat. Chem.*, 2018, **10**, 225-230.
209 M. J. Leitl, D. M. Zink, A. Schinabeck, T. Baumann, D. Volz and H. Yersin, *Top. Curr. Chem.*, 2016, **374**, 25.
210 H. Yersin, A. F. Rausch, R. Czerwieniec, T. Hofbeck and T. Fischer, *Coord. Chem. Rev.*, 2011, **255**, 2622-2652.
211 F. So, C. Adachi, H. Yersin, M. J. Leitl and R. Czerwieniec, *Organic Light Emitting Materials and Devices XVIII 2014*, Proc. of SPIE **9183**, 91830N.
212 K. Tsuge, *Chem. Lett.*, 2013, **42**, 204-208.
213 M. J. Leitl, F. R. Kuchle, H. A. Mayer, L. Wesemann and H. Yersin, *J. Phys. Chem. A*, 2013, **117**, 11823-11836.
214 D. M. Zink, M. Bachle, T. Baumann, M. Nieger, M. Kuhn, C. Wang, W. Klopper, U. Monkowius, T. Hofbeck, H. Yersin and S. Brase, *Inorg. Chem.*, 2013, **52**, 2292-2305.
215 A. Schinabeck, M. J. Leitl and H. Yersin, *J. Phys. Chem. Lett.*, 2018, **9**, 2848-2856.
216 P. Liang, A. Kobayashi, W. M. C. Sameera, M. Yoshida and M. Kato, *Inorg. Chem.*, 2018, **57**, 5929-5938.
217 A. Kobayashi, T. Hasegawa, M. Yoshida and M. Kato, *Inorg. Chem.*, 2016, **55**, 1978-1985.
218 K. Shimada, A. Kobayashi, Y. Ono, H. Ohara, T. Hasegawa, T. Taketsugu, E. Sakuda, S. Akagi, N. Kitamura and M. Kato, *J. Phys. Chem. C*, 2016, **120**, 16002-16011.
219 J. Nitsch, F. Lacemon, A. Lorbach, A. Eichhorn, F. Cisnetti and A. Steffen, *Chem. Commun.*, 2016, **52**, 2932-2935.
220 J. Chen, T. Teng, J.-Y. Wang, L. Kang, X.-L. Chen, L.-J. Xu, R. Yu and C.-Z. Lu, *Eur. J. Inorg. Chem.*, 2016, 3036-3041.
221 B.-L. Chen, L. Liu, X.-X. Zhong, A. M. Asiri, K. A. Alamry, G.-H. Li, F.-B. Li, N.-Y. Zhu, W.-Y. Wong and H.-M. Qin, *J. Coord. Chem.*, 2017, **70**, 3907-3919.
222 A. Tsuboyama, K. Kuge, M. Furugori, S. Okada, M. Hoshino and K. Ueno, *Inorg. Chem*., 2007, **46**, 1992-2001.
223 J. C. Deaton, S. C. Switalski, D. Y. Kondakov, R. H. Young, T. D. Pawlik, D. J. Giesen, S. B. Harkins, A. J. M. Miller, S. F. Mickenberg and J. C. Peters, *J. Am. Chem. Soc.*, 2010, **132**, 9499-9508.
224 D. Volz, D. M. Zink, T. Bocksrocker, J. Friedrichs, M. Nieger, T. Baumann, U. Lemmer and S. Bräse, *Chem. Mater.*, 2013, **25**, 3414-3426.
225 X. Hong, B. Wang, L. Liu, X.-X. Zhong, F.-B. Li, L. Wang, W.-Y. Wong, H.-M. Qin and Y. H. Lo, *J. Luminescence*, 2016, **180**, 64-72.
226 L. Hu and G. Xu, *Chem. Soc. Rev.*, 2010, **39**, 3275-3304.
227 W. Miao, J.-P. Choi and A. J. Bard, *J. Am. Chem. Soc.*, 2002, **124**, 14478-14485.
228 N. E. Tokel and A. J. Bard, *J. Am. Chem. Soc.*, 1972, **94**, 2862-2863.
229 S. Sun, Y. Yang, F. Liu, Y. Pang, J. Fan, L. Sun and X. Peng, *Anal. Chem.,* 2009, **81**, 10227-10231.
230 M. Zhou, J. Roovers, *Macromolecules,* 2001, **34**, 244-252.
231 M. Zhou, J. Roovers, J. P. Robertson, C. P. Grover, *Anal. Chem*., 2003, **75**, 6708-6717.
232 M. M. Richter and A. J. Bard, *Anal. Chem.,* 1998, **70**, 310-318.
233 S. Stagni, A. Palazzi, S. Zacchini, B. Ballarin, C. Bruno, M. Marcaccio, F. Paolucci, M. Monari, M. Carano and A. J. Bard, *Inorg. Chem.,* 2006, **45**, 695-709.
234 W. Kaim, A. Klein and M. Glöckle, *Acc. Chem. Res*., 2000, **33**, 755-763.
235 Q. H. Wei, Y. F. Lei, Y. N. Duan, F. N. Xiao, M. J. Li and G. N. Chen, *Dalton Trans.*, 2011, **40**, 11636-11642.
236 S. Welter, K. Brunner, J. W. Hofstraat and L. De Cola, *Nature*, 2003, **421**, 54-57.
237 E. H. Kim, S. Hong, J. M. Lee, D. N. Lee, Y. M. Jun, W.-Y. Lee and B. H. Kim, *Inorg. Chim. Acta*, 2009, **362**, 1577-1584.
238 M. Kim, C. H. Kang, S. Hong, W.-Y. Lee and B. H. Kim, *Inorg. Chim. Acta*, 2013, **395**, 145-150.
239 M. Li, J. Liu, C. Zhao and L. Sun, *J. Organomet. Chem.*, 2006, **691**, 4189-4195.
240 M. Li, J. Liu, L. Sun, J. Pan and C. Zhao, *J. Organomet. Chem.*, 2008, **693**, 46-56.
241 M. Staffilani, E. Höss, U. Giesen, E. Schneider, F. Hartl, H.-P. Josel and L. De Cola, *Inorg. Chem.,* 2003, **42**, 7789-7798.
242 S. Carrara, A. Aliprandi, C. F. Hogan and L. De Cola, *J. Am. Chem. Soc.*, 2017, **139**, 14605-14610.

243 K. Rangan, S. M. Arachchige, J. R. Brown and K. J. Brewer, *Energy. Environ. Sci.*, 2009, **2**, 410-419.
244 Z. Zou, J. Ye, K. Sayama and H. Arakawa, *Nature*, 2001, **414**, 625-627.
245 Y. You and W. Nam, *Chem. Soc. Rev.*, 2012, **41**, 7061-7084.
246 K. Maeda and K. Domen, *J. Phys. Chem. Lett.*, 2010, **1**, 2655-2661.
247 H. Ozawa, M. Haga and K. Sakai, *J. Am. Chem. Soc.*, 2006, **128**, 4926-4927.
248 H. Ozawa, Y. Yokoyama, M. A. Haga and K. Sakai, *Dalton Trans.*, 2007, 1197-1206.
249 T. Kowacs, L. O'Reilly, Q. Pan, A. Huijser, P. Lang, S. Rau, W. R. Browne, M. T. Pryce and J. G. Vos, *Inorg. Chem.*, 2016, **55**, 2685-2690.
250 L. O'Reilly, Q. Pan, N. Das, K. Wenderich, J. P. Korterik, J. G. Vos, M. T. Pryce and A. Huijser, *Chemphyschem*, 2018, **19**, 3084-3091.
251 M. G. Pfeffer, B. Schafer, G. Smolentsev, J. Uhlig, E. Nazarenko, J. Guthmuller, C. Kuhnt, M. Wachtler, B. Dietzek, V. Sundstrom and S. Rau, *Angew. Chem. Int. Ed.*, 2015, **54**, 5044-5048.
252 S. Tschierlei, M. Karnahl, M. Presselt, B. Dietzek, J. Guthmuller, L. Gonzalez, M. Schmitt, S. Rau and J. Popp, *Angew. Chem. Int. Ed.*, 2010, **49**, 3981-3984.
253 M. Karnahl, C. Kuhnt, F. Ma, A. Yartsev, M. Schmitt, B. Dietzek, S. Rau and J. Popp, *Chemphyschem*, 2011, **12**, 2101-2109.
254 S. Rau, B. Schafer, D. Gleich, E. Anders, M. Rudolph, M. Friedrich, H. Gorls, W. Henry and J. G. Vos, *Angew. Chem. Int. Ed.*, 2006, **45**, 6215-6218.
255 P. Lei, M. Hedlund, R. Lomoth, H. Rensmo, O. Johansson and L. Hammarström, *J. Am. Chem. Soc.*, 2008, **130**, 26-27.
256 M. Elvington, J. Brown, S. M. Arachchige and K. J. Brewer, *J. Am. Chem. Soc.*, 2007, **129**, 10644-10645.
257 T. A. White, S. L. Higgins, S. M. Arachchige and K. J. Brewer, *Angew. Chem. Int. Ed.*, 2011, **50**, 12209-12213.
258 G. F. Manbeck, E. Fujita and K. J. Brewer, *J. Am. Chem. Soc.*, 2017, **139**, 7843-7854.
259 A. Fihri, V. Artero, M. Razavet, C. Baffert, W. Leibl and M. Fontecave, *Angew. Chem. Int. Ed.*, 2008, **47**, 564-567.
260 C. Li, M. Wang, J. Pan, P. Zhang, R. Zhang and L. Sun, *J. Organomet. Chem.*, 2009, **694**, 2814-2819.
261 S. Jasimuddin, T. Yamada, K. Fukuju, J. Otsuki and K. Sakai, *Chem. Commun.*, 2010, **46**, 8466-8468.
262 S. Soman, G. Singh Bindra, A. Paul, R. Groarke, J. C. Manton, F. M. Connaughton, M. Schulz, D. Dini, C. Long, M. T. Pryce and J. G. Vos, *Dalton Trans.*, 2012, **41**, 12678-12680.
263 Y. Miyake, K. Nakajima, K. Sasaki, R. Saito, H. Nakanishi and Y. Nishibayashi, *Organometallics*, 2009, **28**, 5240-5243.
264 L.-C. Song, L.-X. Wang, M.-Y. Tang, C.-G. Li, H.-B. Song and Q.-M. Hu, *Organometallics*, 2009, **28**, 3834-3841.
265 P. Zhang, M. Wang, C. Li, X. Li, J. Dong and L. Sun, *Chem. Commun.*, 2010, **46**, 8806-8808.
266 X. Chen, C. Li, M. Gratzel, R. Kostecki and S. S. Mao, *Chem. Soc. Rev.*, 2012, **41**, 7909-7937.
267 F. E. Osterloh, *Chem. Soc. Rev.*, 2013, **42**, 2294-2320.
268 S. Berardi, S. Drouet, L. Francas, C. Gimbert-Surinach, M. Guttentag, C. Richmond, T. Stoll and A. Llobet, *Chem. Soc. Rev.*, 2014, **43**, 7501-7519.
269 S. Neudeck, S. Maji, I. Lopez, S. Meyer, F. Meyer and A. Llobet, *J. Am. Chem. Soc.*, 2014, **136**, 24-27.
270 L. Duan, F. Bozoglian, S. Mandal, B. Stewart, T. Privalov, A. Llobet and L. Sun, *Nat. Chem.*, 2012, **4**, 418-423.
271 P. Garrido-Barros, C. Gimbert-Surinach, R. Matheu, X. Sala and A. Llobet, *Chem. Soc. Rev.*, 2017, **46**, 6088-6098.
272 C. J. Richmond, R. Matheu, A. Poater, L. Falivene, J. Benet-Buchholz, X. Sala, L. Cavallo and A. Llobet, *Chem. Eur. J.,* 2014, **20**, 17282-17286.
273 R. Zong and R. P. Thummel, *J. Am. Chem. Soc.*, 2005, **127**, 12802-12803.
274 I. López, M. Z. Ertem, S. Maji, J. Benet-Buchholz, A. Keidel, U. Kuhlmann, P. Hildebrandt, C. J. Cramer, V. S. Batista and A. Llobet, *Angew. Chem. Int. Ed.*, 2014, **53**, 205-209.
275 D. E. Polyansky, J. T. Muckerman, J. Rochford, R. Zong, R. P. Thummel and E. Fujita, *J. Am. Chem. Soc.*, 2011, **133**, 14649-14665.
276 J. L. Boyer, D. E. Polyansky, D. J. Szalda, R. Zong, R. P. Thummel and E. Fujita, *Angew. Chem. Int. Ed.*, 2011, **50**, 12600-12604.
277 Y. M. Badiei, D. E. Polyansky, J. T. Muckerman, D. J. Szalda, R. Haberdar, R. Zong, R. P. Thummel and E. Fujita, *Inorg. Chem.*, 2013, **52**, 8845-8850.
278 J. T. Muckerman, M. Kowalczyk, Y. M. Badiei, D. E. Polyansky, J. J. Concepcion, R. Zong, R. P. Thummel and E. Fujita, *Inorg. Chem.*, 2014, **53**, 6904-6913.
279 S. W. Gersten, G. J. Samuels and T. J. Meyer, *J. Am. Chem. Soc.*, 1982, **104**, 4029-4030.
280 X. Sala, S. Maji, R. Bofill, J. García-Antón, L. Escriche and A. Llobet, *Acc. Chem. Res.*, 2014, **47**, 504-516.
281 F. Bozoglian, S. Romain, M. Z. Ertem, T. K. Todorova, C. Sens, J. Mola, M. Rodríguez, I. Romero, J. Benet-Buchholz, X. Fontrodona, C. J. Cramer, L. Gagliardi and A. Llobet, *J. Am. Chem. Soc.*, 2009, **131**, 15176-15187.
282 F. Li, Y. Jiang, B. Zhang, F. Huang, Y. Gao and L. Sun, *Angew. Chem. Int. Ed.*, 2012, **51**, 2417-2420.
283 Y. Gao, L. Duan, Z. Yu, X. Ding and L. Sun, *Faraday Discuss.*, 2014, **176**, 225-232.
284 N. Kaveevivitchai, R. Chitta, R. Zong, M. El Ojaimi and R. P. Thummel, *J. Am. Chem. Soc.*, 2012, **134**, 10721-10724.
285 T. M. Laine, M. D. Karkas, R. Z. Liao, T. Akermark, B. L. Lee, E. A. Karlsson, P. E. Siegbahn and B. Akermark, *Chem. Commun.*, 2015, **51**, 1862-1865.
286 Y. Jiang, F. Li, B. Zhang, X. Li, X. Wang, F. Huang and L. Sun, *Angew. Chem. Int. Ed.*, 2013, **52**, 3398-3401.
287 F. Li, C. Xu, X. Wang, Y. Wang, J. Du and L. Sun, *Chinese J. Catal.*, 2018, **39**, 446-452.
288 Y. Kuramochi, O. Ishitani and H. Ishida, *Coord. Chem. Rev.*, 2018, **373**, 333-356.
289 J. Hawecker, J.-M. Lehn, R. Ziessel, *J. Chem. Soc., Chem. Commun.*, 1983, 536-538.
290 Y. Tamaki and O. Ishitani, *ACS Catalysis*, 2017, **7**, 3394-3409.
291 E. Kimura, X. Bu, M. Shionoya, S. Wada and S. Maruyama, *Inorg. Chem.*, 1992, **31**, 4542-4546.
292 Y. Tamaki, T. Morimoto, K. Koike and O. Ishitani, *Proc. Natl. Acad. Sci. U S A*, 2012, **109**, 15673-15678.
293 Y. Tamaki, K. Koike and O. Ishitani, *Chem. Sci.*, 2015, **6**, 7213-7221.
294 E. Kimura, S. Wada, M. Shionoya and Y. Okazaki, *Inorg. Chem.*, 1994, **33**, 770-778.
295 N. Komatsuzaki, Y. Himeda, T. Hirose, H. Sugihara and K. Kasuga, *Bull. Chem. Soc. Jpn.*, 1999, **72**, 725-731.
296 Y. Kuramochi and O. Ishitani, *Inorg. Chem.*, 2016, **55**, 5702-5709.

297 Y. Tamaki, K. Koike, T. Morimoto, Y. Yamazaki and O. Ishitani, *Inorg. Chem.*, 2013, **52**, 11902-11909.
298 K. Kiyosawa, N. Shiraishi, T. Shimada, D. Masui, H. Tachibana, S. Takagi, O. Ishitani, D. A. Tryk and H. Inoue, *J. Phys. Chem. C*, 2009, **113**, 11667-11673.
299 J. Schneider, K. Q. Vuong, J. A. Calladine, X. Z. Sun, A. C. Whitwood, M. W. George and R. N. Perutz, *Inorg. Chem.*, 2011, **50**, 11877-11889.
300 G. Dordelmann, T. Meinhardt, T. Sowik, A. Krueger and U. Schatzschneider, *Chem. Commun.*, 2012, **48**, 11528-11530.
301 C. D. Windle, M. W. George, R. N. Perutz, P. A. Summers, X. Z. Sun and A. C. Whitwood, *Chem. Sci.*, 2015, **6**, 6847-6864.
302 C. Matlachowski, B. Braun, S. Tschierlei and M. Schwalbe, *Inorg. Chem.*, 2015, **54**, 10351-10360.
303 B. Gholamkhass, H. Mametsuka, K. Koike, T. Tanabe, M. Furue, O. Ishitani, *Inorg. Chem*., 2005, **44**, 2326-2336.
304 S. Sato, K. Koike, H. Inoue and O. Ishitani, *Photochem. Photobiol. Sci.*, 2007, **6**, 454-461.
305 K. Koike, S. Naito, S. Sato, Y. Tamaki and O. Ishitani, *J. Photochem. Photobio. A: Chemistry*, 2009, **207**, 109-114.
306 Y. Tamaki, K. Watanabe, K. Koike, H. Inoue, T. Morimoto and O. Ishitani, *Faraday Discuss.*, 2012, **155**, 115-127.
307 E. Kato, H. Takeda, K. Koike, K. Ohkubo and O. Ishitani, *Chem. Sci.*, 2015, **6**, 3003-3012.
308 T. Nakajima, Y. Tamaki, K. Ueno, E. Kato, T. Nishikawa, K. Ohkubo, Y. Yamazaki, T. Morimoto and O. Ishitani, *J. Am. Chem. Soc.*, 2016, **138**, 13818-13821.
309 K. Ohkubo, Y. Yamazaki, T. Nakashima, Y. Tamaki, K. Koike and O. Ishitani, *J. Catal.*, 2016, **343**, 278-289.
310 A. Nakada, K. Koike, T. Nakashima, T. Morimoto and O. Ishitani, *Inorg. Chem.*, 2015, **54**, 1800-1807.
311 A. Nakada, K. Koike, K. Maeda and O. Ishitani, *Green Chem.*, 2016, **18**, 139-143.
312 S. Meister, R. O. Reithmeier, A. Ogrodnik and B. Rieger, *ChemCatChem*, 2015, **7**, 3562-3569.
313 Z.-Y. Bian, H. Wang, W.-F. Fu, L. Li and A.-Z. Ding, *Polyhedron*, 2012, **32**, 78-85.
314 Z. Y. Bian, K. Sumi, M. Furue, S. Sato, K. Koike and O. Ishitani, *Dalton Trans.*, 2009, 983-993.
315 Y. Yamazaki, A. Umemoto and O. Ishitani, *Inorg. Chem.*, 2016, **55**, 11110-11124.
316 Y. Yamazaki and O. Ishitani, *Chem. Sci.*, 2018, **9**, 1031-1041.
317 M. Furue, T. Yoshidzumi, S. Kinoshita, T. Kushida, S. Nozakura and M. Kamachi, *Bull. Chem. Soc. Jpn*., 1991, **64**, 1632-1640.
318 M. Furue, M. Naiki, Y. Kanematsu, T. Kushida, and M. Kamachi, *Coord. Chem. Rev*., 1991, **111**, 221-226.
319 A. Fujishima and K. Honda, *Nature*, 1972, **238**, 37-38.
320 T. Hisatomi, J. Kubota and K. Domen, *Chem. Soc. Rev.*, 2014, **43**, 7520-7535.
321 C. Jiang, S. J. A. Moniz, A. Wang, T. Zhang and J. Tang, *Chem. Soc. Rev.*, 2017, **46**, 4645-4660.
322 B. O'Regan and M. Grätzel, *Nature*, 1991, **353**, 737-740.
323 D. L. Ashford, M. K. Gish, A. K. Vannucci, M. K. Brennaman, J. L. Templeton, J. M. Papanikolas and T. J. Meyer, *Chem. Rev.*, 2015, **115**, 13006-13049.
324 G. Leem, B. D. Sherman and K. S. Schanze, *Nano Converg.*, 2017, **4**, 37.
325 F. Li, K. Fan, B. Xu, E. Gabrielsson, Q. Daniel, L. Li and L. Sun, *J. Am. Chem. Soc.*, 2015, **137**, 9153-9159.
326 J. R. Swierk and T. E. Mallouk, *Chem. Soc. Rev.*, 2013, **42**, 2357-2387.
327 J. A. Treadway, J. A. Moss and T. J. Meyer, *Inorg. Chem.*, 1999, **38**, 4386-4387.
328 W. J. Youngblood, S.-H. A. Lee, Y. Kobayashi, E. A. Hernandez-Pagan, P. G. Hoertz, T. A. Moore, A. L. Moore, D. Gust and T. E. Mallouk, *J. Am. Chem. Soc.*, 2009, **131**, 926-927.
329 G. F. Moore, J. D. Blakemore, R. L. Milot, J. F. Hull, H.-e. Song, L. Cai, C. A. Schmuttenmaer, R. H. Crabtree and G. W. Brudvig, *Energy Environ. Sci.*, 2011, **4**, 2389-2392.
330 K. Hanson, D. A. Torelli, A. K. Vannucci, M. Kyle Brennaman, H. Luo, L. Alibabaei, W. Song, D. L. Ashford, M. R. Norris, C. R. K. Glasson, J. J. Concepcion and T. J. Meyer, *Angew. Chem. Int. Ed*., 2012, **51**, 12782-12785.
331 B. D. Sherman, D. L. Ashford, A. M. Lapides, M. V. Sheridan, K.-R. Wee and T. J. Meyer, *J. Phys. Chem. Lett.*, 2015, **6**, 3213-3217.
332 Y. Gao, X. Ding, J. Liu, L. Wang, Z. Lu, L. Li and L. Sun, *J. Am. Chem. Soc.*, 2013, **135**, 4219-4222.
333 J. J. Concepcion, M.-K. Tsai, J. T. Muckerman and T. J. Meyer, *J. Am. Chem. Soc.*, 2010, **132**, 1545-1557.
334 W. Song, C. R. K. Glasson, H. Luo, K. Hanson, M. K. Brennaman, J. J. Concepcion and T. J. Meyer, *J. Phys. Chem. Lett.*, 2011, **2**, 1808-1813.
335 B. Gholamkhass, K. Koike, N. Negishi, H. Hori, T. Sano and K. Takeuchi, *Inorg. Chem*., 2003, **42**, 2919-2932.
336 D. L. Ashford, W. Song, J. J. Concepcion, C. R. Glasson, M. K. Brennaman, M. R. Norris, Z. Fang, J. L. Templeton and T. J. Meyer, *J. Am. Chem. Soc.*, 2012, **134**, 19189-19198.
337 L. Wang, D. L. Ashford, D. W. Thompson, T. J. Meyer and J. M. Papanikolas, *J. Phys. Chem. C*, 2013, **117**, 24250-24258.
338 L. Alibabaei, M. K. Brennaman, M. R. Norris, B. Kalanyan, W. Song, M. D. Losego, J. J. Concepcion, R. A. Binstead, G. N. Parsons and T. J. Meyer, *Proc. Natl. Acad. Sci. U S A*, 2013, **110**, 20008-20013.
339 L. Zhang, Y. Gao, X. Ding, Z. Yu and L. Sun, *ChemSusChem*, 2014, **7**, 2801-2804.
340 M. Yamamoto, L. Wang, F. Li, T. Fukushima, K. Tanaka, L. Sun and H. Imahori, *Chem. Sci.*, 2016, **7**, 1430-1439.
341 B. D. Sherman, M. V. Sheridan, K. R. Wee, S. L. Marquard, D. Wang, L. Alibabaei, D. L. Ashford and T. J. Meyer, *J. Am. Chem. Soc.*, 2016, **138**, 16745-16753.
342 B. D. Sherman, Y. Xie, M. V. Sheridan, D. Wang, D. W. Shaffer, T. J. Meyer and J. J. Concepcion, *ACS Energy Lett.*, 2017, **2**, 124-128.
343 D. Wang, B. H. Farnum, M. V. Sheridan, S. L. Marquard, B. D. Sherman and T. J. Meyer, *ACS Appl. Mater. Interfaces*, 2017, **9**, 33533-33538.
344 D. Wang, S. L. Marquard, L. Troian-Gautier, M. V. Sheridan, B. D. Sherman, Y. Wang, M. S. Eberhart, B. H. Farnum, C. J. Dares and T. J. Meyer, *J. Am. Chem. Soc.*, 2018, **140**, 719-726.
345 G. Sahara, R. Abe, M. Higashi, T. Morikawa, K. Maeda, Y. Ueda and O. Ishitani, *Chem. Commun.*, 2015, **51**, 10722-10725.
346 R. M. Duke, E. B. Veale, F. M. Pfeffer, P. E. Kruger and T. Gunnlaugsson, *Chem. Soc. Rev.*, 2010, **39**, 3936-3953.
347 X. Huang, J. Song, B. C. Yung, X. Huang, Y. Xiong and X. Chen, *Chem. Soc. Rev.*, 2018, **47**, 2873-2920.
348 Z. Liu, W. He and Z. Guo, *Chem. Soc. Rev.*, 2013, **42**, 1568-1600.
349 Y. You, *J. Chin. Chem. Soc*., 2018, **65**, 352-367.
350 X. He and V. W.-W. Yam, *Coord. Chem. Rev.*, 2011, **255**, 2111-2123.

351 K. Wong and V. Yam, *Coord. Chem. Rev.*, 2007, **251**, 2477-2488.
352 M. C. Yeung and V. W. Yam, *Chem. Soc. Rev.*, 2015, **44**, 4192-4202.
353 D. J. Cram and J. M. Cram, *Science*, 1974, **183**, 803-809.
354 D. J. Cram, *Angew. Chem. Int. Ed*., 1988, **27**, 1009-1020.
355 V. W.-W. Yam, C.-K. Li and C.-L. Chan, *Angew. Chem. Int. Ed*., 1998, **37**, 2857-2859.
356 C.-K. Li, X.-X. Lu, K. M.-C. Wong, C.-L. Chan, N. Zhu and V. W.-W. Yam, *Inorg. Chem.*, 2004, **43**, 7421-7430.
357 C.-K. Li, E. C.-C. Cheng, N. Zhu and V. W.-W. Yam, *Inorg. Chim. Acta*, 2005, **358**, 4191-4200.
358 X.-X. Lu, C.-K. Li, E. C.-C. Cheng, N. Zhu and V. W.-W. Yam, *Inorg. Chem.*, 2004, **43**, 2225-2227.
359 S. H. Kim, H. J. Kim, J. Yoon and J. S. Kim, *Fluorescent chemosensors the pathway to molecular electronics. In Calixarenes in the Nanoworld*, 2007, 311-333.
360 B. Valeur and I. Leray, *Coord. Chem. Rev.*, 2000, **205**, 3-40.
361 V. W.-W. Yam, S.-K. Yip, L.-H. Yuan, K.-L. Cheung, N. Zhu and K.-K. Cheung, *Organometallics*, 2003, **22**, 2630-2637.
362 X. He, W. H. Lam, N. Zhu and V. W. Yam, *Chem. Eur. J.,* 2009, **15**, 8842-8851.
363 H.-S. Lo, S.-K. Yip, K. M.-C. Wong, N. Zhu and V. W.-W. Yam, *Organometallics*, 2006, **25**, 3537-3540.
364 P. Zhang, L. Pei, Y. Chen, W. Xu, Q. Lin, J. Wang, J. Wu, Y. Shen, L. Ji and H. Chao, *Chem. Eur. J.,* 2013, **19**, 15494-15503.
365 T. D. Ashton, K. A. Jolliffe and F. M. Pfeffer, *Chem. Soc. Rev.*, 2015, **44**, 4547-4595.
366 P. A. Gale and C. Caltagirone, *Chem. Soc. Rev.*, 2015, **44**, 4212-4227.
367 H. J. Mo, Y. Shen and B. H. Ye, *Inorg. Chem.*, 2012, **51**, 7174-7184.
368 X. He, F. Herranz, E. C. Cheng, R. Vilar and V. W. Yam, *Chem. Eur. J.,* 2010, **16**, 9123-9131.
369 X. He, W. H. Lam, E. C. Cheng and V. W. Yam, *Chem. Eur. J.,* 2015, **21**, 8447-8454.
370 G. Li, Y. Chen, J. Wang, Q. Lin, J. Zhao, L. Ji and H. Chao, *Chem. Sci.*, 2013, **4**, 4426-4433.
371 E. B. Ford, V. Lystad and F. A. Rasio, *Nature*, 2005, **434**, 873-876.
372 A. Lichtenstein, E. Havivi, R. Shacham, E. Hahamy, R. Leibovich, A. Pevzner, V. Krivitsky, G. Davivi, I. Presman, R. Elnathan, Y. Engel, E. Flaxer and F. Patolsky, *Nat. Commun.*, 2014, **5**, 4195.
373 X. Sun, Y. Wang and Y. Lei, *Chem. Soc. Rev.*, 2015, **44**, 8019-8061.
374 M. H. Wong, J. P. Giraldo, S. Y. Kwak, V. B. Koman, R. Sinclair, T. T. Lew, G. Bisker, P. Liu and M. S. Strano, *Nat. Mater.*, 2017, **16**, 264-272.
375 N. Jiang, G. Li, W. Che, D. Zhu, Z. Su and M. R. Bryce, *J. Mater. Chem. C*, 2018, **6**, 11287-11291.
376 D. Peng, L. Zhang, F. F. Li, W. R. Cui, R. P. Liang and J. D. Qiu, *ACS Appl Mater. Interfaces*, 2018, **10**, 7315-7323.
377 C. F. Pereira, F. Figueira, R. F. Mendes, J. Rocha, J. T. Hupp, O. K. Farha, M. M. Q. Simoes, J. P. C. Tome and F. A. A. Paz, *Inorg. Chem.*, 2018, **57**, 3855-3864.
378 T. Fei, K. Jiang and T. Zhang, *Sensors and Actuators B*: *Chemical*, 2014, **199**, 148-153.
379 X. G. Hou, Y. Wu, H. T. Cao, H. Z. Sun, H. B. Li, G. G. Shan and Z. M. Su, *Chem. Commun.*, 2014, **50**, 6031-6034.
380 B. Xu, X. Wu, H. Li, H. Tong and L. Wang, *Macromolecules*, 2011, **44**, 5089-5092.
381 L.-L. Wen, X.-G. Hou, G.-G. Shan, W.-L. Song, S.-R. Zhang, H.-Z. Sun and Z.-M. Su, *J. Mater. Chem. C*, 2017, **5**, 10847-10854.
382 W. Che, G. Li, X. Liu, K. Shao, D. Zhu, Z. Su and M. R. Bryce, *Chem. Commun.*, 2018, **54**, 1730-1733.
383 K. Kavallieratos, J. M. Rosenberg, W.-Z. Chen and T. Ren, *J. Am. Chem. Soc.*, 2005, **127**, 6514-6515.
384 R. Sun, X. Huo, H. Lu, S. Feng, D. Wang and H. Liu, *Sensors and Actuators B*: *Chemical*, 2018, **265**, 476-487.
385 J. Li and K. Pu, *Chem. Soc. Rev.*, 2019, **48**, 38-71.
386 K. K. Ng and G. Zheng, *Chem. Rev.*, 2015, **115**, 11012-11042.
387 S. K. Fung, T. Zou, B. Cao, T. Chen, W. P. To, C. Yang, C. N. Lok and C. M. Che, *Nat. Commun.*, 2016, **7**, 10655.
388 T. Huang, Q. Yu, S. Liu, W. Huang and Q. Zhao, *Dalton Trans.*, 2018, **47**, 7628-7633.
389 S. Sun, J. Wang, D. Mu, J. Wang, Y. Bao, B. Qiao and X. Peng, *Chem. Commun.*, 2014, **50**, 9149-9152.
390 X. Zheng, H. Tang, C. Xie, J. Zhang, W. Wu and X. Jiang, *Angew. Chem. Int. Ed.*, 2015, **54**, 8094-8099.
391 D.-L. Ma, C. Wu, W. Tang, A.-R. Gupta, F.-W. Lee, G. Lic and C.-H. Leung, *J. Mater. Chem. B*, 2018, **6**, 537-544.
392 Y. You, *Curr. Opin. Chem. Biol.*, 2013, **17**, 699-707.
393 Q. Zhao, C. Huang and F. Li, *Chem. Soc. Rev.*, 2011, **40**, 2508-2524.
394 J. M. Vanderkooi, G. Maniara, T. J. Green and D. F. Wilson, *J. Bio. Chem*., 1987, **262**, 5476-5482.
395 Y. Feng, J. Cheng, L. Zhou, X. Zhou and H. Xiang, *Analyst*, 2012, **137**, 4885-4901.
396 D. B. Papkovsky and R. I. Dmitriev, *Chem. Soc. Rev.*, 2013, **42**, 8700-8732.
397 C. Shi, D. Tu, Q. Yu, H. Liang, Y. Liu, Z. Li, H. Yan, Q. Zhao and W. Huang, *Chem. Eur. J.,* 2014, **20**, 16550-16557.
398 T. Yoshihara, Y. Yamaguchi, M. Hosaka, T. Takeuchi and S. Tobita, *Angew. Chem. Int. Ed.*, 2012, **51**, 4148-4151.
399 H. Chen, B. Dong, Y. Tang and W. Lin, *Acc. Chem. Res.*, 2017, **50**, 1410-1422.
400 C. Shi, Q. Li, L. Zou, Z. Lv, A. Yuan and Q. Zhao, *Eur. J. Inorg. Chem.*, 2018, 1131-1136.
401 T. Huang, X. Tong, Q. Yu, H. Yang, S. Guo, S. Liu, Q. Zhao, K. Y. Zhang and W. Huang, *J. Mater. Chem. C*, 2016, **4**, 10638-10645.
402 R. I. Dmitriev and D. B. Papkovsky, *Cell. Mol. Life Sci.*, 2012, **69**, 2025-2039.
403 U. Neugebauer, Y. Pellegrin, M. Devocelle, R. J. Forster, W. Signac, N. Moran and T. E. Keyes, *Chem. Commun.*, 2008, 5307-5309.
404 A. Martin, A. Byrne, C. S. Burke, R. J. Forster and T. E. Keyes, *J. Am. Chem. Soc.*, 2014, **136**, 15300-15309.
405 Y. Chen, T. W. Rees, L. Ji and H. Chao, *Curr. Opin. Chem. Biol.*, 2018, **43**, 51-57.
406 S. A. Detmer and D. C. Chan, *Nat. Rev. Mol. Cell. Biol.*, 2007, **8**, 870-879.
407 J. Nunnari and A. Suomalainen, *Cell*, 2012, **148**, 1145-1159.
408 V. Fernandez-Moreira, F. L. Thorp-Greenwood and M. P. Coogan, *Chem. Commun.*, 2010, **46**, 186-202.
409 M. J. Pisani, D. K. Weber, K. Heimann, J. G. Collins and F. R. Keene, *Metallomics*, 2010, **2**, 393-396.
410 D. L. Ma, H. Z. He, K. H. Leung, D. S. Chan and C. H. Leung, *Angew. Chem. Int. Ed.*, 2013, **52**, 7666-7682.
411 A. D. Richards and A. Rodger, *Chem. Soc. Rev.*, 2007, **36**, 471-483.

412 A. E. Friedman, J.-C. Chambron, J.-P. Sauvage, N. J. Turro and J. K. Barton, *J. Am. Chem. Soc.*, 1990, **112**, 4960-4962.

413 B. Önfelt, P. Lincoln and B. Nordén, *J. Am. Chem. Soc.*, 2001, **123**, 3630-3637.

414 Y. Liu, A. Chouai, N. N. Degtyareva, D. A. Lutterman, K. R. Dunbar and C. Turro, *J. Am. Chem. Soc.*, 2005, **127**, 10796-10797.

415 D. L. Carlson, D. H. Huchital, E. J. Mantilla, R. D. Sheardy and W. R. Murphy, Jr., *J. Am. Chem. Soc*., 1993, **115**, 6424-6425.

416 E. Tuite, P. Lincoln and B. Nordén, *J. Am. Chem. Soc*., 1997, **119**, 239-240.

417 B. Önfelt, P. Lincoln and B. Nordén, *J. Am. Chem. Soc*., 1999, **121**, 10846-10847.

418 T. Paramanathan, F. Westerlund, M. J. McCauley, I. Rouzina, P. Lincoln and M. C. Williams, *J. Am. Chem. Soc*., 2008, **130**, 3752-3753.

419 P. Nordell, F. Westerlund, A. Reymer, A. H. El-Sagheer, T. Brown, B. Nordén and P. Lincoln, *J. Am. Chem. Soc*., 2008, **130**, 14651-14658.

420 C. Rajput, R. Rutkaite, L. Swanson, I. Haq and J. A. Thomas, *Chem. Eur. J.,* 2006, **12**, 4611-4619.

421 D. A. Lutterman, A. Chouai, Y. Liu, Y. Sun, C. D. Stewart, K. R. Dunbar and C. Turro, *J. Am. Chem. Soc.*, 2008, **130**, 1163-1170.

422 C. A. Puckett and J. K. Barton, *J. Am. Chem. Soc.*, 2007, **129**, 46-47.

423 A. J. Amoroso, M. P. Coogan, J. E. Dunne, V. Fernandez-Moreira, J. B. Hess, A. J. Hayes, D. Lloyd, C. Millet, S. J. Pope and C. Williams, *Chem. Commun.*, 2007, 3066-3068.

424 M. R. Gill, J. Garcia-Lara, S. J. Foster, C. Smythe, G. Battaglia and J. A. Thomas, *Nat. Chem.*, 2009, **1**, 662-667.

425 P. S. Chelushkin and S. P. Tunik, *Progress in Photon Science*, Springer Press, 2019, 109-128.

426 E. Baggaley, J. A. Weinstein and J. A. G. Williams, *Time-Resolved Emission Imaging Microscopy Using Phosphorescent Metal Complexes: Taking FLIM and PLIM to New Lengths*, Springer Press, 2015, **165**, 205-256.

427 K. Y. Zhang, Q. Yu, H. Wei, S. Liu, Q. Zhao and W. Huang, *Chem. Rev*., 2018, **118**, 1770-1839.

428 F. R. Svensson, M. Abrahamsson, N. Strömberg, A. G. Ewing and P. Lincoln, *J. Phys. Chem. Lett*., 2011, **2**, 397-401.

429 A. Wragg, M. R. Gill, D. Turton, H. Adams, T. M. Roseveare, C. Smythe, X. Su and J. A. Thomas, *Chem. Eur. J.,* 2014, **20**, 14004-14011.

430 T. F. Anjong, G. Kim, H. Y. Jang, J. Yoon and J. Kim, *New J. Chem*., 2017, **41**, 377-386.

431 L. Lu, M. Wang, Z. Mao, T. S. Kang, X. P. Chen, J. J. Lu, C. H. Leung and D. L. Ma, *Sci. Rep.*, 2016, **6**, 22458.

432 G. Bridge, S. Rashid and S. A. Martin, *Cancers (Basel)*, 2014, **6**, 1597-1614.

433 T. J. Kinsella, *Clin. Cancer Res.*, 2009, **15**, 1853-1859.

434 S. A. Martin, C. J. Lord and A. Ashworth, *Clin. Cancer Res.*, 2010, **16**, 5107-5113.

435 J. F. Lovell, T. W. B. Liu, J. Chen and G. Zheng, *Chem. Rev*., 2010, **110**, 2839-2857.

436 T. J. Dougherty, C. J. Gomer, B. W. Henderson, G. Jori, D. Kessel, M. Korbelik, J. Moan, Q. Peng, *J. National Cancer Institute*, 1998, **90**, 889-905.

437 P. Agostinis, K. Berg, K. A. Cengel, T. H. Foster, A. W. Girotti, S. O. Gollnick, S. M. Hahn, M. R. Hamblin, A. Juzeniene, D. Kessel, M. Korbelik, J. Moan, P. Mroz, D. Nowis, J. Piette, B. C. Wilson and J. Golab, *CA Cancer J. Clin.*, 2011, **61**, 250-281.

438 D. W. Felsher, *Nat. Rev. Cancer*, 2003, **3**, 375-380.

439 M. Ethirajan, Y. Chen, P. Joshi and R. K. Pandey, *Chem. Soc. Rev.*, 2011, **40**, 340-362.

440 A. Kamkaew, S. H. Lim, H. B. Lee, L. V. Kiew, L. Y. Chung and K. Burgess, *Chem. Soc. Rev.*, 2013, **42**, 77-88.

441 W. Lv, Z. Zhang, K. Y. Zhang, H. Yang, S. Liu, A. Xu, S. Guo, Q. Zhao and W. Huang, *Angew. Chem. Int. Ed.*, 2016, **55**, 9947-9951.

442 F. E. Poynton, S. A. Bright, S. Blasco, D. C. Williams, J. M. Kelly and T. Gunnlaugsson, *Chem. Soc. Rev.*, 2017, **46**, 7706-7756.

443 B. Liu, S. Monro, L. Lystrom, C. G. Cameron, K. Colon, H. Yin, S. Kilina, S. A. McFarland and W. Sun, *Inorg. Chem.*, 2018, **57**, 9859-9872.

444 C. Wang and Z. Li, *Mater. Chem. Front*., 2017, **1**, 2174-2194.

445 Z. Chi, X. Zhang, B. Xu, X. Zhou, C. Ma, Y. Zhang, S. Liu and J. Xu, *Chem. Soc. Rev.*, 2012, **41**, 3878-3896.

446 Y. Dong, B. Xu, J. Zhang, X. Tan, L. Wang, J. Chen, H. Lv, S. Wen, B. Li, L. Ye, B. Zou and W. Tian, *Angew. Chem. Int. Ed.*, 2012, **51**, 10782-10785.

447 Z. Ma, Z. Wang, X. Meng, Z. Ma, Z. Xu, Y. Ma and X. Jia, *Angew. Chem. Int. Ed.*, 2016, **55**, 519-522.

448 J. Yang, Z. Ren, Z. Xie, Y. Liu, C. Wang, Y. Xie, Q. Peng, B. Xu, W. Tian, F. Zhang, Z. Chi, Q. Li and Z. Li, *Angew. Chem. Int. Ed.*, 2017, **56**, 880-884.

449 S. Perruchas, X. F. Le Goff, S. Maron, I. Maurin, F. Guillen, A. Garcia, T. Gacoin and J.-P. Boilot, *J. Am. Chem. Soc.*, 2010, **132**, 10967-10969.

450 Q. Benito, B. Baptiste, A. Polian, L. Delbes, L. Martinelli, T. Gacoin, J. P. Boilot and S. Perruchas, *Inorg. Chem.*, 2015, **54**, 9821-9825.

451 K. Yang, S. L. Li, F. Q. Zhang and X. M. Zhang, *Inorg. Chem.*, 2016, **55**, 7323-7325.

452 V. N. Kozhevnikov, B. Donnio and D. W. Bruce, *Angew. Chem. Int. Ed.*, 2008, **47**, 6286-6289.

453 G. G. Shan, H. B. Li, H. T. Cao, D. X. Zhu, P. Li, Z. M. Su and Y. Liao, *Chem. Commun.*, 2012, **48**, 2000-2002.

454 S. Lu, G. Xiao, L. Sui, T. Feng, X. Yong, S. Zhu, B. Li, Z. Liu, B. Zou, M. Jin, J. S. Tse, H. Yan and B. Yang, *Angew. Chem. Int. Ed.*, 2017, **56**, 6187-6191.

455 K. Ishizuki, H. Oka, D. Aoki, R. Goseki and H. Otsuka, *Chem. Eur. J*., 2018, **24**, 3170-3173.

456 C. Calvino, L. Neumann, C. Weder and S. Schrettl, *J. Poly. Sci., Part A: Poly. Chem*., 2017, **55**, 640-652.

457 M. Karman, E. Verde-Sesto, C. Weder and Y. C. Simon, *ACS Macro Lett*., 2018, **7**, 1099-1104.

458 A. K. Chaudhari and J. C. Tan, *Nanoscale*, 2018, **10**, 3953-3960.

459 D. Umeyama, Y. Lin and H. I. Karunadasa, *Chem. Mater*., 2016, **28**, 3241-3244.

460 A. Jaffe, Y. Lin, W. L. Mao and H. I. Karunadasa, *J. Am. Chem. Soc.*, 2015, **137**, 1673-1678.

461 Y. Han, H.-T. Cao, H.-Z. Sun, Y. Wu, G.-G. Shan, Z.-M. Su, X.-G. Hou and Y. Liao, *J. Mater. Chem. C*, 2014, **2**, 7648-7655.

462 X.-Y. Wang, J. Zhang, Y.-B. Dong, Y. Zhang, J. Yin and S. H. Liu, *Dyes and Pigments*, 2018, **156**, 74-81.

463 G.-G. Shan, H.-B. Li, D.-X. Zhu, Z.-M. Su and Y. Liao, *J. Mater. Chem*., 2012, **22**, 12736-12744.

464 T. Seki, K. Sakurada and H. Ito, *Angew. Chem. Int. Ed.*, 2013, **52**, 12828-12832.

465 T. Seki, Y. Takamatsu and H. Ito, *J. Am. Chem. Soc.*, 2016, **138**, 6252-6260.

466 T. Seki, K. Ida and H. Ito, *Mater. Chem. Front*., 2018, **2**, 1195-1200.

467 Z. Chen, G. Liu, S. Pu and S. H. Liu, *Dyes and Pigments*, 2018, **159**, 499-505.
468 Y. Hu, Y. Dong, X. Sun, G. Zuo, J. Yin and S. H. Liu, *Dyes and Pigments*, 2018, **156**, 260-266.
469 H. Ito, M. Muromoto, S. Kurenuma, S. Ishizaka, N. Kitamura, H. Sato and T. Seki, *Nat. Commun.*, 2013, **4**, 2009.
470 M. Jin, T. Seki and H. Ito, *J. Am. Chem. Soc.*, 2017, **139**, 7452-7455.
471 M. Jin, T. Sumitani, H. Sato, T. Seki and H. Ito, *J. Am. Chem. Soc.*, 2018, **140**, 2875-2879.
472 K. Kawaguchi, T. Seki, T. Karatsu, A. Kitamura, H. Ito and S. Yagai, *Chem. Commun.*, 2013, **49**, 11391-11393.
473 H. Ito, T. Saito, N. Oshima, N. Kitamura, S. Ishizaka, Y. Hinatsu, M. Wakeshima, M. Kato, K. Tsuge and M. Sawamura, *J. Am. Chem. Soc.*, 2008, **130**, 10044-10045.
474 C. H. Woodall, C. M. Beavers, J. Christensen, L. E. Hatcher, M. Intissar, A. Parlett, S. J. Teat, C. Reber and P. R. Raithby, *Angew. Chem. Int. Ed.*, 2013, **52**, 9691-9694.
475 J. Liang, F. Hu, X. Lv, Z. Chen, Z. Chen, J. Yin, G.-A. Yu and S. H. Liu, *Dyes and Pigments*, 2012, **95**, 485-490.
476 T. Seki, T. Ozaki, T. Okura, K. Asakura, A. Sakon, H. Uekusa and H. Ito, *Chem. Sci.*, 2015, **6**, 2187-2195.
477 Z. Chen, J. Zhang, M. Song, J. Yin, G. A. Yu and S. H. Liu, *Chem. Commun.*, 2015, **51**, 326-329.
478 Z. Chen, Z. Li, F. Hu, G.-A. Yu, J. Yin and S. H. Liu, *Dyes and Pigments*, 2016, **125**, 169-178.
479 Z. Chen, Z. Li, L. Yang, J. Liang, J. Yin, G.-A. Yu and S. H. Liu, *Dyes and Pigments*, 2015, **121**, 170-177.
480 M. Song, Z. Chen, G.-A. Yu, J. Yin and S. H. Liu, *Chin. J. Org. Chem.*, 2015, **35**, 681-687.
481 Z. Chen, G. Liu, S. Pu and S. H. Liu, *Dyes and Pigments*, 2018, **152**, 54-59.
482 M. Jin, T. Seki and H. Ito, *Chem. Commun.*, 2016, **52**, 8083-8086.
483 A. Deak, C. Jobbagy, G. Marsi, M. Molnar, Z. Szakacs and P. Baranyai, *Chem. Eur. J.*, 2015, **21**, 11495-11508.
484 S. Yagai, T. Seki, H. Aonuma, K. Kawaguchi, T. Karatsu, T. Okura, A. Sakon, H. Uekusa and H. Ito, *Chem. Mater.*, 2016, **28**, 234-241.
485 J. Liang, Z. Chen, L. Xu, J. Wang, J. Yin, G.-A. Yu, Z.-N. Chen and S. H. Liu, *J. Mater. Chem. C*, 2014, **2**, 2243-2250.
486 G.-G. Shan, H.-B. Li, H.-Z. Sun, D.-X. Zhu, H.-T. Cao and Z.-M. Su, *J. Mater. Chem. C*, 2013, **1**, 1440-1449.
487 G.-G. Shan, H.-B. Li, H.-T. Cao, H.-Z. Sun, D.-X. Zhu, Z.-M. Su, *Dyes and Pigments*, 2013, **99**, 1082-1090.
488 Y. Han, H.-T. Cao, H.-Z. Sun, G.-G. Shan, Y. Wu, Z.-M. Su and Y. Liao, *J. Mater. Chem. C*, 2015, **3**,2341-2349.
489 Z. Song, R. Liu, Y. Li, H. Shi, J. Hu, X. Cai and H. Zhu, *J. Mater. Chem. C*, 2016, **4**, 2553-2559.
490 K.-Y. Zhao, G.-G. Shan, Q. Fu and Z.-M. Su, *Organometallics*, 2016, **35**, 3996-4001.
491 K.-Y. Zhao, H.-T. Mao, L.-L. Wen, G.-G. Shan, Q. Fu, H.-Z. Sun and Z.-M. Su, *J. Mater. Chem. C*, 2018, **6**, 11686-11693.
492 G. G. Shan, H. B. Li, J. S. Qin, D. X. Zhu, Y. Liao and Z. M. Su, *Dalton Trans.*, 2012, **41**, 9590-9593.
493 Y. Wang, T. Yang, X. Liu, G. Li, W. Che, D. Zhu and Z. Su, *J. Mater. Chem. C*, 2018, **6**, 12217-12223.
494 S. Mizukami, H. Houjou, K. Sugaya, E. Koyama, H. Tokuhisa, T. Sasaki and M. Kanesato, *Chem. Mater.*, 2005, **17**, 50-56.
495 H. Achira, Y. Hoga, I. Yoshikawa, T. Mutai, K. Matsumura and H. Houjou, *Polyhedron*, 2016, **113**, 123-131.
496 T. Lu, J. Y. Wang, D. Tu, Z. N. Chen, X. T. Chen and Z. L. Xue, *Inorg. Chem.*, 2018, **57**, 13618-13630.
497 J. Mei, N. L. Leung, R. T. Kwok, J. W. Lam and B. Z. Tang, *Chem. Rev.*, 2015, **115**, 11718-11940.
498 M. R. Bryce, *Sci. China Chem.*, 2017, **60**, 1561-1562.
499 Y. Xie and Z. Li, *Chem*, 2018, **4**, 1-29.
500 G. Feng and B. Liu, *Acc. Chem. Res.*, 2018, **51**, 1404-1414.
501 J. A. Li, J. Zhou, Z. Mao, Z. Xie, Z. Yang, B. Xu, C. Liu, X. Chen, D. Ren, H. Pan, G. Shi, Y. Zhang and Z. Chi, *Angew. Chem. Int. Ed.*, 2018, **57**, 6449-6453.
502 H. Liu, J. Zeng, J. Guo, H. Nie, Z. Zhao and B. Z. Tang, *Angew. Chem. Int. Ed.*, 2018, **57**, 9290-9294.
503 T. Qin, J. Ding, L. Wang, M. Baumgarten, G. Zhou and K. Müllen, *J. Am. Chem. Soc.*, 2009, **131**, 14329-14336.
504 R. D. Costa, E. Ortí, H. J. Bolink, S. Graber, C. E. Housecroft and E. C. Constable, *J. Am. Chem. Soc.*, 2010, **132**, 5978-5980.